

KU Leuven  
Biomedical Sciences Group  
Faculty of Medicine  
Department of Imaging and Pathology  
Division of Nuclear Medicine & Molecular Imaging



# IMPROVED QUANTIFICATION OF MYOCARDIAL FDG UPTAKE COMBINING 4D PET/CT AND ANATOMICAL IMAGING

Anna TURCO

## Jury:

Promoter: Prof. Dr. Piet Claus  
Co-promoters: Prof. Dr. Jens-Uwe Voigt  
Dr. Ir. Kathleen Vunckx  
Chair: Prof. Dr. Werner Budts  
Jury members: Prof. Dr. Ir. Frederik Maes  
Prof. Dr. Paul Herijgers  
Dr. Kris Thielemans  
Dr. Stephan G. Nekolla

Dissertation presented in  
partial fulfilment of the  
requirements for the  
degree of Doctor in  
Biomedical Sciences

December 2016

© Copyright KU Leuven

Without written permission of the promoters and the author it is forbidden to reproduce or adapt in any form or by any means any part of this publication. Requests for obtaining the right to reproduce or utilize parts of this publication should be addressed to KU Leuven, Faculty of Medicine, Department of Imaging and Pathology, Division of Nuclear Medicine, Herestraat 49 - bus 7003, B-3000 Leuven, tel. +32-16-343715.

A written permission of the author is also required to use the methods, products, schematics and programs described in this work for industrial or commercial use, and for submitting this publication in scientific contests.

# ACKNOWLEDGEMENTS

*"Forget injuries, never forget kindnesses"* – Confucius

The past four years of PhD felt like a long and very uneven journey, with a few joyful highlights and many moments where I would have liked to trash everything and open a cupcake shop instead. I cannot believe I am actually writing the acknowledgements of my thesis...! However, if I look at it retrospectively, I am glad I went through all of this, as it was for me a learning opportunity like no other. It enriched me tremendously both professionally and personally, I took a peek into the academic world that I so much wanted to experience, and I had the chance to meet absolutely fabulous people on the way. Some of them were crucial for the completion of this work, and I would like to spend a few words and thank each of them here for their contribution.

First things first, I would like to thank KU Leuven for allowing me to start my PhD here and for providing the funding for my first year of research (OT/12/084). Along with that, I acknowledge the FWO-Research Foundation Flanders for having given me all the financial support to reach the end of this PhD, and for having seen the potential of this research project three years ago.

I want to express my deepest gratitude to all the internal and external members of my doctoral jury, Prof. Maes, Prof. Herijgers, Dr. Thielemans and Dr. Nekolla. Thank you for your immediate availability, for all the time you invested in reading my work and for all the very interesting and diverse insights you provided. I learned from them and I feel that the thesis has much improved after implementing your suggestions. For the same reasons and more, I am very grateful at the very supportive presence and thoughtful guidance of my promotor, Prof. Claus, especially in the last final run, at the enthusiasm of Prof. Voigt as first leader of this project and at the exceptional dedication of my daily supervisor, Dr. Vunckx, to the cause of my research topic even after leaving the lab. I also would like to thank Prof. Gheysens for his nuclear medicine insights, and I owe a very special thanks to Prof. Nuyts, who was not officially involved in this project but always made some time for it if needed. Johan, thank you for showing me what genuine interest in research means, for always asking the right questions, and for your selfless scientific and human support. Halfway through the PhD, that has been really crucial for me to decide to hang in there.

In the course of this work, I was lucky to work with and benefit from the expertise of other exceptional people. Thanks to Prof. Rega for developing the animal model that we used in all our experiments, to Walter Coudyzer for his availability for the CT scans and all data transfers, and to the humble but fabulous help of David Célis during our *sheep nights*. Thank you Jürgen, for having shared the joys and pains of scanning vomiting sheep and radioactive hearts until 3 in the morning, for the informal crash courses on cardiac physiology, and for all the discussions that made me feel less alone when little seemed to work. Thanks to all my colleagues in the nuclear medicine group, Ahmad, Esmaeel, Georg, Matthew and Tao. Thank you for all the honest opinions and insights on my work and presentations, for being superb cheerleaders before my so-dreaded oral presentations, for listening to creepy sheep experiment details, and for all the silly and serious lunchtime discussions that made the days a bit less gray. A special thanks goes to Matthew, for his out-of-

this-world patience with my English and my "words of the day", and with my often convoluted questions. I can't remember a day when he was not smiling and ready to give a hand. Thanks a billion Matt, especially for the Methods section of the paper derived from Chapter 3 ;-)

I also want to share my deepest gratitude towards a few special people that did not strictly contribute to the scientific content of the thesis, but they were absolutely crucial in making me reach its end with a guise of positivity. Thanks to Caitlin, who shares most of the amazing virtues of her husband and adds to that a pinch of very inspiring out-of-the-box thinking. To Maryam and Sara, for sharing their perspectives on PhD life. Thanks to Fatih and Ioanna, for sharing your life ideas so genuinely and joyfully, for the ahead-of-time template for the PhD invitation and for all the beautiful unwinding evenings. Thanks to Serena, Chiara, Clara and Martina for the long-distance support and WhatsApp presence. It was so, so important to know that I could talk to you about everything happening here. Thanks to Sofia, a beautiful soul who, completely undeservedly, always makes me feel like I am a genius. Thanks to Anna, for your discrete but trustworthy presence, for sharing your PhD path at a distance (without mentioning all the great pre-PhD years!) and for making me understand that some of my experiences here are common everywhere you go.

Last but not least, two essential thanks are missing. The first goes to my amazingly supportive family. Grazie Giuli, per avermi aiutato a trovare casa la prima volta a Leuven e per essermi venuta a trovare in questo splendido paradiso tropicale ben più di qualunque altro abbia osato. Grazie mamma, grazie papi. Per avermi sempre lasciato la libertà di decidere della mia vita, senza mai imporvi, interferire o giudicare. Per avere accettato senza esitazione la mia partenza, per il cuoricino giornaliero e per il supporto fenomenale a qualsiasi ora del giorno e della notte. Per avermi ascoltato ore e ore su Skype e per esservi sempre fatti in no quattro, diciotto per rendermi la vita un po' meno complicata in questi anni. GRAZIE, non avrei potuto immaginare di meglio. The last person that deserves a heartfelt thanks has entered my life in the descending portion of my PhD path, so he deserves bonus points for surviving it and still wearing a smile :-) Thank you Thomas, for now knowing everything about cardiac partial volume correction even though you are an industrial purchaser. For all the listening and for your awesome patience, both with my over-enthusiastic moments and with my tears. For being a safe and stable harbour in my life, for all the times I came back home disappointed and I found a smile and a warm hug to wait for me. For encouraging me to work whenever I needed to, be it a Sunday or a late evening, and at the same time for reminding me that life is not only made of that. For uplifting me whenever possible, for never doubting that I could have made it. For your joyful spirit, your love, and all your support and understanding.

## Abstract

The measurement of  $^{18}\text{F}$ -Fluorodeoxyglucose (FDG) uptake by positron emission tomography (PET) for the characterization of ischemic and non-ischemic cardiac disease is progressively increasing. In recent years, for example, the application of  $^{18}\text{F}$ -FDG PET for the prediction, follow-up and characterisation of dilated cardiomyopathy has become a subject of investigation. It has been hypothesized that hemodynamic or mechanical indicators of the cardiac workload collected from a patient can be correlated to specific uptake patterns identifiable by means of PET. However, the use of PET imaging for cardiac applications is challenged by the low spatial resolution of the clinical PET scanners, which results in blurring and does not allow for accurate quantification of very thin or small structures (partial volume effect). Additionally, the moving nature of the heart and the organs around it further complicates the measurements and introduces additional blurring in the acquired data.

In the past decade, several algorithms have been presented for the enhanced reconstruction of PET datasets, among which some that made use of additional anatomical information during reconstruction. In those works, the use of prior information had shown extremely promising results in brain, thus leading us to explore its applicability to other anatomical districts, i.e. in cardiac PET studies. Previous attempts to correct for the limited spatial resolution in cardiac studies used simpler post-reconstruction techniques or were applied on PET acquisitions which were not, or not fully, corrected for motion.

The aim of this project was to implement and validate image processing algorithms that enable the motion compensation and anatomy-guided partial volume correction of cardiac FDG-PET images, in order to evaluate whether they provide a more accurate extraction of parameters representing the regional energy consumption in the left ventricle. The application of anatomy-based partial volume correction techniques to PET dataset relies on a good alignment between the anatomical image and the low-resolution PET. Hence, any source of mis-registration needs to be avoided. In this scenario, PET attenuation correction might play a role in compromising the registration results, and subsequent PVC. Additionally, an evaluation of the effects of misalignments between the anatomical and the emission datasets is essential for exact quantification. All the aforementioned analyses need to be combined with a correction for the cardiac and respiratory motion that affect the cardiac measurements. The selected methods were evaluated using both simulations and a newly-designed animal model for dilated cardiomyopathy, which aimed at producing realistic cardiac datasets in controlled conditions with ground-truth datasets for validation.

The study of the relationship between the cardiac FDG uptake and the regional myocardial deformation as measured with echo, MR or other functional measurements, should ultimately help to better select patients for, and foresee the impact of, cardiac resynchronization therapy in the clinical practice.

# CONTENTS

<b>A</b>	<b>Introduction and objectives</b>	<b>3</b>
I	Clinical context . . . . .	5
II	Background . . . . .	6
II.1	Positron Emission Tomography (PET) . . . . .	6
II.2	Image reconstruction . . . . .	14
II.3	Partial volume effect and correction . . . . .	17
II.4	Priors . . . . .	19
II.4.1	Non-anatomical priors . . . . .	20
II.4.2	Anatomical priors . . . . .	21
II.5	How to obtain the anatomical information . . . . .	22
II.5.1	Computed tomography . . . . .	22
II.5.2	Magnetic Resonance Imaging . . . . .	23
II.6	Image registration . . . . .	24
II.7	Motion estimation and motion correction for cardiac datasets . . . . .	25
II.7.1	Signal extraction: external tracking devices vs data-driven methods . . . . .	25
II.7.2	Motion correction . . . . .	27
II.8	Obtaining the datasets: simulations and animal experiments . . . . .	29
II.8.1	Simulated datasets . . . . .	29
II.8.2	Animal experiments . . . . .	29
III	Objectives . . . . .	31
IV	Performed studies . . . . .	32
<b>B</b>	<b>Performed studies</b>	<b>35</b>
1	Impact of CT-based attenuation correction on the registration between dual-gated cardiac PET and high-resolution CT . . . . .	37
I	Introduction . . . . .	38

II	Methods . . . . .	39
III	Results . . . . .	50
IV	Discussion . . . . .	57
V	Conclusions . . . . .	63
<b>2</b>	<b>Generating ground truth datasets for cardiac PET studies using a small-animal PET scanner.</b>	<b>65</b>
I	Introduction . . . . .	66
II	Methods . . . . .	67
III	Results . . . . .	73
IV	Discussion and conclusions . . . . .	77
V	Acknowledgements . . . . .	79
<b>3</b>	<b>Analysis of partial volume correction on quantification and regional heterogeneity in cardiac PET</b>	<b>81</b>
I	Introduction . . . . .	82
II	Methods . . . . .	83
III	Results . . . . .	87
IV	Discussion . . . . .	92
V	Conclusions . . . . .	95
<b>4</b>	<b>Lesion quantification and detection in myocardial <math>^{18}\text{F}</math>-FDG PET using edge-preserving priors and anatomical information from CT and MRI: A simulation study</b>	<b>97</b>
I	Background . . . . .	98
II	Methods . . . . .	100
III	Results . . . . .	112
IV	Discussion . . . . .	124
V	Conclusions . . . . .	129
<b>5</b>	<b>Partial volume and motion correction in cardiac PET: first results from an <i>in</i> vs <i>ex vivo</i> comparison using animal datasets.</b>	<b>131</b>
I	Introduction . . . . .	132
II	Methods . . . . .	133
III	Results . . . . .	137
IV	Discussion and conclusion . . . . .	141
<b>C</b>	<b>Discussion, conclusions and future perspectives</b>	<b>147</b>

## **A INTRODUCTION AND OBJECTIVES**



# I CLINICAL CONTEXT

Left ventricular (LV) dyssynchrony is a pathological condition by which a temporal non-uniformity in the contraction of the LV walls is observed, which eventually causes heart failure. In left bundle branch block (LBBB), this dyssynchrony is mainly found between the intraventricular septum and the LV lateral wall. Cardiac resynchronization therapy (CRT) with bi-ventricular pacemakers has become an accepted treatment for patients with heart failure and LV intraventricular dyssynchrony, but this costly and invasive therapy still fails in more than 30% of the cases [1].

Echocardiographic measurements have been proposed in the past to assess the severity of dilated cardiomyopathy (DCM) and the eligibility for CRT by measuring myocardial deformation and deformation velocity [2, 3]. However, the sole use of echocardiography for the characterisation of cardiac disease and for therapy planning might not be sufficient for increasing the success rate of CRT, as such methods are not able to distinguish the reason of the observed cardiac dyssynchrony and to fully reflect the complex underlying cardiac function and energetics [4, 5]. It has been hypothesised that only the patients whose dyssynchrony is caused by a certain pattern of abnormal conduction might benefit from CRT [6], thus ways to distinguish the aetiology of the dyssynchronous LV behaviour might be needed to increase the success rate of this therapy.

The dyssynchrony between septal and lateral wall results in an imbalance in mechanical workload within the left ventricle which can be assessed with deformation imaging. The combined analysis of echocardiographic measures and the regional loading conditions of the heart, i.e. wall stress, has shown to have a better predictive value for the success of CRT [7]. The estimation of regional wall stress is, however, not measurable *in vivo*. Attempts to extract this parameter have been performed using, for example, finite-element models of the left ventricle [8]. On a parallel track, it was attempted to use other parameters, for example LV pressure, as surrogates of wall stress with encouraging results [9–11]. The integration of pressure measurements and echocardiographic measures of deformation led to the development of the concept of myocardial workload, which has shown to be a predictor for the response of patients to CRT [12, 13]. The changes in myocardial workload are mirrored by changes in myocardial metabolism. To assess the latter, positron emission tomography is the non-invasive modality of choice, but a need for optimization of absolute quantification in cardiac PET still remains. This will be the topic of this thesis.

## *PET for assessing myocardial energetics*

The use of positron emission tomography (PET) for the characterization of cardiac pathologies is progressively increasing [14]. PET, compared to both single-photon emission computed tomography (SPECT) and computed tomography (CT), has a greater sensitivity and is able to assess a wide range of known or suspected cardiac conditions with an outstanding predictive and diagnostic value. Myocardial perfusion and perfusion reserve as well as metabolism can be characterized with the help of PET imaging. Moreover, thanks to the use of different tracers tailored to specific imaging needs, myocardial pathologies such as sarcoidosis or amyloidosis can be diagnosed [15–18].

The measurement of  $^{18}\text{F}$ -FDG uptake by PET is a validated and robust tool to investigate regional metabolism. In recent years, the application of  $^{18}\text{F}$ -FDG PET for the prediction, staging and characterisation of DCM has become a subject of investigation. It has been hypothesized that hemodynamic or mechanical indicators of the cardiac workload collected from a patient can be correlated to specific uptake patterns identifiable by means of PET [11]. If such correlation was proven, PET images could be safely used in substitution to, or more likely in combination with workload measurements to extract, in a non-invasive fashion, parameters useful to assess even more effectively the progression and status of cardiac pathologies and to evaluate the severity of heart failure and the responsiveness to CRT.

Regional differences in myocardial  $^{18}\text{F}$ -FDG uptake have been observed in the past [19], but they can be influenced by the inhomogeneous regional wall thickness in DCM hearts, which can cause a different apparent uptake within the heart due to the limited spatial resolution of the imaging system. In addition to the blurring introduced by the spatial resolution of the PET scanner, the motion of the heart which occurs during the entire PET examination, due to the heartbeat and to the breathing motion to which the heart is indirectly subject, introduces further blurring and causes additional uncertainty on the estimated  $^{18}\text{F}$ -FDG distribution. Previous attempts to correct for this limited spatial resolution in cardiac studies were applied on PET acquisitions which were not corrected for motion (thus yielding remaining quantification errors) and used simple post-reconstruction methods [20, 21], or performed only the correction of (one of the two) motions which affect cardiac measurements and did not take into account the blurring due to the limited spatial resolution [22].

The work here presented is part of a broader project whose aim is to assess regional myocardial energy consumption using  $^{18}\text{F}$ -FDG as marker of regional workload. The relationship between these two measurements was studied using an animal model with inhomogeneous LV function and wall thickness due to pacemaker stimulation. The hearts were then scanned with and without conduction abnormalities in order to determine changes in regional workload distribution. In this project, ways to correct for the limited spatial resolution of the imaging system during the reconstruction of the PET datasets were evaluated as a means to guarantee exact quantification of the left ventricular uptake and with this, regional work. The evaluated methods were analysed in combination with ways to correct for the cardiac and respiratory motion that affect the cardiac measurements. The aim is to obtain images with high qualitative and quantitative accuracy, free from motion- and resolution-related blurring, which could be used in the future to investigate the regional work load–function interaction in ischemic and non-ischemic pathologies.

## II BACKGROUND

### II.1 POSITRON EMISSION TOMOGRAPHY (PET)

Emission tomography (ET) is a branch of medical imaging with two main unique characteristics. Firstly, the purpose of emission tomography is to pinpoint *metabolic* changes that occur within the patient's body. Other modalities – e.g. MRI or CT

– traditionally focus, on the other hand, on an accurate morphological description of the anatomies, regardless of their metabolism. Secondly, while CT or MRI make use of sources of X-Rays (CT) or magnetic fields that are external to the patient’s body, ET acts in the opposite way by administrating to the patient a substance that is radioactive and will highlight the metabolic patterns of the patient *from the inside* of the patient’s body.

Positron emission tomography was developed and perfected in the second half of the twentieth century [23]. Together with SPECT, PET is one of the imaging modalities belonging to the family of ET imaging. The use of PET in this work is justified by its superior spatial resolution and its high sensitivity compared to SPECT, coupled to the fact that, at the moment this work was started, it allowed for a more quantitative evaluation of the cardiac metabolism when compared to SPECT. Moreover, even though in recent years there has been increasing interest into MRI techniques to assess myocardial viability, the use of PET is still widespread and often the only imaging option, e.g. in patients with non-compatible MRI pacemakers or claustrophobia [24, 25].

## RADIOTRACERS

In a typical PET examination, the patient is injected with (or swallows, or inhales) a radioactive tracer, that is an analogue of a biological molecule normally circulating in the human body labelled with a radionuclide emitting positrons. One fundamental property of any radiotracer is that it has to be injected in very small amounts, in order not to perturb nor modify the normal metabolic pathway.

All radioactive compounds decay, with different decay rates and half-lives, to a more stable, lower energy state compound. In the case of **positron** emission tomography, all radiotracers must achieve a lower energy state by emitting a *positron* (or *beta+ decay*). One of the protons in the nucleus of the radioactive atom turns into a neutron, and a positron and a neutrino are emitted from it. The positron travels a very small distance in the matter surrounding the atom, until it collides with an electron (*annihilation*). The annihilation results in the production of two anti-parallel (approximately 180 degrees apart) photons or *gamma rays*, whose energy is equal to the rest energy of the positron before annihilation.

Several radioactive tracers have been developed in the past for cardiac studies. They differ by the molecular mechanism in which they take part, by the patient compliance and uptake, by how well they bind to the site of interest and by the decay time (half-life) [26,27]. In this work, we are interested in assessing the changes in glucose uptake as a possible measure of cardiac workload, hence tracers that pinpoint such process were of interest.

A tracer widely used in the clinical practice tracking **glucose** is fluorodeoxyglucose (**<sup>18</sup>F-FDG**). This tracer is obtained by substituting one of the hydroxyl groups of a glucose molecule, with a radiation-emitting isotope of fluorine (<sup>18</sup>F). The resulting molecule follows the same metabolic pathways as glucose but, differently from glucose, it emits radiation and it remains trapped (thus, accumulates) in the glucose-avid organs. The use of <sup>18</sup>F-FDG is well-established in the clinical practice. The tracer has a long half-life which facilitates long acquisitions for motion-corrected or dynamic studies, thus facilitating the application and the introduction into the

clinical practice of the techniques evaluated in this work. Additionally, under clamping conditions, it is known that the heart metabolism can switch from consuming fatty-acids to consuming a prevalence of glucose under certain circumstances [28]. Therefore, the assessment of cardiac viability by means of  $^{18}\text{F}$ -FDG PET is further facilitated and enhanced.

## TYPES OF PET SCANNERS USED

A typical PET scanner consists of a set of detectors arranged to form a cylinder, in which the patient is inserted and scanned.

In this work, we make a distinction between pre-clinical and clinical PET scanners. The pre-clinical PET scanner we used was the Siemens Focus 220 (**microPET**). As most pre-clinical scanners, the microPET scanner has a very small bore size, which allows the imaging of mostly rats, mice, or very small objects that would fit in its field-of-view (FOV). The advantage of pre-clinical PET scanners is their superior spatial resolution compared to clinical PET scanners, which allows for a more accurate representation of the distribution of the radioactive tracer.

Clinical PET scanners are nowadays always hybrid systems that feature not only a PET module, but also an MRI or a CT module combined to the PET module. The PET/CT scanner available in our center at the time when this work was started was the Siemens Biograph 16 PET/CT (**Hirez**, [29]). The PET module of such scanner features state-of-the-art detecting elements for a non-TOF (time-of-flight) PET device, and its use is widespread in the clinics. The details of the microPET and of the Hirrez scanner are in Table 1.

*Table 1: Salient technical specifications of the microPET and of the Hirrez scanner [29–31]*

	microPET	Hirez
Diameter [cm]	26	83
Transxial FOV [cm]	19	58.5
Axial FOV [cm]	7.6	16.2
Axial sampling interval [mm]	0.79	2.0
No. crystals/ring	2016	624
No. crystals/block	12 x 12	13 x 13
No. block rings	48	39
Radial resolution [mm], FWHM@1cm	n/a	4.61
Axial resolution [mm], FWHM@1cm	n/a	5.10
Radial resolution [mm], FWHM@center	1.3	n/a
Axial resolution [mm], FWHM@center	1.46	n/a
Scatter fraction [%]	19	34.1

## DETECTORS AND DATA COLLECTION

Upon decay of the radioactive  $^{18}\text{F}$ -FDG molecule, an annihilation of a positron with an electron takes place, resulting in the emission of two gamma rays which travel from the annihilation point until they hit the detectors of the scanner (Figure 1, A). The energy of the gamma rays is 511 keV for  $^{18}\text{F}$ -FDG.

The detectors used for PET are generally arrays of scintillation crystals, that emit energy in the form of light when they are hit by a gamma ray. The light photon emitted by the scintillation crystal is converted to an electron and later collected by a photomultiplier, which amplifies the electron into a stream of electrons to be processed by the scanner's electronics.

In PET, an event is recorded when two gamma rays are absorbed (almost) simultaneously within two different crystals (Figure 1, B). The *coincidence window* is the maximum time difference allowed between the hits of two gamma rays. If a longer time elapses, the two photons are discarded. A couple of photons that hit two distinct detectors within the same coincidence window form a *coincidence*.

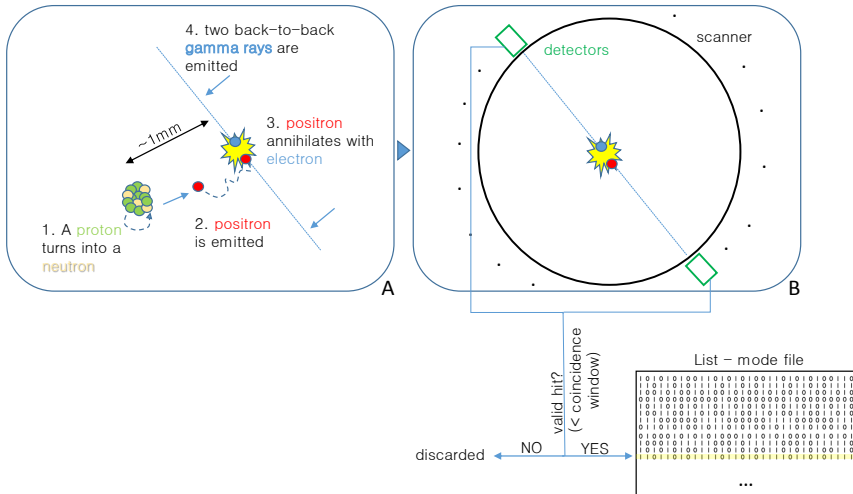
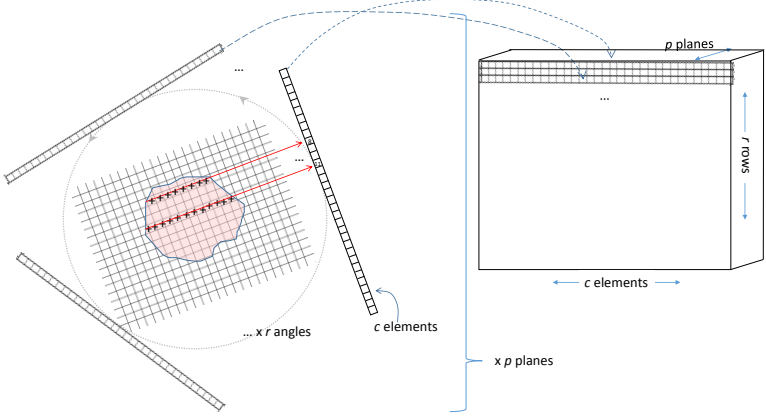


Figure 1: Flow of events, from the nucleus decay and annihilation of the positron with an electron (A), to the detection of a coincidence (B).

The photons that hit the detectors and qualify as part of a valid coincidence can be stored in a *list-mode* or *raw* file. In such a file, all the events are simply listed one after the other. Each event contains the address of the detector that has been hit. Regular time stamps are also stored in the list-mode file. Additionally, the list mode file can contain information (tags) on particular events that occurred during the acquisition. For example, if an electrocardiograph (ECG) device is connected to the scanner and is set to send a signal to the scanner at each occurrence of an R-wave of the ECG, such event will be recorded in the listmode as a "cardiac tag". A similar process occurs when a respiratory tracking device is connected to the scanner. The list-mode files are informative and complete, but typically very lengthy. A more efficient and commonly used way to store the information that is collected is to make use of *sinograms* (Figure 2), despite the non-reversibility of such listmode-to-sinogram conversion.

## DATA FORMATION

In the ideal case-scenario, if two gamma rays are detected within the same coincidence window, and assuming that they are emitted back-to-back from the annihila-



*Figure 2: Forward projection and sinogram formation.* A sinogram is a 3D matrix with  $c$  columns,  $r$  rows and  $p$  planes. We can imagine to build a sinogram by placing  $r$  rows of  $c$  elements at  $r$  different angles (projection angles) around the object. The value in each of the elements of each row is the sum of all the events that hit that detector during the whole duration of the PET scan at that projection angle. The process of calculating the total events per row, per projection angle is called (forward-)projection. This is repeated for all the  $p$  planes of interest. The sinogram is the collection of all the projections at different projection angles and at different axial positions ( $c \times r \times p$  matrix).

tion site, it is possible to infer the line along which the annihilation must have taken place. This line, that connects the detector pairs hit by the gamma rays, is called *line of response* (LOR). In regular PET, the annihilation event can have occurred with equal probability on any of the points along the LOR. In time-of-flight (TOF) PET – not used in this work, but promising for future applications – it is possible to constrain the estimated annihilation point to a particular segment along the LOR. In both cases, the more lines of response are emitted from that annihilation position and collected, the more accurate it is to infer the exact spot within the body where the annihilation took place.

## ATTENUATION, SCATTER AND RANDOM EVENTS

The process described so far refers to the case where all ideal conditions are respected. Particularly, this assumes that the detectors scintillate as soon as the photon gets in contact with their surface, that the gamma rays proceed unattenuated and not deviating from their ideal trajectory, that no other photon hits the detectors in the same coincidence window as another couple of photons, that the annihilation point is coinciding to the location of the radioactive molecule, etc. However, in reality, these assumptions are often violated. The most significant sources of imperfection in a real PET acquisition are represented by attenuation, scatter and random effects.

## ATTENUATION CORRECTION

All photons travel through the tissues and organs that surround the annihilation point and are **attenuated** (Figure 3, A) by them following the Beer-Lambert law:

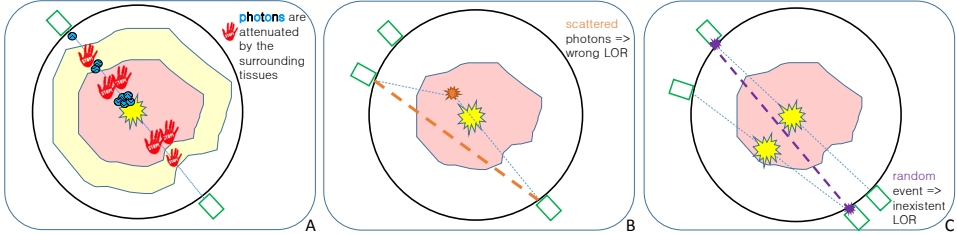


Figure 3: The three main sources of inaccurate image quantification in PET: attenuation (A), scatter (B) and random (C) effects.

$$N = N_0 e^{-F(\mu, l)}$$

where  $F$  is the line integral of the attenuation coefficients along the path  $l$  travelled by the photon on the LOR,  $N$  is the number of photons reaching the detector,  $N_0$  is the initial number of photons and  $\mu$  is the linear attenuation coefficient of (each of) the transgressed tissue(s). If the effect of photon attenuation is not taken into account, no accurate quantification of regional activity can be obtained. The absence of attenuation correction results in images with typical attenuation artefacts, as in the left pane of Figure 4. In addition, the attenuation correction needs to be done in the most accurate possible way. If a photon comes from an attenuating tissue, but the attenuation coefficient of that region is wrongly assigned (e.g., a lower attenuation for that tissue is assumed), the reconstructed activity would also be lower than actual, thus creating artefactual, low metabolism areas. Such errors are particularly common when tissues with a very low attenuation coefficient (e.g. air, lungs) are close to tissues with a stronger attenuating power (e.g. the heart).

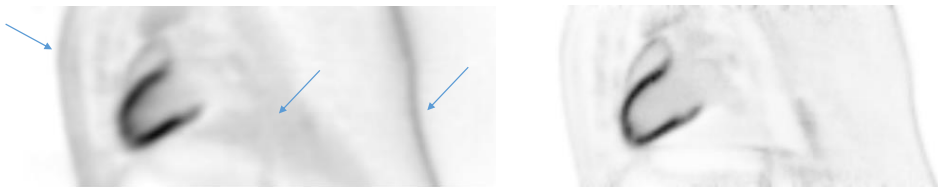


Figure 4: A non-attenuation corrected dataset (left-hand pane) displays typical attenuation artefacts such as apparent overestimation of activity from regions that should not have any (e.g. the skin). On the right-hand side, the same dataset corrected for attenuation.

### Ways to perform attenuation correction

The assignment of the correct attenuation coefficients for the different tissues has been the subject of thorough investigation. Three main strategies for attenuation correction (AC) can be discriminated: using a transmission scan [32], using a CT [33, 34], and estimating the attenuation coefficients directly from the PET scan [35]. In this work, the second AC method was considered, as it is the one most frequently applied in the clinical routine. This method estimates the linear attenuation coefficients ( $\mu$ ) to be assigned to the different PET tissues by acquiring a CT image right before or after the PET scan. In this way, a very accurate map of the body regions within the field of view is obtained. The values of such tissue map

indicate the attenuation that each tissue opposed to the passage of the X-rays. The first method (transmission scans) uses a  $^{68}\text{Ge}/^{68}\text{Ga}$  point source orbiting around the patient to collect the attenuation coefficients. This technique has been widely used in the past, but was slowly discarded due to the long time needed to acquire the transmission image for AC, and to the advent of more accurate AC images that could be obtained from the CT module of hybrid PET/CT scanners. In pre-clinical PET scanners, such as the microPET Focus 220 used in this work, transmission scans are however still in use. The third method estimates the attenuation coefficients directly from the PET data. This method is extremely promising but yields the best results for TOF PET scanners [36] and is not recommended for non-TOF applications.

### ***Difficulties of attenuation correction***

The CT for AC is normally acquired in a few seconds and with a relatively low extra radiation burden for the patient. Despite these benefits, however, the estimation of PET attenuation coefficients using a CT scan is not free from drawbacks. Firstly, the CT image describes the attenuation of the different tissues to photons penetration, but in the case of the CT the energy of the photons emitted by the CT X-Ray tube ranges between 80 and 120 kV (peak voltage). Therefore, a conversion needs to be performed, in order to find the attenuation coefficients for the energy of the PET photons (511 keV). Nowadays, a bilinear interpolation is used to convert the CT attenuation coefficients to PET attenuation coefficients [34,37], and the resulting CT image (which is an approximation of the true attenuation) is used to subsequently correct the PET data for the effects of attenuation. The second major drawback in the use of a CT which has been acquired not simultaneously to the PET for AC is the fact that the patient or the organs of interest can move between or during the two scans, thus introducing discrepancies between the PET and the CT. A mis-alignment of the PET scan relative to the CT scan can produce attenuation artefacts as indicated earlier in this section. Moreover, if one of the two datasets (PET or CT) contains motion and the other is either acquired in a frozen position or corrected for motion post-acquisition, additional discrepancies can occur. This problem has been addressed in the past also for cardiac datasets [38–40]. However, in most of these studies, the PET is blurred due to the breathing and the beating motion of the heart, whereas the AC CT is often not affected, or much less affected, by the breathing motion of the heart. The methods that were proposed to address the mismatch between the PET and CT datasets with regards to motion ranged from improving the alignment of the AC CT and the PET dataset prior to the final reconstruction to using an AC CT that is an average of multiple breathing and beating states (cine-CT, average CT). In all the aforementioned studies, as said, the PET dataset is affected by motion. Conversely, in the current project, the PET datasets are motion-corrected and it is now the AC CT that is too "slow" for correcting one single cardiac PET frame from which both the cardiac and the breathing motion have been removed. This problem has, so far, not been addressed in literature, but it is of fundamental importance for the accurate quantification of the motion-corrected PET datasets. In fact, correcting the motion-corrected PET dataset for attenuation using an AC CT that spans over multiple respiratory and/or cardiac cycles is by all means an approximation, which can introduce artefacts as likely as any other mismatched AC CT.

## SCATTER CORRECTION

A second cause of mistakes in the quantification of PET images is the inaccurate correction for Compton **scattering** of the photons within the medium. As shown in Figure 3 (B), a photon can hit an electron in the surrounding matter, before reaching the detector. The photon is thus deviated from its original trajectory and it loses energy during the hit. Consequent to the deviation of trajectory, a different detector is hit and the estimated line-of-response is wrong, as it does not contain the annihilation point along its path. The typical approach to scatter correction is twofold [41]. Firstly, an energy window is defined for all the photons that hit the detectors, thus immediately discarding those whose detected energy falls below the lower boundary of the window. Secondly, the CT used for attenuation correction is used to estimate the scatter contribution, as scatter is highest in the tissues with higher density. In addition, all areas defined as background in the AC CT should be only affected by scatter and random events in the corresponding PET reconstruction. Therefore, in those areas, the scatter estimate is adjusted so that the estimated scatter activity matches the PET activity (*tail fitting*).

Correction for scattered events is recommended and has become common in clinical nuclear medicine, due to the significant quantification errors that it can yield. In 3D PET cardiac studies, where more than 50% of the collected events can be scattered – especially when the patient is positioned with the arms along the body – the use of such scatter correction techniques is essential [42]. When pre-clinical PET studies are considered, however, scatter correction is often neglected. It has been reported that a fraction ranging e.g. from 7.2 (mice) to 20 % (rat) of the recorded events undergoes Compton scattering in the pre-clinical scanner we used for our experiments [43], which determines minor quantification inaccuracies. When multiple rats are scanned simultaneously in a pre-clinical PET device, or when larger, heterogeneous objects are scanned, performing scatter correction becomes necessary to guarantee accurate image quantification [44, 45]. Given the non-conventional shape and size of the *ex vivo* hearts scanned with the microPET in the scope of our study, the effect of scatter on those datasets needed to be investigated.

## RANDOM EVENTS CORRECTION

**Random** events can also affect correct PET quantification. Random coincidences are recorded when two photons from different annihilations hit the detectors within the same coincidence window, while the other two photons are not detected. In this way, again, a wrong LOR is reconstructed (Figure 3 (C)). Analytical approaches (e.g. *delayed window*) can be used to estimate the contribution of the random coincidences from the initial PET dataset [46].

## SYSTEM RESOLUTION

The **limited spatial resolution** of the imaging system can be defined as the minimum distance at which two distinct point sources can be placed before the imaging system sees them as one single blurred-out point, or as the blurring of a point source caused by the properties of the imaging system. Several physical

factors contribute to the final resolution of the imaging system. The size of the detector elements, together with the acollinearity of the gamma rays, the positron range before annihilation, the depth of interaction within the detectors (determined by the type, the composition and size of the detectors) and decoding errors in the detector modules are the main contributors to it. Its effect is described by the point spread function (PSF) of the scanning device, which is often approximated by a Gaussian function whose full-width at half-maximum (FWHM) corresponds to the spatial resolution of the scanner. Normally, for clinical PET scanners, the spatial resolution ranges between 3 and 8 mm, while for pre-clinical PET scanners the values go as low as 1-2 mm [47].

## II.2 IMAGE RECONSTRUCTION

The goal of PET image reconstruction is to reproduce the initial three-dimensional (3D) distribution of the radioactive tracer, given the data measured about that distribution by an imaging device. For PET, two main types of reconstruction approaches exist: analytical reconstruction and iterative reconstruction.

The process of analytical reconstruction of an image, given a set of measurements, is to apply the inverse of the projection operator (Section II.1) to the measured data to obtain the reconstructed image. A detailed description of the most commonly used implementation of an analytical reconstruction method for PET data can be found in [48]. Each projection is "smeared" back (back-projected) along the path that led to its acquisition. For analytical reconstruction to be mathematically achievable, some assumptions on the acquired data are made: the measurements are not affected by noise, the number of projection angles tends to infinity and the data have been corrected for sensitivity and attenuation. In cases where these approximations are not valid, artefacts are obtained if analytical reconstruction is used.

As a matter of fact, real data are always subject to noise, resolution inaccuracies, detector imperfections, .. and are acquired over a limited set of projection angles. Therefore, the analytical inversion of the forward-projection would produce images that suffer from artefacts and would carry onto the reconstructions the inaccuracies that affect the measurements. In the last few decades, a different approach to reconstruction was proposed, which computes the data in an iterative fashion.

Iterative reconstruction methods have a similar quantitative accuracy to analytic reconstruction methods (e.g. filtered backprojection (FBP)), but they additionally allow for the modelling of spatial resolution, attenuation, sensitivity, ... effects in a very easy and straightforward way and they produce images of superior quality and lower noise [49]. Given that the use of iterative reconstruction is well established and clinically accepted, we decided to use it as our reference reconstruction method. Moreover, an important aspect of this work was the evaluation of resolution modelling in combination with non-linear and/or shift variant priors (anatomical priors, total variation) during reconstruction – which cannot be achieved with FBP.

## ITERATIVE RECONSTRUCTION

Iterative reconstruction does not assume that the reconstruction can be done with one single analytical back-projection. Knowing that the exact inversion of the measurement is impossible, it instead tries to find the tracer distribution that was most likely in the PET system, considering the available measured data. An initial image is first obtained by back-projection of the measurement. Next, a realistic model of the PET system is simulated and the photon pairs that would be expected along every LOR are computed (forward-projection of the image). The resulting, calculated projection is then compared with the real measurement and, based on that comparison, the image is updated. This process is repeated until a stopping criterion is met (e.g. a pre-defined number of iterations is reached). At each iteration, the error between the calculated projection and the real measurement is used to improve the subsequent back-projections, which gradually resemble more the original scanned object. Because the data are noisy and the forward model is not perfect, the final image is not the exact reproduction of the original object, but there is at least reason to assume it should be reasonably close to the true image. In the remaining of this section, a brief mathematical explanation of iterative reconstruction (ML-EM, maximum likelihood-expectation maximization) is given. In Section II.4, we will show how the prior information can be incorporated in such implementation.

Let us consider an object  $O$  scanned in a PET device, so that the measured data  $M$  in sinogram format are obtained. It is assumed that not only the measured data  $M$  are discrete, but also that the object  $O$  is discrete and it consists of voxels with uniform tracer uptake. In each of the pixels of the sinogram is a number  $m_i$ , which represents the total amount of photon pairs that hit that particular detector during the scan (Section II.1). According to the projection model, by which each element of the sinogram is constructed by summing the total activity over projection lines, in each sinogram pixel  $i$  we expect a value equal to  $s_i$ , that is to say:

$$s_i = \sum_{j=1}^J c_{ij} \lambda_j \quad (1)$$

$\lambda_j$  is the activity that is present in the  $j$ -th voxel of the object  $O$  and  $c_{ij}$  models the geometry and the physical effects (eg. attenuation, scanner sensitivity, ...) that occur during the projection of the  $j$ -th voxel to the  $i$ -th sinogram voxel.  $\lambda_j$  is unknown, and the task of iterative image reconstruction is to estimate it as precisely as possible from the measured sinogram  $M$ .

Of all the many photon pairs that are emitted by the object  $O$ , a few of them randomly hit the detector pairs with a predictable rate. The hits follow a Poisson distribution, hence the probability to find exactly  $m_i$  events (the actually measured events) in the  $i$ -th detector, given the expected number of events  $s_i$ , can be described as:

$$p(m_i | s_i) = \frac{e^{-s_i} s_i^{m_i}}{m_i!}$$

Since all the photon pairs arrive independently from one another, that is to say that the previous photon pairs that hit the detectors do not influence the number of photon pairs that will arrive next, and if there is no noise correlation between detector pixels, we can describe the probability of obtaining the full measured dataset M as the product of the individual probabilities of arrival of each photon pair:

$$\begin{aligned} p(M | \lambda) &= p(m_1 | s_1) \times p(m_2 | s_2) \times \dots \times p(m_n | s_n) \\ &= \prod_{i=1}^N p(m_i | s_i) = \prod_{i=1}^N \frac{e^{-s_i} s_i^{m_i}}{m_i!} \end{aligned} \quad (2)$$

where  $\lambda$  is the total activity of the object we want to estimate.

The objective of iterative reconstruction is to maximise the chances of obtaining  $\lambda$  given M, that is to say to maximise  $p(\lambda | M)$ . Since the maximization of  $p(\lambda | M)$  is non-trivial, a probability rule (Bayes' rule) can be used to rewrite  $p(\lambda | M)$  as a combination of factors that is easier to maximize:

$$p(\lambda | M) = \frac{p(M | \lambda)p(\lambda)}{p(M)} \quad (3)$$

$p(M)$  is a constant value, because we actually have the real measurement M. For the moment, we ignore  $p(\lambda)$ , which describes the probability of having a particular activity distribution in the reconstructed image (prior information, see Section II.4). In other words, we assume that all  $\lambda$  distributions are a-priori equally likely and we are only going to deduce the image from the measured data (not from any other source of knowledge). Therefore, after excluding the contribution of these two terms, we can maximize the probability  $p(M | \lambda)$  instead of  $p(\lambda | M)$ , with the advantage that maximizing  $p(M | \lambda)$  is easier.

Additionally, maximizing  $p(M | \lambda)$  is equivalent to maximizing the logarithm of  $p(M | \lambda)$ . We can define the following *log-likelihood* function  $L$ , of which the maximum needs to be found, by taking the logarithm of Equation 2:

$$L = \ln p(M | \lambda) = \sum_{i=1}^N (m_i \ln s_i - s_i + \ln m_i!)$$

where we can drop the contribution of the last term, as it does not depend on  $\lambda$ , and maximize the following function:

$$L = \sum_{i=1}^N (m_i \ln s_i - s_i) = \sum_{i=1}^N (m_i \ln \sum_{j=1}^J c_{ij} \lambda_j - \sum_{j=1}^J c_{ij} \lambda_j) \quad (4)$$

A common way to find the maxima (and minima) of a function is to calculate the derivative of the function and find when it equals zero. Thus, the  $\hat{\lambda}$  that maximises

$L$  can be obtained by calculating the derivative of  $L$  with respect to  $\lambda$ , and imposing it equals zero:

$$\frac{\partial L}{\partial \lambda_j} = \sum_{i=1}^N c_{ij} \left( \frac{m_i}{\sum_{k=1}^J c_{ik} \lambda_k} - 1 \right) = 0 \quad (5)$$

Equation 5 is hard to solve directly. In order to speed up the computations and obtain a solution anyway acceptable, the likelihood of the expected counts (expectation) is maximized instead.

The result is the **ML-EM algorithm**, by which we can estimate, iteration by iteration, the  $\hat{\lambda}$  that best explains the measured activity:

$$\lambda_j^{new} = \frac{\lambda_j^{old}}{\sum_{i=1}^N c_{ij}} \sum_{i=1}^N c_{ij} \frac{m_i}{\sum_{k=1}^J c_{ik} \lambda_k^{old}} \quad (6)$$

From this formula, we can see that the measurement ( $m_i$ ) is compared to the projection of the image in the previous iteration ( $\sum_{k=1}^J c_{ik} \lambda_k^{old}$ ). This ratio ( $r_i$ ), which quantifies to what extent the measurement  $m_i$  would be over- or underestimated based on the current image  $\lambda^{old}$ , is back-projected ( $\sum_{i=1}^N c_{ij} r_i$ ), divided by the sum of the backprojection weights ( $\sum_{i=1}^N c_{ij}$ ) and multiplied with the old image ( $\lambda_j^{old}$ ) to generate the new image ( $\lambda_j^{new}$ ), which more likely resembles the actual activity distribution. This process is repeated iteratively. It can be proved that the iterative application of Equation 6 produces a  $\hat{\lambda}$  that maximises the likelihood  $L$ , hence it is a suitable alternative way to estimate  $\hat{\lambda}$  [50].

Using the expression of Equation 5, this formula can also be rewritten in an additive form, whose use will be clear in Section II.4:

$$\lambda_j^{new} = \frac{\lambda_j^{old}}{\sum_{i=1}^N c_{ij}} \frac{\partial L}{\partial \lambda_j^{old}} + \lambda_j^{old} \quad (7)$$

The estimated  $\hat{\lambda}$  is not the only distribution of activity that can explain the measured data  $M$ , but it is the most likely solution. The additional, *a priori* knowledge that some activity distributions are more likely than others can be used and added to the algorithm by considering the contribution of  $p(\lambda)$  in Equation 3. This will be further elaborated in Section II.4.

## II.3 PARTIAL VOLUME EFFECT AND CORRECTION

### PARTIAL VOLUME EFFECT

Partial volume effect (PVE) is defined as the apparent loss of activity in small objects or regions, because of the combined effect of two distinct factors: the limited resolution of the imaging system (see above section: System resolution) and the poor sampling of the reconstructed image (voxel size).

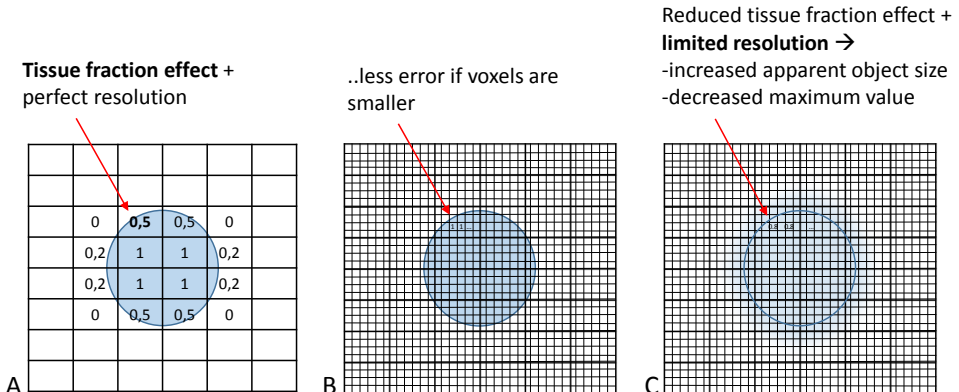


Figure 5: The partial volume effect is the combination of the poor sampling of the image (A), which can be mitigated by reducing the voxel size(B), and the limited spatial resolution of the system(C).

The **finite voxel size** of the reconstructed image causes the intensity of each voxel to be the mean of the signal intensities of the tissues underlying that voxel (also known as *tissue fraction effect*, Figure 5-A). It is present even in the case of perfect spatial resolution of the system, and can be mitigated by reducing the voxel size (Figure 5-B).

The PVE affects the accurate reconstruction of the signals coming from a signal source. In fact, part of the activity present in a certain region is instead blurred out and seen outside the actual boundaries. Additionally, its peak value is decreased (Figure 5-C). In other words, PVE leads to an overestimation of the source size and an underestimation of the source intensity.

Provided that the voxel size can be tuned so that the tissue fraction effect is minimized, structures that are smaller than the spatial resolution of the imaging system are anyway not accurately rendered in the final image, if no additional constraint is applied. In the case of cardiac studies, this could represent a cause of inaccurate quantification when the thinnest myocardial regions are of interest (right ventricle, apex, non-transmural scar, ...). Additionally, in case of inhomogeneous regional wall thickness determined by pathological conditions, e.g. DCM, the thinning of the septal wall could cause an apparent decreased uptake in the corresponding area of the reconstructed image. For these reasons, a way to correct for PVE is desirable. The solutions that have been proposed in the past to overcome the PVEs will be briefly summarized in the next section.

## PARTIAL VOLUME CORRECTION

Partial volume correction (PVC) techniques can be applied to overcome the issues introduced by the partial volume effect (size overestimation and intensity underestimation). In this work, we will use the term PVC to indicate, in general, all techniques that address the problem of partial volume effect, regardless whether they are applied post- or during reconstruction. Among the methods that have been proposed in the past to tackle the PVEs, an effective way is represented by the incorporation of the resolution effects into the system matrix during the iterative

image reconstruction process. This process can effectively deal with PVEs but, due to the ill-posed nature of the problem, reconstruction with resolution recovery can lead to over- and under-shoots of the reconstructed activity, known as Gibbs artefacts, that might hamper accurate image quantification [51]. Consequently, some additional regularization is needed to constrain the solution obtained by means of iterative reconstruction. In this work, PVC is achieved during reconstruction, by combining the modelling of the resolution effects with some additional (prior) information, in turn used to reduce the Gibbs artefacts introduced by the sole modelling of the resolution. The section that follows includes a general introduction on how to incorporate prior information into the iterative reconstruction framework, and describes the priors that have been used in the course of this work.

## II.4 PRIORS

In Section II.2, maximizing the likelihood of the expected counts was considered equivalent to maximizing  $p(\lambda | M)$ , because we assumed that every activity distribution was equally likely, i.e.  $p(\lambda) = \text{constant}$  in Equation 3.  $p(\lambda)$  described the prior knowledge we have on the activity distribution. An example of prior knowledge could be the fact that we know that any intensity transition lower than a certain threshold is noise, that the reconstructed image should consist of piecewise smooth areas, or that the activity in the wall of the heart is much higher than the activity in the lungs. Introducing some additional information on the activity distribution during the reconstruction process should help to correctly select, between all the possible activity distributions allowed by the data, the one that is most clinically useful and sensible.

If  $p(\lambda)$  was not ignored, Equation 4 would become:

$$L = \ln p(\lambda | M) + \ln p(\lambda) = \sum_{i=1}^N (m_i \ln s_i - s_i) + P$$

with  $P = \ln p(\lambda)$  that describes how the prior information should be incorporated during reconstruction. Equation 6, in turn, updates to:

$$\lambda_j^{new} = \frac{\lambda_j^{old}}{\sum_{i=1}^N c_{ij} - \frac{dP}{d\lambda_j}} \sum_{i=1}^N c_{ij} \frac{m_i}{\sum_{k=1}^J c_{ik} \lambda_k^{old}} \quad (8)$$

If  $\frac{dP}{d\lambda_j}$  was evaluated with  $\lambda^{new}$ , then Equation 8 would be exact. However, as  $\lambda^{new}$  is not yet available, Equation 8 can be approximated by calculating  $\frac{dP}{d\lambda_j}$  with  $\lambda^{old}$ , so that the final  $\lambda^{new}$  can be computed from known quantities (one-step-late or OSL approach [52]). This formula is however unstable with large prior weights. For this reason, we use a different algorithm [53], which has been proven to be more stable in the presence of priors:

$$\lambda_j^{new} = \frac{\lambda_j^{old}}{\sum_{i=1}^N c_{ij} - \lambda_j^{old} \frac{\partial^2 P}{\partial \lambda_j^{old}}} \left( \frac{\partial L}{\partial \lambda_j^{old}} + \frac{\partial P}{\partial \lambda_j^{old}} \right) + \lambda_j^{old}$$

The above is the **Maximum-a-Posteriori** (or **MAP**) reconstruction algorithm used in this work.

There are several ways to include prior information (or *priors*) during the iterative process of reconstruction of a dataset. In general terms, the priors can be divided into local or global priors. Both priors act on the whole image, but in the global case the prior considers all voxels simultaneously, while in the local case it considers only a neighbourhood around each voxel of the image.

Another way to classify the priors is by observing if they do or do not make use of additional anatomical images during the reconstruction process. We define the first as anatomical priors.

In this work, we will discuss three techniques that have been proposed in the past to include prior information in the MAP reconstruction to deal with PVC, which attracted our attention for the simplicity of their implementation and the promising results they showed in previous evaluation studies [54–56].

#### II.4.1 NON-ANATOMICAL PRIORS

The two non-anatomical priors used in this work impose some constraints (e.g. piecewise smoothness, edge preservation, ..) during the iterative reconstruction of the PET images. Specifically, the **relative difference (RD) prior** encourages the intensity difference of two neighbouring voxels to be minimized if their relative intensity difference is below a predefined threshold, which in turn is chosen independently for each *local* neighbourhood of a voxel [53]. All intensity differences above such threshold are preserved. The **total variation (TV) prior**, as the naming suggests, encourages the voxels within the neighbourhood to have the lowest total variation (the lowest total absolute difference between neighbouring voxels) while still being in agreement with the measurement [57]. The constraints applied by these two non-anatomical priors can be formalized as follows.

For the RD prior,

$$P = \sum_j \sum_{k \in N_j} P_{jk} \quad (9)$$

$$P_{jk} = \begin{cases} -\beta \frac{(\lambda_j - \lambda_k)^2}{\lambda_j + \lambda_k + \gamma |\lambda_j - \lambda_k|} & \text{if } k \in N_j \\ 0 & \text{otherwise} \end{cases}$$

where  $N_j$  defines the **neighbourhood** of the  $j$ -th voxel,  $\beta$  is the **weight** given to the prior and  $\gamma$  controls the tolerance of the prior towards the edges. If  $\gamma$  is high, intensity transitions tend to be preserved (less smoothing is applied for bigger intensity transitions, hence the *edge-preserving* effect). If  $\gamma$  is small, the prior does not perform any edge-tolerance and smooths proportionally to the local quadratic intensity difference.

For the TV prior,

$$P = -\beta \sum_j \sum_{k \in N_j} |\lambda_j - \lambda_k| \quad (10)$$

If the neighbourhood is well chosen, and if the parameters that regulate the strength (weight) of the prior are appropriate, the RD and the TV prior represent a good way to improve the noise properties of the resulting images and increase the contrast between adjacent structures with different activity levels. We chose to use the RD prior in place of, e.g. the Geman or Huber prior, for its easiness in tuning [53] and for easier comparison with previous work on anatomical priors [54].

The TV prior represents an interesting alternative to the RD prior when small, high-contrast targets (such as cardiac lesions) are of interest [56]. The weight of the TV prior has to be, however, finely tuned, as a too high weight would produce images with a ‘blocky’ and unnatural appearance (the staircase effect), while a too small weight can introduce clustered noise in the resulting images. Several ways to address this issue have been proposed in the past decade, e.g. in [58, 59]. Among these, attempts to improve the look of the TV reconstructions were also performed in our group, by using the TV prior together with a quadratic prior during the reconstruction of breast tomosynthesis images. However, only marginal improvements were achieved when the combined detectability and clinical acceptance were considered [60]. The approach we followed was to assess the potential of the TV for lesion detection and noise reduction on cardiac datasets in the first place. If the unnatural appearance of the resulting TV reconstructions would prove to be the bottleneck for their clinical acceptance, ways to mitigate the staircase effect would be further explored.

#### II.4.2 ANATOMICAL PRIORS

The anatomical priors use, in combination with such smoothing constraints, an anatomical image to provide further information about the edges of the various tissues during reconstruction.

The anatomical image can be obtained by means of MRI, CT, or any other imaging modality that provides a clear and detailed description of the anatomies within the region of interest. If an image with such properties is available, it is possible to use it to further constrain the smoothing applied by a non-anatomical prior (e.g. like the ones described in the previous paragraph). Assuming that the homogeneity of the regions of the anatomical images correlates to the homogeneity of tracer uptake in the same regions, one possible use of the anatomical information is to let it constrain the smoothing to a sub-neighbourhood  $W_j \in N_j$  of the  $j$ -th voxel.  $W_j$  consists of the  $n$  voxels of the neighbourhood  $N_j$  of  $j$  that e.g. have the most homogeneous gray values (lowest absolute difference between each of the voxels and the  $j$ -th voxel) in the anatomical image (Figure 6).

Such technique (called the *Bowsher prior* from now on), proposed by Bowsher et al [61], has been proven to be effective for dealing with PVE, easy to use and free from segmentation issues. Additionally, the asymmetrical version of this prior (used in this work) outperformed the original implementation in terms of bias, noise and edge-preservation [62]. Other methods to incorporate anatomical information during the reconstruction of the PET datasets have been proposed and evaluated [54], revealing a superiority of the Bowsher prior in terms of easiness of tuning and acceptance of the results. A segmentation-based method for applying anatomical information for cardiac datasets, such as in [63], would be considered here only if

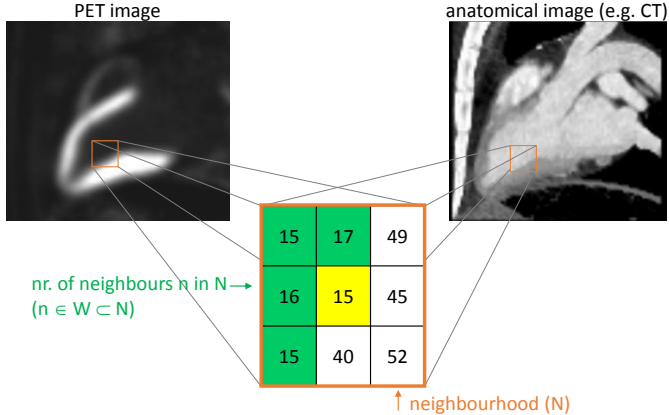


*Figure 6: The Bowsher prior constrains the smoothness of the PET to the  $n$  voxels of the neighbourhood that have the most similar intensity in the anatomical (here, CT-) image (green region).*

any segmentation-free method would fail for cardiac datasets. In fact, the segmentation of cardiac datasets is still a subject of investigation due to the inter- and intra-subject variability when the delineation of the structures is performed, due to the highly moving nature of the organ of interest which can introduce artefacts and imprecise image boundaries and due to the noise or the acquisition-related properties of the anatomical images [64]. Both manual and automated segmentations are therefore, at present, not fully capable of producing a segmentation that is as accurate and reliable as segmentation-based PVC techniques would require to be. Hence, given the previous study that warns about the sensitivity of segmentation-based methods on the quality of the subsequent PVC [54], the choice of incorporating segmentation-free prior anatomical information seems, in the case of cardiac datasets, the most appropriate.

## II.5 HOW TO OBTAIN THE ANATOMICAL INFORMATION

### II.5.1 COMPUTED TOMOGRAPHY

Computed tomography (CT) is a common and widespread imaging modality. Reasons for its wide usage include well-established techniques to acquire and reconstruct an image of good quality and sufficient detail, its relatively low cost when compared to other imaging modalities (e.g. magnetic resonance imaging), and its ability to faithfully portray the anatomical regions of interest.

In the past decade, dual-source CT scanners have been made available. As the definition suggests, these systems consist of two X-ray sources, positioned at 90 degrees from each other. With this, twice the amount of data can be obtained in the same time frame, thus allowing to obtain images with a better temporal resolution and reduction of the artefacts that would occur due to motion. Cardiac examinations are regarded as the ones that should maximally benefit from this technology: the scanner can acquire data from a region as big as a regular human heart in a fraction of a heartbeat, thus reducing the blur due to the beating of the

heart and the breathing of the patient. This improvement, however, holds true only if certain conditions (e.g. heart frequency  $\leq$  60 beats per minute) are satisfied [65]. One example of such dual-source scanner is the Siemens Somatom Definition Flash [65], which was used during the animal experiments at the beginning of this work.

Other CT images that are used in this work came from the CT module of the Siemens Biograph 16 PET/CT hybrid scanner. This scanner has a lower temporal resolution, which made it unsuitable for partial volume correction of patient or alive animal datasets as it could not fully resolve the heart in one single respiratory and cardiac phase without the introduction of significant motion artefacts. However, we used the CT images from this scanner for partial volume correction (and attenuation correction) of the *ex vivo* (static) animal datasets, as the temporal resolution was in that case not relevant.

## II.5.2 MAGNETIC RESONANCE IMAGING

Magnetic resonance imaging (MRI) is another anatomical imaging technique that is gradually being integrated in the clinical practice.

The patient or object is inserted into a magnetic bore, which administers a constant magnetic field and some smaller, pulsed radio-frequency (RF) magnetic fields to all the hydrogen atoms of the body within the bore. The human body contains a large amount (more than 60% of its weight) of water, which is rich in hydrogen, thus making the technique effective. Different tissues have a different hydrogen content, thus allowing their differentiation as they react differently to the application of the magnetic fields.

To enhance the visibility of tissues otherwise barely distinguishable, contrast agents can be administered (via the blood stream) which change the way the tissues they target respond to the electro-magnetic pulses administered during an MR scan. Gadolinium chelated contrast agents are commonly used.

In cardiac imaging, several sequences have been proposed for MR imaging purposes. One of the sequences that is particularly interesting in the scope of cardiac PVC is the *late gadolinium enhancement* (or late enhancement, or delayed enhancement) acquisition technique. This MR acquisition sequence is particularly useful for obtaining images with a clear distinction between infarct tissue and normal healthy tissue, thanks to the different amount of extra-cellular tissue fraction that characterises these two types of tissue. In fact, the infarcted tissue contains a higher fraction of extra-cellular volume when compared to normal tissue, especially when the rupture of the membrane of the myocardial cells occurs. The contrast medium accumulates more easily in the extra-cellular matrix. Moreover, Gadolinium-based contrast agents enter and exit the infarcted tissue more slowly than in normal tissue. Therefore, there will be a point in time where the infarct region will be rich in Gadolinium chelates, while the healthy portion of myocardium has already washed it out. At this point (about 10-30 minutes after Gadolinium administration), the MRI sequence of choice is performed, so that the highest contrast between the healthy and the infarct tissue in the MR images is achieved [66]. An MR acquisition is also particularly promising when combined with a simultaneous PET acquisition. In this case, the patient does not need to be transferred from one scanner bed to the other to perform the two acquisitions, thus minimizing the chances of misalignment

between the two resulting images. Therefore, if all the technical difficulties of simultaneous PET/MR were solved [67], the use of such technique would potentially allow for a more accurate PVC.

## II.6 IMAGE REGISTRATION

Image registration is the process by which one image (*floating* image) is spatially aligned to a second image (*fixed* or *reference* image). The goal of image registration is to find the transformation that maps all voxels of the floating image to the corresponding anatomical structures of the reference image. Once the transformation that describes this alignment is found, the floating image needs to be shifted, rotated or elastically deformed to achieve such correspondence of the same anatomical features. The image registration techniques can be broadly classified into rigid, affine and non-rigid registration techniques. Rigid registration techniques aim at finding up to three global shifts and up to three rotations of the floating image, so that it matches the reference image. Affine registration also allows the use of global skew and rescaling parameters to further improve the alignment of the floating to the reference images. Both rigid and affine registrations are appropriate to align non-deformable objects (e.g. bones, brain), but fail to reach the goal when deformable objects are considered. Non-rigid deformations are, in such cases, the only viable solution to achieve a voxel-by-voxel correspondence between the anatomical structures of the floating and the reference images. They act locally, thus a transformation is computed for each voxel of the floating image. This leads to longer computation times to achieve the desired image registration, and larger space requirements to store the resulting transformation matrix. Despite the deformable registration algorithms seem more promising for certain anatomical regions, they are also the most sensitive to small imperfections, artefacts or noise that can occur in one of the two images of interest. A fine tuning of such algorithms, that would constrain the registration within pre-defined maximum shift values or that would take into account the local behaviour of the surrounding voxels, is in this case strongly recommended to obtain sensible registration outcomes [68].

In this study, the registration of the emission (PET) and the anatomical (CT, MRI) datasets was of interest. Despite the organ of interest (the heart) is highly deformable, a rigid registration approach was used. In fact, the deformation of the heart occurring in the emission dataset is here ideally removed by the motion correction technique of choice (i.e. gating, see Section II.7), whereas the anatomical dataset is acquired with a high temporal and spatial resolution so that the motion within each gate is negligible. Given these assumptions, and having assumed to consider the same cardiac and respiratory frame for both the anatomical and the emission datasets, the only remaining differences are due to the different positioning and/or coordinate system of the two datasets, both of which can be corrected for using rigid registration techniques.

Normalized mutual information was chosen as the matching criterion, since it has been proved particularly effective when inter-modality image registration is required [69].

## II.7 MOTION ESTIMATION AND MOTION CORRECTION FOR CARDIAC DATASETS

Motion blurring in the thoracic region is an important cause of artefacts and mis-evaluation of regional myocardial metabolism [70]. The heart is a naturally moving organ that, in normal conditions, beats at a regular – although varying between individuals and species – pace. Additionally, being located in the thoracic cage, the heart is indirectly subject to the motion of the lungs, due to the respiration. Both motions cannot be arrested, thus they both need to be taken into account when any PET scan (which lasts more than a few seconds) is performed. In addition to these involuntary motions of the heart, during a PET examination a patient can also sneeze, cough, talk or generate involuntary twitches that cause motion of the organs in the thorax. Finally, voluntary motion of the patients (e.g. change in position for better comfort) can also occur during the scan. All these sources of motion result in image blurring, which needs to be taken into account and corrected for if quantitative PET reconstructions are aimed at.

The problem of motion correction can be further distinguished into two sub-problems, each of which is currently subject of extensive research. The first issue concerns the **extraction of the biological trace** to be used for the motion correction. This can be done by using external tracking devices, or by extracting the biological traces directly from the ET dataset itself (*data driven* approaches). Once a reliable trace of both the respiratory and the cardiac motions is obtained and accurately synchronized to the PET dataset, the second step is to **correct for the motion** using the extrapolated biological trace(s). In the remainder of this section, we further elaborate on the advantages and disadvantages of the most widely used techniques.

### II.7.1 SIGNAL EXTRACTION: EXTERNAL TRACKING DEVICES VS DATA-DRIVEN METHODS

Different methods are currently available to extract the motion parameters. They can be subdivided into two main categories: hardware-based and data-driven.

#### HARDWARE-BASED METHODS: AN OVERVIEW OF THE AVAILABLE TRACKING DEVICES

The **hardware-based** methods rely on an external tracking device. A common characteristic of these devices is that they track external motion of the body, and assume that the motion that is recorded is a perfect surrogate for the internal motion of the organs or regions of interest. The external tracking device can be, in the most general case, a video-recorder, or a device that mechanically moves together with the organ being tracked (e.g. a respiratory belt with a pressure sensor to measure the thoracic motion), or a device that monitors other biological parameters that can be later on correlated with the motion of the organ of interest (e.g. an ECG or a pulse-oximetry [71] recording device).

The use of optical motion recorders has the advantage of recording both voluntary patient motion and respiratory motion. The use of a device of this type

has been successfully tested during cardiac SPECT [72]. However, this method has not been further validated and it might have shortcomings in the detection of the markers especially when oversized patients, or patients with a very small external breathing motion, are considered. Moreover, the shift of the markers relative to the body surface might hamper the correct acquisition and utilization of the collected data. Finally, optical tracking devices are generally costly and, with some specific models, trained personnel would be needed to set them up and calibrate them prior to the beginning of the scan. Other, cheaper, marker-free devices have been tested for motion tracking [73], which would mitigate some of the aforementioned shortcomings. However, discrepancies between the expected and the recorded motion have been reported [74]. Other methods, which rely on simpler digital cameras to pick up variations due to heartbeat and breathing during the scan, have been also proposed [75], but no extensive validation studies have been performed so far.

At present, the use of devices that track the motion by direct contact with the patient is often the preferred choice, particularly for the tracking of the respiratory motion. The Anzai AZ773V pressure-sensors, already available in our department and extensively validated in multiple studies [76,77], provide a simple way to extract the respiratory motion of the patient. A few studies have investigated the latter assumption [78,79], confirming on average a good correlation between internal organ motion and the motion of the external tracking devices. However, such correlation is not always guaranteed.

As for the cardiac motion, the most common and efficient solution is to use an ECG tracking device to monitor the electrical variation determined by the heart pulse. From the collected signal, the cardiac beating motion can be inferred.

## DATA-DRIVEN METHODS

In a truly clinical setup, the burden associated with installing the respiratory or the cardiac tracking machines, together with the possible discomfort for the patient with a belt and several electrodes on his body, have pushed the research towards the direction of device-less gating techniques, or **data-driven** gating techniques (DDG). Such techniques do not rely on an external tracking device, but try to estimate the motion of the internal structures based on the acquired dataset itself, based on the variations in e.g. image intensities, sensitivity, center of mass, or on the principal component analysis of the dataset over time [80–85].

A large quantity of DDG techniques has been developed over the past decade, which can be categorised into two main groups: image-based and sinogram-based techniques. Image-based techniques are based on the assumption that the respiratory and cardiac motions are responsible for fluctuations in the image space. Therefore, they are derived by monitoring the changes in the images over time. Various research groups have explored the use of such techniques, basing the estimation of the respiratory trace on large ROIs [84] or on a voxel-by voxel basis [85]. An advantage of this type of techniques is that the signal to be extracted is clear, as it is not obfuscated by the forward projection of all other points of the object. However, this comes at the price of increased computational burden, as each time frame has to be reconstructed before motion information can be extracted. An alternative to image-based techniques are sinogram-based DDG techniques [81–83].

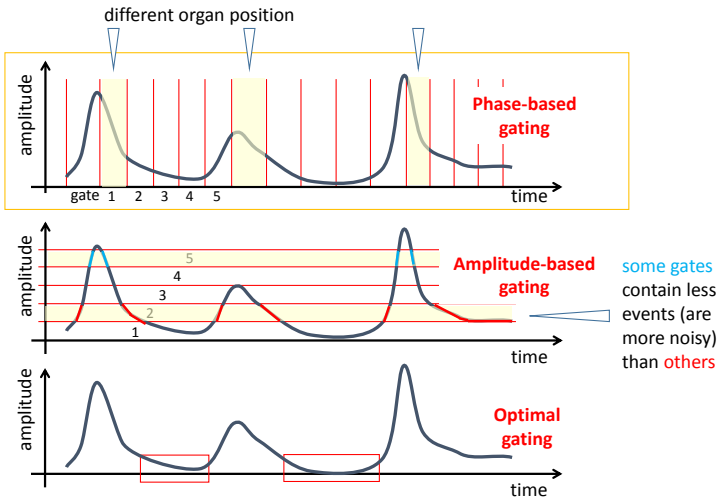


*Figure 7: The three gating techniques that have been implemented in this work based on previous literature. The yellow box indicates the gating method that has been chosen for the processing of the animal datasets acquired in the scope of this project. For regular breathing, the phase-based gating method is the simplest to implement. Amplitude-based and optimal methods in the current implementation improve the gating outcome if the breathing has irregular amplitudes and a constant baseline throughout the scan.*

Sinogram-based algorithms have opposite advantages and disadvantages. They are computationally faster and more straightforward, even though the signal recovery might be less accurate because of the nature of the measurement process as a contribution of multiple points to one single point in a projection. In fact, the motion is extracted, in this case, from the fluctuations occurring in the sinograms of the scan over time.

### II.7.2 MOTION CORRECTION

Once the biological trace is available, the traditional approach requires that the PET dataset is corrected for motion, based on the information provided by such trace.

The process of ***gating*** is a well-established technique to remove the motion from cardiac PET datasets by relying on the periodicity of the recorded motion. The full list-mode dataset is split into a certain number of *gates*, typically according to the position of each recorded event within the cycle, or to the amplitude of the trace at each time point, or trying to maximize the counts in one specific gate. These three common approaches are referred to as phase-based gating, amplitude-based gating and optimal gating (Figure 7).

In phase-based gating, each respiratory (or cardiac) cycle is divided into an equal number of gates within which the motion is considered negligible. This gating method works well if the patient breathes regularly or is externally ventilated, so that the occurrence of a specific phase in the respiratory cycle correlates well with the occurrence of a specific position of the organs in the thorax. In amplitude-based

gating, on the other hand, all the events collected during the PET scan are sorted into gates based on the amplitude of the respiratory trace. This technique is more reliable in case the amplitudes of the various breathing cycles of one patient vary significantly from one another (irregular breathing patterns), which is more likely to occur when (non-ventilated) patients are analysed [86]. Finally, in the optimal gating case [87], all the PET events that happen during end-expiration are used, and the rest of the data is discarded. The end-expiration phase is chosen because it is the longest and most stable phase of the respiratory cycle.

Various studies have tried to compare the different gating approaches for patient studies [88, 89], concluding that amplitude-based and optimal gating methods generally outperform phase-based gating strategies in terms of motion recovery. This comes at the price of noisier images, as in the most basic implementation of amplitude-based methods the counts are not equally subdivided between the gates. Means to solve the aforementioned issue include amplitude-based variable gate subdivision, so that the number of counts in each gate is kept constant, but this in turn comes at the price of variable motion blur in each frame and a less straightforward processing – which might push further away the introduction of motion correction strategies in the clinical work flow.

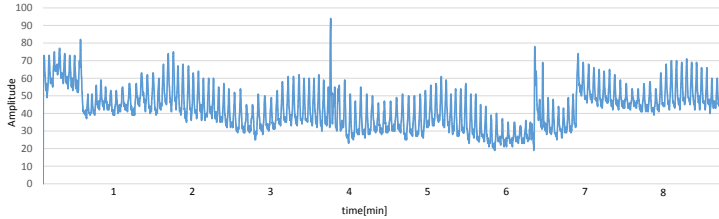


*Figure 8: An example of respiratory trace extracted from a real patient scan. Clearly, the amplitudes values span over a very wide and not-constant range, which makes the use of any of the mentioned techniques inefficient for motion correction.*

In spite of the improved results obtained when using the amplitude-based and the optimal gating methods, a fundamental limitation of all the aforementioned techniques lies in the fact that they all assume that the breathing amplitudes are oscillating around a constant average amplitude value. However, this assumption is not always reflected in real patient acquisitions (e.g. Figure 8), and several clinical cases show sudden or gradual baseline drifts due to hardware or to physiological reasons or to changes in the breathing pattern of the patients due to stress or external stimuli (e.g. blood samples taken during the PET scan, relaxation of the patients during the scan, loss of contact between the respiratory tracker and the patient, ...). This effect has been already observed in the past [90], and a possible negative influence of the baseline drift on amplitude-based gating methods was described. In the study just mentioned, the method that was believed to produce more accurate results was based on data-driven extraction of the respiratory trace. This could represent a solution, provided that the extracted DDG signal is reliable and that the drift is only due to hardware reasons. Another possible alternative, currently not yet investigated, is to extract the rigid motion transformation for the entire duration of the scan in a DDG fashion, and subsequently apply rigid motion correction to each event contained in the list-mode datasets, such that all events

are correctly placed before the cardiac gating and the subsequent reconstruction can take place.

## II.8 OBTAINING THE DATASETS: SIMULATIONS AND ANIMAL EXPERIMENTS

### II.8.1 SIMULATED DATASETS

The use of simulated datasets is a very valuable tool to pinpoint the significance and the effectiveness of a reconstruction technique, as they allow a direct comparison of the results with a well-known ground truth, in an ideal-case scenario where all variables are under control. In the scope of this work, software-based simulations were performed both to initially validate the effect of AC on the motion correction and the PVC techniques and to prove some important effects of the use of misaligned anatomical information in a more rigorous and accurate way. The 4D cardiac-torso virtual phantom (XCAT [91]) was used to accurately model a thorax dataset with realistic breathing and heart beating capabilities. The XCAT software produces 3D datasets with a high level of accuracy of the anatomies. Particularly, for the heart, this software allows to insert lesions and different degrees of apical wall thinning. Additionally, the XCAT software models the breathing and the beating motion following patient-based models, such that different 3D datasets, one for each cardiac and respiratory phase, can be obtained. These datasets can be forward-projected, so to simulate the process of acquisition as if they were scanned in a real PET scanner. The reconstruction of such forward projections can then be performed, using the same algorithms as those that would be applied to a real measured dataset.

All simulated datasets were projected and reconstructed using in-house developed software that simulates the behaviour of the routine clinical scanner (Hirez) or of the Siemens Focus 220 microPET scanner. In the scope of this work, the software was carefully cross-validated against the different platforms (Hirez and microPET), so that the same quantitative images would be obtained when using either of the scanners involved in this study.

### II.8.2 ANIMAL EXPERIMENTS

The use of animals as a first step towards the acceptance of a technique is widespread. The PVC techniques presented in this work have been already tested in a simulated environment for brain, or in human patient datasets. Despite useful to assess the performances of the selected algorithms in the first place, simulations are anyway a simplification of the complex reality of a real scan. On the other hand, patient scans have the disadvantage of not providing a ground truth for a rigorous comparison of the performances of the reconstruction techniques of choice. Therefore, animal experiments were carried out on a regular basis during the course of this PhD to validate the presented techniques for cardiac applications.

For all the aforementioned reasons, the animal model that was chosen to be developed was the one of dilated cardiomyopathy (DCM) with asymmetric left ventricular remodelling due to an left-bundle branch block (LBBB)-like conduction

delay. Some of the typical features to be expected from hearts affected by such DCM are a dilation of the LV chamber over time, together with a thinning of the septal wall and a thickening of the lateral wall of the LV during the progression of the disease. Such variations in the wall thicknesses were hypothesised to generate problems with relative tracer uptake quantification, due to the partial volume effects mostly affecting the thinned walls.

Sheep were chosen to be the best candidates for the purpose of our study, thanks to the slow rate of increase of their body mass over the planned experimental duration.

## THE IMAGING PROTOCOL

Each animal underwent several imaging and surgical procedures (i.e. pacemaker implantation, echocardiography, MRI, catheterization, PET/CT, CT, ...), in order to obtain and evaluate the planned model and to yield the datasets of interest.

For the specific purposes of this PhD project, in agreement with the local ethical committee, each animal underwent several scans using a newly designed protocol. Figure 9 illustrates the experimental set-up. After eight weeks of rapid cardiac pacing (180 beats/minute), necessary to obtain cardiac remodelling, the pacing rhythm was reduced to 110 beats/minute during the imaging procedures. The value of 110 beats/minute was chosen as the best compromise between overriding the intrinsic heartbeat of the animal of about 90-100 beats/minute (necessary to guarantee a consistent beating pattern throughout all the experiments) and acquiring acceptable images with the available instrumentation (i.e. avoid artefacts or missed data due to the limited sampling rates of some of the considered imaging systems). Each animal underwent a high-resolution CT on the Siemens Somatom Definition Flash scanner, to obtain high-resolution CT images of the heart which were expected to be frozen in a specific cardiac and respiratory phase. This was achieved by disconnecting the ventilator from the sheep at the moment of the scan, thus forcing the animal into a prolonged end-expiration state, and by acquiring the CT measurement simultaneously to the ECG. Such datasets were meant to be used for anatomy-based partial volume correction of the *in vivo* sheep datasets. At the end of such scan, each sheep underwent hyperinsulinemic-euglycemic clamping [28], in order to maximize glucose consumption in the heart. When steady state was achieved, each sheep was injected with  $^{18}\text{F}$ -FDG. An activity of 370 MBq was foreseen, for each sheep, at the time of injection. However, the amount of radioactivity actually reaching the heart varied from sheep to sheep, due to the unpredictable time needed to achieve the steady-state during the clamping procedure and due to the animal-specific metabolism. Thirty minutes after injection, an  $^{18}\text{F}$ -FDG PET scan of the same animal was performed on the currently available clinical PET/CT system (Siemens Biograph 16, Hirez). The mean whole-body activity at the start of such PET scan was  $310,5 \pm 87$  MBq. A CT for attenuation correction was also acquired on the same scanner. The resulting *in vivo* datasets were used both for testing the implementation of the motion correction algorithms described in Section II.7 and the effects of attenuation correction on the alignment between the PET and the HRCT (Chapter 1).

In addition, motion-free cardiac PET datasets were also acquired to assess the

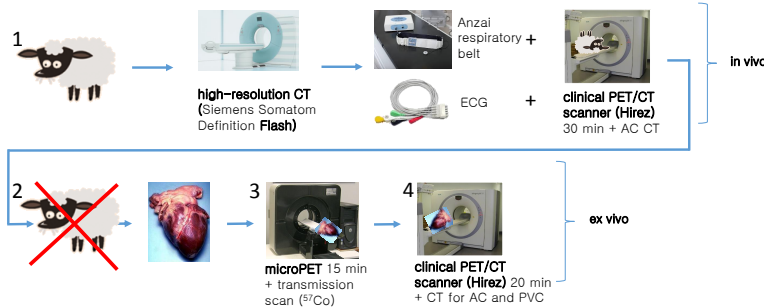


Figure 9: Flowchart of the experimental setup.

efficacy of the PVC techniques without the interference of motion. The rationale behind the *ex vivo* scans was as follows. The acquisitions on the Hirez scanner were performed to obtain real cardiac datasets without the blurring caused by the motion of the heart (which was present in the corresponding *in vivo* scans), with the same settings that would be applied in a clinical patient PET scan. The acquisitions on the microPET scanner, on the other hand, were performed to obtain an ideal, high-resolution ground-truth to be used to validate the PVC techniques of choice (described in Section II.3). In fact, the microPET has a resolution of 1.3/1.5 mm (transaxial/axial respectively), hence the chances for it to suffer from PVE are limited.

To obtain such *ex vivo* datasets, each sheep was sacrificed after the *in vivo* scans and had the heart excised. Each heart was filled with a low-attenuating, hardening foam in order to preserve the shape of the heart throughout the subsequent scans. We verified that the foam was stable over time by scanning (by means of CT) a pilot *ex vivo* heart, every 5 minutes and for the first 50 minutes after foam insertion (10 measurements). We subsequently calculated the overlap (DICE-Sørensen coefficient [92]) between each of the reconstructed CT measurements and the first, reference CT and verified that the variation of the overlap converged to a stable value at the end of the test scanning period. We performed only CT-based tests as we assumed that the introduction of the foam would induce only mechanical changes in the considered hearts. We did not consider that a change in metabolism was likely, as the hearts are excised - hence not supplied with blood (and FDG) - and we assumed that the FDG remained irreversibly trapped in the cardiac cells after excision. Once the stability of the foam was ensured, the *ex vivo* hearts were scanned both on a high-resolution preclinical PET scanner (Siemens Focus 220, microPET) and on the same clinical PET/CT scanner as used for the *in vivo* acquisitions.

### III OBJECTIVES

The aim of this project is to investigate the effectiveness of image processing algorithms that enable motion compensation and partial volume correction (PVC) of cardiac FDG-PET images, in order to provide a more accurate extraction of parameters representing the regional energy consumption in the left ventricle of the heart. Specific objectives of this work are:

- The validation of the microPET as an effective ground truth for cardiac studies.
- The comparison of available partial volume correction techniques applied to static cardiac datasets, with the aim of pinpointing the algorithm that produces the best absolute and relative quantification for PET datasets, both in healthy and diseased cardiac tissue.
- The software implementation of motion-correction techniques, to allow the accurate analysis of measured *in vivo* datasets.
- The accurate analysis of the effects of motion, occurring during the CT and the PET scan, on anatomy-based partial volume correction of simulated emission datasets.

In the scope of a broader project whose aim is to non-invasively assess the progression and status of DCM by means of PET, the metabolic parameters obtained from the motion-free, PVC PET images are correlated with other mechanical parameters extracted from functional measurements. The study of the relationship between the cardiac FDG metabolism (as a measure of energy consumption) and the regional myocardial workload as characterized with echo, MR or other functional acquisition techniques, could lead to a better understanding of the relation between regional function and regional work load and a better pathophysiologic understanding of different pathologies.

## IV PERFORMED STUDIES

The first challenge to the project was given by the fact that no ground truth datasets were available for the validation of the new image acquisition and processing approaches. Both simulations and animal experiments were performed to overcome this fundamental limitation.

In Chapter 1, the attenuation problem is explored using the XCAT phantom. In the case of cardiac studies, the CT for AC is often acquired at low dose and low temporal resolution, and the cardiac or respiratory motion during this scan can be significant enough to cause motion artefacts. These artefacts might not only hamper LV quantification, but also negatively influence the subsequent alignment of the emission image to the corresponding anatomical dataset for PVC. Chapter 1 analyses and compares different AC strategies and defines the best approach to obtain quantitatively correct images that can be effectively aligned to the corresponding anatomical image for subsequent PVC.

In Chapter 2 and 3, the efficacy of various PVC techniques is evaluated by using *ex vivo* static datasets. The choice of the ground truth (microPET) and the correct reconstruction of such dataset is presented in Chapter 2. Due to the non-conventional shape of the object (heart) being scanned in such device, the application of scatter and attenuation correction steps was non trivial and needed extended investigation.

In Chapter 3 the problem of PVC of cardiac datasets is first addressed, considering a simplified motionless scenario. In this way, the benefits introduced by the

selected PVC techniques could be evaluated without any confounding factor (i.e. motion). For this purpose, excised sheep hearts were obtained. We used different algorithms, which did or did not make use of additional anatomical information, to reconstruct these datasets and we investigated their effect on the relative, as well as absolute distribution of activity within the myocardium when compared to the chosen ground truth.

In Chapter 4 it is analysed with the help of the XCAT software whether anatomy-based PVC is useful for the improvement of lesion quantification. Additionally, the practical necessities for a successful anatomy-based PVC are described and highlighted. We define the properties and features of the ideal anatomical image and the problems that can occur during anatomy-based PVC due to misalignments between the anatomical and the emission datasets (e.g. patient voluntary or involuntary motion, organ displacements or deformations between subsequent acquisitions, etc).

Finally, Chapter 5 describes the first steps that were taken to correlate the values extracted from the *ex vivo* datasets to the values extracted from the motion-corrected *in vivo* datasets, in the attempt to find the motion-correction algorithm that guarantees quantitatively accurate results.



## **B PERFORMED STUDIES**



# 1 IMPACT OF CT-BASED ATTENUATION CORRECTION ON THE REGISTRATION BETWEEN DUAL-GATED CARDIAC PET AND HIGH-RESOLUTION CT

*This chapter is based on the published article: Impact of CT-based attenuation correction on the registration between dual-gated cardiac PET and high-resolution CT, A. Turco, J. Nuyts, O. Gheysens, J. Duchenne, J-U. Voigt, P. Claus, K. Vunckx, Trans Nuc Sci 2016 Feb.*

## **Abstract**

A high-resolution CT (HRCT) used as anatomical prior information during PET reconstruction can enhance the quality of a corresponding low-resolution PET image, provided that it is accurately registered to the PET dataset of interest.

In this work, the impact of different PET/CT attenuation correction (AC) protocols on the registration between a dual-gated cardiac  $^{18}\text{F}$ -FDG PET image and an HRCT image is investigated. The aim is to explore the impact of AC on PET-to-HRCT registration, and to identify the AC strategy that yields the best alignment between the left-ventricles in the PET and the HRCT images for subsequent partial volume correction.

Simulations were performed using XCAT phantoms. Shallow breathing and a regular beating pattern were simulated and both noise-free and noisy data were evaluated.

Respiratory motion during the acquisition of the CT used for attenuation correction strongly affected the dual-gated PET reconstructions, resulting in artefacts and quantification errors in the PET image and poor PET-to-HRCT registration accuracy. The blurring introduced by the beating heart, on the other hand, proved to have a negligible effect on PET-CT registration. Dual-gated PET images reconstructed without attenuation correction could be well registered to the HRCT if a good initial alignment between the starting images was provided.

A commercially available strategy to deal with an AC CT that is acquired in the wrong respiratory phase was also evaluated, and yielded

not only enhanced quantitative accuracy but also accurate PET-to-HRCT registration.

The effect of a high level of noise, as present in a dual-gated cardiac PET study, was also investigated. Registrations proved to be sensitive to noise, but noise is not a major limiting factor for PET-to-HRCT registration.

A selection of the investigated attenuation correction procedures was also evaluated using cardiac PET/CT data measured in sheep. The PET-to-HRCT registration performance confirmed the XCAT-based predictions.

## LIST OF ABBREVIATIONS

PET	Positron emission tomography
HRCT	High-resolution CT (high spatial and temporal resolution, contrast)
AC	Attenuation correction
AC CT	CT acquired and reconstructed for AC
C1-exp	ideal AC CT (end-diastole, end-expiration)
C2-exp	as C1-exp, but mismatch in the cardiac phase
C1-insp	end-inspiration AC CT (end-diastole)
AVGC-exp	AC CT averaged over the cardiac cycle (end-expiration)
AVGC-insp	AC CT averaged over the cardiac cycle (end-inspiration)
C1-AVGR	AC CT averaged over the breathing cycle (end-diastole)
AVGC-AVGR	AC CT averaged over both breathing and beating cycle
sh(AVGC-insp)	AC CT averaged over the breathing cycle (end-inspiration), shifted
NOATTEN	no attenuation correction

## I INTRODUCTION

The measurement of  $^{18}\text{F}$ -fluorodeoxyglucose (FDG) uptake by positron emission tomography (PET) is a validated and robust tool to investigate regional metabolism and myocardial viability [93] and can provide insights into regional myocardial workload. Limitations of the current PET imaging instrumentation can, however, compromise its diagnostic accuracy. The low spatial resolution (5-6 mm) of PET does not allow to accurately quantify the tracer uptake in very thin or small structures due to partial volume effects (PVE) [94], thus hampering correct estimation of glucose uptake. In addition to PVE, extracting valuable and correct information from *cardiac* images is not straightforward since the heart beats and moves in the thorax because of respiration.

The contribution of motion to cardiac images can be mitigated with different techniques [88] [82] [95]. One of the most common and straightforward methods, although not optimal for image quality, is to sort the PET dataset into a set of frames corresponding to the different phases of the periodic motion (gating), and then independently reconstruct and use each of them.

The issue related to PVE has also been frequently addressed. Among all available techniques, the application of anatomical information obtained with an HRCT

or magnetic resonance imaging during the PET reconstruction with resolution modelling has been proven promising [96]. Recently, particular attention was given to brain image enhancement using the aforementioned method [97]. Even though efforts have been recently made to ensure robustness against small misalignments [98], the application of such a partial volume correction (PVC) technique to a measured PET dataset relies on a good alignment between the anatomical image and the low-resolution PET. Hence, any source of misregistration needs to be avoided. In this scenario, PET attenuation correction might play a role in compromising the registration results.

Almost every contemporary PET scanner nowadays incorporates a CT module, that can be used to acquire a CT from which a PET attenuation map can be derived. From such map, a sinogram with PET attenuation correction factors (ACF) is obtained by forward projection and exponentiation. However, the CT for AC is often acquired at low dose and low resolution, and it is sometimes averaged over one or more breathing or beating cycles [99]. Therefore, artefacts can be introduced in the attenuation-corrected PET images, which in turn might negatively influence subsequent PET-to-HRCT registration.

To our knowledge, nothing has been reported about the influence of using a mismatched or motion-blurred map for AC on the quality of PET to high-resolution CT registration in cardiac imaging. The aim of this work is to assess the influence of attenuation correction on the quality of image registration between dual-gated cardiac PET images and high-resolution CT images, when either or both respiratory and cardiac motion are present during the AC CT acquisition. The effect of different attenuation correction strategies is investigated by means of simulations, using a realistic digital anthropomorphic phantom (XCAT [91]) and cardiac PET/CT datasets measured in sheep.

The rest of this paper is organized as follows. In Section II, the details of the phantoms used for the simulations are given, together with a description of the simulations, reconstructions, registration and evaluation methods, and real datasets. In Section III, an overview of the results obtained with noise-free and noisy datasets is presented. The results are discussed in Section IV and the conclusions are summarized in Section V.

## II METHODS

XCAT-based simulations were designed to mimic a dual-gated PET study acquired on a Siemens Biograph 16 PET/CT scanner. Sinograms containing attenuation correction factors (ACF) were derived from CTs acquired on the same device using different CT protocols. Each simulated AC CT differs from the others in the way it handles the respiratory and beating motion during the scan. After gating and after performing AC, the PET frame of interest is registered to a high-resolution CT virtually acquired on a dedicated scanner, which can image the heart in a single cardiac and respiratory phase, with contrast enhancement of the blood pools. The reason for this registration is to enable a subsequent anatomy-enhanced PET reconstruction for PVC. The accuracy of the registration will determine which AC CT protocols can be used if PVC is aimed for. Fig. 1.1 summarizes the workflow

of the simulations.

## PHANTOM GENERATION

A number of XCAT thorax phantoms were generated in order to realistically simulate the HRCT, the PET and the various AC CT datasets. All attenuation and activity maps were created using a voxel size of 0.8 mm.

All phantoms represented an average male, arms up [100]. Realistic and homogeneous activity values were assigned to the different tissues of the simulated activity phantom, based on average activity values observed in available measured datasets (see Table 1.1).

Respiratory and cardiac motion were modelled when needed. In order to be adherent to an average patient study protocol, attention was focused on the shallow breathing scenario, using the default values provided by the XCAT software [91] to describe antero-posterior (AP) expansion and diaphragm translation. A heart-rate of 60 beats per minute was also modelled. An overview of the main common parameters used to generate all the phantoms can be found in Table 1.1.

*Table 1.1: Key parameters for phantom generation.*

Antero-posterior (AP) expansion [cm]	1.2
Diaphragm motion [cm]	2.0
Resp. cycle duration [s]	5
Card. cycle duration [s]	1
No. resp gates/cycle	5
No. card gates/cycle	10
Phantom size [pixel]	600x600x203
Phantom pixel size [mm]	0.8
Left ventricle activity [kBq/cc]	26
Lung activity [kBq/cc]	0.9
Blood pool activity [kBq/cc]	5.5
Liver activity [kBq/cc]	6.3

This paper focuses on the registration between a dual-gated PET image and a HRCT image in a fixed cardiac and respiratory phase. Hence, the most stable phases of the breathing and of the beating cycles were chosen for simulating these datasets. Particularly, it is known that the diastolic phase normally has a longer duration and a higher stability, compared to other phases within a cardiac cycle. Furthermore, patients with a regular shallow breathing pattern are known to spend a large amount of time in the end-expiration phase of the breathing cycle. Therefore, aiming at a doubly-gated acquisition, the choice of end-expiration phase could allow to use more data than any other phase of the breathing cycle and minimize the chances of contamination of the gate by motion (e.g. if an optimal gating strategy was used, as in [101]). For this reason, the HRCT and the dual-gated PET image of interest are simulated to be acquired in the end-diastolic cardiac phase and in the end-expiration breathing phase.

More details about the different datasets are given in the following of this section.

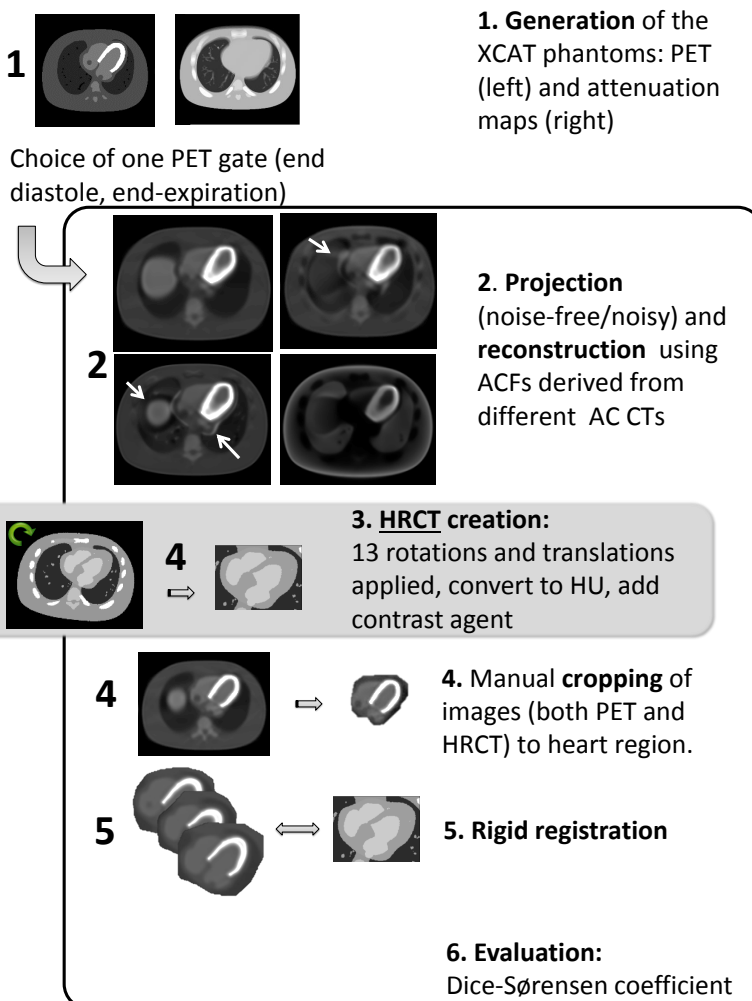


Figure 1.1: Phantom generation, registration and analysis flowchart.

## HRCT DATASET

In order to generate the HRCT frame of reference, a dataset with blood-pool contrast and high spatial and temporal resolution was generated. The cardiac cycle of the XCAT phantom was divided into 10 equally spaced time frames (gates), for a total cycle duration of 1s. The gate corresponding to end-diastole was chosen, while the other frames produced with the XCAT phantom were discarded. The respiration phase of the simulated HRCT phantom was kept fixed to end-expiration. This image, generated with the XCAT software, was converted to Hounsfield units and small rotations and translations were applied to it, to simulate patient positioning differences between the PET/CT scan and HRCT scan. Thirteen different initial roto-translations were simulated, where the sets of three rotation and three translation values were obtained by randomly sampling a uniform distribution of rotation and translation values in the range of [0, 0.3] rad and [0, 4] cm respectively. The resulting HRCT images served as the target high-resolution CT, to which the PET frame of interest should be registered.

## PET DATASET

The phantom from which the HRCT dataset was extracted was also used to obtain the corresponding PET dataset. The selected PET frame, therefore, was the one that captured the heart in end-expiration and end-diastole.

## AC CT DATASETS

Additional phantoms were generated to obtain various attenuation maps (see also Fig. 1.2), which differ in the way the AC CT is acquired in the presence of the cardiac and respiratory motion.

- **C1-exp** : the attenuation map perfectly matches the PET respiratory and cardiac phase, thus leading to **ideal**, artefact-free PET reconstructions.

In practice, this can be obtained with a very fast CT scan or with a medium speed CT scan coupled with ECG-gating during breath-hold. However, a cardiac-gated CT results in a higher dose for the patient. In addition, a breath-hold in end-expiration, for an amount of time sufficient to acquire such AC CT, can be difficult for many patients. Therefore, C1-exp is not the most desirable protocol in clinical practice. For this reason, other AC CT protocols have to be considered.

- **C2-exp** : similar to *C1-exp*, but the attenuation map is **slightly mismatched** with respect to the **cardiac phase** of the corresponding PET image.
- **C1-insp** : similar to *C1-exp* the beating phase of the CT for attenuation correction corresponds to the one of the PET and the HRCT, but it is simulated to be in a completely **different respiratory phase** (i.e., end-inspiration, because breath-hold in this phase is typically easier for patients).

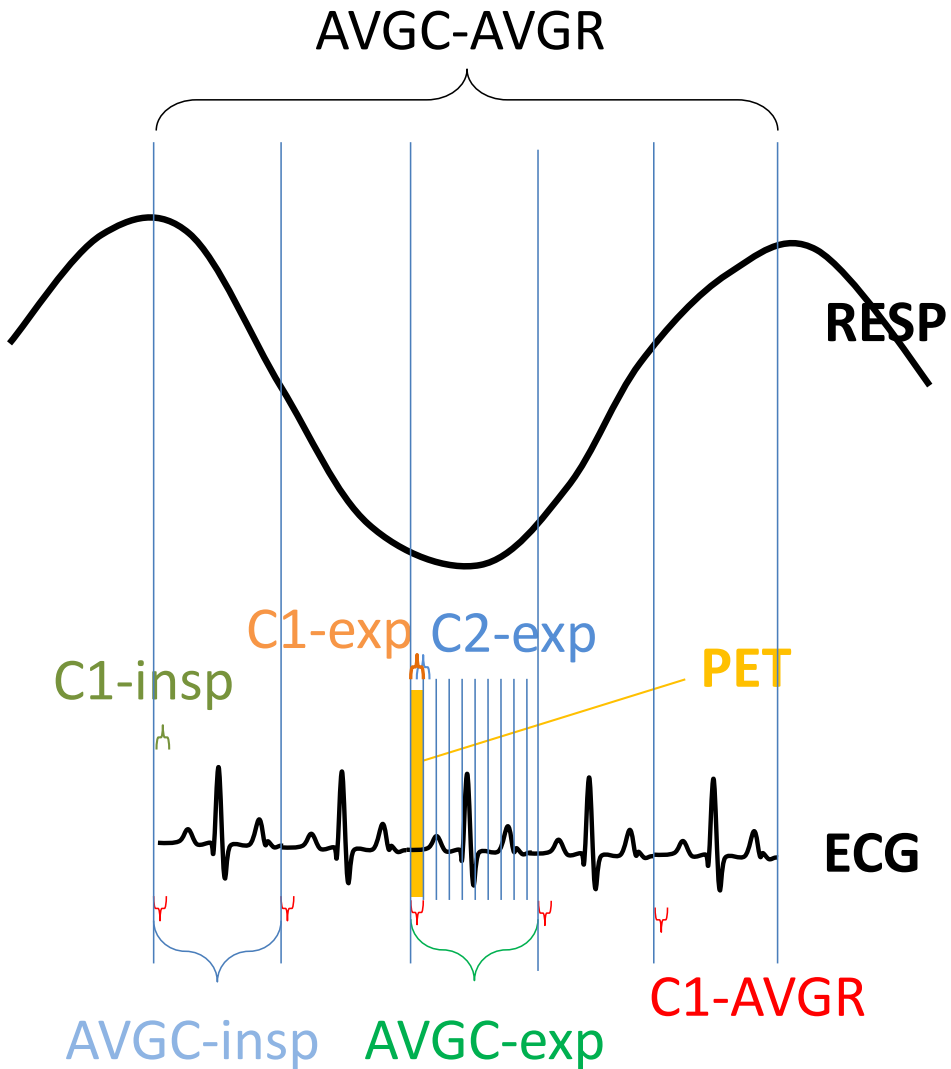


Figure 1.2: ACCTs generated with the XCAT software and their position with respect to cardiac and respiratory motion.

- **AVGC-exp** : the AC CT corresponds to the **average over** a complete **heart cycle**. This is equivalent to a breath-hold CT acquired at end-expiration.
- **AVGC-insp** : similar to *AVGC-exp*, but the **respiratory phase is different** (i.e., end-inspiration instead of end-expiration). Since this AC CT is an average over one full beating cycle, it represents the result of a CT acquired at medium scanning speed with breath-hold.
- **C1-AVGR**: the AC CT perfectly corresponds to the cardiac gate of the PET being reconstructed, but it is **affected by** motion blur due to **respiration**. This AC CT could be the result of an ECG-gated CT acquired during free breathing with a low pitch.
- **AVGC-AVGR**: an AC CT obtained by **averaging** all AC CTs **over** one **breathing and** several **beating** cycles was obtained with the XCAT software. This would correspond to a scenario where the patient is breathing regularly during a CT acquisition with a very low pitch.
- **sh(AVGC-insp)** : the same AC CT as *AVGC-insp* is used. However, it is **aligned to the PET dataset before using it for AC** of the PET dataset. In order to align the myocardium of the AVGC-insp image to the myocardium of the PET image, binary masks corresponding to the myocardium were automatically generated, both in the PET and in the AC CT. For simplicity, the delineation of the myocardium in the AC CT was performed by thresholding the corresponding gate of the *activity* map to the myocardial tissue. The mask image corresponding to the AC CT was subsequently rigidly registered (only translations allowed) to the PET mask image using normalized cross-correlation. The registration parameters were then applied to the AVGC-insp and the resulting, shifted attenuation map ('sh(AVGC-insp)') was used for attenuation correction. This procedure is only possible in a simulation study. In practice, the creation of such mask images could be cumbersome, especially for what the AC CT is concerned. The most practical solution in this case, currently implemented on several PET/CT systems from various manufacturers, is to proceed with a rough manual alignment of the myocardium of the AC CT to the myocardium of the PET [102] [103].
- **NOATTEN** : as a final alternative, the PET gate was also reconstructed **without any attenuation correction**.

## PROJECTION AND RECONSTRUCTION OF THE ACTIVITY PHANTOM

The image generated with the XCAT software and corresponding to the PET gate of interest was projected using in-house developed software that simulates an acquisition with the PET component of a Siemens Biograph 16 PET/CT (Hirez) scanner [29]. Attenuation and a shift-invariant camera resolution were modelled, but scatter and randoms were not.

A noise-free sinogram was obtained. In addition, ten noisy sinograms were generated by adding Poisson noise to the noise-free sinogram, corresponding to a 36

s-acquisition. The rationale behind this value is as follows. An average PET scan can last up to 30 minutes. If motion-free images need to be obtained, the easiest way is to perform a double gating pass on the original listmode data set. This way, the initial dataset is first divided into, e.g., 5 respiratory gates, and after that every respiratory gate is further divided into, e.g., 10 cardiac gates. Thus, a 30-min PET scan must be equally divided into 50 gates, resulting in an actual contribution of 36 s to each gate.

In order to verify whether shorter scan times influence the results obtained, we additionally generated noisy PET reconstructions with lower count levels. Particularly, Poisson noise was added to the noise-free sinogram to simulate 6 s-, 12 s-, 24 s- and 30 s-acquisitions, which correspond to a total scan time of 5, 10, 20 and 25 minutes respectively. The activity sinogram was then reconstructed using a 3D OSEM algorithm with resolution recovery (4 iterations and 12 subsets per iteration). Both the projection and the reconstruction of the datasets were done using the same projector, which included ray tracing and modelling the system resolution as a shift-invariant Gaussian convolution (FWHM = 4.3 mm and 4.5 mm in the transaxial and axial direction, respectively). The voxel size of the reconstructed PET images was set to 2 mm x 2 mm x 2 mm. The different AC CTs, described in Section II, were converted to PET attenuation maps with voxel size of 0.8 mm x 0.8 mm x 0.8 mm. Sinograms containing the ACFs were computed from the forward projection of these maps with a ray tracing projection method, with no modelling of resolution effects. Each of those sinograms was used during each iteration of the reconstruction to correct for the effect of attenuation. The same reconstruction procedure was applied to the noisy sinograms.

## IMAGE PRE-PROCESSING

The reconstructed noisy and noise-free PET datasets were roughly cropped to the heart region, by manually delineating the region of interest (ROI) in the central transaxial slice of each volume and automatically propagating the same ROI to all other image planes. The cropping procedure was found to be beneficial for registration and drastically reduced the total computation time [104]. The shape of the cropped ROI was arbitrary as long as it contained the whole heart, both axially and transaxially. All PET reconstructions received the same cropping, in order not to influence registration results with an additional, possible source of variation. The thirteen roto-translated HRCT images were manually cropped too, with a different cropping for each HRCT, and not identically as the cropped PET images.

## QUANTIFICATION OF IMAGE ARTEFACTS

Various degrees of artefacts are to be expected in the reconstructed PET images, depending on the attenuation map used for reconstruction. The reconstruction with C1-exp is here regarded as the gold standard, because it perfectly matches both the respiratory and the cardiac phase of the corresponding PET, yet being more realistic than the initial phantom as projected and reconstructed with software that simulates the behaviour of the scanner.

As a measure of the severity of the artefacts in the heart region, we computed difference images between the PET images corrected with the various attenuation maps and the PET image corrected with C1-exp. Moreover, the sum of squared differences between such images was also calculated, after cropping the datasets as explained in II.

## QUANTIFICATION OF ACTIVITY

In those fields where accurate quantification of the activity is required, attenuation correction might play a role in under- or over-estimating activity values in the region of interest. In this work, the reconstructed activity within the left ventricle (LV) is of interest. For this reason, the quantification accuracy of the total reconstructed activity within the LV in the PET images corrected with the various ACF sinograms was also briefly investigated.

First, the total reconstructed activity in the LV was calculated. Based on the XCAT phantom, a binary mask images was created, where the LV was set to 1 and all other image pixels were set to 0. All the reconstructed, noisy PET datasets, corrected with the various AC CTs, were then multiplied by such mask, and the total activity was calculated. The mask used is one for all PET reconstructions. We opted for this strategy in order to clearly evaluate the artefacts within the original LV region. The other approach, that is to optimize the mask for each PET corrected with a different AC CT, introduces increased chances of hiding the artefacts produced by the various AC CTs.

The mean total activity over the ten noise realizations was calculated. A paired t-test was performed between the values obtained in the (ideal) case of PET images corrected with C1-exp and with each of the other ACF sinograms. C1-exp was chosen as ground truth, instead of the phantom, in order to rule out any possible effect of the reconstruction process on the results.

In addition, the quantification of the LV was evaluated for an artificially-created AC CT. In case the HRCT was registered directly to the NOATTEN PET, because no suitable AC CT was available for accurate image registration (see Section III), quantification could be performed on a subsequent PET reconstruction using the aligned HRCT as AC CT. However, often the HRCT available does not cover the full field-of-view (FOV) being imaged. Therefore, it would be necessary to paste such HRCT into the corresponding region of a full-FOV AC CT (acquired at low-resolution, low-dose) in order to have all the necessary information for performing AC on the full-FOV PET image. Such a scenario was simulated with the help of the XCAT phantom by ‘pasting’ a cropped high-resolution CT, deprived of blood-pool contrast, into a full-FOV AVGC-AVGR. The simulated PET gate of interest was then reconstructed using such a ‘pasted-HRCT’, and the effect of the discontinuities on the LV quantification was studied.

Additional analyses were also performed on the most interesting AC strategies: C1-exp, AVGC-AVGR, AVGC-exp, sh(AVGC-insp) and pasted-HRCT. C1-exp was chosen as the reference or gold standard. The AVGC-AVGR and AVGC-exp were further studied because they would be the easiest to perform in the clinical practice. The sh(AVGC-insp) has a promising potential of restoring the total LV activity to

values closer to the reference. Finally, the pasted-HRCT would be the only reason to justify the registration of NOATTEN PET datasets to the HRCT.

For this purpose, a 17-segments polar map [105] was generated for each of the noisy PET reconstructions corrected with ACFs derived from the aforementioned AC CTs. For visual assessment, the average activity value over the 10 noise realizations was computed, for each segment of each polar map. For a more quantitative assessment, a value describing the uniformity of each of the polar maps was defined as follows:

$$R_s = \frac{\bar{x}_s}{\bar{x}}, s = 1 \dots 17$$

$$U = stddev(R)$$

with  $R = [R_1, \dots, R_{17}]$ . In other words, the ratios between the mean activity value in each of the segments ( $\bar{x}_s$ ) and the mean overall activity value ( $\bar{x}$ ) was computed, for each segment of each attenuation strategy. The closer these ratios to 1, the more uniform the polar map is. The standard deviation  $U$  of these ratios over the 17 segments was then computed. The closer  $U$  to 0, the less the ratios are spread around the value of 1 (ideal, perfectly uniform polar map), thus giving an indication on the LV uniformity.

Wall ratio calculations were also performed to quantify more regional changes in uniformity. To this end, the average polar maps were divided in 5 areas, corresponding to the anterior wall (segments 1, 7, 13), posterior wall (segments 4, 10, 15), lateral wall (segments 5, 6, 11, 12, 16), septum (segments 2, 3, 8, 9, 14) and apex (segment 17). The mean activity in each of these regions was calculated, and the antero-posterior (AP) and lateral-septal (LS) wall ratios were then computed.

## REGISTRATION APPROACH

Rigid registration of the PET frame to the HRCTs was performed using the cropped images. Normalized mutual information (NMI) was chosen as the matching criterion, since it has been proved particularly effective for inter-modality image registration of cropped datasets [106]. Registration was performed in three steps, in a multiresolution fashion. One hundred bins were used to histogram the intensity ranges of the images being registered. This value was chosen to ensure a clear distinction of the intensities of the LV and the blood pools both in the PET and in the HRCT images.

Poor registration results were obtained at times. In order to exclude from the causes of this failure the initialization of the PET dataset, whose initial orientation was relatively different from that of the HRCT image, a preliminary image alignment was attempted. To this end, we performed the same PET-to-HRCT registrations, but starting from parameters that yielded a very good initial positioning of the PET dataset if compared to the orientation of the HRCT. A drift from this initial and ideal positioning during the registration process would confirm the role of the artefacts in hampering the registration outcome.

For the NOATTEN datasets, which were the only ones that proved to benefit from such initialization, a manual preliminary alignment was also attempted. This

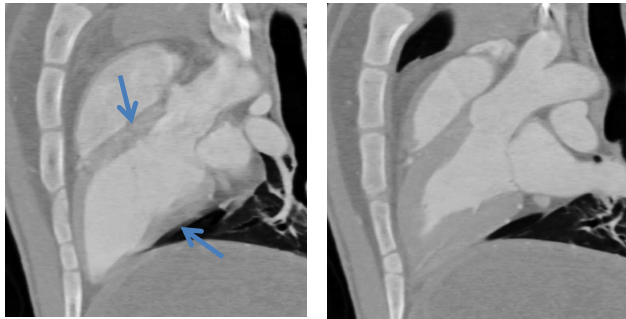


*Figure 1.3: Comparison between a HRCT affected (left) and not affected (right) by motion blur. The slice is representative for the whole volume.*

procedure, albeit less accurate, provided a more viable and realistic alternative to roughly initialize the datasets of interest.

## EVALUATION OF REGISTRATION RESULTS

Evaluation of PET-to-HRCT registration was done in PET space, as this will be the space where PVC is applied. The registered images were evaluated visually and quantitatively. DICE-Sørensen coefficients (DSC) were calculated to quantify the overlap between the left ventricular region in the PET image and the LV region in the registered high-resolution CT. For this purpose, the same mask images as for quantification were used (see Section II) and the overlap between them was measured by means of the DSC.

Since the evaluation needed to be performed in PET space, but only the parameters corresponding to PET-to-CT registration were available, the inverse registration transformations were applied to the CT mask before calculating the DSCs.

## REAL DATASETS

Finally, we verified whether the findings from the simulation studies found correspondence with results obtained on sheep. To this purpose, two sheep experiments approved by the local ethical committee were carried out. Detailed information on the two animals, together with an overview of the settings used during the scans, are in table 1.2.

Each sheep underwent the following scans (all at constant heart rate of 110 beats per minute):

1. a high-resolution CT with contrast enhancement acquired on a Siemens SOMATOM Definition scanner, using a pre-defined ECG-gated spiral protocol (CoronaryCTA). Ten different cardiac gates were reconstructed. The respiratory phase during which the whole dataset was acquired was known and represented end-expiration. One volume corresponding to one cardiac phase was selected, thus obtaining a real HRCT where the heart is in a fixed and known respiratory and cardiac position.

*Table 1.2: Key information on the animal experiments.*

General information

Weight, sheep 1 [kg]	42.0
Weight, sheep 2 [kg]	55.0
Age, sheep 1 [days]	345
Age, sheep 2 [days]	376

HRCT generation parameters

Scanner	Siemens SOMATOM Definition AS
kVp	120
mAs	257
pitch	0.34

PET scan information

<sup>18</sup> F-FDG administered dose, sheep 1 [MBq]	374,30
<sup>18</sup> F-FDG administered dose, sheep 2 [MBq]	237,12
scan time [min post-injection]	30
scan duration [min]	30

The cardiac phase was chosen based on a visual analysis of the entire HRCT, i.e., the cardiac gate that showed the least amount of motion and contrast-related artefacts in the LV region was chosen. In fact, it was observed that the use of a HRCT in which the uniformity of the LV was compromised and the distinction between the LV walls and the LV chamber was less neat (e.g. left pane of Fig. 1.3) resulted in poor registration outcomes. In the animals, the respiratory phase during which the HRCT was acquired was obtained by means of a mechanical ventilator. In patient studies, a fixed respiratory phase could be obtained by means of an active breathing control system (as in [107]).

2. a 30-minute <sup>18</sup>FDG-PET scan, acquired on the Siemens Biograph 16 (Hirez) scanner. Triggers corresponding to both the cardiac (ECG) and the respiratory signal (from the Respiratory Gating System AZ-733V) were inserted into the listmode during acquisition, and subsequently used to double-gate the dataset using in-house software. A phase-based gating approach was used for the respiratory motion, as the respiration of the sheep was artificially controlled by a ventilator, hence very regular in its pattern. The chopped listmode data corresponding to the same cardiac and respiratory phase as the best HRCT gate was selected, by taking the end-expiration chunk and selecting the same cardiac phase according to the ECG triggering. Such short listmode was converted to a sinogram and reconstructed using the different attenuation maps listed in the remainder of this section.
  
3. different AC CTs, acquired on the Siemens Biograph 16 (Hirez) scanner:
  - (a) an average low-dose AC CT at low pitch, hence spanning over multiple cardiac and respiratory cycles. This acquisition corresponds to the AVGC-AVGR AC CT simulated with the XCAT phantom.

- (b) an average low-dose AC CT at low pitch, again spanning over multiple beating cycles. However, differently from a), the respiratory phase in which this AC CT was acquired was known and fixed to end-expiration. Such acquisition mimics the AVGC-exp simulated with the XCAT.
- (c) a cardiac-gated CT acquisition at low pitch, thus spanning over multiple respiratory cycles. This CT resembles the C1-AVGR.
- (d) a cardiac-gated CT acquisition, when the respiration of the sheep is forced to end-expiration, reproducing the behaviour of the simulated C1-exp.

All the AC CTs were converted to 511 keV attenuation maps using the hybrid scaling method [33], forward-projected using in-house software that simulates the behaviour of the PET scanner and used as AC sinograms during the reconstruction of the selected PET gate. One PET reconstruction was performed without any attenuation correction, too. The activity sinogram was reconstructed using a 3D OSEM algorithm with resolution recovery (4 iterations and 12 subsets per iteration). The voxel size of the reconstructed PET images was set to 1.35 mm x 1.35 mm x 2 mm.

Each of the resulting reconstructions was manually cropped to the heart region (as for the simulation study, only transaxial cropping was performed). The HRCT from the dedicated, high-resolution scanner was cropped as well to delineate the heart. All PET reconstructions of the same sheep received the same cropping, but PET and HRCT were cropped differently.

Finally, the cropped PET datasets were registered to the cropped HRCT. The resulting registrations were evaluated by visual inspection.

### III RESULTS

#### QUANTIFICATION OF IMAGE ARTEFACTS

Fig. 1.4 shows the artefacts that can be caused by using different AC CTs in the simulated noise-free datasets. Table 1.3 confirms what can be intuited from the images. A high SSD (sum of squared differences) is obtained when the artefacts are more pronounced.

#### QUANTIFICATION OF ACCURACY

The total activity was calculated within the LV wall of the different attenuation-corrected, noisy PET reconstructions. The results are summarized in Table 1.4. Although the artefacts produced by the use of different attenuation maps are not always visually striking, the AC CT used does have an effect on the total reconstructed activity within the LV. Moreover, a procedure to align the myocardial volumes in the AC CT to that in the PET before the PET reconstruction ( $sh(AVGC\text{-}insp)$ ) seems to be beneficial when compared to the reconstruction using the un-shifted version of the same attenuation map ('AVGC-insp'). The usage of a 'pasted-HRCT'

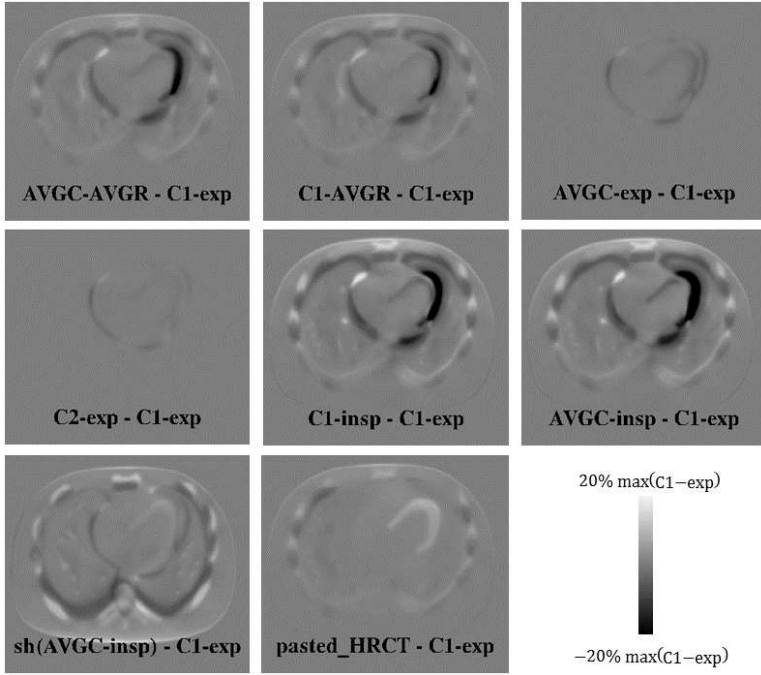


Figure 1.4: PET reconstructions corrected with C1-exp subtracted from the PET datasets reconstructed with different attenuation maps. Clear artefacts are present, both around and within the myocardium.

AC CT overestimated the overall activity, due to the fact that the pasted box containing the HRCT is wide enough to add un-compensated attenuation in the lungs region.

Fig. 1.6 shows the polar map analysis. Uniformity is best preserved when C1-exp (gold standard) and AVGC-exp are used, whereas AVGC-AVGR shows the largest variations. Using a 'pasted-HRCT' also seems to preserve uniformity, and yields improvements when compared to the usage of AVGC-AVGR. The U-values calculated for each polar map, together with the wall activity ratios presented in table 1.5, confirm such findings.

The best compromise between preservation of total activity and uniformity is obtained when using AVGC-exp as AC CT for deriving the ACF sinogram.

## REGISTRATION

In multimodal image registration, (N)MI has become a technique of reference. To our knowledge, however, the effect of the mis-alignment between the anatomical and emission image on PVC *for cardiac imaging* has not yet been addressed in previous literature.

Alignment tasks using MI for PET and MR images have shown an accuracy below 2 mm in brain [108]. Slightly worse accuracy values can be expected in cardiac imaging, where residual motion present in the datasets might deviate the

Table 1.3: SSD between the cardiac region of the PET reconstructions (corrected with the ACF derived from the different AC CTs) vs the ideal reconstruction (C1-exp)

	SSD
AVGC-AVGR	6.83e+11
C1-AVGR	6.19e+11
AVGC-exp	2.74e+10
C2-exp	1.22e+10
C1-insp	1.92e+12
AVGC-insp	2.07e+12
sh(AVGC-insp)	3.48e+11
pasted-HRCT	9.40e+10

Table 1.4: Mean activity values in the LV, for the PET reconstructed with different attenuation maps.

	Mean act. LV [MBq]	% act. difference from C1-exp	p-value
AVGC-AVGR	$3.945 \pm 0.111$	-4.8%	7.6E-19
C1-AVGR	$4.033 \pm 0.113$	-2.7%	2.6E-14
AVGC-exp	$4.076 \pm 0.115$	-1.7%	1.4E-10
<b>C1-exp</b>	<b><math>4.144 \pm 0.115</math></b>	-	-
C2-exp	$4.136 \pm 0.116$	-0.3%	0.17
C1-insp	$3.848 \pm 0.110$	-7%	5.6E-22
AVGC-insp	$3.692 \pm 0.109$	-10.9%	2.5E-25
sh(AVGC-insp)	$4.276 \pm 0.120$	+3.4%	1.9E-15
pasted-HRCT	$4.317 \pm 0.120$	+4.5%	1.4E-17

registration algorithm from the optimal solution. On the other hand, the accuracy of the registration between ungated whole-body PET and CT is pretty low (around 5-6 mm in the thorax) [109], but we believe these accuracy values can be improved with the application of double gating on the emission datasets.

A small simulation study allowed us to establish a rough correlation between the DSC of two simulated emission images of the LV and a mono-directional shift progressively applied to one of the two. Fig. 1.5 illustrates the result. The DSC decreases linearly with increasing shift values. Shifts in the three different directions were tested, with comparable results.

## EFFECT OF AC

From the registration results of the noise-free as well as of the noisy datasets, we can conclude that the use of different attenuation maps does play a role in the final registration outcome. Fig. 1.8 shows the amount of overlap after aligning the PET images reconstructed with the different ACF sinograms to the HRCT. Both in the noisy and in the noise-free case, the blur introduced by the beating of the heart does not influence the subsequent registration to the HRCT (cfr. AVGC-exp and C1-exp). In the light of the findings illustrated in Figure 1.5, the DSC values obtained in these cases correspond to a mismatch of less than 2 mm between the PET and the HRCT, compatible with the best performances of the currently available registration

Table 1.5: U-values and wall ratios, calculated on the average polar maps.

	AP ratio	LS ratio	U-value
AVGC-AVGR	1.067	0.942	0.054
AVGC-exp	1.055	1.003	0.033
<b>C1-exp</b>	<b>1.031</b>	<b>1.015</b>	<b>0.030</b>
sh(AVGC-insp)	1.067	1.007	0.0417
pasted-HRCT	0.983	1.015	0.034

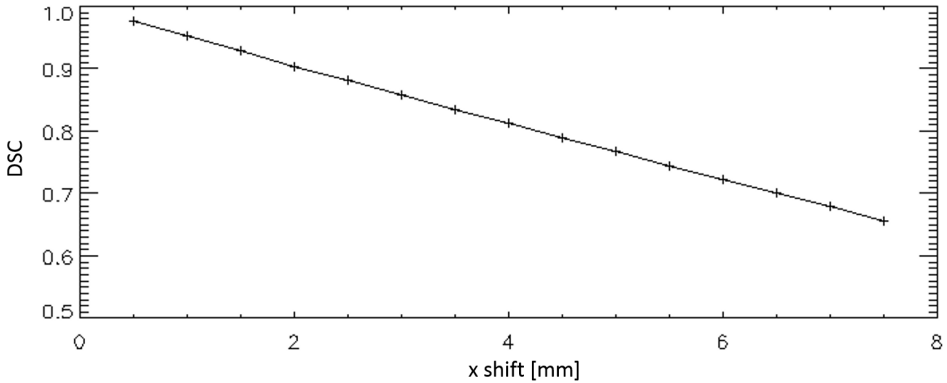


Figure 1.5: DSC obtained by overlapping a reference image of the LV to its shifted versions. Increasing shift values were tested, ranging from 0.5 mm to 7.5 mm.

techniques and below the PET resolution (about 4.5 mm FWHM). On the other hand, a mismatch in the respiratory phase during which the AC CT is acquired does influence the subsequent PET-to-HRCT registration (e.g. see C1-insp and C1-AVGR vs C1-exp).

Evident artefacts could already be noted in the difference images presented in Fig. 1.4, and from the values shown in table 1.3. The reconstructions with the highest SSD values also produced the worst registration results, thus allowing to establish a relationship between artefacts introduced by the attenuation process and final registration outcome.

## NOISE CONTRIBUTION

When noise is added to the PET datasets, the trend is maintained. A simulation of the PET with different count levels shows that we can even decrease the total scan duration down to 20 minutes, without affecting the registration outcome. Figure 1.7 illustrates the findings. When scans of very short duration are simulated, i.e. 5 and 10 minutes (corresponding to 6 and 12 s-duration per gate), we can notice a general increase of the variance and a decrease of the mean of the DSC values for almost all AC strategies. The decrease in performance at higher counts for AVGC-AVGR and C1-AVGR might be explained by the fact that, at lower noise levels, the artefacts introduced by the wrong respiratory phase are also more crisp and less confounded with noise, and therefore hamper more the registration. The DSCs obtained are

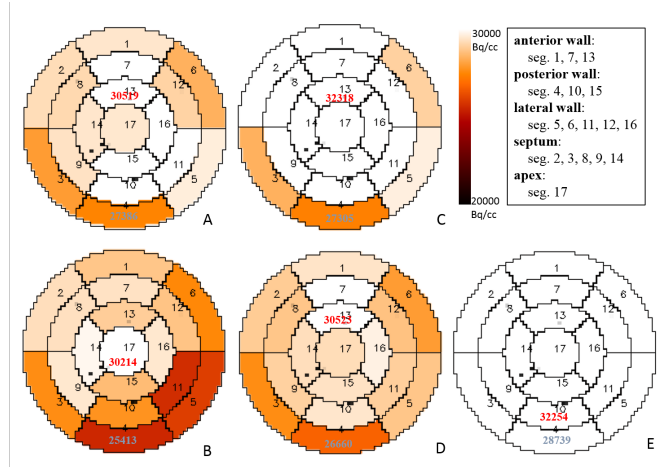


*Figure 1.6: Average 17-segments polar maps for the simulation study. The value assigned to each segment is the mean value of the segment, averaged over 10 noise realizations. PET corrected with (A) C1-exp, (B) AVGC-AVGR, (C) sh(AVGC-insp), (D) AVGC-exp, (E) pasted-HRCT*

anyway not acceptable for PVC.

In order to get rid of the slight decrease in performance introduced by the presence of noise, a smoothed version of the PET images was generated and used for subsequent registration to the HRCT. The results, presented in Fig. 1.8, confirm that improved DSCs can typically be obtained if the PET is smoothed with a Gaussian kernel of 4.3 mm (equal to the detector resolution), except if the PET datasets were reconstructed without AC (i.e., NOATTEN).

## ROBUSTNESS TO INITIAL POSITIONING

The robustness of the AC strategies to the initial difference in position between the PET and the HRCT was also analysed. Thirteen different rotations and translations were applied to the HRCT before registering it to the PET datasets corrected with the different ACF sinograms. Fig. 1.9 shows the results obtained when noise-free datasets are considered. Results proved to be fairly robust against different initializations of the HRCT dataset, except when NOATTEN datasets were used (last column in Fig. 1.9). In order to improve the un-satisfactory results obtained with AVGC-AVGR, C1-AVGR, C1-insp and In-C1-AVGR, the effect of the initial rotation was undone by initializing the PET-to-HRCT registration with a good parameter set, as explained in Section II. The results obtained after the initial alignment did not change, compared to the case where un-initialized registrations were performed. Only NOATTEN datasets seemed to benefit from such procedure (see Fig. 1.9, solid black line).

## NOATTEN DATASETS

The NOATTEN PET-to-HRCT registration can be as good as in the ideal case of C1-exp-to-HRCT, but it can also be very poor (see Fig. 1.9), showing that the

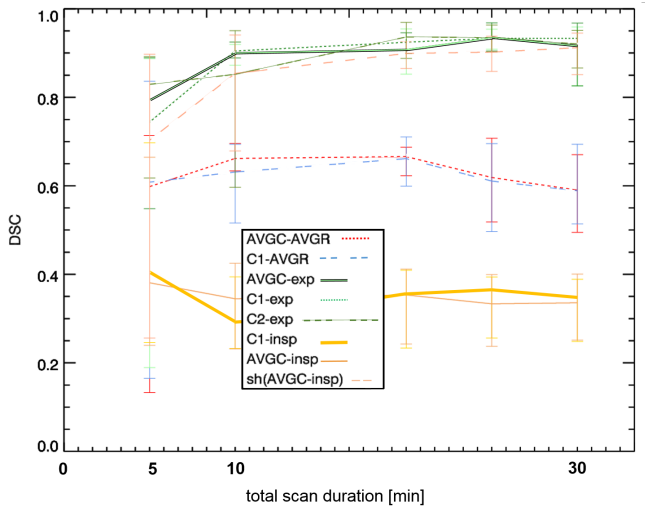


*Figure 1.7: Mean DSCs and min-max errors after PET-to-HRCT registration. The duration of the PET gates is progressively increased from 6s/gate (corresponding to a 5-min total scan duration, doubly-gated with 5 respiratory and 10 cardiac gates) to 36s/gate (corresponding to a 30-min total scan time).*

registration outcome depends on the initial alignment between the PET and the HRCT. Possible strategies to overcome the problem were evaluated, including an initial, rough manual alignment of the two volumes of interest, an initial HRCT-to-AC CT (AVGC-AVGR) automatic rigid registration or an histogram equalization of the NOATTEN-PET. The initial manual alignment produced the best results (results not shown).

The addition of noise increased the instability of the registration results in the NOATTEN case. Again, a rough manual alignment mitigates the problem (not shown).

## SH(AVGC-INSP) DATASETS

When aligning the PET corrected with AVGC-insp to the HRCT, a low registration accuracy is achieved, both in the noise-free and in the noisy case, due to the artefacts produced by the difference in respiratory phases between the PET and the AC CT (see Fig. 1.8, AVGC-insp). A procedure that can be rather easily applied in the clinic is therefore to align the AC CT to the PET before applying the new, shifted AC CT for attenuation correction, as described in Section II. The AC CT alignment can be manual or automatic. In this simulation study, the automatic alternative was chosen for simplicity. Fig. 1.10 and Fig. 1.8 show the registration accuracy obtained with this shifted attenuation map (sh(AVGC-insp)). The sh(AVGC-insp) procedure yields markedly improved registration to the HRCT, when compared to the usage of the un-shifted version of the same attenuation map (i.e. AVGC-insp). These improved results are very similar to those obtained with the ACF sinogram derived from the perfect AC CT (i.e. C1-exp).

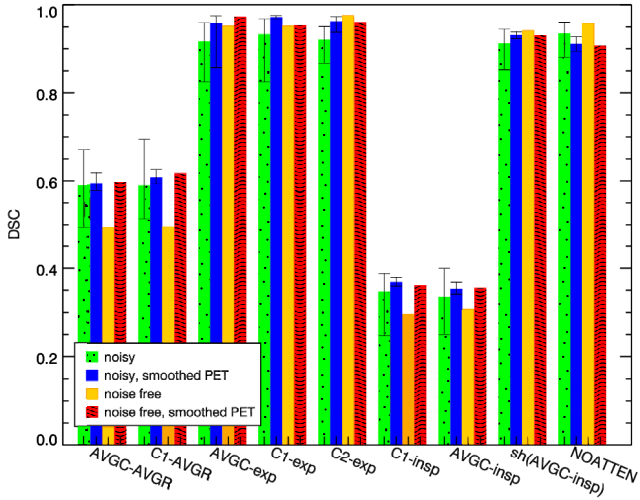


Figure 1.8: Mean, minimum and maximum DSC values over 10 noise realizations, for different AC strategies and a 30-min PET scan time. Cardiac motion is irrelevant, whereas the choice of the right respiratory phase is mandatory to achieve an acceptable final overlap ( $DSC \geq 0.9$ ). PET smoothing helps to improve overall image alignment.

## REAL DATASETS

The results obtained for the sheep datasets confirmed those predicted by the XCAT simulations (see Fig. 1.11). In the first sheep the results are striking, whereas for the datasets acquired with the second sheep the effects of AC on PET-to-HRCT registration are less pronounced. In both cases, however, a PET image corrected with an attenuation map that matches its respiratory phase results in the best alignment with the HRCT, regardless whether the cardiac phase was matched or not. On the other hand, the use of an AVGC-AVGR AC CT yielded clear misalignment, which is in agreement with the results obtained with the XCAT simulations. The polar maps of the first sheep, together with a table reporting uniformity values and AP-LS ratios, are also included in this study and shown in Fig. 1.12 and table 1.6 respectively. The ratios and the uniformity values are most similar to the ideal attenuation-corrected PET (C1-exp) when the ACCT is acquired in a fixed respiratory phase, cfr. ACGC-R1 and AVGC-AVGR.

Table 1.6: U-values and wall ratios for the first animal dataset.

	AP ratio	LS ratio	U-value
AVGC-AVGR	1.034	1.24	0.0649
AVGC-exp	1.036	1.27	0.0584
<b>C1-exp</b>	<b>1.043</b>	<b>1.270</b>	<b>0.0598</b>
C1-AVGR	1.037	1.249	0.0636

The usage of C1-AVGR hampered an accurate registration between volumes acquired with the first sheep, whereas for the second sheep the differences in terms of registration outcome, if compared to the registrations of the PET corrected with e.g. C1-exp, are less obvious. This may be partially due to the fact that the

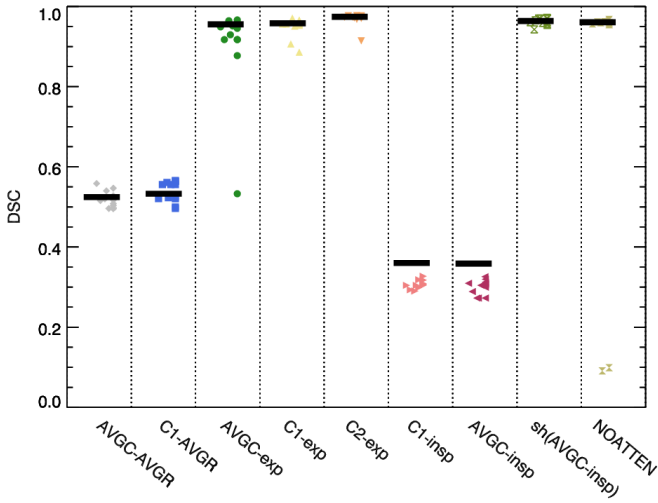


*Figure 1.9: Effect of different initial positions (parms 0-12) of the HRCT on the PET-to-HRCT registration (noise-free datasets). Each point cloud stands for a different AC strategy. Each point in a cloud represents the result of the registration of the PET to a HRCT roto-translated with a different set of parameters (0-12). The black line represents the result of the registration with an ideal initialization of the datasets.*

first sheep dataset was acquired in optimal conditions and on a healthy animal. The second dataset available, on the other hand, was acquired on a diseased sheep (myocardial infarction). In addition, a visual inspection of the C1-AVGR for the second sheep revealed that this scan was probably performed at a moment when the sheep was not breathing enough to produce visible blur or motion artefacts.

## IV DISCUSSION

The present work addresses one of the problems introduced by the attenuation correction process, when the breathing and beating motions of the heart are taken into account. In particular, it analyses the effect of the attenuation artefacts produced on the reconstruction of an  $^{18}\text{F}$ -FDG PET dataset, on a subsequent registration to an HRCT for partial volume correction purposes.

An accurate PVC of the emission datasets could, in turn, improve the diagnostic quality and the quantitative information of cardiac  $^{18}\text{F}$ -FDG PET images. This could have an impact on several clinical conditions as exemplified below.

First of all, even though both delayed-enhancement MRI (DE-MRI) and  $^{18}\text{F}$ -FDG PET have been recommended for viability assessment [24], DE-MRI is increasingly used and has nearly replaced FDG-PET. However,  $^{18}\text{F}$ -FDG PET is still used for viability assessment in a conspicuous number of patients, particularly those that cannot undergo an MRI scan (e.g. due to pacemakers, implanted defibrillators, claustrophobia).

In addition,  $^{18}\text{F}$ -FDG PET is not limited to assess viability in heart failure patients, but can also provide metabolic information in patients with conduction delays. Cardiac resynchronization therapy (CRT) with bi-ventricular pacemakers

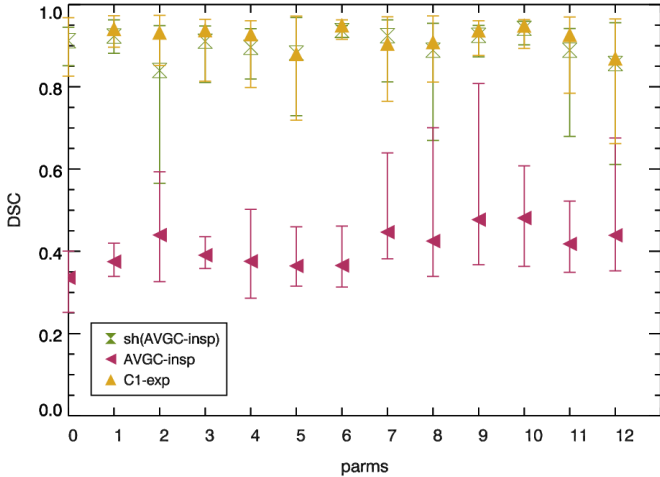
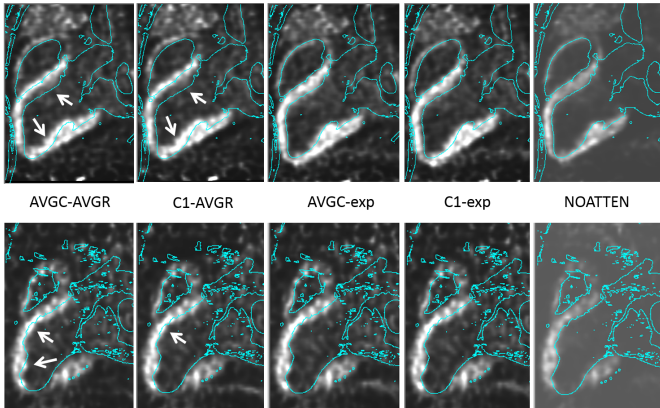


Figure 1.10: Mean, minimum and maximum DSC values over 10 noise realizations, for 13 different initial HRCT rotations. Cropped images, shallow breathing, PET-to-HRCT registration. The results of the *sh(AVGC-insp)* procedure are shown in comparison with the non-shifted version of the same AC CT (*AVGC-insp*), and to the ideal case of a perfectly matching AC CT (*C1-exp*).

has become an accepted treatment in patients with conduction delays (eg. dilated cardiomyopathy), but more than one third of the patients selected for CRT with the available guidelines fail to respond to the treatment [1, 110]. Hence, better predictors for adequate therapy or new guidelines are needed to avoid unnecessary implantations. Recently, a relationship between inhomogeneous glucose uptake and delayed LV activation has been observed in patients with dilated cardiomyopathy, suggesting that  $^{18}\text{F}$ -FDG PET might be used as a tool for better patient selection for CRT [19, 111, 112]. However, the limited spatial resolution of the PET scanners currently available might not allow to distinguish a thin myocardial wall with normal metabolism from a thick wall with reduced metabolism due to possible partial volume effects. Therefore, the use of additional morphological information from other imaging modalities (eg. HRCT) to correct for PVC might give a better insight into the true activity distribution of the  $^{18}\text{F}$ -FDG PET and, as a consequence, improve its predictive value. In order to perform this partial volume correction, a necessary step would be to accurately align the PET emission and the anatomical datasets. This work underlines the need for using an appropriate AC CT to achieve a satisfactory image alignment, which is a necessary condition for accurate PVC.

Nowadays, dedicated CT scanners with high spatial and temporal resolution entered the clinical practice. These scanners are able to image the heart in a ‘frozen’ cardiac and respiratory phase with a significantly reduced radiation burden for the patient [65], thus avoiding the acquisition of a dedicated, high-dose HRCT. In addition, the methodology used in the current work could be extended to other imaging modalities as source of morphological information, such as MRI, instead of HRCT. This would exclude the need of a dedicated HRCT scan, and further reduce the radiation burden for the patient.

Finally, the emission images obtained with various other tracers could benefit from the results of this study, especially if the tracer distribution and the signal-



*Figure 1.11: Results of the registration between double-gated PET sheep datasets corrected with the ACF sinograms derived from the different AC CTs and the HRCT obtained for the same animal in the corresponding cardiac and respiratory phase. Each column represents the result of the registration of PET images corrected with different ACF sinograms. The blue contours are from the HRCT. Top row: sheep no.1, Bottom row: sheep no.2.*

to-noise ratio in the heart region is similar to that in an  $^{18}\text{F}$ -FDG PET image. However, to keep this work focused, we limited our study to the case of  $^{18}\text{F}$ -FDG PET.

The following of this section discusses the results obtained in terms of quantification and registration outcomes.

## QUANTIFICATION

As shown in previous literature, the use of an attenuation map that is mismatched to the corresponding, un-gated PET dataset induces artefacts that compromise the quantitative accuracy of the images under examination [38–40]. In the same studies, methods to circumvent the problem were proposed, namely shifting the AC dataset to better align with the PET dataset (similarly to what we call sh(AVGc-insp)), or to acquire an AC CT that spans over multiple respiratory positions (cine-CT, average CT). Those studies often showed improved results, in terms of reduced artefacts in the final un-gated PET datasets, when the latter technique was implemented.

The results presented in our study seem to confirm the previous findings, and provide a further insight on the effect of AC when a *gated* PET dataset is used instead. More specifically, although the artefacts produced by the use of different attenuation maps are not always visually striking, we noticed that the AC CT used does have an effect on the reconstructed activity within the LV of the emission image. If an AC CT had to be chosen for quantification purposes, it would be advisable to go for the AVGc-exp, if a(n almost) perfectly matching AC CT cannot be obtained with the available instrumentation. In case of a mismatch in respiratory phase in the AC CT, a preliminary (manual or automatic) alignment of the myocardium is advisable before attenuation correction.

The artefacts highlighted in our study, when an average CT is used, are somehow more striking than what was previously documented in literature. This could

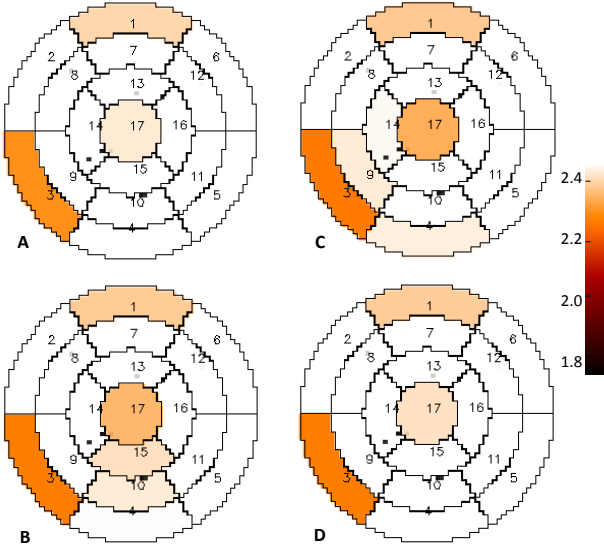


*Figure 1.12: Average 17-segments polar maps for the first sheep dataset (SUV values). The value assigned to each segment is the mean value of the segment. PET corrected with (A) ideal ACCT (C1-exp, reference), (B) AVGC-AVGR, (C) C1-AVGR, (D) AVGC-exp*

be explained by the fact that our PET dataset is gated, hence represents one single cardiac and respiratory state of the patient. Correcting such dataset with an ACF sinogram derived from an AC CT that spans over multiple respiratory and/or cardiac cycles is by all means an approximation, which can introduce artefacts as likely as any other mismatched AC CT. In other words, such averaging introduces a mismatch between the temporal resolution of the PET (which, after gating, accounts only for one precise respiratory and cardiac phase) and the temporal resolution of the CT, now spanning over the full respiratory cycle. The studies mentioned above, on the other side, apply AC to non-gated PET datasets. It is therefore logical that such 'averaged' PET datasets, corrected with an ACF sinogram derived from an averaged AC CT, overall show a lower degree of artefacts.

## REGISTRATION

The artefacts caused by breathing motion mislead the registration algorithm by producing a maximum mutual information for incorrectly aligned images. This result suggests that performing attenuation correction on the PET datasets can be deleterious for subsequent PET-to-HRCT registration if the respiratory phase of the attenuation map is not matching the respiratory phase of the PET gate. This happens regardless of the initial alignment between the emission and the anatomical dataset, thus suggesting that the AC strategy per se can hamper correct registration. In other words, even in the ideal case where no differences in patient positioning or body habitus can be found between the two datasets of interest, the PET-to-HRCT registration would fail if the AC CT was poorly chosen. Even if the patient positioning (and therefore the position of the internal organs relative to each other)

were to differ slightly between scans, this is not expected to hamper the registration outcome since the cropping applied would mask out these differences. We assume that when the cardiac phase is matched, rigid registration suffices to align the cropped hearts.

Given that the choice of the correct respiratory phase seems to be important for proper attenuation correction and subsequent PET-to-HRCT registration, the following alternatives for AC are possible:

- an AC CT that almost perfectly matches the respiratory phase of the PET gate being reconstructed. Although this is the way to achieve the best and most stable registration results, this procedure would require the acquisition of a CT in a controlled respiratory phase (which would ask for some additional way to monitor or control the breathing [107]); if not, artefacts that might hamper subsequent registration will appear.
- an AC CT acquired over one or more cardiac phases and in any (fixed) respiratory phase, subsequently aligned to the PET dataset of interest (as in sh(AVGC-insp)).
- an AC CT acquired over one or more cardiac and respiratory phases, with low radiation burden for the patient. In this case, the non-attenuation corrected PET dataset should be used for registration to the HRCT (after a preliminary rough alignment to it, if necessary). After PET-to-HRCT registration, a pasted-HRCT could be used for AC. This option could be particularly useful if the patient is not able to hold his breath in a fixed respiratory phase for a time sufficient to acquire the CT scan. However, this comes at the price of an overall overestimation of the LV activity. This is likely due to the fact that the 'pasting' process produces a final hybrid attenuation image (thus, with a different amount of lung, liver tissue and ribcage present in the FOV when compared to the PET respiratory phase, despite having the correct cardiac phase and position), whose inaccuracies affect the quantification. Therefore this solution, in spite of preserving uniformity better than other attenuation strategies, is not ideal when absolute quantification is aimed at.

## NOATTEN DATASETS

Without attenuation correction, the final PET reconstructions show e.g. increased activity in the body contours or increased activity in tissues of relatively low attenuation (e.g. lungs). Therefore, the use of NOATTEN datasets for accurate registration was not an obvious choice. However, according to the results obtained from our XCAT simulations, confirmed by visually inspecting the results of the sheep datasets, a NOATTEN PET can be aligned much more efficiently to the HRCT than e.g. a PET corrected with attenuation map that spans over multiple breathing phases, provided that the datasets of interest are **properly initialized**. Once this is achieved, the registration of the NOATTEN datasets to the HRCT yields registration results comparable to the ones obtained using a perfectly matching attenuation map, even in the presence of noise (cfr. C1-exp and NOATTEN in Fig. 1.8 and the black bars in Fig. 1.9).

On the contrary, when other non-ideal AC CTs (eg. AVGC-AVGR, C1-insp, ..) are used, the artefacts present in the resulting PET datasets do not allow for a correct registration of the PET and the HRCT datasets – even after a preliminary alignment of such AC PET datasets and the HRCT (Fig. 1.9, cfr the black bars of the NOATTEN datasets with those of the C1-insp datasets, for example).

The advantage of using NOATTEN datasets lies in the reduced burden for the patient, who would be relieved from holding his breath during the acquisition of the low dose AC CT. The attenuation correction of the PET dataset could be improved by pasting the registered HRCT, also used as anatomical prior, into such a full-FOV AC CT. This procedure would improve the LV quantification, even though leaning towards overestimation, as the simulations in Section III report.

## SH(AVGC-INSP) DATASETS

The registrations obtained with the sh(AVGC-insp) technique, already implemented on many PET/CT systems, are confirmed to be almost as good as the ones obtained with a perfectly matching attenuation map, with the substantial advantage of being easier and more patient-friendly to acquire. In fact, most patients can be asked to hold their breath in a non-predefined respiratory phase for the time of the AC CT acquisition, and no control over the cardiac cycle is needed.

The sh(AVGC-insp) procedure only requires little user interaction, namely checking the alignment of a fast (dual-gated) PET reconstruction to the corresponding AC CT, which can possibly be substituted by an automatic registration procedure. Moreover, it has the advantage of being relatively robust to noise and to different initial positions of the HRCT (see Fig. 1.10).

Although this research covers various aspects of the problems introduced by AC in a doubly-gated PET scan on which PVC needs to be performed, the study has a few limitations that need to be discussed.

In the first place, we assume an ideal-case scenario where the patient has a shallow, regular breathing and beating pattern, in order to rule out any possible influence of the gating technique or of the pattern of the biological traces on the results obtained, and to demonstrate the effect of a motion-affected attenuation map, even when e.g. an ideal breathing or beating pattern are considered. Shallow breathing was here simulated since it is the most relevant for the clinic. It is known that, in real measurements, variable breathing patterns can be encountered [113]. The gating of the PET or the CT datasets of such patients would be influenced by such variability by increasing the inter-frame motion encountered. In addition, the patient might move during the PET scan, further degrading the final gated images. Although this effect is unavoidable, reducing the scan times could represent a solution to at least minimize the chances of occurrence of gross patient motion. Moreover, it is up to the gating technique of choice to be able to cope with such differences in the biological traces, and to possibly correct for other types of motion before reconstruction. The results here presented might worsen, in case the motion correction technique did not properly correct for all the motion within the PET frame of interest, but a study on the effect of gating on the subsequent registration to the HRCT is beyond the scope of this paper.

Also, the present study does not attempt to implement any motion compensation during reconstruction, to improve the statistics of the PET datasets. However, in the light of the simulations here performed at different noise levels, we believe that an image with better statistics would not dramatically improve the registration outcome. Moreover, in the case where attenuation is not jointly estimated during the PET reconstruction, we believe that the questions addressed by this study would remain even in the case of motion compensated PET images. In fact, if we assume that the respiratory motion compensation was performed using motion parameters obtained from the registration of different respiratory gates to a reference gate, we would need a sufficiently well-aligned attenuation map for every individual PET gate, in order to avoid the artefacts introduced by AC. If this was not the case, such artefacts might hamper the accurate registration of the different PET gates to the reference gate as much as they do when registering the PET to the HRCT, thus possibly impairing the respiratory motion estimation and subsequent compensation.

Regarding the adherence of the present work to a realistic scenario, a first comment goes for the simulated PET scanner. The Siemens Hirez PET scanner, despite its lack of time-of-flight (TOF) capabilities, is still in use for clinical routine work in many centres and has a spatial resolution comparable to most non-TOF PET/CT scanners. In TOF-PET, the problem of attenuation is less stringent thanks to the recent developments of MLAA and MLACF algorithms for joint estimation of activity and attenuation [114] [115]. In all non-TOF PET scanners however, which are still widespread and otherwise well-performing, the attenuation problem still remains.

Secondly, no noise was added to the simulated CT images, as its effect on the reconstruction and registration is considered negligible, if compared to the high noise level in the PET data.

A possible limitation of this study is that the cropping of the images before registration is performed manually. Even if such manual step requires very little user interaction, a possible improvement would be to develop an algorithm for automatic cropping of the datasets to be registered.

Finally, in this study, a homogeneous distribution of the tracer in the LV was simulated (i.e. no areas of infarction). Even though studying an inhomogeneous distribution of the tracer might be more interesting from a medical point of view, a possible drawback of such simulated scenario would be a more difficult image registration, due to the infarction area, visible in the emission image but not on the HRCT. In this case, the registration might fail or perform worse not due to the sole effect of attenuation, but possibly also because of the characteristics of the datasets under examination. The use of an homogeneous distribution of activity, instead, allowed us to rule out any other cause of mis-registration except attenuation. In addition, it enabled the study of erroneous inhomogeneous uptake, which was solely caused by AC errors and different for the different AC maps used.

## V CONCLUSIONS

In this work, the effect of the use of different attenuation correction strategies on the subsequent registration between a dual-gated cardiac PET/CT and a HRCT

acquired on a dedicated scanner was assessed. This registration procedure is a necessary step, if the aim is to reconstruct the PET dataset with high-resolution anatomical a-priori information.

The use of an attenuation map that perfectly matches the corresponding respiratory gate of the PET image is necessary to guarantee acceptable alignment between the PET gate and the HRCT. The blurring introduced by the beating heart, in contrast, does not influence the subsequent PET-to-HRCT registration and does not hamper left-ventricular quantification.

If the AC CT is not acquired in the same respiratory phase as the PET, it is necessary to first align it to the PET before proceeding to the attenuation correction step. This procedure clearly improves the registration results as well as the quantification of the uptake in the left ventricle. If only an AC CT is available that is corrupted by respiratory motion blur, the best alignment can be obtained by registering the non-attenuation-corrected PET to the HRCT. Once an aligned HRCT is obtained, usually only partially covering the full FOV, it can then be pasted into the blurred AC CT for attenuation correction to improve the left ventricular quantification and uniformity.

The results obtained with the simulations are confirmed in a proof-of-principle sheep experiment.

## ACKNOWLEDGEMENTS

Anna Turco is a PhD fellow of the Research Foundation - Flanders (FWO). Olivier Gheysens and Jens-Uwe Voigt are senior clinical investigators of the Research Foundation - Flanders. Kathleen Vunckx is a post-doctoral researcher of the Research Foundation - Flanders.

The authors wish to thank C. Watson, J. Jones et al. for their help with the Siemens data processing.

## **2 GENERATING GROUND TRUTH DATASETS FOR CARDIAC PET STUDIES USING A SMALL-ANIMAL PET SCANNER.**

*This chapter is based on an article submitted to the IEEE Transactions on Radiation and Plasma Medical Sciences journal as: Generating ground truth datasets for cardiac PET studies using a small-animal PET scanner., A. Turco, J. Nuyts, J. Duchenne, O. Gheysens, J-U. Voigt, P. Claus, K. Vunckx*

### ***Abstract***

Scatter correction is believed to be not essential when reconstructing data from small-animal positron emission tomography (PET) scanners. However, there is evidence that the effect of scatter and attenuation cannot always be neglected, depending on the animals and organs of interest.

The purpose of this article is to describe the impact of scatter and attenuation on the reconstructions of cardiac  $^{18}\text{F}$ -fluorodeoxyglucose (FDG) PET datasets acquired with a clinical PET/CT scanner (Siemens Biograph 16 Hirez) and with a small-animal PET scanner (microPET Focus 220), in order to obtain a reliable reconstruction of such datasets to be used in turn as ground truth for cardiac studies. To this aim, we initially analysed the recovered mean values, contrast and the signal-to-noise-ratio on the microPET reconstructions of a physical heart phantom, corrected with various attenuation and scatter strategies. Secondly, the small-animal PET results were also compared to the results of the corresponding datasets scanned with a clinical PET/CT scanner. Ex vivo ovine hearts were also used to interpret and further corroborate the findings.

We propose a correct procedure to reconstruct the *ex vivo* cardiac datasets from both the pre-clinical and the clinical scanner and, when needed, to obtain a reliable scatter distribution. Our findings suggest the necessity of both accurate attenuation and scatter correction of the microPET datasets to obtain quantitatively acceptable reconstructions, whereas the reconstructions of the available datasets from the clinical scanner did not benefit from additional scatter correction.

# I INTRODUCTION

PET is a sensitive and quantitative technique used for several cardiovascular applications such as assessing myocardial viability. However, clinical PET scanners have a limited spatial resolution (3 - 6 mm full-width at half-maximum (FWHM) [29, 47]), which is suboptimal to image small structures. Several strategies have been proposed in an attempt to recover the true activity distribution and perform partial volume correction (PVC) of the regions of interest by using e.g. post-reconstruction methods, resolution modelling techniques, edge-preserving or anatomical priors [61, 116, 117].

Despite the encouraging results, the validation of the effectiveness of any of the proposed PVC techniques against a *measured* ground truth dataset remains important. This is particularly challenging when the heart is the organ of interest. Even though computer-generated or physical phantoms offer good ground truth datasets for many applications, they often can not adequately represent the cardiac complexity making them less suitable for cardiac applications. To our knowledge, the validation of PVC techniques against a measured cardiac ground truth has not been performed in the past.

Additionally, cardiac PET is also affected by the motion of the heart due to the respiration and the cardiac beating, which makes the assessment of the performance of PVC techniques in real datasets even more challenging. Therefore, measured static datasets which retain the original cardiac complexity are a valuable alternative.

The use of *ex vivo* imaging is a non-standard approach to assess the effectiveness of the PVC techniques. It has been proposed by our group and used to evaluate and compare the performance of edge-preserving and anatomical priors on real datasets, without degradation in image quality caused by motion artefacts [118]. In the context of this study, *ex vivo* hearts were scanned on a clinical PET/CT scanner (Siemens Biograph 16 Hirez [29]) and corrected for PVC. In addition, they were scanned on a high-resolution, small animal PET scanner (Siemens Focus 220, microPET) in order to obtain reconstructions almost free from resolution artefacts, due to the very good spatial resolution of the microPET scanner (1.3/1.5 mm in the transaxial/axial direction, respectively). The microPET datasets are meant to serve as ground truth, to which all other reconstructions from the clinical scanner should be compared. Therefore, a very accurate reconstruction of the microPET datasets is needed.

In small-animal PET imaging, the attenuation and scatter corrections are often neglected, due to the small size of the animals being scanned. However, this might not hold true for larger or heterogeneous objects, or when multiple objects are scanned at once [44, 45]. Given the non-conventional shape and size of the *ex vivo* hearts scanned with the microPET in the scope of our study, we investigated the effect of scatter and attenuation correction on those datasets.

Scatter correction can be implemented in several ways, depending on the specific task to accomplish. An effective and popular way to perform scatter estimation is by using a single-scatter model, based on the reconstructed transmission dataset and a preliminary reconstruction of the activity to estimate the distribution of the scatter

events [41]. This estimation method is currently implemented in the reconstruction software provided by many vendors, and it represents an easy and reliable way to estimate the scatter of an inhomogeneous object, provided that the contribution of the scatter occurring outside the field-of-view (FOV) of the scanner is negligible.

This work aimed at evaluating the impact of scatter and attenuation correction on the reconstruction of *ex vivo* cardiac datasets. We evaluated the effect of using:

- a 3D or single-slice rebinned attenuation sinogram
- a "cleaner" attenuation sinogram for the purpose of scatter estimation
- different scatter estimates to obtain the best qualitative and quantitative microPET images

Additionally, for this study, we use our own software as well as that of the vendor for the reconstruction of microPET datasets. We validated our software against the vendor's by verifying that for similar regularization the images were similar qualitatively and quantitatively. Eventually, the microPET reconstruction should effectively serve as reliable ground truth for further studies evaluating the effectiveness of PVC algorithms on cardiac image reconstruction of clinical PET datasets. Hence, we also developed a protocol to reconstruct images of the *ex vivo* datasets obtained with both the clinical and preclinical camera with comparable quality and quantitative information.

## II METHODS

### DATASETS

#### CARDIAC PHANTOM

A cardiac phantom with a simplified left-ventricular (LV) shape (Cardiac phantom insert, Bidex Medical Systems, Shirley, NY) was filled with an  $^{18}\text{F}$ -FDG solution with a uniform activity concentration of 11.3 kBq/cc at the time of the Hirez scan (see below). Two lesions were also inserted in the LV wall. One was a solid lesion with 0 activity ( $45^\circ \times 1.53\text{ cm}$  (height)  $\times 10\text{ mm}$  (thickness)), whereas the other ( $90^\circ \times 2\text{ cm}$  (height)  $\times 10\text{ mm}$  (thickness)) was filled with an activity concentration that was 1/4 of the concentration in the LV wall. After the filling, the phantom was securely sealed, connected to its support, and scanned as indicated in Section B.

#### ***EX VIVO* HEART DATASETS**

Thirteen sheep were enrolled in an animal study, approved by the local Ethical Committee, whose wider scope was to assess the effectiveness of PVC on the PET reconstructions of the heart. After scanning each of the animals alive (*in vivo* PET scan), they were sacrificed and had their heart excised (*ex vivo* datasets). The mean activity at the injection time of the *in vivo* animals was  $310 \pm 87\text{ MBq}$ . The hearts were excised after an average time of 80 minutes post-injection. After the excision,

each heart was filled with a low-attenuating, polyurethane hardening foam which ensured the stability of the shape of the heart throughout the subsequent scans (Section B).

## INSTRUMENTATION AND PERFORMED SCANS

The microPET Focus 220 and our clinical PET/CT scanner (Siemens Biograph 16, Hirez) were used to perform all the experiments of this work. The microPET scanner has a spatial resolution at the center of the field-of-view of 1.3 mm in-plane and 1.5 mm axially, whereas the clinical scanner has a resolution of 4.3/4.5 mm (transaxial/axial).

Each of the hearts was placed in the center of the FOV of the microPET scanner and scanned for 15 minutes using a 6 ns coincidence window and a 350-650 keV energy window. A transmission (tx) scan for attenuation and scatter estimation was also performed on the microPET scanner. The transmission data were acquired using a  $^{57}\text{Co}$  rotating point source, for a scan duration of 515 s. The *ex vivo* datasets were acquired a few months apart from each other and over a total duration of about 1.5 years. During the whole duration of the study, the transmission source used for acquiring the transmission image on the small-animal PET scanner for attenuation and scatter estimation continued its decay process. Therefore, with time, a decrease in the signal-to-noise (SNR) ratio of the resulting transmission maps is expected. We verified whether this decrease in the quality of the transmission image would affect the scatter estimation over time, by comparing each individual scatter estimate to the corresponding emission acquisition.

After the microPET scans, each dataset was transferred to our Nuclear Medicine facility and scanned for 20 minutes in the clinical PET/CT scanner. A high resolution CT (HRCT) was also acquired in the clinical PET/CT scanner, to be used for attenuation correction and as anatomical information during the reconstruction of both the microPET and the Hirez datasets with in-house software. The heart phantom and 10 of the 13 heart datasets were acquired on the Hirez scanner in sinogram format and precorrected for randoms. The remaining three heart datasets were acquired in list-mode format.

## CARDIAC PHANTOM: DATASET BINNING AND IMAGE RECONSTRUCTION

The cardiac phantom was used for the quantitative and thorough analysis of attenuation and scatter effects. Therefore, several combinations of attenuation and scatter correction methods were evaluated.

## MICROPET DATASETS

The emission dataset, acquired in list-mode format, was binned into sinograms (3D sinogram with span 3 and ring difference 47) using the microPET manager software provided by the vendor (microPET manager (TM) – release version 2.4.1.1, based

on Siemens e7-tools). Randoms subtraction was performed as pre-correction before reconstruction, together with deadtime correction (global average).

The transmission datasets, acquired in list-mode format, were processed in different ways to verify the effects of such processing on the reconstructed activity and on the scatter estimation. Particularly, each transmission list-mode dataset was binned either into 3D sinograms (3Dtx, both direct and indirect sinogram planes considered) or 2D sinograms (2Dtx, only direct planes, obtained by single-slice re-binning [119]), using the 3D or 2D blank sinograms respectively. Due to the decay of the transmission source, the acquired transmission datasets showed an increased background noise and a signal-to-noise-ratio that progressively decreased with time (Figure 2.1). Therefore, to verify whether the quality of the transmission scan influenced the attenuation correction and the subsequent scatter estimation, a "cleaned" version of the 2Dtx sinograms was also obtained. To this purpose, each 2Dtx sinogram was reconstructed with the vendor's software using maximum-a-posteriori for transmission (MAP-tr [120] with 10 iterations and a smoothing parameter of 1), and a fixed thresholding was subsequently applied to the reconstructed transmission images to remove the background noise. All voxels below 0.02 were set to 0. The thresholded attenuation image was visually inspected and subsequently forward-projected using full 3D sinogram binning using in-house software and saved in a file format compatible with the microPET software. All transmission sinograms obtained from the "cleaned" (thresholded) transmission reconstruction will have the prefix *clean-* in the rest of this article. We used both the original transmission sinograms (2Dtx and 3Dtx) and the clean-transmission sinograms during the reconstruction of the microPET dataset corresponding to the cardiac phantom using the vendor's software.

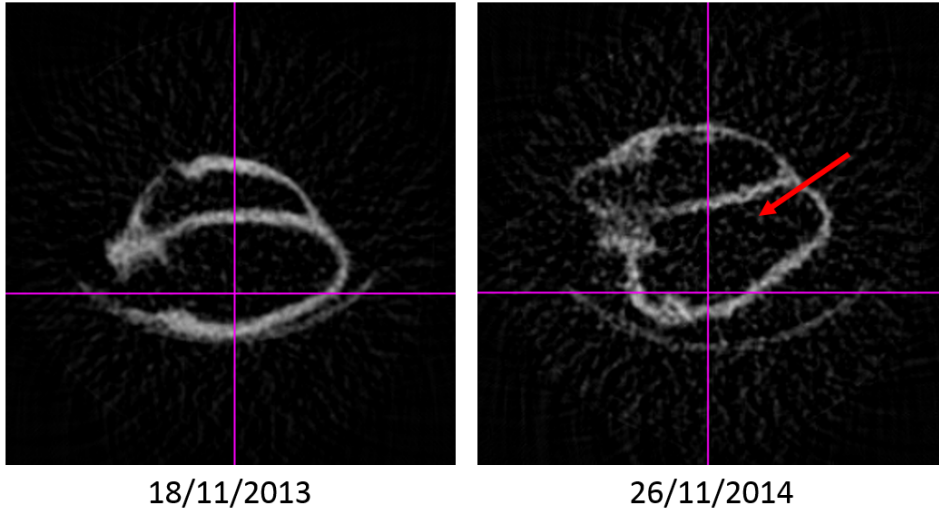


Figure 2.1: Filtered backprojection reconstructions of the transmission scan of one of the first heart datasets (left) and one dataset acquired about one year later (right). The difference in signal-to-noise ratio is already noticeable.

Once all sinograms were obtained, reconstructions of the emission dataset were

performed using both the microPET manager software (*vendor MAP* reconstructions from now on) and in-house developed software (*Bowsher-MAP* reconstructions). The vendor-MAP reconstructions had the purpose to produce the scatter estimation and to provide a reference for comparison of the in-house Bowsher reconstructions. The Bowsher-MAP reconstructions were performed as the reconstructions of the microPET datasets with an anatomical prior [61] (hence using our own software) proved to better represent the ground truth activity distribution in terms of bias and noise – according to a previous simulation study (not shown).

The vendor-MAP reconstructions of the microPET scans were obtained using 18 iterations and imposing a uniform resolution of 1.5 mm. Attenuation correction was performed during reconstruction, using either of the attenuation sinograms described above (3Dtx, 2Dtx or 2Dtx-clean). Additionally, we attempted to perform a reconstruction using the 'MAP-tr for attenuation' option offered (and automatically performed) by the vendor's software during the reconstruction of the emission datasets. The use of each of these attenuation strategies produced an equal number (4) of corresponding scatter estimates. The reconstruction voxel size was set to  $0.63 \times 0.63 \times 0.796 \text{ mm}^3$  (in the x, y and z direction, respectively) in all cases. The Bowsher-MAP reconstructions of the microPET dataset using the in-house software were performed with 5 iterations and 28 subsets, using the distance driven projector and a reconstruction voxel size of  $0.47 \times 0.47 \times 0.796 \text{ mm}^3$  (in the x, y and z direction, respectively) and the Bowsher prior in its asymmetrical variant [62] using the HRCT as anatomical side information (weight = 50, neighbours = 9 out of a spherical neighbourhood of 18 elements around the central voxel) and for attenuation correction. The resolution recovery of the dataset was performed by including a Gaussian point-spread-fuction of  $\text{FWHM} = 1.3 \text{ mm} / 1.5 \text{ mm}$  (transaxial/axial values, respectively) in the system matrix. This was implemented as a Gaussian smoothing of the sinograms in each forward and backprojection step with a Gaussian kernel with the same FWHM. We additionally reconstructed the dataset with our software, with exactly the same parameters and corrections, but using the 2Dtx-clean attenuation sinogram instead. This allowed a closer comparison of the in-house software against the vendor's software.

Both scatter-corrected and uncorrected reconstructions were obtained both with in-house and the vendor's software, using in all cases the scatter estimates obtained with the vendor's software [41] (starting from the different attenuation sinograms mentioned above). Normalization, attenuation and scatter correction were applied during reconstruction. All the microPET images were corrected both for in-frame decay and for decay to the start time of the *ex vivo* Hirez scan.

## HIREZ DATASETS

A scatter estimate was obtained off-line for the phantom dataset, using proprietary software provided by the vendor (e7 tools, Siemens, Knoxville). The attenuation sinogram to be used during the reconstructions of these datasets was obtained by forward-projecting with in-house software the HRCT acquired on the PET/CT scanner, previously converted from Hounsfield Units (HU) to 511 keV attenuation factors [37]. The reconstruction of the emission dataset was performed using in-house developed software that modelled attenuation, scatter and normalization at

each iteration. A MAP reconstruction (Bowsher prior in its asymmetrical variant [62], weight = 30, neighbours = 9 out of a spherical neighbourhood of 18 elements around the central voxel) was performed with the following iteration scheme (iterations x subsets): [3, 2, 2] x [42, 24, 1], using a reconstruction voxel size of 1.35 mm in the three directions and the distance driven projector. When needed, resolution recovery was performed by incorporating a sinogram smoothing with a Gaussian kernel of 4.3mm/4.5mm (transaxial/axial values, respectively) into each of the backprojection steps of the iterative reconstruction.

## **EX VIVO HEART DATASETS: DATASET BINNING AND IMAGE RECONSTRUCTION**

The *ex vivo* heart datasets were used to demonstrate the changes in the attenuation image over time. This was in turn useful to select the an approach for improved scatter estimation. Additionally, we used the *ex vivo* heart datasets to corroborate the findings of the cardiac phantom study. We applied the optimal attenuation and scatter estimation method to such datasets and we verified that the same good agreement found for the phantom between the Hirez and the microPET mean LV activities would hold true for the real animal datasets. For this reason, only a selection of the reconstructions performed for the cardiac phantom was also performed for the *ex vivo* cardiac datasets.

### **MICROPET DATASETS**

The acquired *ex vivo* emission and transmission datasets of all animals were rebinned as for the cardiac phantom. The resulting emission sinograms were reconstructed only with the in-house developed software, using the same voxel size, iteration scheme and prior weight as for the cardiac phantom. The attenuation correction of the *ex vivo* datasets was performed during reconstruction using the HRCT acquired on the PET/CT scanner (aligned and converted from HU to 511 keV attenuation factors). Scatter correction of these datasets was performed using the scatter estimate provided by the vendor's software, starting form the 2Dtx-clean attenuation sinogram.

### **HIREZ DATASETS**

The *ex vivo* emission datasets of all animals, acquired on the Hirez scanner, were rebinned and reconstructed as for the cardiac phantom.

### **CARDIAC PHANTOM: IMAGE ANALYSIS**

Several different combinations of scatter and attenuation correction were evaluated, using the cardiac phantom.

We initially compared the microPET reconstructions obtained using the vendor's software (vendor-MAP). A first analysis of the LV mean value was conducted on non-attenuation corrected against attenuation corrected microPET images of

the cardiac phantom, to corroborate previous findings on the necessity of attenuation correction of microPET datasets. Then, a comparison was performed between the vendor-MAP reconstructions of the cardiac phantom that were corrected for attenuation using either the 3D-tx or the 2D-tx.

Secondly, we evaluated the scatter effects on the vendor-MAP reconstructions. With the help of the ex vivo cardiac datasets, we analysed how the scatter estimate changed with time (hence, with the decaying  $^{57}\text{Co}$  source). We compared the scatter estimates obtained with the vendor's software when feeding it either with the 3Dtx, the 2Dtx, the clean-2Dtx or by using the built-in MAPtr attenuation correction method. To this purpose, the profiles of the scatter and the emission sinograms were calculated by summing the sinogram values over the planes and over the sinogram angles (rows).

Thirdly, we compared the vendor-MAP and the Bowsher-MAP reconstructions, to verify that our software produces results that are comparable with the state-of-the-art reconstruction software provided by the vendor.

Finally, we compared the results from the two systems (Bowsher-MAP from microPET and Hirez) by analysing the mean activity values within the left ventricle of the heart phantom. The in-house reconstructions that led to a similar mean activity concentration within the LV were chosen for the subsequent reconstructions of the measured sheep heart datasets.

For all the aforementioned comparisons, the mean reconstructed activity within the LV of the heart phantom was considered. To calculate it, a mask for the LV was obtained by growing a region within the LV of all microPET and all Hirez reconstructions, using a lower bound of 7.3 kBq/cc. For the vendor-MAP reconstructions of the microPET, the mask was also dilated with a cubic kernel of 3x3x3 to fill the gaps due to noise, and subsequently eroded with the same kernel to ensure the preservation of the original shape. The mean over all voxels within the masked region was computed for all reconstructions.

Additionally, we calculated the contrast ( $C$ ) between either the non-zero lesion (les) or the LV and the background (bkg), and the signal-to-noise ratio (SNR) in the LV wall of the cardiac phantom. These regions (LV, les, bkg) were defined first on the microPET image. The Hirez and the microPET images were then aligned using in-house developed software for image visualization. The regions were copied, using the same software, from the microPET to the corresponding Hirez reconstruction and, thanks to visual landmarks, they were manually adjusted to lie in corresponding positions. Figure 2.2 shows a slice of the microPET reconstruction with the regions that were used for the contrast and SNR calculations. The contrast was calculated as in [44]:

$$C_r = \frac{|I_r - I_{bkg}|}{I_r + I_{bkg}} \times 100 \quad (2.1)$$

where  $r$  is either the LV or the non-zero lesion (les). The ideal contrast is 1 (100%), which would be here obtained in case of a zero-background. The higher the background activity, or the lower the activity in  $r$ , the lower the contrast value.

The SNR was calculated by taking the ratio between the mean activity in the LV ROI and the standard deviation of the activity within the same ROI.

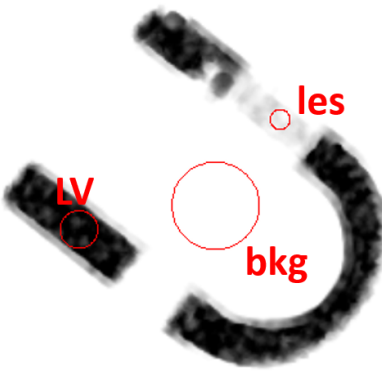


*Figure 2.2: Central slice of the microPET reconstruction, with the lesion (les), the left-ventricle (LV) and background (bkg) regions.*

## EX VIVO HEART DATASETS: IMAGE ANALYSIS

The reconstructions of all sheep datasets were reoriented and converted into polar maps [121] for a convenient and standardized comparison of the LV values. The mean LV activity was calculated on the polar maps of the LV of both the microPET and the Hirez reconstructions. A scatter plot reporting the correlation of the obtained mean values was generated, and the  $R^2$  value and the slope of the linear fit were reported to describe the agreement between the calculated mean values in the Hirez and in the microPET.

## III RESULTS

Table 2.1 summarizes the findings obtained for the cardiac phantom. The remaining of this section offers more insights into the individual values.

### VENDOR-MAPS OF THE MICROPET CARDIAC PHANTOM: 3DTX VS 2DTX VS NO ATTENUATION CORRECTION

The computed mean activity in the LV when using the 3Dtx for attenuation correction was lower than when using the 2Dtx instead (7636 Bq/cc vs 9276 Bq/cc). The reconstructions without attenuation correction produced an even lower mean activity value (5193 Bq/cc). Additionally, the estimation of the scatter fraction from the 3Dtx, using the vendor's software, proved incorrect. Figure 4.9 shows some examples of the scatter (red and green lines) and activity profiles (black line) obtained using either the 2Dtx (red line) or the 3Dtx (green line). It is clear that the scatter estimate produced by the software, when the 3Dtx is used as input, is too high (often, even higher than the activity profile) to be correct. Therefore, the 2Dtx was chosen as attenuation sinogram to be used for a more reliable estimation of the scatter using the vendor's software.

Table 2.1: Mean LV values computed from the various microPET and Hirez reconstructions (cardiac phantom). All values in Bq/cc.

	microPET	Hirez
<u>calculated</u>	11300	11300
<u>in-house developed software</u>		
> with HDCT for AC (no scatter)	9966	9709
> with HDCT for AC + 2Dtx-clean(microPET)/vendor-estimate (Hirez) for scatter	<b>9517</b>	<b>9665</b>
> with 2Dtx-clean for AC + 2Dtx-clean for scatter	9282	-
<u>vendor's software</u>		
> without AC (no scatter)	5193	-
> with 3Dtx (no scatter)	7636	-
> with 2Dtx (no scatter)	9276	-
> with 2Dtx-clean (no scatter)	9545	-
> with MAPtr (no scatter)	9433	-
> with 2Dtx-clean for AC + 2Dtx-clean for scatter	9279	-

#### **ATTENUATION EFFECTS ON THE VENDOR-MAP (MICROPET) RECONSTRUCTIONS OF THE CARDIAC PHANTOM: 2DTX (WITH AND WITHOUT MAP-TR) VS CLEAN-2DTX**

The computed mean activity in the LV when using the 2Dtx for attenuation correction was lower than when using the clean-2Dtx instead (9276 Bq/cc vs 9545 Bq/cc). The use of the MAP-tr algorithm for attenuation during the reconstruction of the emission datasets, starting from the 2Dtx attenuation sinogram, increased the reconstructed mean LV activity concentration (9433 Bq/cc) towards the result obtained with the clean-2Dtx.

#### **SCATTER ESTIMATION FOR THE VENDOR-MAP (MICROPET) RECONSTRUCTIONS: 2DTX VS CLEAN-2DTX ON THE SHEEP DATASETS**

The plot of the scatter profiles vs the activity profiles of all the sheep datasets showed a decrease in the performances of the scatter estimator over time. Figure 2.3 shows some examples of such progression. The use of the clean-2Dtx for scatter estimation improved the scatter estimate for the most recent datasets, and produced equally reasonable scatter estimates for the oldest datasets. The blue profiles in Figure 2.3 illustrate the finding, which held true for all other sheep datasets (not shown here). The use of the MAP-tr algorithm for attenuation during the recon-

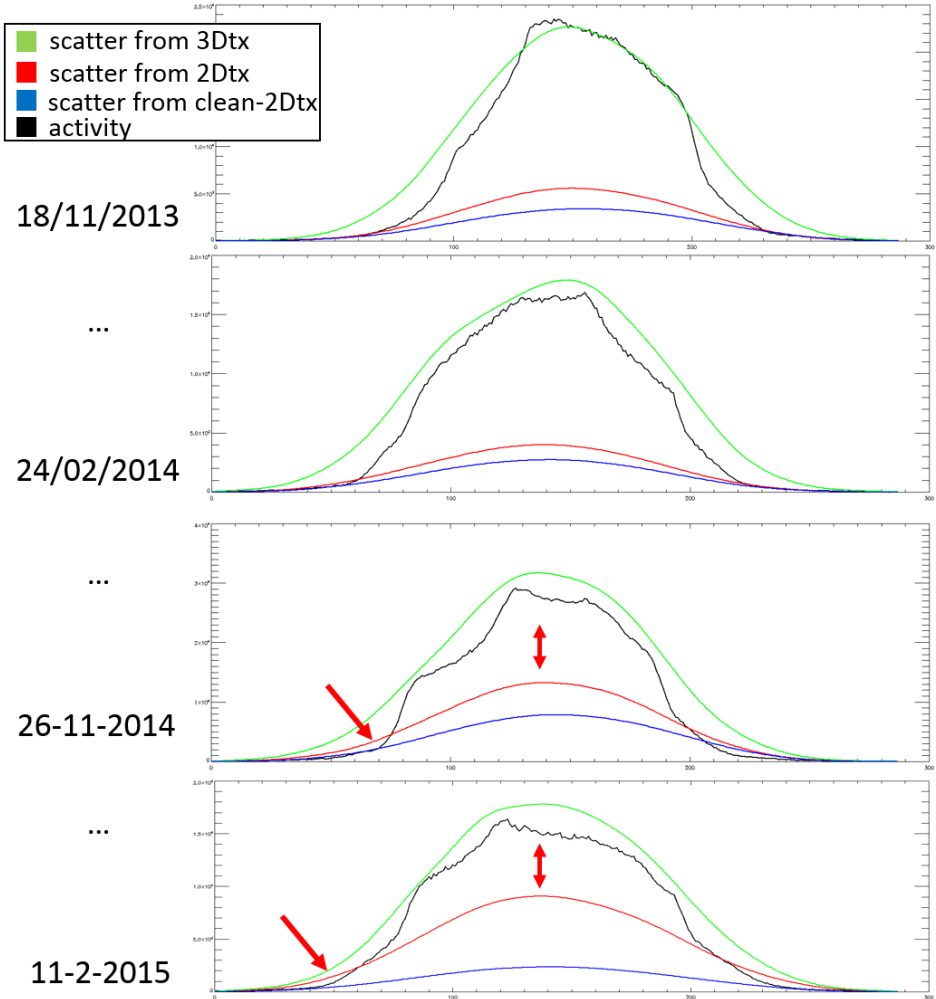


*Figure 2.3: Profiles of the activity sinogram (black), together with the scatter profiles obtained with the vendor's software starting from the 2Dtx (red), the 3Dtx (green) or the clean-2Dtx (blue). The scatter estimate obtained from the 3Dtx is unlikely to be correct. The scatter estimate from the 2Dtx appears more reasonable but, as time goes, the estimated scatter is higher than expected (red arrows). 4 ex vivo datasets, acquired at those 4 different time points, were used to generate this Figure.*

struction of the emission datasets did not change the resulting scatter estimate, if the initial given transmission sinogram was unchanged<sup>1</sup>. Hence, we decided to always feed the vendor's software with a clean-2Dtx, in order to obtain a reasonable scatter and attenuation estimate.

---

<sup>1</sup>This behaviour, where the scatter estimation seems to be based on the blanks and on the initial transmission sinograms, is a peculiar feature of the software used in this work and may not apply to other software packages.

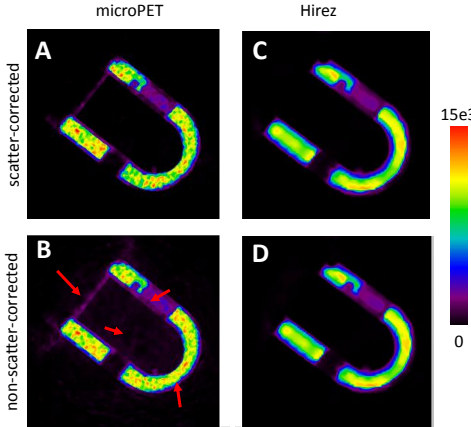


*Figure 2.4: microPET (A, B) and Hirez (C, D) reconstructions obtained with in-house software which performed OSEM3D reconstructions with resolution modelling and the use of a moderate anatomical prior information. The top panes (A, C) are a representative slice from the scatter-corrected reconstructions, the bottom panes (B, D) are from the non-scatter-corrected reconstruction. Both the microPET and the Hirez images are corrected for attenuation using the HDCT coming from the Hirez scanner.*

#### MICROPET RECONSTRUCTIONS OF THE CARDIAC PHANTOM: COMPARISON BETWEEN VENDOR'S SOFTWARE AND IN-HOUSE DEVELOPED SOFTWARE

We compared the mean LV concentrations using our software and the vendor's software. The difference in the mean LV activity concentrations between the two algorithms is negligible (vendor-MAP, clean-2Dtx for AC and scatter: 9279 Bq/cc. MAP recon (Bowsher prior) with our software, clean-2Dtx for AC and scatter: 9282 Bq/cc). The use of the HDCT for attenuation correction (using in-house software and the same scatter correction) produces an increased mean activity value (9516.85 Bq/cc), possibly because of the better tissue delineation and SNR of such attenuation image when compared to the transmission image.

#### SCATTER CORRECTION OF THE MICROPET PHANTOM DATASETS, IN-HOUSE DEVELOPED SOFTWARE

The comparison of in-house reconstructions of the microPET datasets with and without scatter correction (obtained from the clean-2Dtx), using our software, confirm that a decrease (-4.7%) in the mean LV concentration can be observed when scatter correction is performed (9966 Bq/cc vs 9517 Bq/cc, respectively). Figure 2.4 (A and B, red arrows) shows that the scatter additionally leads to artefactual, observable background activity and also affects the distribution of activity within the LV.

## SCATTER CORRECTION OF THE HIREZ PHANTOM DATASETS, IN-HOUSE DEVELOPED SOFTWARE

The comparison of in-house Bowsher reconstructions of the Hirez datasets, with and without scatter correction, shows a very small decrease in the mean LV activity when scatter correction is performed (-0.46%, 9709 Bq/cc vs 9665 Bq/cc, respectively). Figure 2.4 (C and D) confirms that the scatter influence is, in this case, negligible.

## LESION-TO-BACKGROUND CONTRAST AND CNR (CARDIAC PHANTOM)

The contrast values between the lesion, the LV and the background, both in the microPET and in the Hirez, are in Table 2.2. These results confirm that the effect of scatter is more prominent in the microPET reconstructions, whereas the Hirez reconstructions suffer much less from the influence of scatter.

Table 2.2: Contrast and SNR for microPET and Hirez, with and without scatter correction.

	microPET		Hirez	
scatter correction?	Yes	No	Yes	No
% C (les-bkg)	92.5	77.5 (-16.3%)	96.0	95.7 (-0.3%)
% C (LV-bkg)	98.4	93.9 (-4.5%)	98.9	98.8 (-0.1%)
SNR (LV)	10.5	11.0	22.5	22.9

## EX VIVO HEART DATASETS: AGREEMENT BETWEEN THE HIREZ AND THE MICROPET RECONSTRUCTIONS

The graph reporting on the mean activities calculated on the polar maps of the Hirez and on the microPET reconstructions is on Figure 2.5. The mean activities computed on the polar maps of the Hirez reconstructions show an excellent agreement to the mean activities computed on the polar maps of the ground truth ( $R^2 = 0.99$ , slope = 0.97), similarly to what reported for the cardiac phantom (bold values in Table 2.1).

## IV DISCUSSION AND CONCLUSIONS

The purpose of this study was to investigate the effects of scatter correction on *ex vivo* cardiac datasets scanned in a small-animal PET device. We performed a comparison between scatter corrected and uncorrected reconstructions, by evaluating changes in quantitative accuracy, contrast and signal-to-noise ratio.

Applying scatter correction to the microPET datasets is necessary to preserve both contrast and mean activity values, and to obtain images of good visual quality that are in agreement with the expected activity distribution. A decrease in SNR caused by the elimination of the scattered events is expected. In the scope of the current study, whose broader aim was to use the microPET as the gold standard

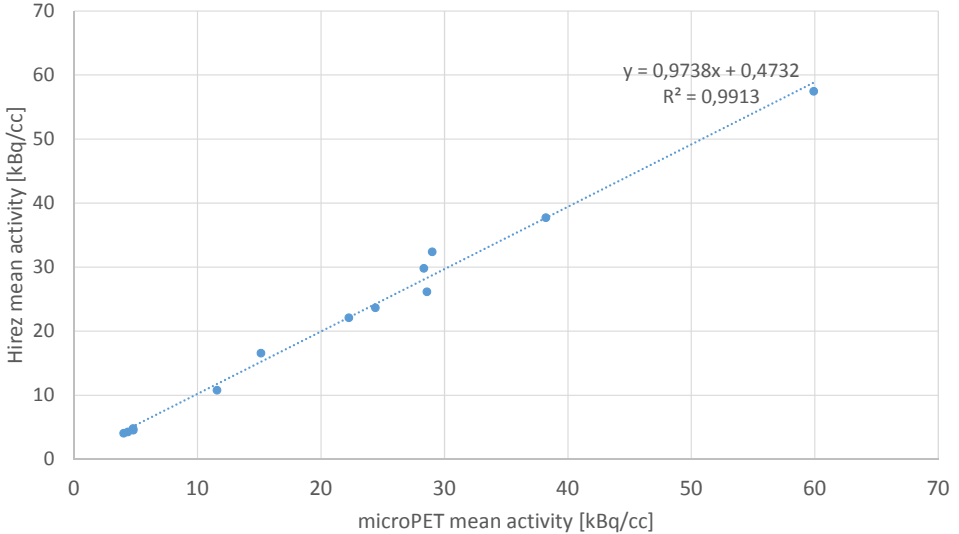


Figure 2.5: Scatter plot showing the correlation of the mean LV tracer uptake, computed on microPET and Hirez reconstructions, in the available sheep cohort (each dot is one animal).

for quantitative accuracy, this minor loss of SNR is acceptable when compared to the improvements in contrast and bias. Our results are in line with a previous study demonstrating that scatter and attenuation correction for larger subjects on a microPET scan are important for accurate quantification [44]. The results shown in this study are somewhat in-between the non-human primate study by Naidoo-Variawa et al. and the studies on rats and mice (where attenuation and scatter correction are often ignored), as the *ex vivo* hearts and phantom are big objects scanned in a small-sized bore, but they are not as compact and as heterogeneous as the baboon's brain.

In contrast to microPET images, applying scatter correction on Hirez datasets has negligible impact. This behaviour can be partly attributed to the diameter of the bore. In a small bore such as the microPET, the backprojection of the scatter events are more likely to intersect the scanned object and therefore contribute to the reconstructed activity distribution, as illustrated in Figure 2.6. In our experimental conditions, the correction of the scatter effects is particularly relevant and was applied to all subsequent measured cardiac datasets.

This study additionally underlines the importance of the choice of the algorithm and of a good quality transmission scan for scatter correction. A possible solution to compensate for a poor quality transmission scan consists of thresholding the attenuation images before forward-projecting them to attenuation sinograms. In addition, this study highlighted that, for the Focus 220, the use of a 3D transmission scan is not recommended, and only single-slice-rebinned attenuation sinograms can be effectively used for correctly estimating the scatter sinograms – provided that the source is still radioactive enough.

Given the excellent correlation between the mean values of the ground truth and the Hirez *ex vivo* datasets, which corroborates the findings obtained on the cardiac phantom, a protocol for the reconstruction of the cardiac datasets for further studies

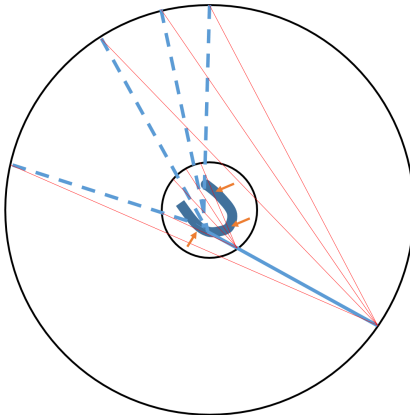


*Figure 2.6: Comparison of the scatter effects in the microPET (smaller circle) and in the Hirez (bigger circle), for the object of interest (heart phantom or ex vivo hearts placed in the center of the FOVs). The diameters of both scanners are a scaled replica of the real scanner dimensions (FOV Hirez = 4.3 x FOV microPET). As the photons depart from the annihilation point (yellow dot) and scatter occurs for one of the two photons, the latter hits the detector ring in various wrong positions, depending on the scattering angle (dashed lines). The red lines represent the LORs that would be reconstructed starting from the detectors (wrongly) hit by the different photons. It is clear that, with a smaller bore size, most of the wrongly reconstructed LORs will cross either a portion of the myocardium (orange arrows) or the background region corresponding to the heart cavity, thus impacting on both the distribution of activity within the heart and the lesion-to-background contrast. The effect is much less prominent in a scanner with a bigger bore, e.g. the Hirez PET/CT, where most of the wrongly reconstructed LORs would lie well away from a small, centred object like our ex vivo hearts.*

can be defined. To summarize, all the *ex vivo* reconstructions will be done using both attenuation and scatter correction, as this combination provided the most comparable and sensible results in particular for the microPET. For the microPET datasets, the scatter estimate will be produced by the vendor's software always fed with a clean-2Dtx. For the Hirez, the scatter estimate will be produced by the e7-tools. The attenuation correction for both Hirez and microPET datasets will be performed starting from the HRCT obtained on the clinical PET/CT. This can be extended to studies carried out with, for example, small-animal integrated PET/CT systems with a good quality CT module. The CT image acquired with such systems could be sufficient for the attenuation correction of the corresponding PET datasets.

## V ACKNOWLEDGEMENTS

Anna Turco is a PhD fellow of the Research Foundation - Flanders (FWO). Olivier Gheysens (1831812N) and Jens-Uwe Voigt are senior clinical investigators of the Research Foundation - Flanders. Kathleen Vunckx is a post-doctoral researcher of the Research Foundation - Flanders.



### **3 ANALYSIS OF PARTIAL VOLUME CORRECTION ON QUANTIFICATION AND REGIONAL HETEROGENEITY IN CARDIAC PET**

*A modified version of this chapter has been accepted for publication in the Journal of Nuclear Cardiology as: Analysis of Partial Volume Correction on Quantification and Regional Heterogeneity in Cardiac PET, A. Turco, J. Nuyts, J. Duchenne, O. Gheysens, J-U. Voigt, P. Claus, K. Vunckx*

#### ***Abstract***

The partial volume correction (PVC) of cardiac PET datasets using anatomical side information during reconstruction is appealing but not straightforward. Other techniques, which do not make use of additional anatomical information, could be equally effective in improving the noise characteristics of the reconstructed cardiac PET datasets and in dealing with the artefacts that occur when modelling the resolution during reconstruction.

The effect of PVC in cardiac  $^{18}\text{F}$ -FDG PET during iterative reconstruction is evaluated by performing resolution modelling in combination with different noise suppressing priors. More specifically, we compare anatomical priors based on a HRCT to edge-preserving priors such as total variation (TV) and the relative difference prior (RD). The validation of our methods is performed using *ex vivo* imaging data from ovine hearts with asymmetric ventricular remodelling.

Simple resolution modelling during data reconstruction resulted in over- and under- estimation of activity which hampers the absolute quantification when compared to the ground truth. Absolute quantification benefited from either using edge-preserving (RD, TV) or anatomy-based PVC techniques, with comparable results. The relative tracer distribution was preserved with any reconstruction technique. Anatomical priors outperformed edge-preserving priors only when the thinnest structures were of interest.

The use of non-anatomical, edge-preserving priors emerged as the

optimal choice for quantification of tracer uptake in the left-ventricular wall of the available datasets.

## I INTRODUCTION

Positron emission tomography (PET) is a sensitive and quantitatively precise pre-clinical and clinical tool for cardiovascular applications. PET allows accurate assessment of absolute myocardial blood flow and function at rest and during stress and is currently considered as gold standard for evaluating myocardial flow reserve [15, 122].  $^{18}\text{F}$ -FDG PET is also the most sensitive method to identify myocardial viability [17, 123]. In addition to these well-validated applications, PET imaging has emerged as a valuable tool for characterization of atherosclerotic plaques and infiltrative cardiomyopathies such as sarcoidosis and amyloidosis [16, 124]. Cardiac PET imaging leads to a panel of clinically relevant parameters that can be interpreted visually (viability, tracer uptake in plaques or sarcoid lesions, regional differences in tracer uptake) but some of these require a quantitative analysis (absolute blood flow, function). Even though visual assessment is currently performed in daily clinical routine for several parameters, quantification improves reproducibility, reduces inter-observer variability and might enhance the diagnostic accuracy [18]. Therefore, accurate quantification is important but cardiac PET images inherently suffer from severe blurring, due to both the finite resolution of the imaging system (partial volume effect, PVE) and cardiac and respiratory motion during the entire PET examination [125].

The use of partial volume correction (PVC) techniques based on high resolution anatomical information to correct for this PVE has been successfully applied for PET brain imaging, which resulted in improved quantitative information [96, 97]. In previous work, we also demonstrated that this technique, in combination with respiratory and ECG-gating, yields improvements in cardiac lesion detection and quantification, provided that a very good alignment between the anatomical and the emission dataset is achieved [126]. Besides evaluation of focal lesion uptake, regional differences in tracer distribution are equally important and traditionally based on visual assessment, (e.g. regional hypoperfusion or metabolism). However in several conditions, it might be difficult to distinguish between true low tracer uptake and apparent reduced activity due to increased PVE in thinner walls (e.g. apical thinning, right ventricular wall, asymmetric wall thickness [127]). In those conditions, PVC techniques could also improve quantification and might enhance the diagnostic accuracy.

The main objective of this study is to evaluate the influence of two types of advanced reconstruction algorithms (anatomy-based and edge-preserving priors) on regional quantification in comparison to the currently used clinical algorithms (with or without resolution modelling). All algorithms were applied on *ex vivo* datasets excised from sheep with asymmetric cardiac remodelling. The use of *ex vivo* (static) datasets allowed to rule out quantification errors caused by cardiac or respiratory motion.

## II METHODS

### ANIMAL MODEL AND EXPERIMENTAL DESIGN

We used an ovine model of rapid pacing-induced dilated cardiomyopathy with LBBB-like morphology leading to asymmetric remodelling of the septal and lateral wall. All experiments and procedures were approved by the local ethical committee.

Each of the thirteen available sheep was instrumented with a pacemaker with epicardial leads implanted in the right ventricular and atrial walls. Rapid pacing (180 beats/min) for 8 weeks was carried out [128]. After 8 weeks of pacing, a <sup>18</sup>F-FDG PET was performed under hyperinsulinemic-euglycemic clamping conditions [28], in order to maximize glucose consumption in the heart. The *in vivo* PET scan was performed 30 minutes post-injection. The mean whole-body activity at the start of such PET scan was 310,5 (range: 109-477) MBq. A computed tomography (CT) for attenuation correction was also acquired on the same scanner (Siemens Biograph 16 HiRez [29]).

After the *in vivo* scan, the animals were sacrificed and the heart was excised and filled with a non-attenuating, hardening poly-urethane foam in order to ensure a stable shape of the heart in time. The following *ex vivo* datasets were acquired:

- a 15-minute acquisition on a small-animal PET scanner (Siemens Focus220 microPET), which served as gold standard because of the high spatial resolution of this PET system (1.5 mm), resulting in almost PVE-free images. A transmission scan with a rotating <sup>57</sup>Co point source was also obtained for scatter correction.
- a 20-minute PET scan on the clinical PET/CT scanner (Siemens Biograph 16, Hirez). These datasets were reconstructed with different algorithms and compared to the ground truth images provided by the microPET.
- a high-dose, HRCT on the clinical PET/CT scanner. It was used for accurate attenuation correction (AC) and for PVC of both the clinical and the microPET datasets.

### SIMULATION STUDY

A simulation study was designed to clarify whether there is a relationship between the apparent thickness of the reconstructed structures and the different reconstruction algorithms.

For this purpose, a cylindrical phantom resembling the shape of the left ventricle was designed as shown in Figure 3.1. The initial voxel size of the phantom was 1 mm in the three directions. The total height of the phantom was 65 mm and the outer radius of the cylinder was set to 30 mm. The inner radius of the cylinder varied with the wall thickness, which was set to range between 1 and 12 mm (representative of the thicknesses that can be encountered in a cardiac setting).

The phantom was filled with a known and fixed activity concentration of 4 kBq/cc. A second identical phantom was then created to simulate a uniform attenuation map and filled with a known and fixed attenuation value of 0.0999428

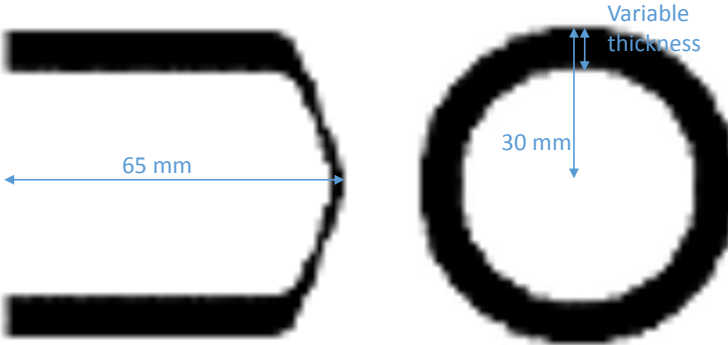


*Figure 3.1: Transaxial (left) and axial (right) view of one of the phantoms simulated to demonstrate the effect of the reconstruction algorithms against different phantom thicknesses.*

(attenuation  $\times \text{cm}^{-1}$ ), which corresponds to the mean attenuation value found for muscle at 511 keV [129]. Finally, a third copy of the phantom was used to simulate the anatomical prior information, perfectly aligned to the emission dataset.

The generated emission phantoms were forward-projected using in-house developed software that simulates an acquisition with the Hirez scanner. Each phantom was corrected for attenuation and sensitivity during projection and reconstruction. Scatter and randoms were not modelled to exclude the influence of their contribution from the analysis. A noise-free sinogram was obtained for each phantom. In addition, a noisy sinogram was generated for each phantom by adding Poisson noise to the noise-free sinogram, corresponding to a 20 minute-acquisition.

A second, similar simulation was performed starting from a phantom filled with a higher, homogeneous activity concentration ( $25 \text{ kBq/cc}$ ).

## IMAGE RECONSTRUCTION

### HIREZ PET/CT DATASETS

Both simulated and real measured datasets were reconstructed using the same reconstruction scheme. A maximum-likelihood (ML) or penalized ML (or maximum-a-posteriori, MAP) reconstruction algorithm, accelerated with ordered subsets (ordered subsets-expectation maximisation, OSEM) algorithm with a  $[3,2,2] \times [42,24,1]$  iteration scheme (iterations x subsets) was chosen, which represented a compromise between good convergence and reasonable computation times. All measured datasets were precorrected for randoms, whereas sensitivity and attenuation (using the HRCT) were modelled during reconstruction. Projection and backprojection were done using a distance-driven projector modelling the 3D PET scanner geometry. When requested, the system resolution was modelled as a shift-invariant Gaussian convolution in the sinogram space (full-width at half-maximum – FWHM = 4.3 mm and 4.5 mm in the transaxial and axial direction, respectively). The voxel size of the reconstructed PET images was set to  $1.35 \times 1.35 \times 1.35 \text{ mm}^3$  for all datasets.

An overview of the different algorithms used to reconstruct each of the available sinograms is listed below:

1. OSEM without resolution recovery (RR)
2. OSEM with RR (*OSEM + RR* in the rest of this work), modelling the resolution of the scanner during reconstruction. Such technique is commonly used to compensate for the blurring of the activity in reconstructed emission images. However, Gibbs artefacts in the final images are expected, which might hamper the correct quantification of activity [130].
3. MAP with RR, with CT-based side anatomical information (*Bowsher*), as it represents one possible way to mitigate the Gibbs artefacts introduced by the modelling of the resolution during reconstruction. The anatomical information was incorporated in the reconstruction process by means of the Bowsher prior [131], in its modified asymmetrical version [132]. Bowsher reconstructions with different prior weights (4, 10, 80) and different number of selected neighbours (4, 6, 9, 13) out of an 18-voxels spherical neighbourhood were performed.
4. MAP with RR in combination with the relative differences (RD) prior [133] in its smoothing-only mode (*RD*, gamma = 0). Different weights of the prior have been tested (0.1, 4).
5. MAP with RR in combination with the RD prior in its edge-preserving mode (*RD*, gamma ≠ 0). Different weights of the prior have been tested (0.1, 4), as well as different gamma values (10, 30).
6. MAP with RR, with a different edge-preserving prior (isotropic total variation prior, *TV* [57]). Different weights of the prior have been tested (0.005, 0.01).

The selection of these prior parameters was based on a previous simulation study, where reconstructions with a similar count level were compared to a ground truth dataset in terms of bias and noise. A visual inspection of the datasets confirmed that the choice was an appropriate compromise between noise reduction and excessive smoothing of the structures.

## MICROPET DATASETS

The microPET list-mode datasets of the *ex vivo* hearts were rebinned into sinograms and reconstructed using a MAP reconstruction algorithm (5 iterations x 28 subsets) modelling the resolution of the scanner and using the aligned HRCT as anatomical information (Bowsher prior in its modified asymmetrical version). A spatially invariant Gaussian kernel with a FWHM of 1.3 mm and 1.5 mm (transaxial and axial values, respectively), applied in the sinogram space, was used to model the resolution of the microPET scanner. For a more accurate correction for attenuation, the aligned HRCT from the Hirez scanner was also used as AC map for the microPET, after conversion to 511 keV attenuation values. A weight (w) of 50 and 9 neighbours (n) out of an 18-voxels spherical neighbourhood were used for the

Bowsher reconstruction of the microPET dataset, as they resulted in the best performances (minimization of the bias and the noise) when compared to a simulated ground truth (not shown).

Scatter and sensitivity correction were performed during reconstruction. Randoms and deadtime were precorrected. The microPET images were reconstructed with a voxel size of  $0.4745^2 \times 0.796$  mm<sup>3</sup>. For comparison to the Hirez datasets, they were rigidly aligned to the Hirez reconstructions and simultaneously resampled to match the voxel size of the latter ( $1.35 \times 1.35 \times 1.35$  mm<sup>3</sup>).

## IMAGE POST-PROCESSING

A polar map (or bull's eye) representation [121] of the simulated and *ex vivo* reconstructions was chosen to illustrate the regional and absolute differences within the myocardium. To create the bull's eye plots, the algorithm must compute a single value for the activity on line segments perpendicular to the wall and enclosed by the endocardial and the epicardial contours. This value is chosen by either computing the maximum or the mean along those segments. Both types of polar maps were created in this work, by taking the maximum or the mean count over the LV thickness (*max-count* and *mean-count* polar maps in the rest of this work, respectively) [126].

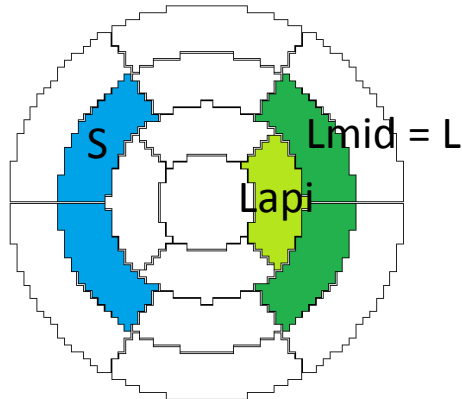


Figure 3.2: Regions of the 17-segment polar map that were considered for the calculation of the S/L ratios and for the Lapi/Lmid ratios.

## PET QUANTIFICATION AND STATISTICAL METHODS

### MEASURED EX VIVO DATASETS

The **absolute** values of the *ex vivo* reconstructions were compared. The mean difference between the microPET polar map and the *ex vivo* Hirez polar maps, relative to the mean activity of the microPET polar map, was computed and plotted, for each animal. A repeated ANOVA between the different reconstructions methods was performed, to establish whether a statistical difference in the means could be

found. The values extracted from the mean-count polar maps were compared to the values extracted from the max-count polar maps.

For every polar map, the S/L ratio was additionally calculated by dividing the mean activity in the free septal wall by the mean activity in the free lateral wall (see Figure 3.2 to visualize the corresponding segments). This analysis aimed to quantify whether the prior-based reconstructions improve or preserve the **regional variations** of activity within the heart, when compared to the S/L ratio computed on the polar map of the corresponding ground truth reconstructions. A repeated ANOVA test between the different reconstructions methods was performed, to establish whether a significant difference between the mean S/L ratios from the various reconstructions could be found.

Additionally, the ratio between the activity in the apical segment of each polar map and the activity of the mid-wall segments of each polar map for the lateral wall ( $L_{ap}/L_{mid}$ , see Figure 3.2) was computed, as a first indication of the sensitivity of the PVC techniques to the thickness of the structures examined. In fact, assuming a uniform activity concentration throughout the same wall of the heart, a good PVC technique should restore equally well the thin (apical) and the thick (middle) segments of that same wall. Therefore, the smaller the  $L_{ap}/L_{mid}$  ratio, the poorer is the recovery of the activity in the apical segment ( $L_{ap}$ ) due to PVE. The ideal  $L_{ap}/L_{mid}$  ratio should be close to 1, assuming a homogeneous activity distribution within the same wall.

## SIMULATED DATASETS

The mean activity in the middle ring of each max-count polar map of the simulated phantoms was plotted for the different phantom thicknesses in comparison to the mean activity expected in that particular region ( $4 \text{ kBq/cc}$  or  $25 \text{ kBq/cc}$ ).

Additionally, profiles were obtained through the middle section of the noisy heart phantom by averaging 20 central subsequent axial slices to minimise random effects. These mean profiles were plotted for all different reconstruction algorithms.

## III RESULTS

### MEASURED EX VIVO DATASETS

A representative dataset with a selection of the performed reconstructions is shown in Figure 3.3. The OSEM reconstructions without any RR yield an underestimation of the activity and a blurring over the myocardial edges, whereas the OSEM reconstructions with RR show the opposite behaviour, with the typical artefactual peaks in the middle of the reconstructed tissues and an apparent thinning of all the structures. The use of an edge-preserving prior seems to work reasonably well, especially in the left ventricular walls. The Bowsher reconstructions – when the parameters were chosen carefully – are visually appealing and show moderately sharper edges when compared to the edge-preserving priors. In all cases, the visual assessment of the different reconstructions did not reveal dramatic changes in the relative activity distribution.

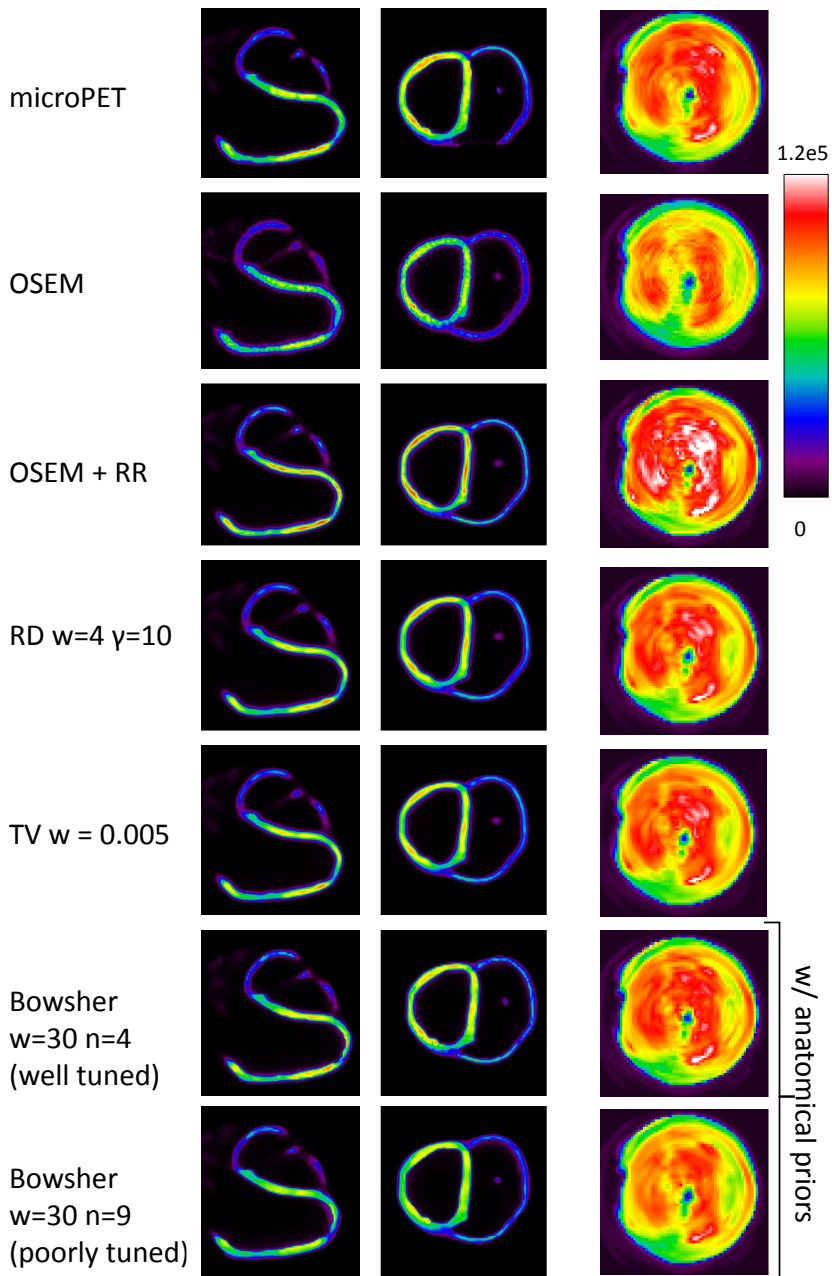


Figure 3.3: Representative images of an ex vivo sheep heart (s4238) reconstructed with different algorithms. On the right, the corresponding (max-count) polar maps for the same sheep are shown.

The polar maps obtained for all the *ex vivo* datasets were also compared visually (right column of Figure 3.3) and revealed a similar underestimation of the recovered activity with OSEM while OSEM+RR overestimated the activity. The RD and the TV prior produced satisfactory results, visually similar to what was obtained with a well-tuned Bowsher prior.

The accurate **absolute recovery** of the activity concentrations within the LV was then considered. Figure 3.4 shows the findings. The reconstruction without resolution recovery (OSEM) underestimates the activity due to the PVE, which causes an underestimation of the mean value in both the max-count and the mean-count polar maps. Due to Gibbs artefacts, the OSEM reconstructions with RR suffer from over- and undershoots, which in turn cause a significant overestimation in the corresponding max-count polar maps. These findings hold true when the mean-count polar maps are used (bottom pane of Figure 3.4), but the differences between the different algorithms are more subtle. However, we can clearly appreciate the role of the regularization included during the reconstruction process. No matter which type of bull's eye plot is constructed, the reconstructions with edge-preserving and anatomical priors always manage to restore the most correct activity concentration values when compared to the ground truth (cfr the error computed from the TV, RD and Bowsher reconstructions in the top and bottom panes of Figure 3.4), thus ensuring stability of the results against the choice of the polar map used.

The **S/L ratios** were further calculated for the polar maps of each of the clinical reconstructions. They were compared to the ground truth S/L ratio extracted from the corresponding microPET reconstruction. The results are in Figure 3.5. Within each animal, the S/L ratios do not significantly change with different reconstruction algorithm, further supporting our visual evaluation of the polar maps. The ANOVA test showed no significant differences in the mean S/L ratios recovered from the different reconstruction algorithms ( $F = 0.13$ ,  $p = 0.99$ ).

We verified whether the results obtained were dependent on the thickness of the structures. The Lapi/Lmid ratios for all *ex vivo* sheep datasets are plotted in Figure 3.6. The Bowsher prior seems to outperform all other reconstruction algorithms in recovering the activity of the thinnest parts of the LV (e.g. apex, whose thickness is below 2 mm).

## SIMULATED DATASETS

The analysis of the mean reconstructed activity at different phantom thicknesses is shown in Figure 3.7. As hypothesized, the thinnest phantoms benefit more from the additional use of anatomical information (black line), while the non-anatomical priors (or the anatomical priors where the number of neighbours over which the smoothing is performed is too large) blur over the edges and therefore struggle to fully restore the activity within the walls of the thinnest phantoms. The OSEM with RR alone displays the typical overestimation of activity at a thickness of 6-8 mm (roughly double the spatial resolution of the system), which becomes less apparent with increasing wall thickness of the cardiac phantom ( $\geq 10$  mm).

The analysis of the mean recovered value in the max-count bull's eye plots of the heart phantom at different thicknesses (Figure 3.8) confirms the findings of the profile analysis and of the analysis of the *ex vivo* measured datasets. The OSEM

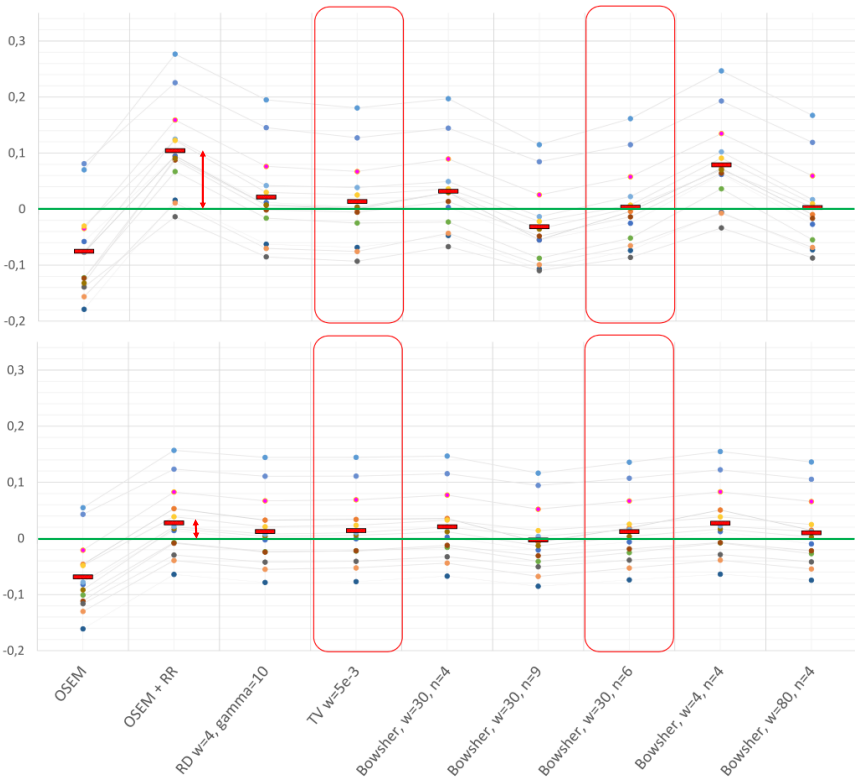


*Figure 3.4: Mean difference between the polar maps of the ground truth (microPET) and the polar maps of the Hirez images, reconstructed with the various algorithms, relative to the mean activity of the polar map of the corresponding microPET. The use of a different way to obtain the polar maps changes the amount of error that is computed, especially for OSEM+RR (red arrows). The use of edge-preserving or anatomical priors leads to a more accurate absolute quantification of the activity in the LV, regardless of the type of polar map that is used. The red boxes highlight this behaviour for two representative cases (other parameter choices for the Bowsher prior – e.g.  $w=80$  and  $n=4$  – would be equally effective).*

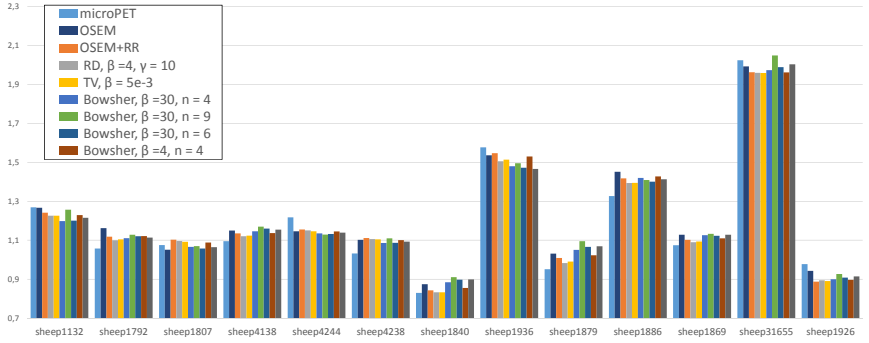


Figure 3.5: *S/L ratios for all the ex vivo sheep datasets, extracted from the max-count polar maps of the reconstructions using the different algorithms. No matter which reconstruction algorithm is used, all the polar maps are able to accurately represent the regional differences within the LV.*

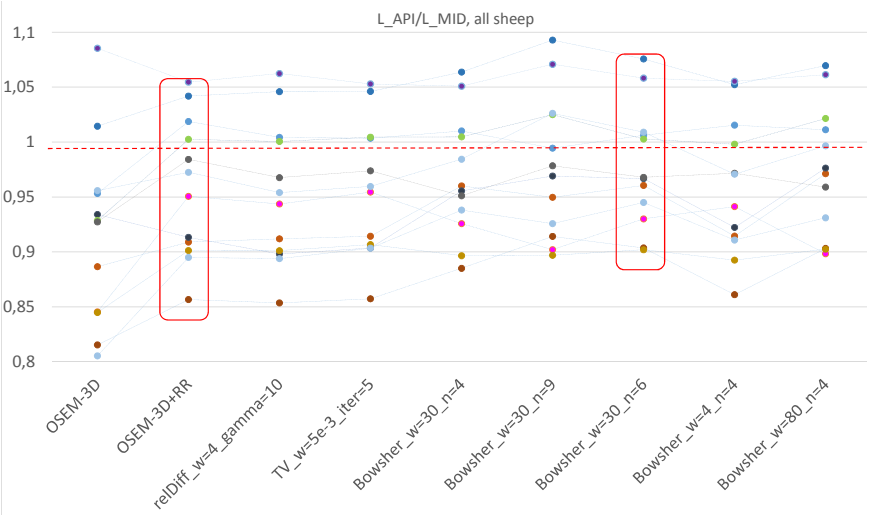


Figure 3.6: *Apical vs middle segment activity ratios, for all the ex vivo sheep datasets ( $n = 13$ ), extracted from the polar maps of the reconstructions using the different algorithms. Assuming the uniformity of activity concentration within the lateral wall of each heart, the Lapi/Lmid ratio should tend to 1. The best reconstruction algorithm for the Hirez is the one that most closely reaches this value. In our case, the Bowsher prior is the one that overall achieves the best performances, thus suggesting that the anatomical information might still be of use when very thin or small structures are of interest. The red boxes encircle the Lapi/Lmid ratios obtained from two representative reconstruction algorithms (OSEM+RR vs a well-tuned Bowsher), so that the shift in the mean Lapi/Lmid can be more clearly appreciated.*

+ RR overestimates the activity above 4 mm, with a peak at 6-7 mm, while the Bowsher reconstruction with proper selection of parameters manages to recover best the activity even within the thinnest structures. The 1-mm thick phantom is expected to be less active, due to the reconstruction voxel size (1.35 mm in the three directions) which is bigger than the actual phantom thickness (1 mm).

The visual inspection of the thinnest structures of the sheep datasets (e.g. right ventricle) confirms the improved reconstruction of such areas when an adequately

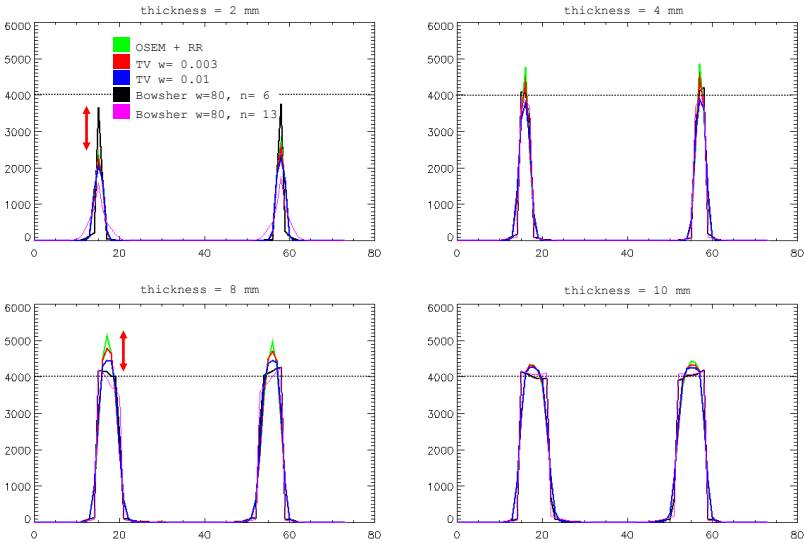


Figure 3.7: Profiles over a section of the heart phantom (simulated, homogeneous activity of 4000 Bq/cc), for a selection of phantom thicknesses.

chosen anatomical prior is used. Figure 3.9 shows a comparison between the short-axis slices of two Bowsher and two TV reconstructions. The thinnest details are better resolved and the sharpness of the edges is improved when anatomical information is used. Even though the main activity patterns of activity are detectable in all the reconstructions, the use of anatomical priors is beneficial if very specific regions are of interest, particularly if their size is below the resolution of the scanner used to acquire the datasets.

## IV DISCUSSION

The use of anatomical side information for the improved quantification of cardiac PET datasets stemmed from previous, successful experiences in brain PET imaging, where similar techniques have been applied during the reconstruction of PET datasets [97]. The results obtained in the current study are in line with previous findings and add interesting insights into the discriminating factors for choosing an anatomy-based prior.

The modelling of the resolution during reconstruction is essential for dealing with the PVE. However, our findings confirm that the resolution recovery is an ill-posed problem [130] and, alone, is not sufficient for accurate image quantification. Some kind of regularization is needed to produce more quantitatively accurate results, in addition to the modelling of the resolution during reconstruction. In this study, the use of priors proves to improve the absolute quantification of the left ventricles, when compared to both OSEM and OSEM + RR alone. For the OSEM + RR a post-smoothing could be applied to mitigate the over-estimation, but this practice would reduce the benefits introduced by the modelling of the resolution during reconstruction. Moreover, the amount of smoothing needed is often arbitrarily chosen,

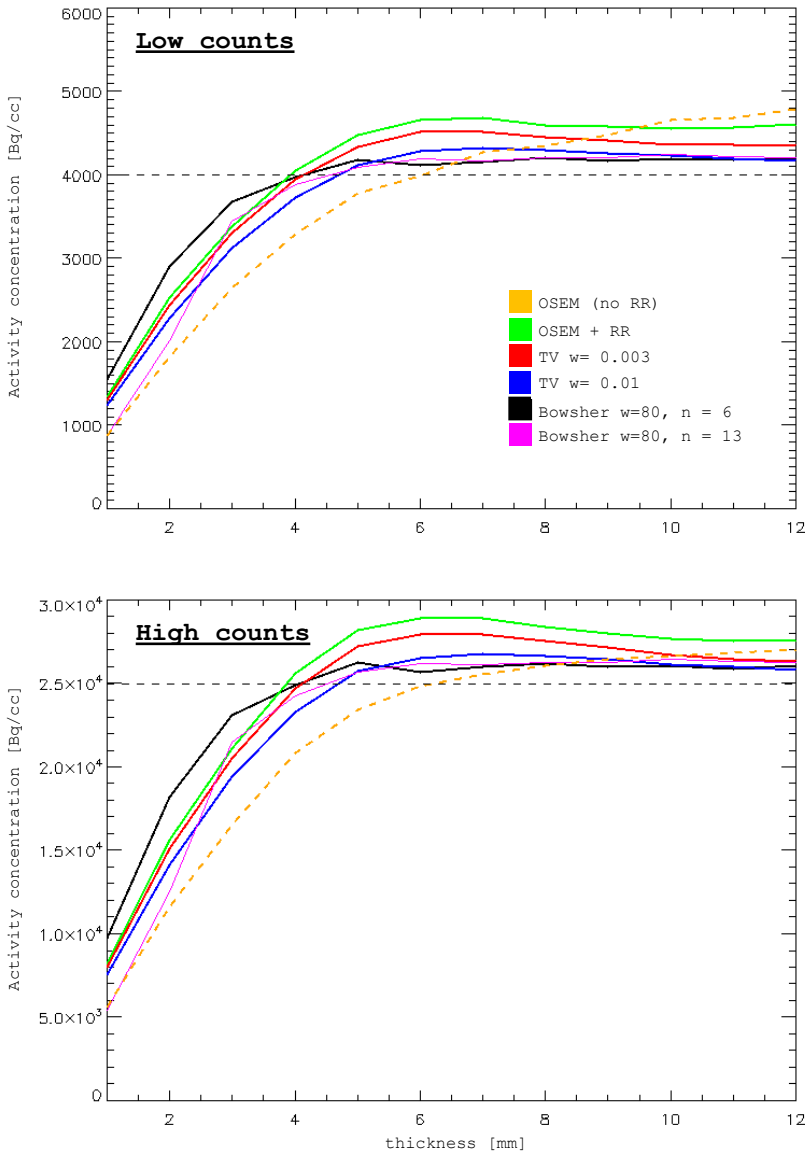


*Figure 3.8: Mean value in the max-count polar maps of the heart phantoms, at increasing phantom thicknesses. The Bowsher algorithm, with a well chosen neighborhood, is the only one that improves the recovery of the mean activity concentration, starting from a thickness of 2 mm. The higher value observed with the OSEM reconstructions is attributed to the noisiness of the images from which the polar maps are extracted. In turn, the higher noise level is due to the long iteration scheme used, which was chosen to ensure convergence of the regularized reconstructions and was kept unvaried for all algorithms for consistency.*

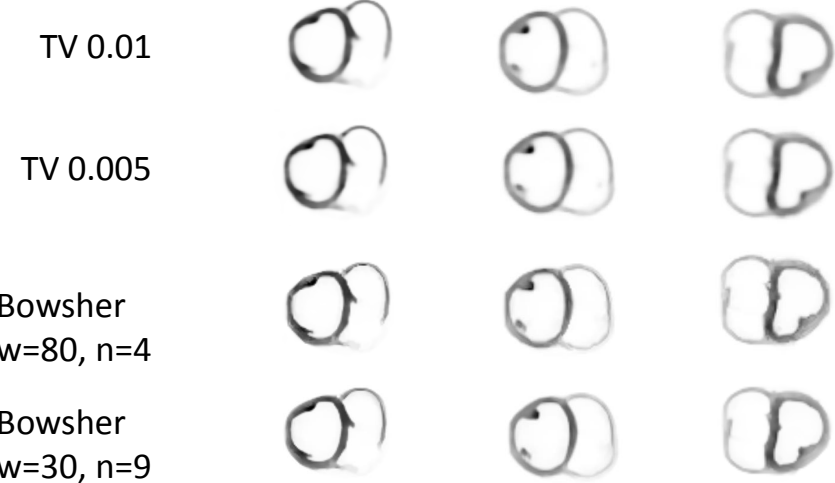


*Figure 3.9: Comparison between TV and Bowsher reconstructions, for three different sheep datasets (from left to right column: s4238, s1869 and s1132). The different rows display the different reconstructions with priors, with two different parameter sets per reconstruction. For all algorithms, the same short-axis slice and the same maximum is shown (they differ for the different animals, to maximize visibility). The Bowsher prior with high weight and a small number of neighbours is visually sharper and more homogeneous than the corresponding non-anatomical prior version.*

therefore it could even result in an under-estimation of the activity concentrations. This paper highlights the role of both anatomical (Bowsher) and non-anatomical edge-preserving priors (RD, TV) applied during the reconstruction of the datasets in stabilizing the resulting images. Even when the weights or the number of neighbours chosen are not fully optimized for the structures of interest (e.g. too many neighbours, or too bland prior weight), the error calculated in the regularised cases is milder than the one obtained in the un-regularised reconstructions.

For regional analysis and relative quantification of the activity distribution within the left ventricle, on the other hand, the use of either reconstruction algorithm (with or without prior information) was sufficient and provided similar information. The S/L ratios are equally well resolved when compared to the ground truth ratio, no matter the reconstruction algorithm that is chosen for reconstructing the datasets obtained on the clinical scanner.

While the use of anatomical information does not seem to be fundamental to obtain quantitatively accurate reconstructions of the cardiac structures (a non-anatomical prior would suffice), the results obtained in this work are not in disagreement with previous studies on the use of anatomical information during reconstruction. A more detailed analysis on simulated phantoms with different thicknesses, in fact, demonstrated that thin structures benefit more than thick structures from anatomical information. This could be the reason why the use of anatomical information is particularly useful, for example, in the reconstruction of brain datasets – where the thickness of the gray matter ranges between 1 and 4.5 mm, with an average of 2.5 mm [134]. Additionally, the brain is a packed organ and the cortex is a corrugated and highly folded tissue where areas that are very thin and very different in activity uptake are in close proximity. This could explain the added value of the

anatomical information, of constraining the smoothing to the respective regions. In the case of the heart, on the other hand, the active structures are not packed nor adjacent to each other. This, added to the thickness of the LV ranging between 8 and 11 mm both in healthy and remodelled left ventricles [135, 136], could explain why the use of anatomical information was not essential to reconstruct the available datasets. However, for the recovery of the thinnest regions of the heart (e.g. the right ventricle, whose thickness is between 3–5 mm [137], or in the case where non-transmural infarctions are present), we provide first evidence that an improvement in the recovery of the activity values when anatomical information is used could be expected. The results shown in this paper are therefore encouraging for applications where the quantification of the RV activity is of interest (e.g. evaluation of pulmonary arterial hypertension associated with congenital heart disease [138]) or, as already previously demonstrated, when non-transmural myocardial lesions are of interest [139].

It is worthwhile to mention that the Bowsher priors presented in the study on the wall thickness for demonstrative purposes use a considerably high weight to achieve such results. In a more realistic scenario where these techniques would be applied, i.e. a dual gated acquisition with the use of anatomical information obtained from a dedicated scanner, the use of a high weight would be risky and could cause artefacts if there is no proper alignment between the PET and the anatomical dataset. Therefore, it is necessary to underline the importance of a correct image alignment and motion correction, before proceeding to anatomy-based PET reconstruction. Additionally, the prior parameters need to be tuned in a case-by-case fashion to obtain optimal results, which can be a limiting factor for a realistic clinical workflow. A way to automatically select the best prior parameters was out of the scope of this work and should be subject of further investigation.

A limitation of this study is the use of *ex vivo*, static cardiac datasets for the assessment of the usefulness of partial volume correction techniques. In patients, the motion of the heart due to the beating and the breathing during the scan can create additional blurring of the PET datasets and needs to be taken into account and fully corrected if accurate quantification is aimed at. We expect a worsening of the quantification performances of any of the presented algorithms in the case where the correction of the motion is inaccurate or missing.

## V CONCLUSIONS

Our study demonstrates that simple resolution modelling during the reconstruction of clinical *ex vivo* datasets results in overestimation of the recovered activity within the left ventricular wall, whereas the omission of the resolution modelling results in an underestimation of the tracer uptake. Both choices hamper the accurate absolute quantification when compared to the ground truth. We show that absolute quantification can be improved by using either edge-preserving (RD, TV) or anatomy-based PVC techniques in combination with the modelling of the resolution, upon proper selection of the different prior parameters. However, in this study the use of anatomical information was not necessary for this purpose, and an edge-preserving prior – which is easier to apply – yielded comparable results for absolute

quantification of the left ventricular activity. In contrast to absolute quantification, the relative activity distribution did not require any specific reconstruction algorithm, even though we would expect a greater benefit of the anatomical prior information if the heart thicknesses would decrease below the 4 mm.

This result is not contradicting previous studies on PVC, as the thickness and the shape of the heart differ greatly from e.g. the thin and convoluted structures present in the brain. The analysis of the simulated data demonstrates that the Bowsher prior could have potential use in the recovery, delineation and analysis of the PET datasets, particularly for the quantification of very thin or small structures (e.g. the right ventricle).

## NEW KNOWLEDGE GAINED

This work addresses the previously unanswered question regarding the usefulness of anatomical and non-anatomical priors for the quantification of cardiac PET images. It provides guidelines for the reconstruction of cardiac emission datasets, partially confirming the results of previous literature on brain PVC, partially adding new insights into the usefulness of the prior information in the reconstruction of different cardiac structures. The study design using *ex vivo* cardiac datasets acquired on both a pre-clinical and a clinical scanner is innovative and original.

## COMPETING INTERESTS

The authors declare that they have no competing interests.

## AUTHOR'S CONTRIBUTIONS

AT was responsible for the study design, the simulation setup, the reconstructions and the data collection and analysis, and drafted the manuscript. JN and KV assisted with the study design, the analysis of data and the careful revision of the manuscript. JUV, PC, JD and OG participated in the study design and critically revised the manuscript. All authors read and approved the final manuscript.

## ACKNOWLEDGEMENTS

AT is a PhD fellow of the Research Foundation - Flanders (FWO). OG (1831812N) and JUV are senior clinical investigators of the Research Foundation - Flanders. KV is a post-doctoral researcher of the Research Foundation - Flanders.

The authors wish to thank Charles Watson, Judd Jones et al. for their help with the Siemens data processing, and Filip Rega for the development of the animal model used in this work.

# **4 LESION QUANTIFICATION AND DETECTION IN MYOCARDIAL $^{18}\text{F}$ -FDG PET USING EDGE-PRESERVING PRIORS AND ANATOMICAL INFORMATION FROM CT AND MRI: A SIMULATION STUDY**

*This chapter has been published in: Lesion Quantification and Detection in Myocardial  $^{18}\text{F}$ -FDG PET using Edge-Preserving Priors and Anatomical Information from CT and MRI: A Simulation Study, A. Turco, J. Nuyts, O. Gheysens, J. Duchenne, J-U. Voigt, P. Claus, K. Vunckx, EJNMMI Phys. 2016 Dec;3(1):9.*

## ***Abstract***

The limited spatial resolution of the clinical PET scanners results in image blurring and does not allow for accurate quantification of very thin or small structures (known as *partial volume effect*). In cardiac imaging, clinically relevant questions, e.g. to accurately define the extent or the residual metabolic activity of scarred myocardial tissue, could benefit from partial volume correction (PVC) techniques.

The use of high-resolution anatomical information for improved reconstruction of the PET datasets has been successfully applied in other anatomical regions. However, several concerns linked to the use of any kind of anatomical information for PVC on *cardiac* datasets arise. The moving nature of the heart, coupled with the possibly non-simultaneous acquisition of the anatomical and the activity datasets, is likely to introduce discrepancies between the PET and the anatomical image, that in turn might mislead lesion quantification and detection. Non-anatomical (edge-preserving) priors could represent a viable alternative for PVC in this case.

In this work, we investigate and compare the regularizing effect of different anatomical and non-anatomical priors applied during maximum-a-posteriori (MAP) reconstruction of cardiac PET datasets. The focus

of this paper is on accurate quantification and lesion detection in myocardial  $^{18}\text{F}$ -FDG PET.

Simulated datasets, obtained with the XCAT software, are reconstructed with different algorithms and quantitatively analysed.

The results of this simulation study show a superiority of the anatomical prior when an ideal, perfectly matching anatomy is used. The anatomical information must clearly differentiate between normal and scarred myocardial tissue for the PVC to be successful. In case of mismatched or missing anatomical information, the quality of the anatomy-based MAP reconstructions decreases, affecting both overall image quality and lesion quantification. The edge-preserving priors produce reconstructions with good noise properties and recovery of activity, with the advantage of not relying on an external, additional scan for anatomy.

The performance of edge-preserving priors is acceptable but inferior to those of a well-applied anatomical prior that differentiates between lesion and normal tissue, in the detection and quantification of a lesion in the reconstructed images. When considering bull's eye plots, all of the tested MAP algorithms produced comparable results.

## I BACKGROUND

Positron emission tomography (PET) images suffer from partial volume effects (PVE) due to the limited spatial resolution of the PET system (2 - 6 mm FWHM [29,47]). This effect is not only observed in the heart, all anatomies can be affected. However, there are very thin or small structures in the heart (e.g. apex, right ventricle) that can be particularly affected by PVE. Moreover, some pathologies might cause a thinning or scarring of the myocardial walls. In all these cases, the blurring caused by PVE might hamper correct interpretation of the resulting image. In order to deal with the PVE in PET, many PV correction (PVC) techniques have been proposed [116].

In cardiac imaging, additional blurring is caused by the breathing motion and the beating of the heart. Dual gating of the cardiac datasets is one possible approach to remove the motion blur [140]. This approach removes the motion blur that affects the PET acquisitions by dividing the initial PET list-mode into a set of *gates*, each of which ideally represents the heart in a fixed cardiac and respiratory phase. Despite effective in removing the motion blur in most cases, the process of gating dramatically reduces the statistics of the final datasets and leads to extremely noisy reconstructions (still to be corrected for PVEs). Alternatively, the use of motion fields extracted e.g. from the PET dataset itself [80,141] or from a simultaneous dynamic magnetic resonance imaging (MRI) scan [142] would correct for the motion and improve the noise characteristics of the final PET dataset, but the PVE would still need to be corrected for.

Among the methods that have been proposed in the past to tackle the PVEs, an effective way is represented by the incorporation of the resolution effects into the system matrix during the iterative image reconstruction process (resolution recovery, RR). This process can effectively deal with PVEs but, due to the ill-posed nature of the problem, reconstruction with resolution recovery can lead to

over- and under-shoots of the reconstructed activity, known as Gibbs artefacts, that might hamper accurate image quantification [51]. Consequently, some sort of regularization is needed to avoid such artefacts. The use of high-resolution anatomical information (e.g. computed tomography (HRCT) or MRI) for improved reconstruction of the activity datasets is appealing and has shown promising results in brain imaging [143]. Clinically relevant questions in the field of cardiac  $^{18}\text{F}$ -FDG PET, e.g. to accurately define the amount of tissue still metabolically active in or around a lesioned site, could benefit from anatomy-based PVC. The acquisition of the anatomical image for PVC is, however, not free from drawbacks. Firstly, the entire examination would be more expensive, longer and more cumbersome than a single PET study. In fact, most PET scanners are hybrid devices that include a CT module, with which a CT for attenuation correction can be acquired. However, the spatial and temporal resolution of most CT modules in the current PET/CT scanners is often insufficient for obtaining a frozen image of the heart in one cardiac and respiratory phase, and with a quality that is adequate for PVC. Therefore, the patient would need to be transferred from the PET scanner to a dedicated scanner for the acquisition of the image to be used as anatomical information. The use of truly simultaneous PET/MR devices would overcome this issue. This technology however, is currently being integrated in the clinical practice and so far very few centres can benefit from its advantages.

Moreover, discrepancies between the selected PET gate and the anatomical gate being used are likely to occur, especially if the two acquisitions come from scanners of two different vendors. In addition, small, residual motion artefacts might still be present after the gating of both datasets, due to changes in the heartbeat or breathing patterns from one scan to the other. Furthermore, the high level of noise present in the PET images, coupled with possible residual motion artefacts and attenuation artefacts [144], might complicate the perfect alignment of the two datasets and therefore increase the chances to introduce additional, anatomy-driven artefacts in the PVC-PET reconstructions. The reconstruction of the PET datasets with the use of anatomical prior information is also not straightforward and more time consuming, as it needs a case-by-case verification of the alignment between the anatomy and the activity images and, if necessary, extra steps (e.g. non-rigid registration or manual initialization of the alignment of the datasets) in order to obtain an acceptable alignment before the actual reconstruction can take place.

On the other hand, edge-preserving and de-noising techniques, which promise noise reduction and edge preservation without the use of any anatomical side information, have also been presented in the past to deal with the Gibbs artefacts caused by the RR [117, 145]. These techniques produce visually appealing images, with better contrast-to-noise ratios when compared to the current standard for PET reconstruction. In addition, they have the advantage of not relying on an external, additional scan for anatomy. Therefore, they are not subject to the previously mentioned complications and they could more easily be introduced in the clinical practice and in the clinical software.

The aim of this article is threefold. Firstly, we aim at assessing the performances of edge-preserving priors for the purpose of lesion detection in cardiac  $^{18}\text{F}$ -FDG PET, in comparison to anatomy-based priors. Secondly, we aim at highlighting the possible risks of anatomy-based PVC, which occur when the anatomical image is mismatched or shifted relative to the corresponding PET dataset, and their effect

on lesion detection and quantification. Finally, we aim at identifying differences in performance when using two different modalities as source of anatomical information. In particular, we compare the use of an MR image where the lesion is visible, to the use of a high-resolution CT image where the lesion is not visible.

This study explores the effect of partial volume correction (PVC) on lesion visibility and quantification, in the ideal case-scenario where all motion has been already removed from the datasets. In fact, only in this way the blurring caused by the PV effect can be clearly distinguished from the one caused by the motion. In doing so, we can therefore clearly identify how well the sole blurring due to PVE is eliminated thanks to edge-preserving and anatomical priors. XCAT-based simulations have been performed to achieve the aforementioned objectives.

## II METHODS

### PHANTOM GENERATION

The XCAT software [91] was used to create the ground truth activity distribution, the attenuation distribution and the high-resolution anatomical images to be used for this study. We generated an XCAT phantom corresponding to a single cardiac and respiratory gate for the PET, the attenuation and the high-resolution anatomical images.

All phantoms represented an average male, arms up [100]. Realistic and homogeneous activity values were assigned to the different tissues of the simulated activity phantom (see Table 4.1), based on average activity values observed in available measured datasets (normally injected with 370 MBq and scanned 30 minutes post-injection). Values in the same order of magnitude were also reported upon in a previous study on myocardial  $^{18}\text{F}$ -FDG uptake [146]. An overview of the main common parameters used to generate all the phantoms can be found in Table 4.1. Figure 4.1 shows a coronal slice of the generated datasets.

### PET AND AC CT DATASETS

One static image of the thorax was obtained with the XCAT software, with the heart captured in a fixed cardiac and respiratory phase. The gate corresponding to end-diastole was chosen. The respiration phase of the simulated PET phantom was kept fixed to end-expiration. This procedure simulates a cardiac  $^{18}\text{F}$ -FDG PET scan where the cardiac and respiratory gating have ideally removed all motion present in the dataset. Two lesions (transmural and non-transmural) were included in the simulation. The non-transmural lesion (L1) transgresses 60% of the mid lateral wall and has a volume of approximately 3 ml. The transmural lesion (L2) is located in the apical portion of the inferior wall and has a volume of 1.5 ml (Figure 4.1).

A corresponding attenuation image at 511keV was automatically generated with the XCAT software, in the same cardiac and respiratory phase as the PET, used to perform attenuation simulation and attenuation correction (AC) of the PET dataset. Both the attenuation and the activity images were created using a voxel size of 0.8 mm in all directions.

Table 4.1: Key parameters for phantom generation.

Antero-posterior (AP) expansion [cm]	1.2
Diaphragm motion [cm]	2.0
Resp. cycle duration [s]	5
Card. cycle duration [s]	1
No. resp gates/cycle	5
No. card gates/cycle	10
Phantom size [pixel]	600x600x203
Phantom pixel size [mm]	0.8
Left ventricle activity [kBq/cc]	18
Right ventricle activity [kBq/cc]	12
Lung activity [kBq/cc]	0.9
Blood pool activity [kBq/cc]	5.5
Liver activity [kBq/cc]	6.5
Non-transmural lesion (L1) activity [kBq/cc]	8
Transmural lesion (L2) activity [kBq/cc]	0

## ANATOMICAL IMAGES (HRCT AND MRI)

In order to generate the HRCT frame of reference, a dataset with blood-pool contrast and high spatial and temporal resolution was generated. To this purpose, the AC CT described above was converted to Hounsfield units (HU) and blood contrast enhancement was performed by thresholding the blood from resulting images. This resulted in a simulated high-resolution contrast-enhanced CT image to be used as perfectly matching anatomical information during the reconstruction of the PET dataset.

A second anatomical image was also obtained by shifting such perfectly matching anatomical image by 2 mm both in the x and in the z direction (the corresponding reconstruction has the suffix *-shift*), with the aim of verifying the robustness of the anatomy-based prior to mis-registration. In addition, to verify the robustness of the conclusions against varying magnitudes and directions of shifts of the anatomical image relative to the PET, 10 random directions were generated in 3D and used to obtain shift vectors with a magnitude of 1, 2, 4, and 6 mm (40 vectors in total). These shift vectors were each applied to the perfectly matching anatomical image to offset it from the activity image.

Another anatomical image was generated in the same respiratory phase and in a slightly different cardiac phase from the activity image (the corresponding reconstruction are referred to with the suffix *-mism*). Four other mismatched anatomical images were simulated too, in order to account for physiological variations of the cardiac volume between different acquisitions [147] or between different heart cycles [148, 149]. To this end, we generated an anatomical image with a diastolic volume reduced by 10% when compared to the PET image (*mism1*). Moreover, we simulated an increase of the heart size by 5% (*mism2*), to account for small increments of the diastolic volume. The same cardiac phase (*ph1*) or the next cardiac phase (*ph2*) – compared to the PET dataset – were used for PVC. The mismatches produced were visually compared to the ground truth and were found representative

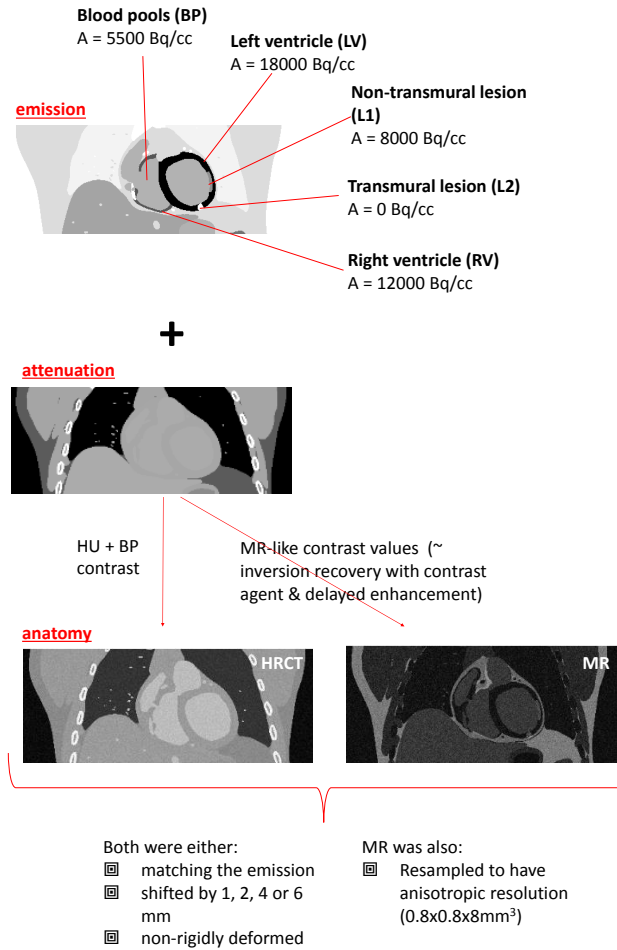
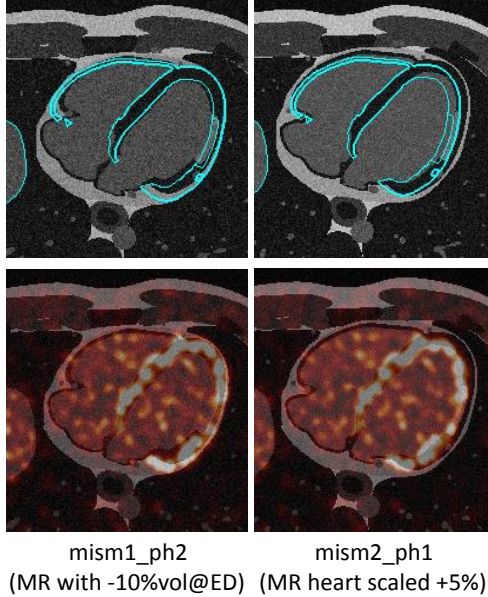


Figure 4.1: Overview of the activity, attenuation and anatomical datasets generated with the XCAT phantom. The anatomical images are obtained starting from the attenuation image generated by the XCAT software, and post-processed manually to obtain the desired anatomical information.

of a realistic scenario (see Figure 4.2).

It is important to highlight that an HRCT cannot distinguish between healthy tissue and scar. A previous preliminary study has suggested that this lack of differentiation might hamper the performances of the anatomical priors used during reconstruction of the PET datasets [150]. Conversely, other imaging modalities (e.g. MRI) are able to produce images where a clear distinction between scarred and normal tissue is present, if particular acquisition sequences are used [66]. Therefore, all anatomical images generated above (perfectly matching, shifted and in a different cardiac phase or volume) were simulated with MR-like contrast values, and also used as anatomical information during the reconstruction of the PET datasets.

The MR image was derived from the XCAT attenuation image by assigning MR-like values to the tissues. These values were extrapolated from one MR pa-



**Figure 4.2: Mis-alignment of PET and MR datasets** Two examples of mismatched MRs: on the left, the diastolic volume in the MR is reduced by 10% and the next cardiac phase is chosen relative to the PET. On the right column, the heart of the MR is up-scaled by 5% when compared to the heart of the corresponding PET dataset. On the top row, the contours of the initial activity phantom are overlapped in blue. In the bottom row, the same phantom was reconstructed using OSEM3D with RR and post-smoothing of 5 mm (red color scale) and it was overlapped to the MR images (gray color scale). While in the top row the misalignment between PET and MR is very easily detectable, it would be harder to identify when using a realistic PET image.

tient scan in short-axis orientation, acquired with inversion recovery and contrast enhancement. Regions of interest were drawn in seven tissue classes (left ventricle, blood pools, cardiac lesion, pericardium, lungs, soft tissue and fat), and the contrast between the different tissues was calculated. These same contrasts were reproduced in the simulated MR image, by assigning a value of 100 to the fat tissue and setting the values for the other tissue classes accordingly. The pericardium was separately generated and integrated into the just described simulated MR, as in the regular AC CT no distinction between pericardium and muscle is possible. The bone tissue (present in the AC CT simulated dataset) was assigned a value of 0 in the simulated MR image. Rician noise was also added to the noise-free XCAT-MR according to [151]. Figure 4.3 shows the regions drawn in the MR and the resulting synthetic, XCAT-based MR used as anatomical prior. Table 4.2 shows the tissue classes and the values used for each of them, in one patient dataset and in the simulated dataset. Comparable contrast values were observed in other two MR human datasets available, acquired with a similar protocol.

Furthermore, we simulated the more realistic case where the MR has an anisotropic resolution (i.e. the slice thickness is much larger – 8 mm – than the in-plane resolution – 0.8 mm). The reconstructions obtained with the use of such anisotropic MR are referred to with the suffix *-aniso* in the remainder of this study.

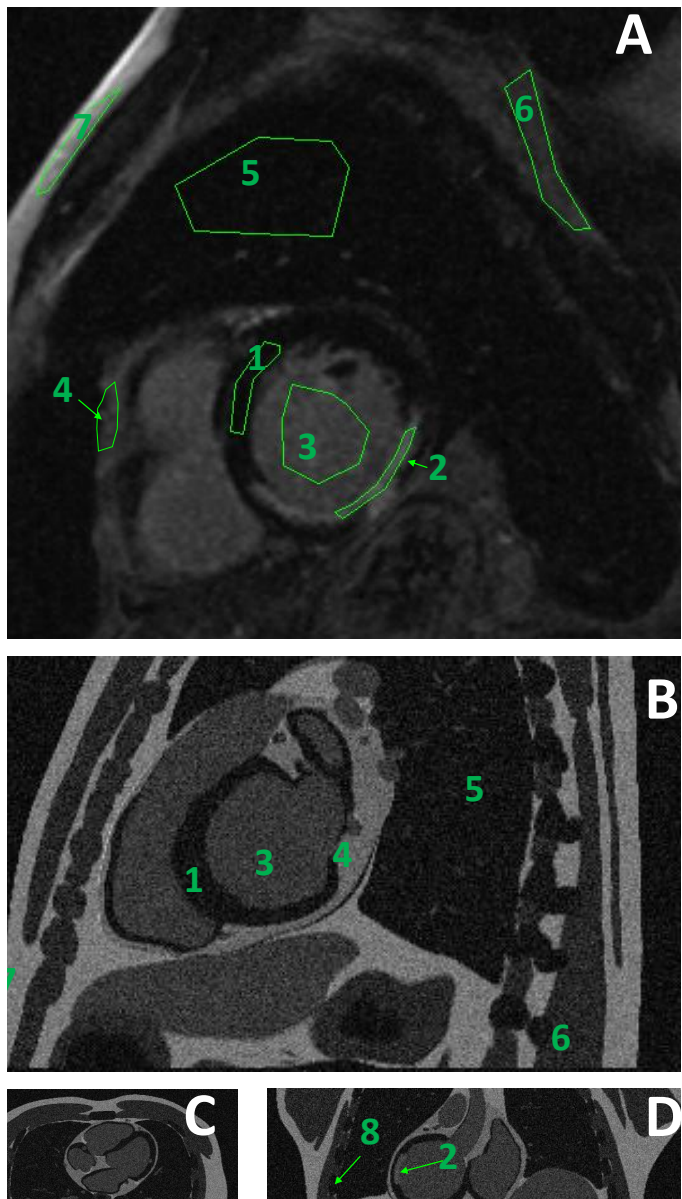


**Figure 4.3: Assignment of tissue values.** ROIs were delineated in a clinical MR (A). Similar contrast values were imposed to the tissues in the attenuation image generated with the XCAT phantom. Panes B, C and D represent the sagittal, transaxial and axial views of the XCAT phantom, respectively, after conversion to MR-like contrast values.

## PROJECTION OF THE ACTIVITY PHANTOM

The activity distribution generated with the XCAT software and corresponding to the PET gate of interest was forward projected with a ray tracing projection method using in-house developed software that simulates an acquisition with the PET component of a Siemens Biograph 16 PET/CT (Hirez) scanner [29]. Attenuation and a

*Table 4.2: Simulated vs real MR values.*

ROI no.	Tissue	MR intensity [mean $\pm$ sd in ROI]	XCAT values
1	Left ventricle (LV)	$8 \pm 2$	10
2	Lesion	$43 \pm 6$	55
3	Blood	$35 \pm 3$	45
4	Pericardium	$50 \pm 5$	70
5	Lung	$8 \pm 2$	10
6	Soft tissue	$24 \pm 3$	30
7	Fat	$78 \pm 12$	100
8	Bone	n.a.	0

shift-invariant camera resolution were modelled, but scatter and randoms were not. The camera resolution was modelled as a Gaussian convolution (FWHM = 4.3 mm and 4.5 mm in the transaxial and axial direction, respectively). As for attenuation, a sinogram containing the attenuation correction factors was computed from the forward projection of the image containing the PET attenuation coefficients, generated by the XCAT software, with a ray tracing projection method and no modelling of the resolution.

A noise-free sinogram was obtained. In addition, twenty-five noisy sinograms were generated by corrupting the noise-free sinogram with Poisson noise, corresponding to a 36 s-acquisition. The scan time of 36 s corresponds to a single gate taken from a doubly gated 30 min PET scan, using 5 respiratory and 10 cardiac gates. The simulated total number of counts amounts to 3.9 million, which is in good agreement with what was observed in previously performed animal and human thorax studies with similar activity concentrations.

We also simulated the (non-ideal) case where the respiratory motion is not corrected for. Since, in the clinical practice, the tracking of the breathing motion is much less common than the tracking of the heart rhythm with an ECG machine, we simulated the case where the **respiratory** motion is **not corrected**, and only the cardiac motion is. To do so, we generated a phantom with a 5x more counts by combining the data from all breathing phases. This corresponds to taking a single cardiac gate from an ECG-gated PET scan lasting 30 minutes using 10 cardiac gates, for an equivalent scan duration of 180 s (instead of 36 s). In addition, we simulated the case where the respiratory motion is ideally removed from the initial list-mode dataset (e.g. by list-mode motion compensation of the respiratory motion, for example as in [152]), and ECG-gating is performed on top of this. As in the previous case, the equivalent cardiac frame duration would be 180 s, but this case would result in sharp images as the motion blur due to the respiration has been eliminated.

## RECONSTRUCTION OF THE ACTIVITY PHANTOM

The activity sinogram was reconstructed using several reconstruction algorithms, listed below. In-house developed software was used to perform reconstruction with a ray-tracing projection method (the same as used during forward projection). The

voxel size of the reconstructed PET images was set to  $1.35^3$  mm $^3$ . The iteration scheme used for all reconstructions consisted of 3i42s (i: iterations, s: subsets), followed by 2i24s and 2i1s. Where Gaussian post-smoothing was performed, we used a spatially-invariant Gaussian kernel with FWHM = 5 mm in the three directions. The same attenuation sinogram as for the forward projection was used during each iteration of the reconstruction of all the datasets. This excludes the effects of inaccurate attenuation correction from this simulation study. The same reconstruction procedure was applied to all the noisy sinograms.

Several reconstruction algorithms were used to reconstruct the activity dataset:

- a 3D ordered-subsets expectation-maximisation (OSEM) algorithm without resolution recovery (*OSEM3D*), with and without Gaussian post-smoothing.
- a 3D OSEM algorithm with resolution recovery (*OSEM3D+RR*), with and without Gaussian post-smoothing. In this work, resolution recovery was achieved by modelling the resolution of the camera with a Gaussian smoothing kernel whose FWHM corresponds to the scanner's spatial resolution. A perfect modelling of the resolution was assumed, by using the same kernel (FWHM=4.3/4.5 mm in the transaxial and axial directions, respectively) during the simulation and the reconstruction of the datasets. At each forward and backward projection step of each iteration of the OSEM reconstruction algorithm, the intermediate reconstructed volumes were smoothed with such convolution kernel. In this way, the resolution of the scanner is taken into account during reconstruction and a de-blurred reconstructed image can eventually be obtained. However, Gibbs artefacts might be present in the final reconstructed image.
- two maximum-a-posteriori (MAP) reconstructions with edge-preserving priors (relative difference, RD [53] and total variation, TV [57]) applied during reconstruction. These priors are one simple way to encourage piecewise smoothness of the reconstructions, so that the Gibbs artefacts and the noise that affect the reconstructions with RR can be mitigated or eliminated. However, since they rely on intensity differences rather than knowing the actual image boundaries, they can smooth the activity over regions that should be considered as distinct.
- MAP reconstructions with anatomical information (HRCT, isotropic MR or anisotropic MR). The anatomical information could be perfectly matching (*-perf*), rigidly shifted (*-shift*) or mismatched (*-mism*) relative to the PET dataset. Local smoothness of the activity image was encouraged (using RD with  $\gamma = 0$ ) within the boundaries of homogeneous regions in the anatomical image during reconstruction, according to the technique proposed by Bowsher [61] and modified by our group [62].

The general expression for the estimation of the activity distribution  $\hat{\Lambda}$  using prior information is in the form:

$$\hat{\Lambda} = \underset{\Lambda}{\operatorname{argmax}}[L(\Lambda) - P(\beta, \gamma, \Lambda)]$$

where  $L$  is the log-likelihood of the activity  $\Lambda$  and  $P$  is the penalty term, where the penalty quantifies how strongly the estimated image disagrees with the prior information.  $\beta$  is the weight of the priors, and  $\gamma$  controls the edge preservation of the RD-prior (where  $\gamma = 0$  corresponds to no preservation of edges). All reconstructions with priors were performed using several parameter sets. For the RD prior, we did reconstructions using  $\beta = 4, 10, 30, 50$  and  $\gamma = 10, 100$ , whereas for the TV prior we reconstructed using  $\beta = 0.0001, 0.001, 0.003, 0.005, 0.01, 0.05, 0.1$ . For each anatomical Bowsher prior, we tested different weights ( $\beta = 0.1, 4, 10, 30, 50$ ) and a spherical neighbourhood of  $3 \times 3 \times 3$  voxels (18 actual neighbours, excluding the 8 most distant ones to obtain an approximately spherical neighbourhood) was chosen. Moreover, a fixed number of neighbours ( $n$ ) within the neighbourhood needs to be set, to define over how many voxels the smoothing is applied. We tested the case where  $n = 3, 6, 9$  and  $13$ .

## CHOICE OF THE RECONSTRUCTION PARAMETERS

### BIAS-NOISE PLOTS

As described at the end of the previous section, several parameters were tested for the MAP reconstructions, but only a few parameter sets were used for the full analysis of the lesions. The bias-noise plots and the contrast-noise plots for the LV and the non-transmural lesion (L1), respectively, were used to select the parameter sets to be used for subsequent further analysis. In other words, the parameter selection has to be seen as preparatory work for the main investigation. The Bowsher reconstructions with the MR were used to assess the bias, the contrast and the noise of the reconstructions with anatomical priors.

To generate bias-noise plots, the bias was calculated as :

$$bias_{LV} = \overline{LV}_{recon} - LV_{true}$$

The contrast was computed as:

$$contrast_{L1} = 1 - \frac{\overline{L1}}{\overline{LV}},$$

and the noise was computed as:

$$noise_{LV} = \overline{stddev(LV)}$$

where  $\overline{LV}$  and  $\overline{L1}$  represent the mean activities calculated in the LV and in L1 over 20 noise realizations, respectively.  $stddev(LV)$  is obtained by calculating the standard deviation on the activity in every voxel in the LV over all noise realizations and then taking the average over all voxels in the LV. Both LV and L1 were defined by thresholding the re-sampled original phantom. All voxels whose value (after the resampling of the phantom) was at least 70% of the original activity value of the LV (or L1) were used to create the mask for the two regions.

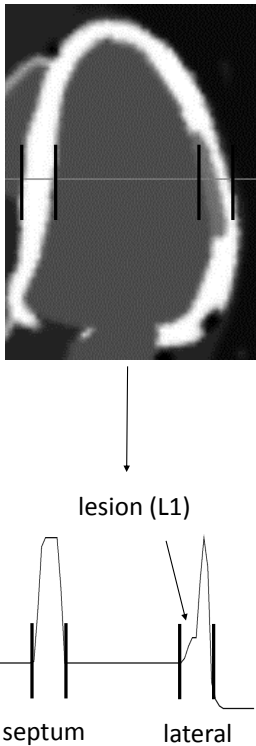


*Figure 4.4: Line segment over which profiles were computed. The bottom pane shows the true line profile.*

## IMAGE PROFILES

The profiles through the middle slice of each reconstruction were also analysed, in order to verify if the parameters chosen based on the bias-noise plots could perform well enough also for what edge-preservation is concerned. Figure 4.4 illustrates the profile, crossing over the non-transmural lesion, over which the intensity profile was computed. The profile in the septal-lateral direction was considered. The profiles of the various noise-free anatomy (MR)-enhanced images, obtained by reconstructing the same dataset with different weights and different numbers of neighbours, were plotted against the ground truth.

## EVALUATION OF RESULTS

The bias-noise plots and the line profiles allowed us to choose which parameter sets were the best compromise in terms of intensity preservation, noise properties of the reconstructions and ability to preserve the edges. Once the reconstructions that yielded the best compromise between these three properties were selected, the images were carefully evaluated by an experienced nuclear medicine cardiologist, who visually chose the reconstruction (among those with the best bias-noise-edge compromise) believed to be the most clinically acceptable. Once the optimal reconstruction parameters were chosen for all the selected algorithms (Bowsher, RD,

TV), the analysis of the lesion areas was performed. The resulting images were evaluated against the ground truth represented by the resampled original datasets generated with the XCAT software.

## FIGURES OF MERIT

A quantitative evaluation of the reconstructions was performed. Three figures of merit were used to analyse the quantitative accuracy and give an indication of the diagnostic value of the reconstructions:

- The recovery coefficient (RC) is defined as follows:

$$RC_r = \frac{\bar{r}_{recon}}{r_{true}}, \quad r = LV, RV, L1$$

where  $\bar{r}$  represents the mean activity in the volume of interest  $r$ , averaged over the 25 noise realizations, and LV, RV and L1 are the volumes of interest containing the left ventricle, the right ventricle and the non-transmural lesion, respectively (see Fig. 4.1). The RC was not calculated for the transmural lesion L2, as its true mean value is zero.

- The contrast recovery coefficient (CRC) was used to identify the algorithm that best preserves the contrast between the region of interest  $r$  and the background region  $b$ , when compared to the ground truth contrast. The CRC was computed as in [153]:

$$CRC_r = \frac{contrast_r^{recon}}{contrast_r^{true}}, r = LV, RV, L1, L2$$

where

$$contrast_r = \begin{cases} \frac{\bar{r}}{BP} - 1 & \text{if } r = LV, RV \\ 1 - \frac{\bar{r}}{LV} & \text{if } r = L1, L2 \end{cases}$$

BP and L2 are volumes of interest containing the blood pool and the transmural lesion, respectively (see Fig. 4.1).

- The contrast to noise ratio (CNR) is another common measure for determining the performance of an algorithm. In fact, while the CRC indicates how well the intensity values of a region are recovered compared to a background region, it does not give any indication on how well the regions are visible when the noise corrupts the reconstructions. In other words, if e.g. a contrast of 10 units is observed between a lesion and the background, but the noise has a comparable magnitude, the lesion will be basically invisible despite the good contrast recovery indicated by the CRC. The CNR was defined as in [154]:

$$CNR_r = \frac{contrast_r^{recon}}{noise_b^{recon}}, r = LV, RV, L1, L2$$

where

$$noise_b = \frac{\overline{stddev(b)}}{\bar{b}},$$

$$b = \begin{cases} BP & \text{if } r = LV, RV \\ LV & \text{if } r = L1, L2 \end{cases}$$

A paired t-test was performed to identify the significant differences in CRC and CNR of the various reconstructions, compared to TV. To this end, a significance level of 0.01 was chosen for all evaluations.

## BULL'S EYE PLOTS (POLAR MAPS)

17-segments polar maps (PMs) or bull's eye plots of the LV were created to further evaluate the visibility and the quantification of the lesions, using a tool commonly adopted by nuclear medicine physicians. For each of the reconstructed datasets and for the ground truth, the bull's eye plots were created as described in [155]. The delineation of the LV was automatically performed by in-house software. A fixed thickness of the LV of 6 mm was imposed, which was verified to fit the simulated LV shape well.

Each pixel in the polar map represents a small transmural portion of the LV wall, enclosed by the endocardial and epicardial contours, for each angular location and at each position along the long axis of the LV. The intensity assigned to each pixel can be computed in two ways, as illustrated in Figure 4.5. On the one hand, the maximum count over the delineated LV can be taken. This method produces polar plots (*max-count polar maps*) that are less affected by delineation errors or inaccuracies, but they can reflect the noise or the artefacts introduced by the reconstruction algorithm (e.g. Gibbs over-shoots). In addition, this method will consistently take the maximum value over the thickness of the myocardium, thus possibly hiding the presence of e.g. a non-transmural lesion. Conversely, it is possible to take the mean value over the thickness of the LV, at each angular location and at each position along the long axis, and assign that mean value to the corresponding voxel in the polar map. The *mean-count polar maps* are more prone to delineation errors but, if the delineation is reliable, have the advantage of depicting more accurately the distribution of activity in the LV region considered.

Both polar map types were generated in this work. When the mean-count polar maps were computed, the delineation coming from the Bowsher reconstructions with the MR as anatomical prior information was used as delineation also for all other reconstructions. The mean value of each of the 17 segments that composed each polar map was computed, for each of the noisy reconstructions. Three regions were additionally identified in each polar map: L1 (segment 11, corresponding to the location of the non-transmural lesion), L2 (segment 13, corresponding to the location of the transmural lesion) and normal tissue (all other segments). The mean values of the normal vs lesion regions were calculated and compared, to verify which algorithm best preserved the lesion contrast and best reflected the values obtained from the polar map of the ground truth.

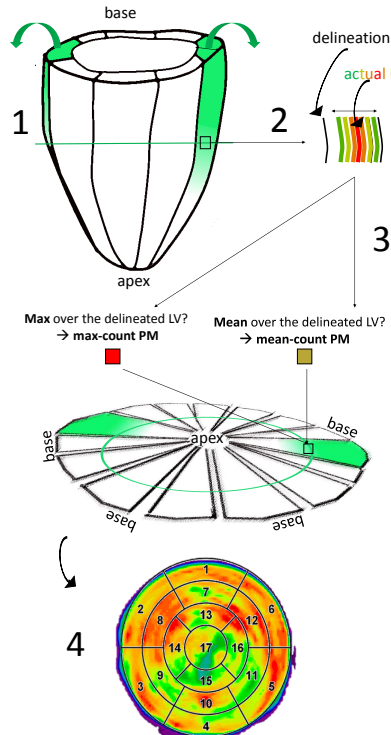


**Figure 4.5: Creation of a polar map (PM) of the LV.** The polar maps, or bulls eye plots, are 2D representations of a 3D cone-shaped object (the left ventricle) (1). By using polar maps, we lose the information related to the distribution of activity within the wall thickness, as only one activity value can be assigned to each angular and longitudinal position of the LV (2). The value that is commonly assigned to each pixel of a bulls eye plot can be the maximum, or the mean value over the LV wall at that angular and longitudinal position (3). Other values can be assigned, too, but the mean or the maximum along the wall thickness are the most commonly used when bulls eye plots are considered. This assigned value is an approximation of the activity over the LV thickness. In most cases, it manages to convey an acceptable, general idea of the myocardial distribution of activity. However, in some cases it might come in defect: for example, when overshoots of activity appear in the reconstructed images as a side effect of resolution modelling during reconstruction, or when images are extremely noisy, the max-count polar maps would assign to the PM values that are an overestimation of the actual mean activity within the LV. On the other hand, the use of mean-count polar maps might be incorrect if the delineation of the myocardial walls is not accurate (e.g. due to the blurring caused by PVE). No matter the method used to select the polar map values, the resulting image is a 2D map of the activity distribution of the LV (4), where the different sections (or segments) can be identified using different conventions. In (4) the "17-segment" subdivision is used, as it is the most widespread in nuclear medicine analyses (used in this work).

## APPLICATION TO AN ANIMAL DATASET

As a proof of concept, we applied some of the techniques described in this simulation study (OSEM3D, OSEM3D+RR, TV) retroactively on a previously measured animal (sheep) dataset, where a lesion in the right ventricle and a lesion in the apical portion of the left ventricle had acutely formed before the PET scan. No Bowsher reconstructions were performed for this dataset, due to the lack of the appropriate anatomical information.

The anaesthetised sheep was injected with 257 MBq of  $^{18}\text{F}$ -FDG and scanned 30

minutes post-injection for 30 minutes. During the scan, the breathing of the animal was mechanically controlled by a ventilating machine. The cardiac and respiratory traces were recorded during the PET scan, using an ECG tracking device and a respiratory belt (AZ-733V, ANZAI Medical Co.). Triggers corresponding to the peak R-wave of the ECG and to the peak-inspiration of the breathing signal were inserted into the PET list-mode by these external tracking devices. They were then exploited to perform off-line phase-based gating of the PET dataset using in-house developed software (5 respiratory gates and 10 cardiac gates). After the gating, the list-mode corresponding to end-expiration and end-diastole was reconstructed using OSEM3D, OSEM3D+RR and the TV prior ( $w=0.005$ ).

A qualitative comparison of the images at the lesion sites was performed.

## III RESULTS

### CHOICE OF THE RECONSTRUCTION PARAMETERS

We made use of the combined information from the bias-noise and contrast-noise plots, alongside with the line profiles through the middle slice of the heart and the opinion of an experienced nuclear medicine clinician, to define which of the Bowsher reconstructions was best to proceed with for the full subsequent analysis of the recovery and visibility of the simulated lesions.

Figure 4.6 shows the bias-noise plot for the LV and the contrast-noise curve for L1, for the different reconstruction algorithms and parameter choices. The curves are produced by varying the weight of the priors. Initially, by visually analysing the same reconstructions at different noise levels, we empirically selected those corresponding to a noise level of 3000-4500 (highlighted in blue in Figure 4.6). The bias- and contrast-noise plots confirmed that this was an acceptable compromise between the noise and the bias levels, both of which should be as low as possible. Most of the curves in the plots bend towards worse contrast/bias values when going below this noise level. In other words, by further lowering the noise, the LV bias would become excessive, and the lesion contrast would start to decrease. We verified that these conclusions were in agreement with the opinion of our nuclear medicine expert.

To supplement the results of the bias-noise and contrast-noise analysis, the profiles through the middle slice of the heart (Figure 4.7) were also considered. The Bowsher reconstructions with 13 neighbours and high weights were discarded, as they appear artificially smooth and they fail to correctly restore both the activity peaks and the sharp intensity transitions. The reconstructions with 3 neighbours show the best edge-preservation, but the noise pattern they display looks unnatural especially at higher weights. The reconstructions with 6 and 9 neighbours appeared the best for the structures of interest, featuring a less artificial look and yet fairly good preservation of the edges. After a visual inspection of the reconstructed images, performed by an experienced nuclear medicine physician, a weight of 10 and a  $n=9$  was chosen for the Bowsher reconstructions. For the TV prior, a weight of 0.005 was chosen to match the selected noise level. For the same reason, the parameters chosen for the RD prior were  $\beta = 4$  and  $\gamma = 10$ . The markers of the final

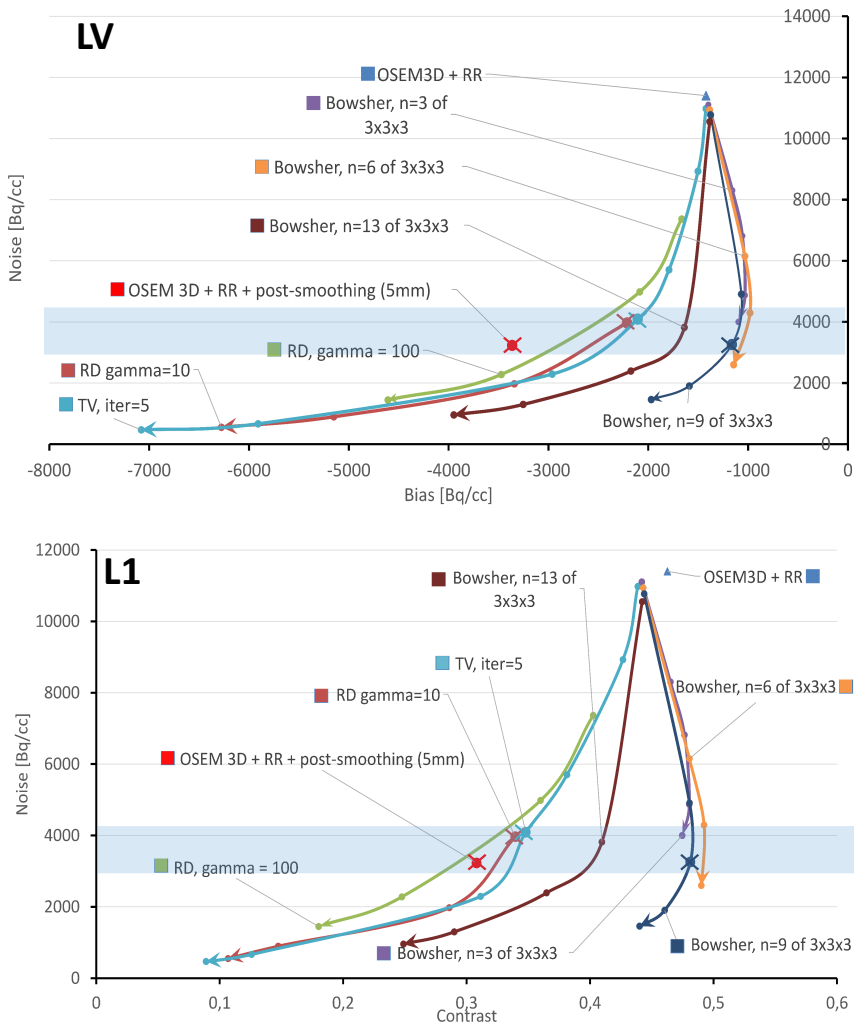
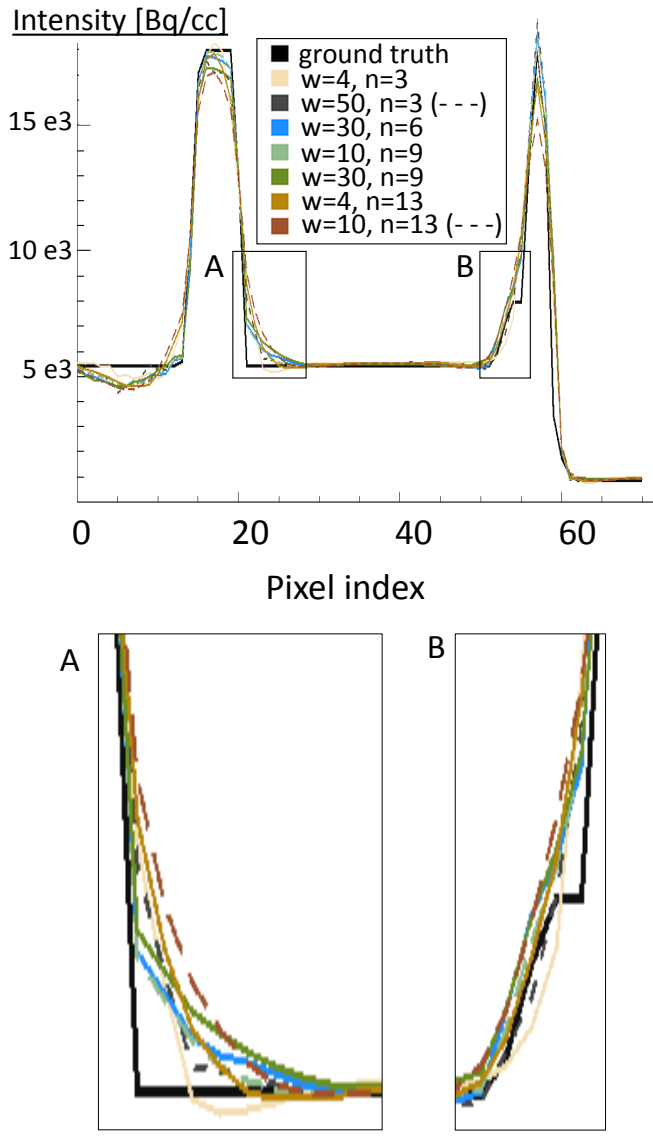


Figure 4.6: Bias-noise plot for the LV (top pane) and contrast-noise plot for the non-transmural lesion L1 (bottom pane). When the Bowsher prior is indicated, the MR is used as anatomical information during reconstruction. 20 noise realizations per reconstruction were used. The light-blue stripe represents the noise range designated as clinically acceptable.

selected reconstructions are in bold and crossed in the bias-noise and contrast-noise plots (Figure 4.6).

## VISUAL ANALYSIS AND SEPTUM-LATERAL PROFILES

As Figure 4.8 shows, the HRCT-based prior moderately outperformed the non-anatomy-based priors in terms of contrast recovery of the ventricles and volume delineation, provided that the anatomical information was well aligned to the corresponding PET image. There was no improvement in terms of lesion visualisation, due to the fact that the HRCT does not show any intensity difference between lesions and healthy tissue.



*Figure 4.7: Profiles through the middle slice of the heart. Noise-free reconstructions.*

The edge-preserving priors, on the other hand, produced visually appealing images, with better contrast-to-noise ratios than the current standard for PET reconstruction (OSEM3D+RR+post-smoothing). The use of MR as anatomical information led to better delineation of the lesions. If, however, the anatomical information was shifted or mismatched when compared to the activity image, the delineation of the LV and of the lesions was affected and artefactual hypo-perfused areas appear in the LV. The use of anatomical information with non-ideal resolution (i.e. anisotropic MR) slightly affected the image quality. However, in most cases the

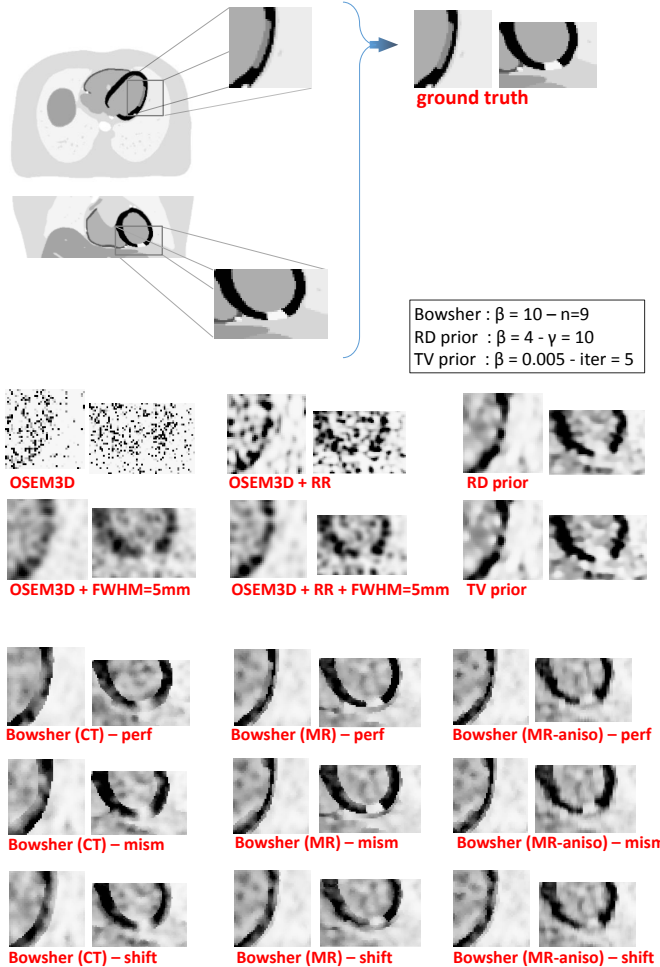
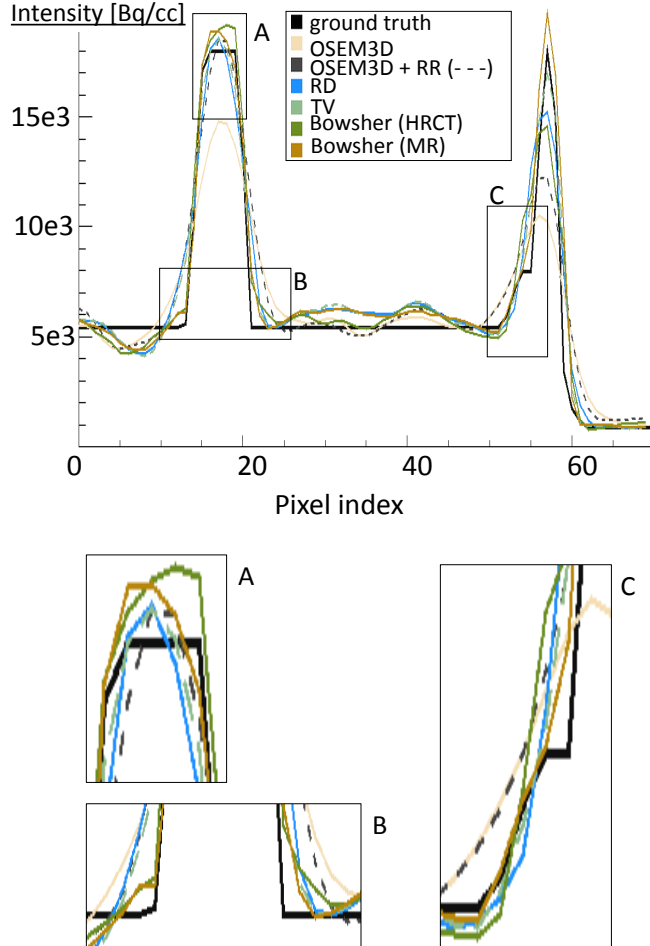


Figure 4.8: Zoomed in images of the lesions reconstructed using the different reconstruction algorithms (example of 1 noise realization).  $3i42s + 2i24s + 2i1s$  iteration scheme. The RD and the TV priors represent a good choice in case no anatomical information is available, if the anatomical information does not highlight the lesions or if the anatomical information is mismatched (see Bowsher (HRCT) or Bowsher (MR)-shift). When the anatomical image is matching the PET dataset and it clearly differentiates between healthy and scarred tissue, then it is definitely the preferred choice (Bowsher(MR)-perf). Please note that the OSEM3D reconstructions suffer more than others from severe noise; this is due to the long iteration scheme, applied to ensure convergence and consistency with the other reconstructions. The suffix -shift indicates the case where the anatomy is displaced by 2 mm in the x and z direction, while -mism represents the case where the heart in the anatomical information has the same morphology but it is in a slightly different cardiac phase relative to the PET dataset.

anisotropic resolution of the MR was not the bottleneck for the reconstruction with anatomical information.

The profiles computed through the middle plane of the heart (Figure 4.9) confirmed these observations. If perfectly aligned to the PET dataset, both HRCT and MR performed equally well as anatomical priors (leftmost part of the profile), except when the lesion was considered (rightmost part). There, again, the CT-

based anatomical prior suffered from the fact that no information on the lesion was present, and therefore blurred the activity of the LV over it. The MR-based prior, on the contrary, managed to correctly recover the activity. The use of MRs that were not perfectly aligned to the PET dataset was not particularly deleterious for the mid-ventricular profile (not shown).



*Figure 4.9: Profiles of the LV activity computed through the middle plane of the heart. The OSEM3D, OSEM3D+RR (both with a 5-mm post-smoothing), the two edge-preserving priors (TV with  $w=0.005$ , RD with  $w=4$  and  $\gamma=10$ ) and the two anatomy-based priors (both with  $w=10$  and  $n=9$ ) are compared. These profiles are the mean over 20 noise realizations. In the bottom part, a zoomed-in version of the most interesting areas is shown. A and B demonstrate that a similar behaviour can be expected between MR-based and CT based anatomical information, where no lesions are considered. In pane C, the MR reconstruction is the one that best follows the contours of the lesion.*

## FIGURES OF MERIT

The CRC and CNR were calculated for all the selected reconstructions. As a first step, we compared the results obtained with the current standard for reconstruction

(OSEM3D+RR+post-smoothing) to the images obtained with the edge-preserving, non-anatomical prior (TV) and the two types of anatomical prior (perfectly matching HRCT and MR, respectively). Figure 4.10 describes the findings. When the lesion is not visible in the anatomy (i.e., HRCT), the use of anatomical priors does not improve the contrast recovery of the lesions, when compared to results obtained with the non-anatomical priors. However, the superior noise performance of the anatomy-based prior makes the lesions slightly better visible in such reconstructions (Figure 4.10, Bowsher(HRCT) columns, CRC vs CNR). The same Figure and the results of the t-test indicate that the improvement of the CNR is moderate (but significant) for Bowsher(HRCT) compared to TV, particularly when a non-transmural lesion (red column) is concerned. When the lesion is visible in the anatomy (i.e., MR), the anatomical prior significantly improves both contrast recovery and noise properties of all the anatomies.

Secondly, we further analysed the behaviour of the best anatomy-based reconstruction when the conditions are not ideal, i.e. the alignment between the anatomical and the PET dataset is disrupted or the anatomical information is acquired with anisotropic resolution (Figure 4.11). The use of a shifted or mismatched anatomy affects both quantification and detectability, with more errors caused by rigid shift than cardiac phase mismatch. The use of a shifted or mismatched anatomy also introduced small, artefactually hypo-perfused areas (not shown), which could possibly be interpreted as false positives. The use of anatomical information with non-ideal resolution (i.e. anisotropic MR) does affect CRC and CNR. However, in most cases it still outperforms the non-anatomy-based priors.

A comparison of all the CRCs (Figure 4.12, top) and the CNRs (not shown) of the Bowsher(MR)-based reconstructions with varying shifts was also performed, to verify the robustness of the findings to different degrees of misalignment. If the overall shift in the three directions is small enough ( $\leq 2$  mm), the contrast recovery of the lesions is still acceptable and improved when compared to images obtained using a non-anatomical prior during reconstruction. On the other hand, particular attention needs to be paid when the shifts are greater than 2 mm. In this case, both the CRC and the CNR of the lesions worsen, when compared to TV. Similar conclusions can be drawn for the different mismatches (Figure 4.12, bottom graph). If the mis-alignment between the image used as anatomical information and the PET image is small enough (eg. mism1-ph1), the good performances of the anatomical prior are maintained. The stronger the mismatches, the higher the decrease in both CRC and CNR, particularly those of the lesions.

The effect of motion correction is clear in Figure 4.13. If the respiratory motion correction is neglected and only ECG gating is performed on the original list-mode dataset (*ECG* bars in the Figure), the lesions are hardly distinguishable due to the motion blur. On the other hand, the use of images with better noise properties and perfectly compensated for respiratory motion (*ECG+R* bars in the Figure) demonstrate that the better noise level improves the CNR as expected, and that the correct recovery of the contrast is independent of the noise level.

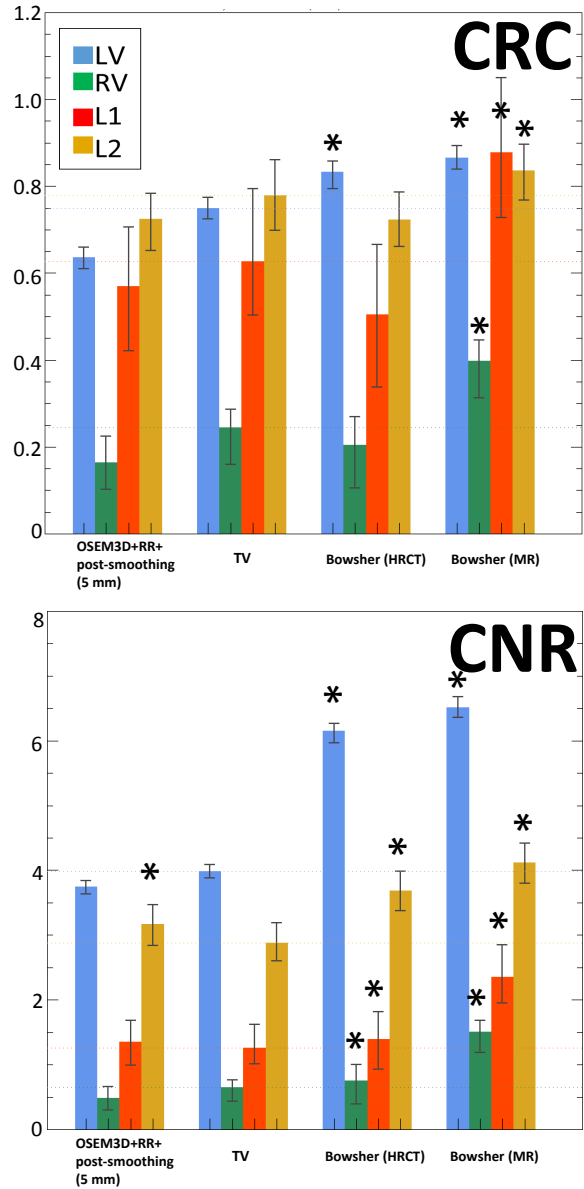
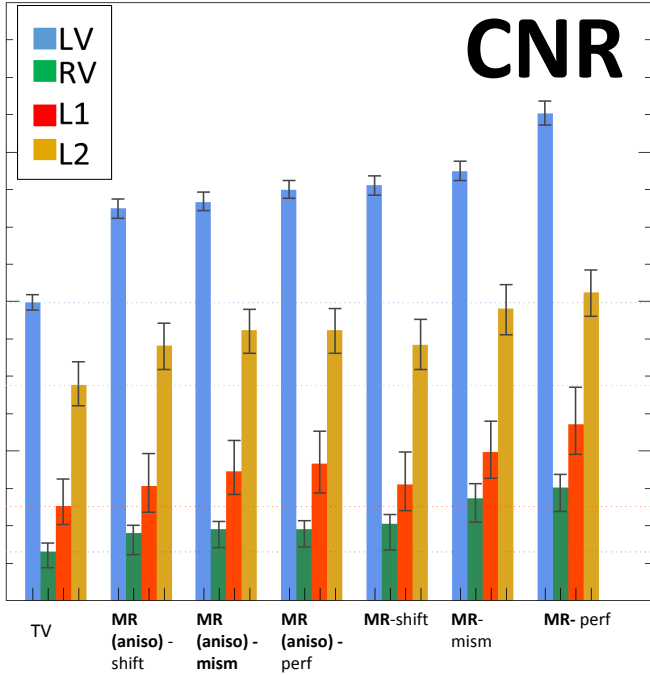


Figure 4.10: CRC and CNR comparison, edge-preserving prior (TV) vs ideal anatomical priors, calculated on 25 noise realizations. Mean values and min/max error bars. \* = significantly better than TV. TV was chosen as reference as it yielded the overall best RC, CRC and CNR in comparison to all other non-anatomy-based reconstructions. L1: non-transmural lesion; L2: transmural lesion.

## BULL'S EYE PLOTS

The bull's eye plots add insight into the activity distribution in both lesions. An in-depth analysis of the LV quantification is out of the scope of this work.

The transmural lesion is clearly identifiable in the bull's eye plots of all reconstructions. The non-transmural lesion, on the other hand, should only be visible in



*Figure 4.11: CNR comparison, edge-preserving prior (TV) vs non-ideal anatomical priors, calculated on 25 noise realizations. Mean values and min/max error bars. All reconstructions are significantly better than the edge-preserving prior (TV). The suffix -shift indicates the case where the MR is shifted by 2 mm in the x and z direction, whereas -mism indicates the case where the MR is in a slightly different cardiac phase relative to the PET. L1: non-transmural lesion; L2: transmural lesion.*

the mean-count PMs, while it should be fully hidden in the max-count PMs, given the fact that such plots have been generated by taking the maximum intensity over the thickness of the LV.

The top row of Figure 4.14 illustrates what is actually obtained. In the max-count polar maps, the healthy tissue situated close to the non-transmural lesion is often reconstructed with decreased intensity due to PVE or to incorrect PVC. Therefore, the bull's eye plots will show an area of decreased activity, as if the segment contained a fully transmural lesion. In the ideal-case scenario, however, the better the healthy portion of the LV is reconstructed, the less we should notice the presence of the non-transmural lesion in the max-count PM. This is the case for the reconstructions with the MR used as anatomical prior, which is the one that most accurately reproduces the polar map of the ground truth.

On the other hand this result, despite correct, might hide the presence of a non-transmural lesion to the clinician's eye. In order to overcome this inconvenience and keep trace of the non-transmural lesion in the bull's eye plots, the use of a mean-count polar map is advised. The anatomical prior allows an accurate delineation of the LV, thus avoiding errors due to incorrect definition of the LV boundaries. At the same time, the presence of a hypo-perfused area is correctly revealed.

In both cases, the use of bull's eye plots needs to be accompanied by a thorough observation of the corresponding short and long axis slices, especially if anatomy-

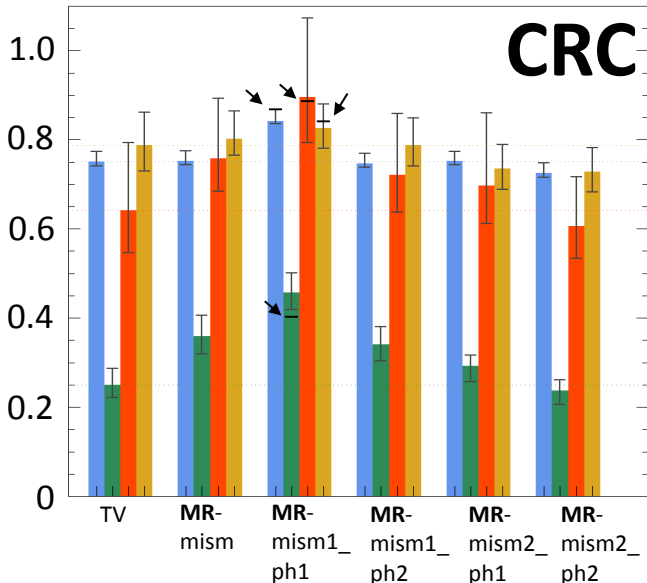
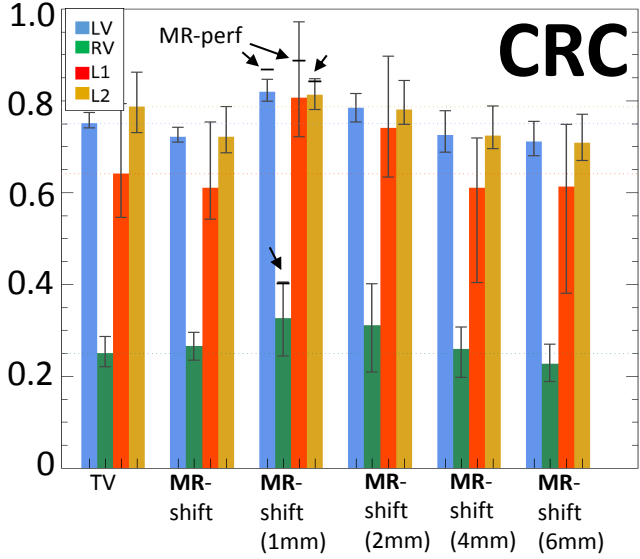


*Figure 4.12: CRC comparison with different shifts or mismatches . Contrast recovery coefficients (CRC) for the different cardiac regions, when different shifts (top) or mismatches (bottom) are applied to the MR before using it as anatomical information during reconstruction. The values here presented are the mean, maximum and minimum values over 10 shift directions per shift magnitude and over 10 noise realizations per mismatched MR, respectively. The MR-mism and MR-shift reconstructions are the same as in Figure 4.11 (MR-shift is shifted by 2 mm in the x and z direction, MR-mism is in a slightly different cardiac phase).*

based PVC is performed during reconstruction, in order to correctly differentiate between transmural and non-transmural lesions.

Figure 4.15 shows the mean values of the normal and lesioned regions, computed

# CRC

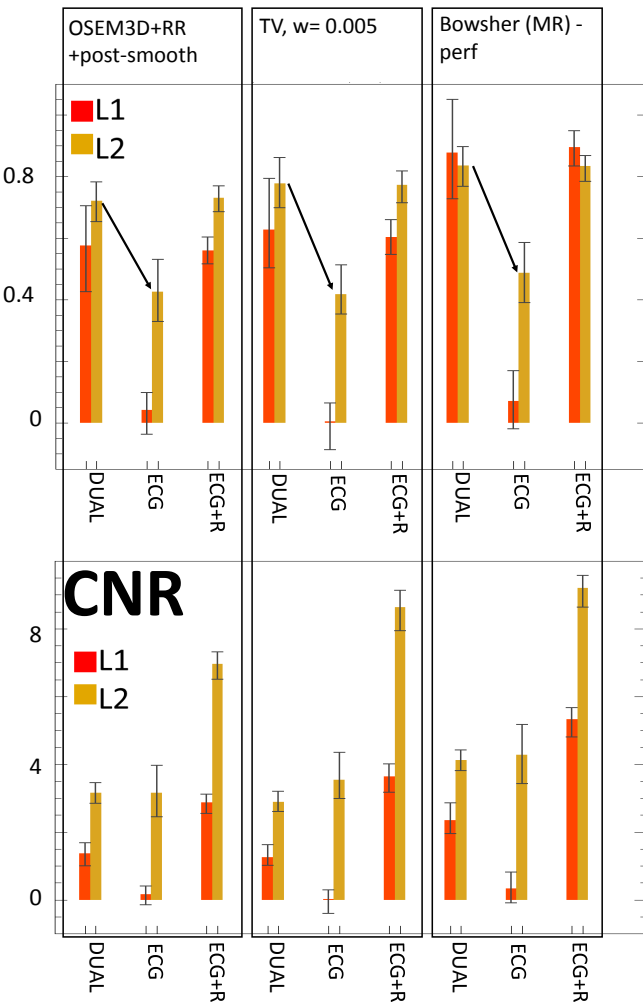


*Figure 4.13: Effect of motion correction on CRC and CNR.* The top plot shows the changes in contrast recovery when motion compensation is fully performed (DUAL, as in dual-gated studies), or only ECG gating is performed (ECG, one cardiac gate blurred by the respiratory motion) or if ECG gating is performed starting from a dataset where the respiratory motion has been compensated (ECG+R, one cardiac gate, less noisy).

on the corresponding segments of the polar maps, for 25 noise realizations.

When the max-count polar maps are used and the non-transmural lesion is considered (top-left pane of Figure 4.15), the mean intensity of the segment corresponding to the non-transmural lesion (L1) is, in the ground truth, very close to the mean intensity of the surrounding normal tissue. As expected, this behaviour is best reproduced when the Bowsher with a perfectly matching MR is used as anatomical information (light blue stripe). This is the reconstruction technique that gets

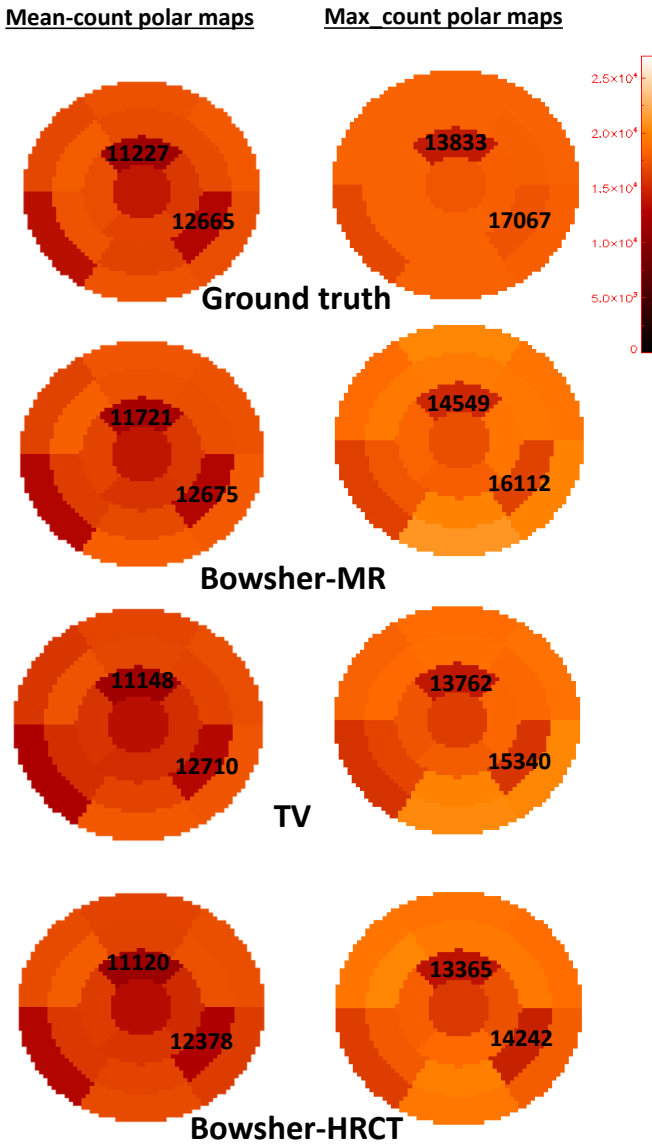


*Figure 4.14: Mean-count vs max-count Bull's eye plots. Segmental 17-segments polar maps obtained from the reconstructions of 1 noise realization. Left column: mean-count polar maps of a selection of the reconstructions performed. The Bowsher reconstruction with MR is overall the most similar to the ground truth, both in absolute and relative terms. In the right column, the max-count polar maps for the same reconstructions are presented. Again, the Bowsher reconstruction with MR produces the polar map with the best intensity preservation, when compared to all other reconstructions.*

closest to the segmental values of the L1 and L2 in ground truth, too. All other reconstruction algorithms artificially increase the contrast between the L1-segment and the normal tissue, due to the incorrect recovery of the surrounding healthy tissue (e.g., when the CT or the non-anatomical priors are used). The OSEM3D and OSEM3D+RR without smoothing are extremely noisy, hence the mean segmental values of the max-count polar maps are all over-estimated. A post-smoothing ap-

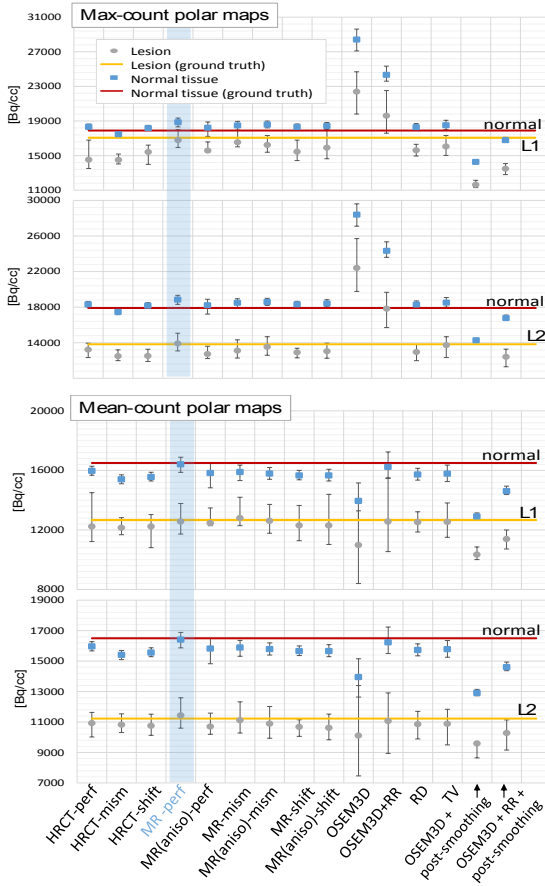


*Figure 4.15: The mean, minimum and maximum values (over 25 noise realizations) of the normal and lesioned regions, computed on the corresponding segments of the polar maps, are compared. On the two graphs from the top, the values computed from the max-count polar maps are illustrated. On the two bottom graphs, the values computed from the mean-count polar maps are presented. For each type of polar map, the top parts (first and third graph) compare the intensity of the normal region to the intensity of the non-transmural lesion (L1), using the different reconstruction algorithms, whereas the bottom parts (second and fourth graph) show the same information for the transmural lesion (L2). The solid lines represent the mean values computed in the ground truth in the normal (red) and lesioned (yellow) tissues. The light-blue stripe highlights the reconstruction algorithm (MR-perf) that performs best in terms of similarity of the mean to the ground truth. To be noted that the mean-count polar maps of the OSEM3D+RR, despite being a good approximation of the ground truth on average, have very large error bars indicating that it can have very poor values for individual noise realisations.*

plied to such reconstructions preserves the contrast between normal and lesioned segments (anyway higher than what it should be), and it underestimates the segmental value for the non-transmural lesion L1.

When the transmural lesion is considered (bottom-left pane of Figure 4.15), all MAP reconstructions behave similarly and preserve both contrast and actual values. This is consistent with the fact that the maximum count over the thickness is anyway zero, regardless the alignment of the anatomical information or the prior

used during reconstruction.

If a better representation of the ground truth values is aimed at, the use of mean-count polar maps is recommended. In this case, the mean intensity of the normal tissue decreases for almost all reconstruction algorithms except the Bowsher-MR and the OSEM3D with RR. In the case of OSEM3D+RR, the computation of a mean polar map (using the LV delineation obtained from the Bowsher(MR)-PET) does mitigate the sharp peaks of activity at the center of the LV of the OSEM3D+RR reconstructions, which are the Gibbs artefacts due to the process of RR. This holds true as long as a correct delineation (in this case, the one from the MR-based reconstructions) is used. As far as the non-transmural lesion L1 is concerned (top-right pane of Figure 4.15), the mean segmental values reflect the mean intensity of the ground truth when both a perfectly matching MR or edge-preserving priors are used. The use of a misaligned MR does hamper the quantification of both normal and lesioned regions, similarly to what the use of an HRCT does. The HRCT does not produce correct results due to the absence of pericardium and of the lesion in the anatomical image. The transmural lesion, again, suffers less from mismatches or incorrect lesion delineation in the anatomical image (bottom-right pane of Figure 4.15).

These results are confirmed by the visual inspection of the polar maps. A selection of the bull's eye plots compared to the ground truth is on Figure 4.14.

## PROOF OF CONCEPT: ANIMAL DATASET

The images resulting from the reconstruction of the animal dataset are in Figure 4.16. The overall image quality improves when using the TV prior, with a noise-suppression and contrast-enhancement effect that is similar to the one observed in the simulation study. The boundaries of both lesions are also more clearly defined when using TV.

## IV DISCUSSION

In the first place, it is important to emphasize the reason why a single cardiac and respiratory PET frame, obtained by double gating the original dataset, was considered here for PVC instead of a motion-corrected PET dataset (using all available data). Several methods to obtain motion fields with which the PET dataset could be corrected for motion have been proposed in the past: using a dynamic CT acquisition [156], via estimation of the motion fields directly from the PET dataset [80,141] or using motion fields derived from a truly simultaneous PET/MR acquisition [142]. In the case of a shorter scan, for example, using a single cardiac gate from a study with motion correction would increase the fraction of the counts that are used to create the motion-free image. However, the additional radiation burden associated with the CT acquisition, the possibly inaccurate and non-trivial motion estimation from the PET dataset and the non-availability of truly-simultaneous PET/MR devices in most of the PET centres, made us opt for simulating the worst-case scenario where a simple double-gating pass was applied to the PET dataset. In this way, all PET datasets are equally noisy and are equally unaffected by possibly inaccurate

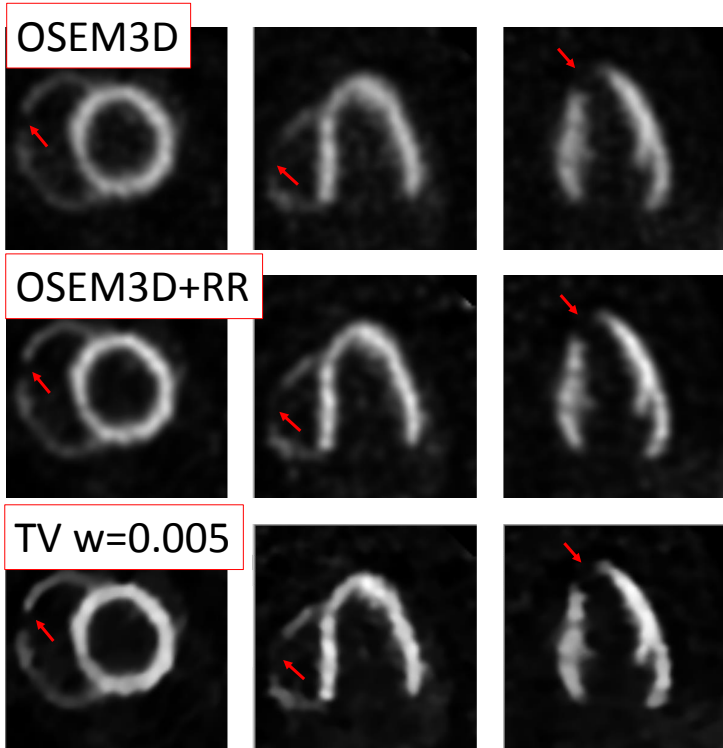


*Figure 4.16: Animal dataset: a proof of concept.* OSEM3D, OSEM3D+RR and TV reconstructions were retroactively performed on a measured animal dataset, after motion correction is applied. Both lesions are more clearly identifiable in the TV reconstruction. From left to right: short axis, horizontal and vertical long-axis views.

motion-correction issues, and a fair comparison of the MR-based and CT-based PVC could be performed. In addition, the results obtained in the simulated, worst-case scenario are also representative for the case where the cardiac uptake was limited, or if the PET scan time was further reduced to optimize the clinical workflow or to limit gross patient motion during the scan [157]. We believe that most of the findings of this work would also apply to reconstructed PET datasets with better statistics and/or accurately corrected for motion.

A second point of interest emerges from the analysis of the preparatory results of this study. The correct choice of the prior parameters (weight, amount of edge-preservation, number of neighbours considered) is the first, fundamental task that needs to be performed before any reconstruction-based PVC. Despite cumbersome (multiple trial reconstructions are needed, in order to find the best parameters to be used), this step is crucial for obtaining images that represent an acceptable compromise between intensity bias and noise suppression – and, most importantly, that are clinically acceptable.

Once the optimal parameters for reconstruction have been found, PVC of doubly-gated cardiac PET images with anatomical information is a delicate task that requires careful evaluation. The use of anatomical information that does not highlight

scar tissue (e.g. HRCT or MR reconstructions where the lesion-to-LV contrast is absent) is not worth the effort and the extra radiation burden for the patient, particularly for lesion detection. If its alignment to the PET dataset was perfect, it would effectively suppress noise and make transmural lesions clearer, provided that the weight of the prior information was not too strong and the appropriate number of neighbours was chosen for the reconstruction. The visibility of the non-transmural lesions would be only marginally improved. If only anatomical information that does *not* highlight the scars can be made available, the improvement in lesion contrast and recovery would be so marginal that its acquisition would not be worth the effort. A non-anatomical, edge-preserving prior applied during reconstruction would be the best alternative.

If the anatomical image does differentiate between normal and scar tissue (e.g. via a properly chosen MR sequence), then its use is advisable for both absolute quantification and improved lesion detectability. However, it is of extreme importance to accurately align ( $\leq 2$  mm mismatch) the anatomical and activity images before proceeding with PVC. If such alignment is not fully achieved, the risk of artefacts in the reconstructions is high and might compromise the diagnostic accuracy. The anisotropic resolution of the anatomical information decreases the performances of the MR-based PVC, particularly if the structures of interest are below the spatial resolution of the anatomical information. However, the anisotropy of the MR does not seem to represent a bottleneck for PVC with anatomical information, as long as a correct alignment is achieved.

The analysis of the polar plots suggests that any of the evaluated MAP algorithms would produce a fairly good preservation of lesion-to-normal tissue contrast. The use of misaligned or shifted anatomical information is not harmful if polar maps are used, particularly if the mismatches are reasonably small. In fact, even if the absolute quantification of the segments might be affected by the use of the wrong anatomy, the contrast between the lesioned segments and the normal segments is not degraded. Therefore, for the sole purpose of identification of segments with lesions in the Bull's eye plots of the LV, the use of any of these MAP algorithms would be acceptable but the anatomical information would not introduce any significant improvement in lesion detection. The polar maps also confirm what was previously noticed in the reconstructed images. If the anatomical information is used, the absolute quantification of all the segments improves when compared to all other algorithms. However, to achieve such improvements, the anatomical image (MR) needs to be perfectly aligned to the PET dataset. In case the alignment is disrupted, the performances of the anatomy-based reconstructions are comparable to those of the reconstructions simply enhanced with an edge-preserving prior.

This simulation study analyses the effects of a badly aligned anatomical image relative to the PET dataset for the purpose of PVC of lesions in PET cardiac datasets. A few limitations of this study come from the ideal-case scenario we are currently considering. First of all, we utilize a single cardiac and respiratory PET gate, assuming that a perfect motion correction of the PET dataset is performed. We believe that this is the best way to clearly assess the effect of the different partial volume correction techniques, without confounding the effect of the motion blur with the partial volume effect. This said, we acknowledge that the breathing and beating motion are a tangible and cumbersome issue when cardiac datasets are of

interest, and that in the current clinical practice there is often no time nor means to perform a fully dual-gated PET reconstruction. For this reason, we performed an additional simulation study where we purposely did not correct for the respiratory motion (i.e. only ECG-gating is performed, which can be easily done in clinical practice) and we just applied the PVC techniques on such datasets. With this additional study, we demonstrated that the heart motions (both due to breathing and beating) need to be corrected for in order for PVC to successfully take place. The optimal compensation of one of the two motions would improve the noise properties of the resulting reconstructions, in all cases. However, a further improvement in lesion visibility can always be observed when the prior information is used. In addition, even in the best case-scenario where dual gating can be performed, sometimes a perfect motion correction simply cannot be achieved. This can be due to delays or imperfections in the insertion of the triggers in the PET dataset, or to gross patient motion that can occur during the scan and is not corrected for, or to the violated assumption of correlation between the external motion tracked by the external tracking devices (e.g. respiratory belts) and the internal motion of the heart, or to the unpredictable motion pattern of a real, patient heart (e.g. deformations occurring during the breathing), or to the too simplistic gating method used for motion correction. In all these non-ideal situations, the gating process can only be correct to a certain extent. If the heart does not behave as modelled by the gating software, part of the activity will be misplaced, and any of the PVC techniques presented would simply smooth over activity regions regardless of how well motion correction was performed.

We believe that the PVC should to be performed only when motion, randoms, scatter and attenuation correction are performed in the most accurate possible way. If this was not the case, the activity distribution before PVC would not be correct in the first place, hence any PVC technique would obviously not improve our knowledge on the actual, underlying activity distribution (on the contrary, it would even possibly emphasize areas of wrongly placed activity).

In this regard, it is important to discuss the need for randoms and scatter correction. Both corrections are necessary for a correct and artefact-free estimation of the myocardial distribution of activity. In our case, we simplify the scenario by assuming the absence of randoms and scatter from our simulated datasets. The results here presented would change, in the direction of a worsening of the image bias, if these corrections were not correctly applied. An analysis of the effects of a wrong randoms and scatter correction was out of the scope of this study. It is also necessary to underline that this study uses a perfectly matching attenuation image to correct for attenuation during the PET measurement. In a previous study [144], we proved that the use of a mismatched attenuation image can affect the subsequent PVC of the PET dataset with anatomical information in two ways. Firstly, the use of a mismatched attenuation correction can create fake, hypo-active areas in the LV depending on the direction and the amount of the displacement of the AC CT relative to the PET dataset. This could result by itself in errors in the quantification of the (lesions in the) LV. In addition, the correction of the PET dataset with a mismatched attenuation image can mislead the registration of the anatomical image for PVC to the activity image. This, in turn, would result in wrong PVC (as in one of our simulated cases where the anatomy is mismatched relative to the activity image). Therefore, the results presented in this work have to be considered as the

best-case scenario, where the attenuation map used does not hamper the registration nor the quantification and image quality.

Investigating ways to improve the alignment between the PET and the anatomical dataset was out of the scope of this work. In the cases where the PET and the anatomical images are slightly misaligned, a registration of the anatomical information to the PET datasets might mitigate the issue, but the registration process is not straightforward. Rigid-registration algorithms normally have an accuracy of 3-4 mm if inter-modality registration is performed [69]. However, we here observed that these mismatch values are not acceptable if the PET dataset needs to be reconstructed with anatomical information. The use of non-rigid registration to correct for small deformations, despite appealing, appears difficult due to the often high level of noise in the PET dataset. One possible solution would be to correct the PET dataset with an edge-preserving prior first, then align it to the anatomical information image of choice and, once a correct alignment is achieved, proceed with a new reconstruction of the PET dataset with the help of anatomical information. We briefly investigated this alternative, but the first results obtained did not represent an improvement to the reconstructions with the original misalignment (not shown). A more in-depth investigation will be needed, to find the optimal registration algorithm and parameters that could lead to a more encouraging result in this direction.

Finally, we would like to conclude with a comment on the feasibility of the acquisition of gated anatomical information of sufficient quality for PVC. As for the acquisition of an HRCT, while hybrid PET/CT devices do not have the necessary resolution for obtaining CT images for PVC, dedicated CT scanners with high spatial and temporal resolution are nowadays part of the clinical practice. With these scanners, it is possible to obtain a 'frozen' image of the heart in a specific cardiac and respiratory phase, with a very low radiation burden for the patient [65]. When the patient requirements asked by the developers of such scanners are met (e.g. the heartbeat of the patient has to be below 70 bpm for optimal image quality), the images obtained with these dedicated CT devices are suited for PVC of healthy (non-lesioned) cardiac tissue. However, the usage of separate or dedicated HRCT scanners for the acquisition of anatomical images for cardiac PVC seems impractical for several reasons. Firstly, in a HRCT, the lesions are not well visible, thus limiting the applicability of the PVC method using HRCT to a better recovery of healthy tissue. Secondly, the fact of moving the patient from one scanner (the PET/CT) to the other (HRCT) for the acquisition of the anatomical information could increase the chances of small motions and deformations of the heart between the two scans, which would in turn increase the chances of incorrect PVC. This would be an issue both for the use of a dedicated HRCT and MR scanner. Additionally, for what dedicated MRI scanners are concerned, the acquisition of images with sufficient temporal and spatial resolution for PVC would be problematic, due to the limited allocated time for such scans. For all these reasons, great interest goes in the recent development of integrated, truly simultaneous PET/MR devices, which we believe could foster the application of anatomy-based PVC techniques in the clinical practice. The use of these scanners would allow the acquisition of an MR image of sufficient resolution, as its acquisition could be performed simultaneously with the PET scan (and, therefore, last at least several minutes). Moreover, the problem of moving the patient from one scanner to the other (or, even worse, to scan the

patient on two different days, for the PET and the MR scan separately) would be fully avoided. Navigators, self-navigated methods and acceleration methods for obtaining MR images with a good temporal resolution, accurately corrected for the periodic cardiac motion and with less motion artefacts (e.g. ghosting) are successfully being used nowadays and are under continuous improvement [158, 159]. We believe that the ongoing research in the field of simultaneous PET/MR (which includes solving the problem of attenuation correction of the PET datasets, using only the MR or the PET information [160]) would not only be useful for improved diagnosis, but it could be the only clinically feasible way to apply anatomy-based PVC on cardiac (and potentially other non-brain) PET datasets.

## V CONCLUSIONS

The aim of this work was to assess the performances of edge-preserving priors for the purpose of lesion detection in cardiac  $^{18}\text{F}$ -FDG PET, in comparison with anatomy-based priors. We also aimed at highlighting the possible risks of anatomy-based PVC on lesion detection and quantification, which occur when the anatomical image is mismatched or shifted when compared to the corresponding PET dataset, and at comparing MR-based and CT-based PVC on lesion quantification.

This study concludes that, as far as lesions are concerned, the use of anatomical information in the form of HRCT is not worth the acquisition and use, as it only marginally improves the noise properties of the images at the price of reduced contrast recovery of the lesions and of an increased radiation burden for the patient. The quantitative evaluations (bull's eye plots, CRC, RC, profiles) show that its performances are equal or inferior to a well-tuned edge-preserving prior. If an MR image acquired with a sequence that well differentiates between the various tissue types is available, and its alignment to a previously reconstructed PET image is optimal ( $\leq 2$  mm), the recovery and visibility of the lesions does improve when a new, anatomy-based PET reconstruction using such well-aligned anatomical information is performed. However, great care needs to be taken in choosing the correct set of parameters for reconstruction and in verifying the correct alignment of the two datasets. If the correct alignment between the anatomical and the PET dataset is in doubt and cannot be otherwise improved, it is recommended to proceed with a non-anatomical prior (e.g. TV) applied during reconstruction. This is also recommended when only the bull's eye plots are of interest.

## COMPETING INTERESTS

The authors declare that they have no competing interests.

## AUTHOR'S CONTRIBUTIONS

AT was responsible for the study design, the simulation setup, the reconstructions and the data analysis, and drafted the manuscript. JN and KV assisted with anal-

ysis of data, helped with the study design, and carefully revised the manuscript. JUV, PC, JD and OG participated in the study design and critically revised the manuscript. All authors read and approved the final manuscript.

## **ACKNOWLEDGEMENTS**

Anna Turco is a PhD fellow of the Research Foundation - Flanders (FWO). Olivier Gheysens and Jens-Uwe Voigt are senior clinical investigators of the Research Foundation - Flanders. Kathleen Vunckx is a post-doctoral researcher of the Research Foundation - Flanders.

The authors wish to thank F. Rega for developing the animal model.

## **FUNDING**

This work is supported by KU Leuven grant OT/12/084 and the Research Foundation - Flanders (FWO)

# **5 PARTIAL VOLUME AND MOTION CORRECTION IN CARDIAC PET: FIRST RESULTS FROM AN *IN* VS *EX VIVO* COMPARISON USING ANIMAL DATASETS.**

*Manuscript in preparation.*

## ***Abstract***

In a previous study on *ex vivo*, static cardiac datasets, we investigated the benefits of performing partial volume correction (PVC) in cardiac  $^{18}\text{F}$ -FDG PET datasets using either anatomical or non-anatomical prior information during reconstruction.

In this study, we aim at extending the findings obtained from the *ex vivo* study by applying the previously selected, non-anatomical PVC technique to *in vivo* cardiac datasets either uncorrected (static) or corrected for the cardiac and respiratory motion. The objective of this study is to highlight differences in the absolute or relative quantification between the static and the motion-corrected *in vivo* reconstructions, by comparing them to the ground truth data provided by a corresponding *ex vivo* dataset. *Ex vivo* scans of the excised sheep hearts were performed on a small-animal PET scanner (Siemens Focus 220, microPET) to provide such high-resolution reference data unaffected by respiratory and cardiac motion.

The results of this study show a different activity pattern between the *ex vivo* and the *in vivo* datasets, hence making it hard to accurately correlate their relative tracer uptake. The additional increase of FDG uptake between the *in vivo* and the reference scans hampers a purely absolute correlation of the tracer uptake between the *ex* and the *in vivo* datasets. We provide a possible explanation for and take into account such increase of activity by analyzing the dynamic left-ventricular total uptake. Afterwards, a comparison of the absolute activity concentrations of the *in vivo* and *ex vivo* reconstructions is attempted.

Despite providing a first indication on the usefulness of motion-correction for absolute quantification, further experiments and improved

motion correction algorithms are needed to strengthen the conclusions drawn here and to guarantee their transferability to human studies.

## I INTRODUCTION

The characterization of cardiac pathologies by means of positron emission tomography (PET) is progressively increasing [14]. In recent years, it has been hypothesized that hemodynamic or mechanical indicators of the cardiac workload collected from a patient (e.g. pressure or echocardiographic measurements) can be correlated to specific uptake patterns identifiable by means of  $^{18}\text{F}$ -FDG PET [11]. If such correlation was proven, PET images could have the potential to offer, in a non-invasive fashion, parameters useful to improve the assessment of the progression and the severity of cardiac pathologies, or to better predict the responsiveness of patients to the planned therapeutical programme (e.g. cardiac resynchronization therapy).

Regional differences in myocardial FDG uptake have been observed in the past [19]. However, the inhomogeneous regional wall thickness in remodelled hearts might cause a different apparent uptake within the reconstructed heart images due to the limited spatial resolution of the PET system. In addition to the blurring introduced by the spatial resolution of the PET scanner, the motion of the heart which occurs during the entire PET examination, due to the heartbeat and to the breathing motion to which the heart is indirectly subject, introduces further blurring in the final image and causes additional uncertainty on the estimated tracer distribution.

In a recent study [161], we investigated the usefulness of partial volume correction (PVC) techniques during reconstruction of cardiac datasets in a simplified scenario where no motion affected the datasets. While the addition of anatomical side information for the reconstruction of cardiac datasets did not appear to be essential neither for the absolute nor for the relative quantification of the tracer uptake in the left ventricle (LV), other techniques (edge-preserving priors) which do not make use of additional anatomical information were shown to be effective in improving the noise characteristics of the reconstructed PET datasets, while dealing with the artefacts that occur when modelling the resolution during reconstruction.

Additionally, several studies have highlighted the necessity of motion correction techniques for the improved reconstruction of cardiac datasets [162, 163]. However, the comparison of the obtained, motion-corrected datasets against a ground truth has not been performed yet. All previous studies perform a comparison between motion-corrected and static reconstructions, based on the changes in indicators such as wall thickness, ejection fraction or cavity volume [81, 164]. Additionally, we explore the combination of motion-correction and of partial volume correction techniques for the reconstruction of cardiac datasets acquired on a clinical PET/CT scanner.

The aim of this work is to utilise the available *in* and *ex vivo* animal datasets to investigate the optimal motion correction and reconstruction workflow for cardiac PET studies.

## II METHODS

Thirteen Swifter x Charolais cross-breed female sheep with body weight  $38 \pm 3$  kg were used for these experiments and subjected to the same pacing and imaging procedure. Each animal had a pacemaker implanted, which was set to pace the heart at 180 beats per minute during 8 weeks to achieve dilated asymmetric cardiomyopathy [128]. At 8 weeks, the remodelling of the heart reached a plateau and the imaging protocol was started. For all imaging procedures and measurements, the pacemaker of the sheep was set to a fixed heart rate of 110 beats per minute and the animals were anaesthetised with isoflurane and mechanically ventilated with an endotracheal tube.

### ACQUISITION OF THE ANIMAL DATASETS

Each of the animals went through euglycemic-hyperinsulinemic clamping to maximize glucose uptake in the heart [28]. Once steady-state was achieved, each sheep was injected with  $^{18}\text{F}$ -FDG and a PET scan of 30 minutes was performed (*in vivo* scan) 30 minutes post-injection on a clinical PET/CT scanner (Siemens Biograph 16, Hirez). The mean activity at the beginning of the *in vivo* scans was 310,5 (range: 109-477) MBq. During this scan, the respiratory and cardiac motion of the animals were recorded with an Anzai AZ773V respiratory belt and an ECG tracking device, to later enable motion correction of the *in vivo* datasets. An attenuation correction (AC) CT was acquired in a fixed cardiac and respiratory phase. This was achieved by disconnecting the endotracheal tube for the duration of the AC CT and by retrospectively gating the acquired CT for cardiac motion. Another AC CT was obtained in a fixed respiratory phase, using the same procedure as above, and no cardiac gating. After the scan, each sheep was sacrificed under isoflurane anaesthesia with intravenous 160 mg/kg pentobarbital and 50 ml of saturated KCl. The mean time elapsed between the end of the *in vivo* scan and the sacrifice, calculated on 8 sheep datasets for which the approximate sacrifice time was available, was 21 minutes (min:15/max:32 minutes). The heart of each sheep was explanted immediately after sacrifice. Each heart was filled with a low-attenuating, hardening polyurethane foam and subsequently underwent several (*ex vivo*) scans. Once the foam was solid, a 15-minute PET scan on a small-animal PET scanner (Siemens Focus220 microPET) was performed, followed by a 20-minutes PET scan of the same heart on the clinical PET/CT Hirez scanner. A high-dose, high-resolution (HR)CT was also acquired on the clinical PET/CT scanner for each of the *ex vivo* hearts. It was used both for attenuation correction (AC) and as anatomical information for both the microPET and the Hirez *ex vivo* datasets.

### MOTION CORRECTION OF THE IN VIVO DATASETS

The acquired *in vivo* animal PET datasets were corrected for motion using a phase-based gating approach [165]. This approach was chosen to be consistent with the algorithm used by the scanner. Additionally, for the kind of datasets available (very regular beating and breathing rate and amplitudes, due to the mechanical ventilation and the pacing imposed to each animal), phase-based gating represents

a straightforward yet reliable way to correct for both the beating and breathing motion. The datasets were either not corrected for motion (*static* datasets), or corrected for both cardiac and respiratory motion (*dual-gated*). In the latter case, the dataset was split into 5 respiratory and 10 cardiac gates. The gating was performed using in-house software which produced as output small list-mode files, each of which contained the events collected in one particular cardiac and respiratory phase. Each list-mode file was rebinned into a sinogram which was then used for further reconstruction. Due to the very low counts obtained after dual-gating of the *in vivo* datasets, two of the sheep datasets were not considered for the subsequent analysis.

## RECONSTRUCTION OF THE DATASETS

### *EX VIVO, GROUND-TRUTH DATASETS*

Given that the purpose of this study was to investigate correction methods against a ground-truth dataset, reconstructions of the microPET *ex vivo* hearts were performed. A maximum-a-posteriori (MAP) algorithm which combined resolution modelling and the aligned HRCT as anatomical information (Bowsher prior in its asymmetrical formulation [62]) was used. A weight (w) of 50 and 9 neighbours (n) out of an 18-voxels spherical neighbourhood were used for the Bowsher reconstruction of the microPET dataset, as they resulted in the best performances (minimization of the bias and the noise) when compared to a simulated ground truth (not shown). Attenuation correction of the *ex vivo* dataset was also performed using the HRCT, duly converted to 511 keV attenuation values before usage. The initial voxel size of the microPET reconstructions was  $0.4745^2 \times 0.796 \text{ mm}^3$ , subsequently resampled to match the voxel size of the Hirez reconstructions ( $1.35 \times 1.35 \times 1.35 \text{ mm}^3$ ).

### GATED AND STATIC *IN VIVO* RECONSTRUCTIONS

The algorithms that were used to reconstruct the **dual-gated** activity sinograms were chosen based on our previous study on PVC of the *ex vivo* datasets:

- a 3D OSEM algorithm with resolution recovery (OSEM3D+RR), with and without Gaussian post-smoothing, was chosen to corroborate the findings of the *ex vivo* study which indicated the necessity of further PVC for accurate absolute quantification of the tracer uptake. As in the previous work, resolution recovery was achieved by modelling the resolution of the camera with a Gaussian smoothing kernel, applied in the sinogram space, whose full-width at half-maximum (FWHM) corresponds to the scanner's spatial resolution. Where Gaussian post-smoothing was performed, we used a spatially-invariant Gaussian kernel with FWHM = 5 mm in the three directions.
- a MAP algorithm using an edge-preserving prior (TV [57]) applied during reconstruction was used as a way to regularize the reconstructions and produce a more reliable representation of the activity distribution. In fact, the TV prior proved effective in mitigating the Gibbs artefacts and the noise that affect the reconstructions with RR. The TV reconstructions were performed

using  $\beta = 0.005$  as weight of the prior. This value was chosen based on a previous optimisation study, where it proved to produce clinically acceptable images with improved noise properties [139]. Additionally, we verified that such choice yielded visually acceptable reconstructions also for the current datasets.

In-house developed software was used to perform reconstruction of all the dual-gated datasets with a distance-driven projection method. The voxel size of the reconstructed PET images was set to  $1.35^3 \text{ mm}^3$ . The iteration scheme consisted of 3i42s (i: iterations, s: subsets), followed by 2i24s and 2i1s.

The **static** reconstructions were obtained using in-house developed software which attempted to reproduce as closely as possible a typical clinical reconstruction. A ray-tracing projection method without resolution recovery was used. The voxel size was set to  $2.66 \times 2.66 \times 2 \text{ mm}$  and 4 iterations  $\times$  8 subsets were chosen.

The breath-hold, cardiac-gated CT was used for the attenuation correction of all the aforementioned reconstructions. Scatter and randoms were also modelled during the reconstruction of these datasets, using the scatter and random estimates provided by third-party software (e7-tools, Siemens, Knoxville).

## DYNAMIC *IN VIVO* RECONSTRUCTIONS

Our study analyses  $^{18}\text{F}$ -FDG PET reconstructions obtained from datasets acquired either 30 minutes post-injection (*in vivo* datasets) or after the sacrifice of the animal (*ex vivo* datasets), which in turn occurred about 1.5 hours after tracer injection. Previous studies have documented a steady increase of FDG tracer uptake in the LV up to 3 hours after patient injection [166]. Hence, we verified whether the datasets used in this study were affected by such dynamic increase and we proposed a method to scale the microPET activity accordingly.

Dynamic reconstructions of the available *in vivo* datasets were performed to this end. The original, ungated listmode was divided into 6 frames of equal length (5 minutes/frame), which were individually reconstructed using a distance-driven projection method, resolution modelling in the sinogram space, the same iteration scheme as for the dual-gated reconstructions and a voxel size of 2 mm in the three directions. Decay correction of each of the dynamic frames was performed to the beginning of the *in vivo* scan.

## IMAGE POST-PROCESSING: POLAR MAPS (OR BULL'S EYE PLOTS)

17-segments polar maps (PMs) or bull's eye plots of the LV were created according to the guidelines of the American Heart Association [167] to evaluate the relative and absolute activity distributions in comparison to the ground truth. The use of polar maps allowed to align the corresponding LV regions of the *in vivo* and *ex vivo* reconstructions without the need for a non-rigid registration between the two datasets. Additionally, polar maps are a commonly used tool to assess the tracer uptake in nuclear medicine studies.

## MAX-COUNT POLAR MAPS

For each of the gated and static reconstructed datasets and for the ground truth, the bull's eye plots were created as described in [168]. The delineation of the LV was automatically performed by in-house software. Max-count polar maps were generated by taking the maximum value over the LV thickness at each radial and longitudinal position, within the automatically-defined endocardial and epicardial contours. A fixed distance of 1.6 cm was imposed between the endocardial and the epicardial contours, to fully encompass the LV wall (thus including, e.g., the entire papillary muscles).

## MEAN-COUNT POLAR MAPS, TOTAL ACTIVITY AND SCALING FACTOR

Additionally, mean-count polar maps were generated for all datasets (gated, static, dynamic, ground-truth) by taking the mean value over the LV thickness at each radial and longitudinal position, within the automatically-defined endocardial and epicardial contours. Corresponding volumetric polar maps were also obtained. The multiplication and subsequent summation of all corresponding voxels of the mean-count polar maps and the volumetric polar maps generated the **total LV activity** for each of the reconstructions. A fixed distance of 1.6 cm was imposed between the endocardial and the epicardial contours, in order to fully encompass the LV while excluding as much as possible the influence of the left-ventricular blood pool and of the right ventricle from the computation of the total activity. Other thicknesses were evaluated to delineate the LV (0.8, 1.2, 2.0 and 2.6 cm), but they were discarded given that they would either exclude parts of LV (if too thin) or include too much of the RV for the subsequent calculation of the polar maps.

The total activity of all 6 dynamic reconstructions was plotted against time, together with the total LV activity computed from the ground-truth dataset and the extrapolated total activity at sacrifice time – in turn obtained by applying a logarithmic fit to the dynamic reconstructions, which we expected would be representative of a biological process such as cardiac LV activity increase. A paired t-test was performed between the extrapolated total activity at sacrifice time and the computed total activity on the microPET reconstructions, to test the efficacy of the logarithmic estimation.

The logarithmic fit is used to extrapolate the LV activity at sacrifice, so that we could compare this value to the microPET value and exclude any increases of activity between the sacrifice and the microPET scan. However, due to the fact that all the *in vivo* datasets (both gated and ungated) contain data spanning over the 30 minutes, they all comprise a portion of the dynamic activity increase (which is not corrected for). Thus, their mean LV activity is always higher than the mean LV activity at the beginning of the scan. As a consequence, the microPET LV activity needs to be scaled to the activity of one of these reconstructions (and not to the beginning of the scan), to be able to compare the absolute values of the microPET with those of the *in vivo* images of interest. A **scaling factor** was therefore computed by dividing the total LV activity of the static reconstruction of the *in vivo* data by the total LV activity of the corresponding microPET reconstruction (*statscale*). The static reconstruction was chosen as a reference in order not to bias the results

towards the dual-gated or partial-volume corrected reconstructions – which are the subject of evaluation.

## DATA ANALYSIS

The max-count polar maps of corresponding *ex vivo* and *in vivo* datasets were compared based on their absolute activity differences and on the relative activity distribution.

For the relative quantification, the mean, volume-weighted activity concentrations of the septal (S, segments 8 and 9) and lateral (L, segments 11 and 12) segments of each polar map were computed, and the S/L ratio within each polar map was calculated as it represents a common measure of regional heterogeneity [169, 170]. Additionally, Bland-Altman plots were computed between the max-count polar maps of the ground truth and all the *in vivo* reconstructions, both normalized to their respective maximum value, and the bias and limits of agreement were reported as in [171]. In so doing, we were able to globally highlight whether the differences in the relative myocardial uptake were relevant or negligible. The analysis of the mean bias per segment, over the entire animal cohort, allowed us to pinpoint if and which (set of) segment(s) was particularly responsible of the observed differences.

For the absolute comparison, the scaling factor (as described in the previous section) was applied to the ground-truth datasets prior to any further comparison. Bland-Altman plots were computed between the max-count polar maps of the so-scaled ground-truth and all the *in vivo* reconstructions, and the bias and limits of agreement were reported. The segments in the Bland-Altman plots were color-coded based on the human vascular regions to which they belong [167], in order to verify whether an increased or decreased bias in any of these regions could be observed.

## III RESULTS

### RELATIVE QUANTIFICATION

As for the relative tracer distribution, the results (Figure 5.1) indicated a similar S/L ratio for all the *in vivo* reconstructions for each sheep, regardless the motion correction applied (green, blue, red bars). The comparison with the S/L ratio extracted from the ground truth datasets (orange bars) highlighted a small but significant ( $p = 0.0004$ ) disagreement.

We attempted to investigate the reasons of such discrepancy further. The observation of the normalised polar maps by means of the Bland-Altman plots shed some light into the location of the differences in the activity distribution between the *in vivo* and the *ex vivo* datasets. The Bland-Altman plots obtained from the normalized max-count polar maps of the dual-gated TV (similar for OSEM3D+RR, thus omitted) and the static reconstructions are on Figure 5.2. We can observe that the differences between the normalized microPET and the normalized *in vivo* polar maps are overall relatively small (less than 20%) and that the bias is in all cases small. The analysis of the bias *per segment* revealed a particularly positive bias for

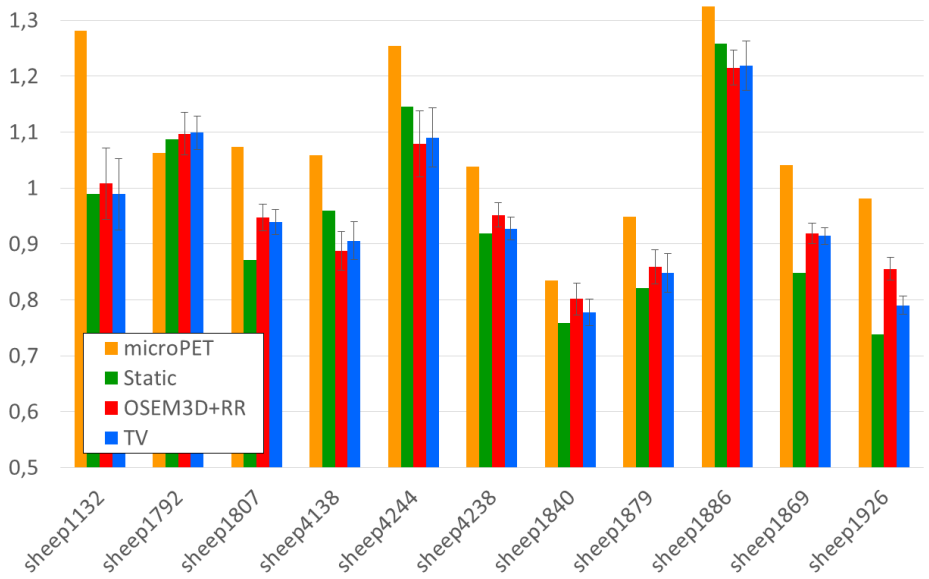


Figure 5.1: Septum-to-lateral ratio for the analysed sheep. The S/L ratio extracted from the ex vivo microPET polar map (orange column) is compared to the S/L ratio computed on the *in vivo* datasets corrected with different motion correction techniques. Max-count polar maps were used in all cases. The error bars represent the standard deviation of the S/L ratios of the dual gated reconstructions over all gates.

the segment 3 (0.219621) and a negative bias for segment 11 (-0.118650), when the static reconstructions are considered. As for the dual-gated TV reconstructions, a particularly positive bias is observed for segments 3 (0.166982) and 9 (0.108928), which could explain why the S/L ratios illustrated in Figure 5.1 show discrepancies. Figure 5.3 visually reports on the mean bias and standard deviation per segment, over the entire animal cohort, and allows us to visualize the aforementioned segments – which are most responsible of the observed differences.

The decreased activity, particularly of the infero-lateral segments, is visible even when visually comparing the ground-truth and the *in vivo* polar maps, as Figure 5.4 shows.

## DYNAMIC LV UPTAKE AND SCALING FACTOR

As for absolute quantification, the reconstruction of the 5-minutes dynamic frames of the *in vivo* PET scan confirmed that an increase of the total activity uptake in the LV was present in our sheep cohort. Each plot of Figure 5.5 shows the activity of the dynamic reconstructions, the extrapolated activity at sacrifice time and the microPET activity for each sheep. The logarithmic fit was optimal for all animals (mean  $R^2 > 0.95$ ). The extrapolated sacrifice value matches well with the calculated total microPET activity (p-value of the paired t-test between the total extrapolated activity at sacrifice and the total microPET activity:  $p = 0.24 \geq 0.05$ ), thus confirming that the dynamic increase was most likely present only during the portion of the experiment where the animal was alive.

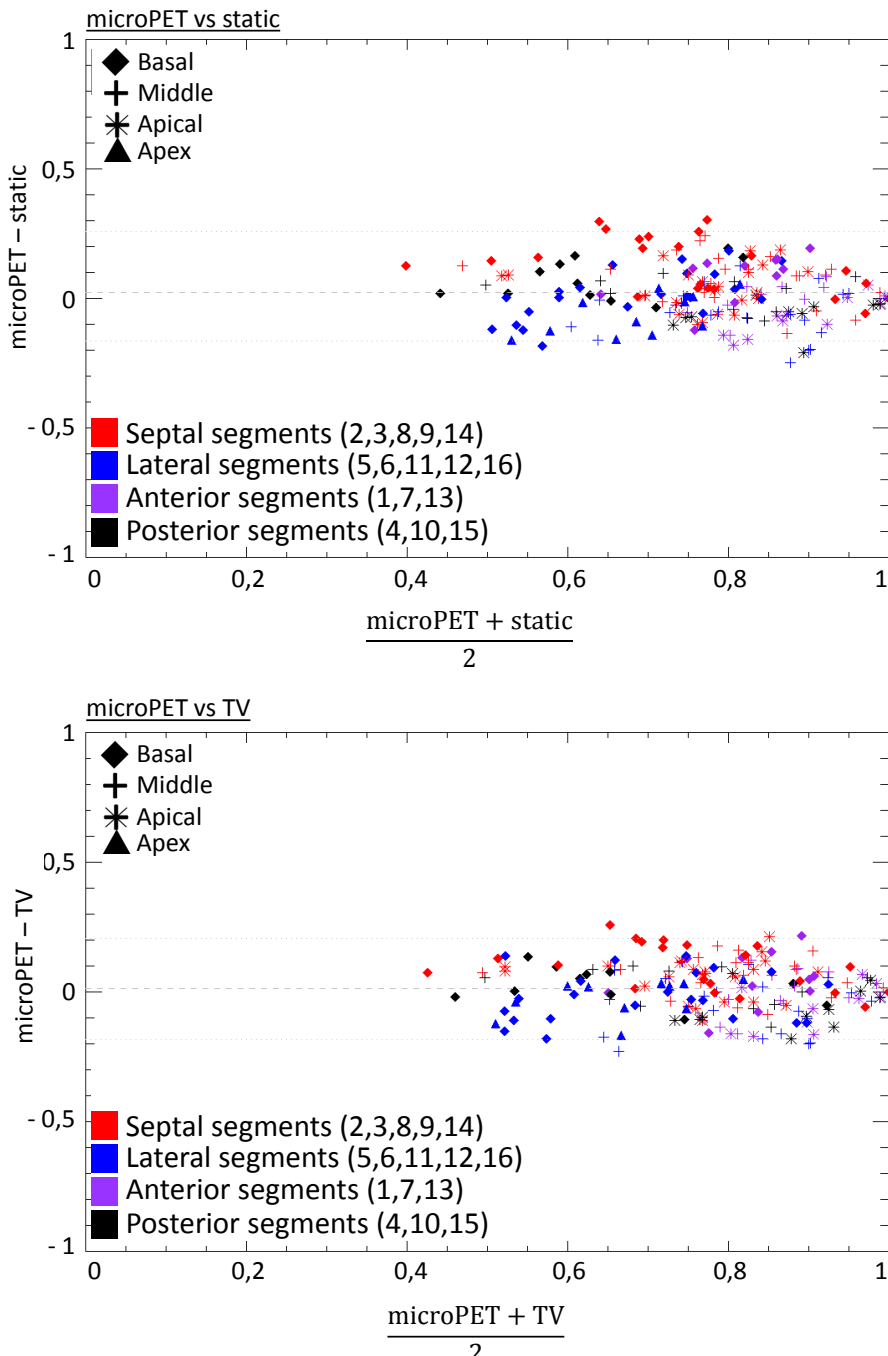
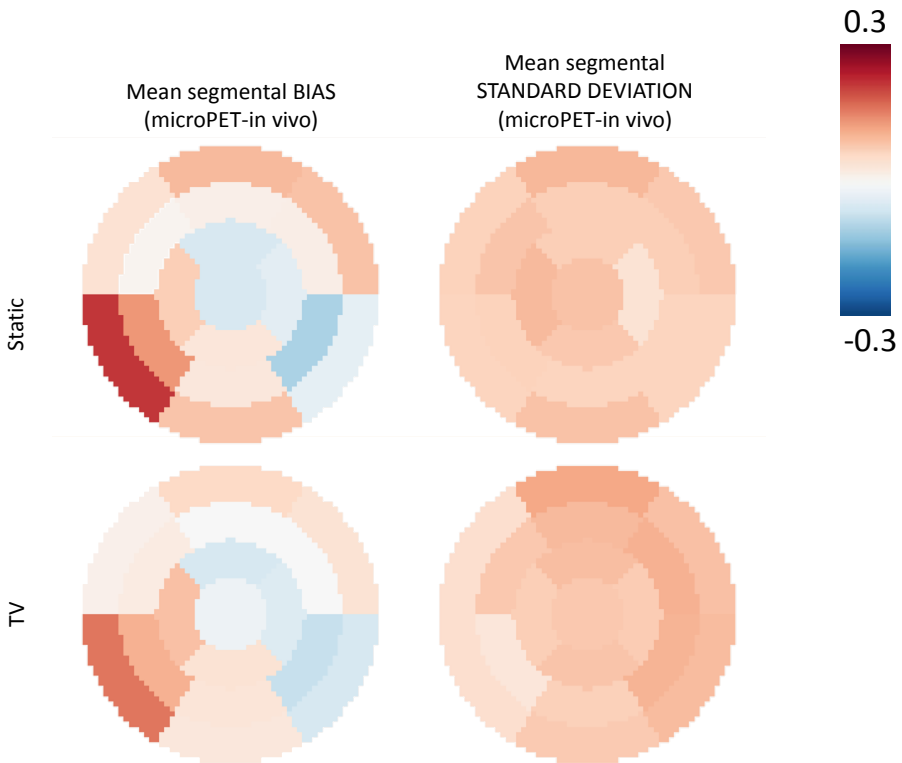


Figure 5.2: Bland-Altman plots for the normalized max-count polar maps. Top pane: TV (dual-gated, end-diastolic gate), bottom pane: static (ungated) reconstructions against the ground truth (microPET). The segments are color-coded based on the quadrant they belong to (septum, lateral, anterior or posterior). Additionally, the segments belonging to the basal, middle, apical and apex rings have each different symbols.



*Figure 5.3: Polar plots visually indicating the mean bias and the mean standard deviation of the differences obtained by subtracting the normalized in vivo reconstructions (top pane: static, bottom pane: TV) from the normalized microPET polar maps. Average values over all animals.*

## ABSOLUTE QUANTIFICATION

The mean *statscale* factor computed over all sheep was 0.84. Using the *statscale* factor (calculated individually for each animal) to scale the microPET down and to account for such dynamic increase, we plotted the Bland-Altman plots for all sheep. In Figure 5.6, the Bland-Altman plots for the dual-gated, TV and OSEM3D+RR reconstructions and the static reconstructions are reported. We can appreciate a decrease in bias when the TV reconstructions are used (1.25 vs 2.7 when static reconstructions are used instead), as well as a narrowing of the limits of agreement (2.7 for TV vs 3.3 for the static reconstructions).

From the same figure, we notice a drop in bias when the OSEM3D+RR reconstructions are considered. This is to be expected, since the such reconstructions are characterized by overshoots of activity which produce an overestimation when compared to the microPET. However, the bias that is obtained is, in absolute value, similar to the one obtained when the TV reconstruction is used instead. This can be attributed to the suboptimal choice of the scaling factor. Figure 5.7 visually shows the reason of this results. If the max-count polar maps are computed for each sheep and for each cardiac gate at end-expiration, and the mean of each of these polar maps is then calculated (similarly to the procedure in [161]), we can observe that

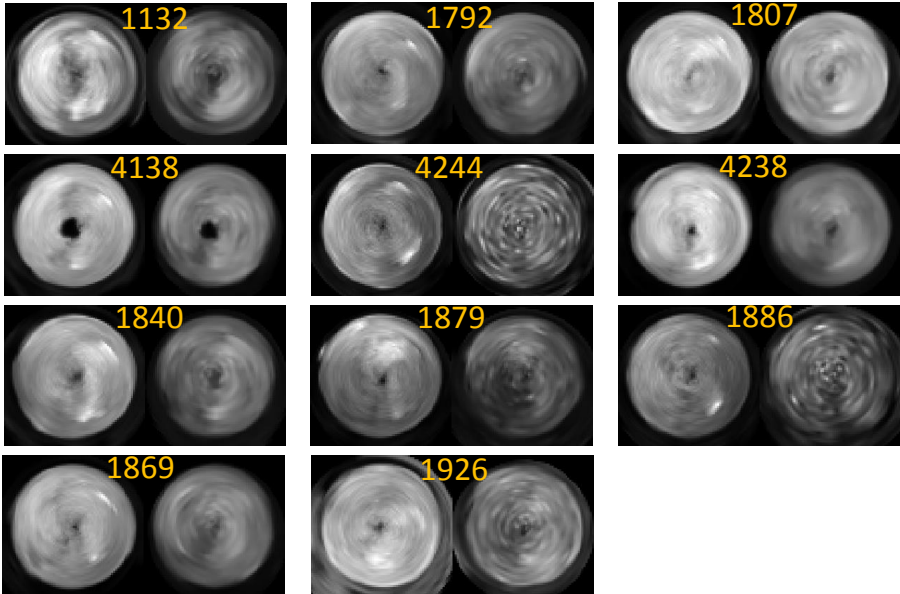


*Figure 5.4:* For each sheep, the max-count polar map of the microPET reconstruction (left side for each pair of images) is visualized next to the max-count polar map of the TV, *in vivo* reconstruction (end-expiration, end-diastolic gate). In several sheep, the decrease in the infero-septal portion is clear when the *in vivo* reconstructions are considered (regardless of the motion correction algorithm that is applied).

the downscaled microPET lies in between the OSEM3D+RR and the TV curves. The red arrows on the same figure indicate which gate has been used for the calculation of the Bland-Altman plots of Figure 5.6, and confirm the obtained bias. Additionally, we can observe that the ranking of the algorithms (OSEM3D+RR is higher than the TV, which is in turn higher than the static reconstruction) is similar to what previously reported on in previous studies [161].

## IV DISCUSSION AND CONCLUSION

The use of the microPET datasets for the accurate quantification of PET images and as ground truth for the validation of PVC and motion correction techniques on cardiac datasets is conceptually interesting but not free from drawbacks.

Firstly, the microPET datasets were scanned about an hour after the end of the *in vivo* scans. A limitation of this study was that the sacrifice was not performed immediately after the scan, but had to be done in a dedicated room at the other side of the hospital. Hence, no scans could be performed during the time between the end of the *in vivo* scans and the sacrifice of the animal, thus making it hard to predict the LV FDG uptake for each animal over time. The reconstruction of the dynamic frames of the acquired *in vivo* datasets were, however, useful for estimating a trend of LV FDG uptake over time. The obtained curves, for each of the analysed animals, corroborated those of a previous study which observed increased LV FDG uptake up to 3 hours after tracer injection [166].

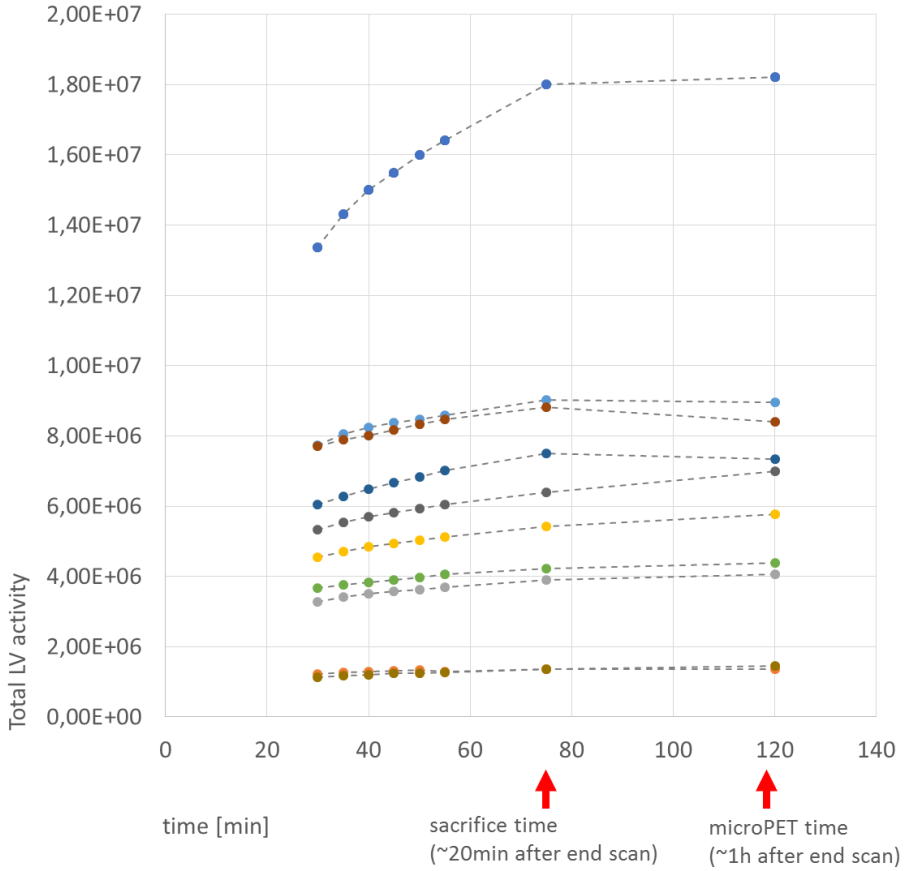


*Figure 5.5: Total LV activity for all sheep datasets (one animal per color). The first 6 time points represent the total LV activity in the polar maps of each dynamic reconstruction of the *in vivo* dataset. The activity at sacrifice is extrapolated based on the logarithmic trendline that fit the dynamic points. The last point is the total LV activity computed from the polar map of the *ex vivo* (microPET) dataset. All reconstructions have been corrected for decay to the beginning of the *in vivo* scan before the computation of the activities.*

A method to correlate the microPET and the *in vivo* absolute values was proposed in this work, which downscaled the total activity of the LV of the microPET reconstructions to match the total reconstructed LV activity of the *in vivo* datasets. We scaled the microPET using the total activity of the static reconstructions, in order not to bias the conclusions towards one of the algorithms we wanted to evaluate. Despite all efforts to calculate the scaling factor in a sensible way, the use of a scaling factor is not ideal when absolute quantification is aimed at, as there is always a risk of under- or over- scaling the ground-truth and therefore biasing all results towards one or the other reconstruction algorithm. For example, a smaller scale factor applied to the microPET datasets could favour the max-count polar maps of the reconstruction algorithms that overestimate the activity concentration (e.g. OSEM3D+RR with associated Gibbs artefacts), while a heavier downscaling of the microPET values would bias the results towards the algorithms that underestimate the activity (e.g. the static reconstruction).

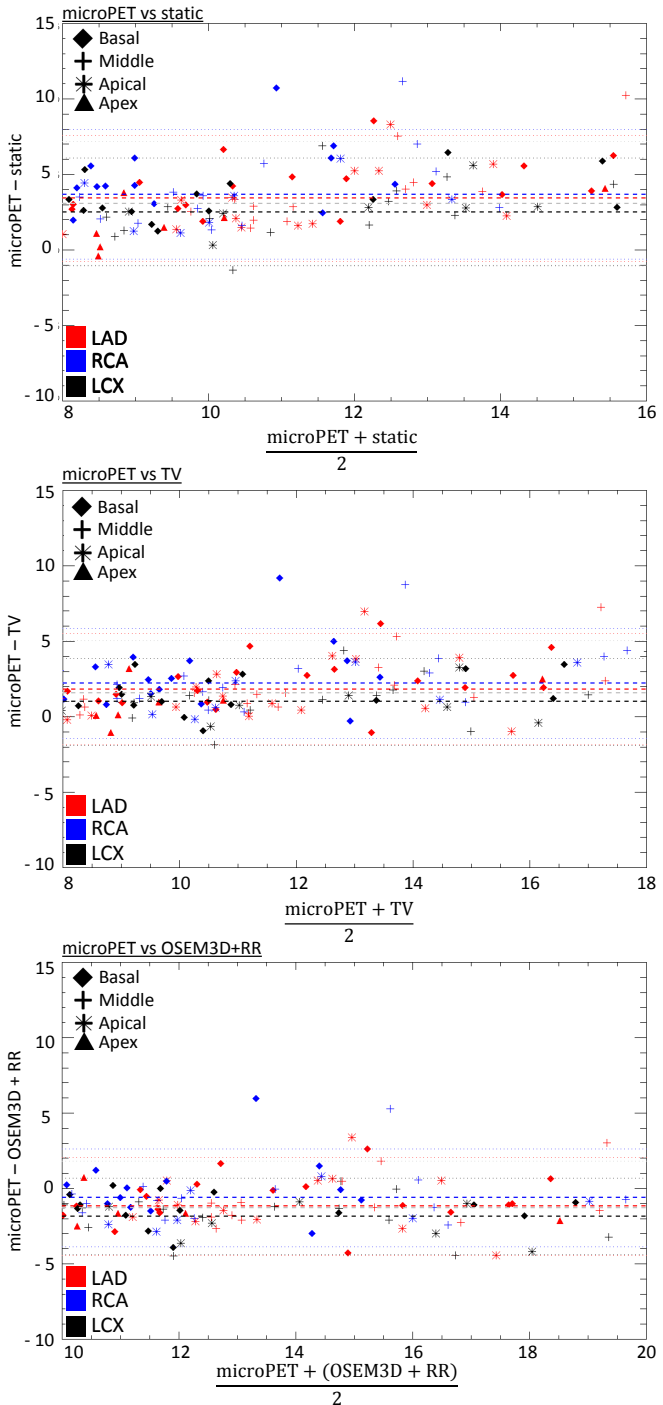


Figure 5.6: Bland-Altman (B-A) plots for the static (ungated), TV(dual-gated, end-diastole) and OSEM3D+RR (dual-gated, end-diastole) reconstructions against the ground truth (microPET). Max-count polar maps were used to calculate the segmental values of both in- and ex-vivo datasets. The microPET was here scaled down using statscale. The segments are color-coded based on the vascular territory they belong to. LAD: left anterior descending artery segments, RCA: right coronary artery segments, LCX:left circumflex artery segments.

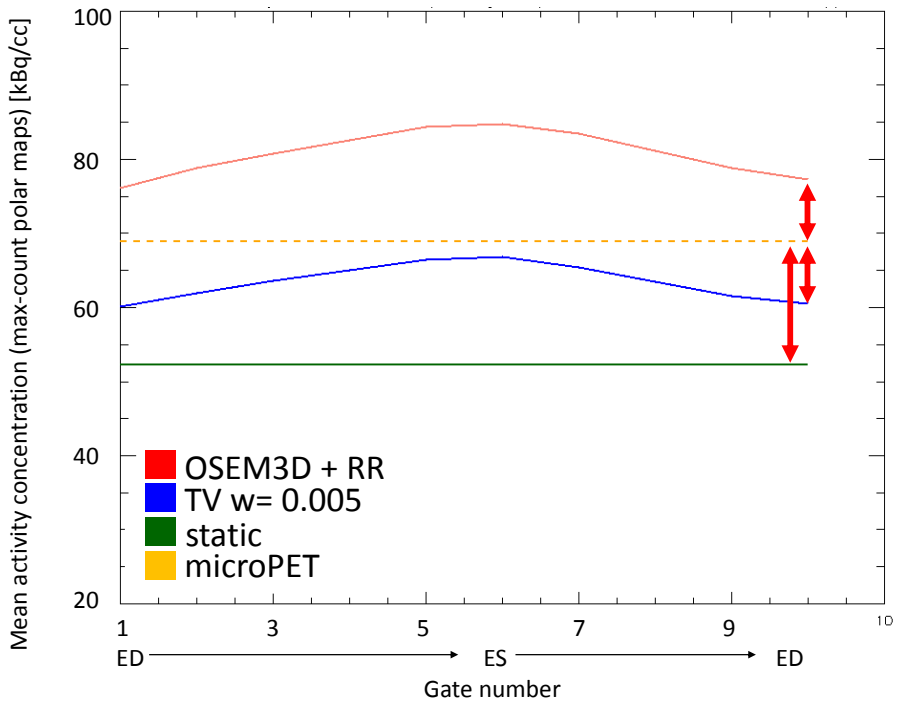


Figure 5.7: The mean activity calculated on the entire max-count polar maps, for all sheep, is plotted in this graph. One mean value per gate is represented. The red arrows are placed in correspondence to the end-diastole gate, based on which the Bland-Altman plots in this work have been computed. The microPET was here downsampled with statscale.

Given the previous limitations, we anyway attempted to correlate the tracer uptake in the motion-corrected and static datasets to the tracer uptake of the scaled *ex vivo* ground truth. While the Bland-Altman plot shows an improvement when motion correction is applied to the datasets, a similar bias (absolute value) is however observed for the TV and the OSEM3D+RR reconstruction – which could indeed make us suspect a suboptimal choice of the scaling factor. However, the graph showing the mean activity computed on the max-count polar maps of the *in vivo* reconstructions shows a ranking that is similar to what was observed in a previous study on *ex vivo* datasets, where the OSEM3D+RR over-estimated the total activity and the TV was the closest to the ground truth [161]. As a consequence, from the sole analysis of such graph and the comparison of the *in vivo* reconstructions, the motion correction of the datasets appears to be beneficial.

We additionally correlated the relative distribution of activity within the LV of the *in vivo* and the *ex vivo* datasets, to assess whether the regional activity distribution (e.g. the S/L ratios) would be affected by the different motion correction techniques. We observed that the use of either reconstruction, both with and without motion correction, did not greatly change the activity distribution within the *in vivo* sheep hearts nor improved the similarity to the ground-truth. This can be explained by the fact that, in the analysed sheep, a similar blurring affected both the septum and the lateral wall due to respiration, and the differences in wall thick-

ness were not so pronounced to determine a stronger blurring on one or the other side of the LV wall due to the partial volume effect. The analysis of the Bland-Altman plots on the normalized polar maps confirmed such visual observation and revealed an overall good similarity of the *in vivo* polar maps to the ground truth. Some segments, in the infero-septal and infero-lateral portion of the LV, revealed however bigger discrepancies in the activity distribution within the LV, when the *in vivo* and the *ex vivo* scans are compared. This could be partially explained by the different shape and size of the *ex vivo* and the *in vivo* datasets, which could affect the reorientation and accurate alignment of the datasets needed prior to the creation of the polar maps. Additionally, the filling of the *ex vivo* hearts with the polyurethane foam might have stretched and possibly modified the relative activity distribution in some of the datasets. Another possible explanation of this change in activity distribution is that the sacrifice of the sheep using KCl determined a sudden and unexpected shift of tracer uptake in the heart. However, none of these hypotheses could be confirmed with the available sheep datasets. Due to this unexpected behaviour, the comparison of the S/L ratios computed from the *ex vivo* and the *in vivo* datasets was affected, and this could also partly justify the differences in absolute quantification observed in this study.

Further experiments, both on animal and on human datasets, would be needed to confirm the results obtained in this work. The animal experiments should feature an additional scan at sacrifice, to be able to clarify whether the total reconstructed activity is indeed following a logarithmic increase and to more accurately estimate a scaling factor for the *ex vivo* datasets. Human experiments would be additionally needed to clarify whether the use of motion correction is as irrelevant as in sheep for relative LV quantification. A comparison of the non-corrected vs the motion-corrected reconstructions of animal and human datasets would be valuable to clarify this point. However, at present, all available human datasets showed a very irregular breathing pattern (acquired via a respiratory tracking system), with baseline drifts and sudden amplitude changes which made it impossible to use to perform accurate motion correction, without having to throw away a significant amount of the data. Improved motion correction techniques should be implemented in the first place, to allow an event-by-event motion correction such that the motion-corrected vs the static reconstructions could be analysed.



## **C DISCUSSION, CONCLUSIONS AND FUTURE PERSPECTIVES**



### **Why $^{18}\text{F-FDG}$ for cardiac PET imaging?**

The use of PET for the diagnosis and follow-up of cardiac diseases is of increasing interest [14], in spite of the conceptual and practical challenges that it presents. One of the first elements that needs to be taken into account is that different cardiac pathologies can alter the underlying substrate utilization, thus making even the choice of the radioactive tracers non trivial.  $^{18}\text{F-FDG}$  has been considered since decades the tracer of choice for assessing hibernating myocardium and ischemia, where a switch to glucose uptake is present and known. In these cases,  $^{18}\text{F-FDG}$  becomes the best way to assess myocardial glucose metabolism and therefore infer energetics. In the past years, the use of  $^{18}\text{F-FDG}$  for the evaluation of other pathologies (in particular non-ischemic cardiomyopathies) has been explored with encouraging results [11, 172, 173]. Additionally, myocardial dysfunction (e.g. non-ischemic dilated cardiomyopathy) can be correlated with a change in metabolism towards the utilization of an increased amount of glucose [174], and early studies on  $^{18}\text{F-FDG}$  uptake in left-bundle branch block (LBBB) demonstrated that  $^{18}\text{F-FDG}$  is a good marker to show changes pre and post CRT [12]. Despite other tracers, e.g.  $^{11}\text{C-acetate}$ , are generally considered a better way to assess myocardial energetics and oxygen consumption, the use of  $^{18}\text{F-FDG}$  – especially in combination with perfusion tracers – might help to shed light and discriminate into the metabolic pathways behind an underlying pathology, thus possibly helping to e.g. understand why CRT fails or succeeds.

In addition to all the aforementioned rationale, and provided that the animals used in this work were induced non-ischemic, LBBB-like cardiac remodeling with a dual-chamber electrical stimulation, other reasons – more connected to our specific experimental setup – led us to select and utilize  $^{18}\text{F-FDG}$  in the course of this work. Firstly, the use of euglycemic-hyperinsulinemic clamping has been proven to enhance myocardial glucose uptake, thus ensuring appropriate tracer uptake in the current experimental conditions and enhanced quality of  $^{18}\text{F-FDG-PET}$  images with a clinically acceptable dose. Additionally, opposite to tracers with a very short half-life and a rapidly changing dynamics,  $^{18}\text{F-FDG}$  allows for the acquisition of a stable frame of sufficient length to successfully apply motion correction techniques and retaining at the same time a sufficient amount of counts. In the context of our animal experiments, where the acquisition of *ex vivo* datasets was also foreseen, using a tracer with a short half-life would not have provided a sufficient amount of counts several hours after tracer injection, while this was easily achieved with  $^{18}\text{F-FDG}$ .

Independent of the animal model and biological question that one wants to address, however, we believe that the techniques developed in this work can be applicable to other tracers, both for perfusion and metabolism, and particularly for those whose half-life is sufficiently long and which reach a stable plateau phase.

For all the aforementioned reasons,  $^{18}\text{F-FDG}$  was chosen as a representative tracer for this work. The indicators extracted from cardiac FDG-PET images could corroborate and emphasize the findings obtained from other techniques (e.g. pressure measurements) and imaging modalities (e.g. echocardiography) [11]. If a correlation between the severity of certain myocardial diseases and the patterns observed in  $^{18}\text{F-FDG-PET}$  was strongly proven, the values extracted from the resulting PET images could be eventually used as indicators of myocardial workload. However, at

present, the limited spatial resolution of the PET system, together with the motion that inevitably occurs during any cardiac PET examination, raises questions on the quantitative accuracy of PET images for this purpose.

### ***Challenges in myocardial $^{18}\text{F-FDG}$ PET***

In this project, partial volume correction performed during reconstruction was evaluated as a means to guarantee exact quantification and regional distribution of the left ventricular uptake, in combination with motion correction techniques. In the past decade, several algorithms have been presented for the enhanced reconstruction of PET datasets, among which some that made use of additional anatomical information during reconstruction [54, 61, 96]. In those works, the use of prior information had shown extremely promising results in brain, thus leading us to explore its applicability to other anatomical districts. The objective of this work was the assessment and comparison of such advanced image reconstruction techniques (with and without the additional use of side anatomical information) in simulated and animal studies, in order to pinpoint the algorithm that produces the most accurate relative and absolute quantification of regional activity in cardiac PET images.

Behind the partial volume correction of cardiac PET datasets, the simultaneous consideration of several additional aspects is needed to produce sensible results. Attention to the attenuation correction, image alignment and motion correction is also of primary importance, if quantitatively informative images are aimed at.

Additionally, the evaluation of the improvements introduced by novel reconstruction and motion-correction techniques against a measured, realistic ground truth dataset was so far unexplored, as most of the previous studies investigated the introduced benefits by evaluating, e.g., the reduction in calculated wall thickness or ejection fraction in comparison to phantoms or un-gated patient studies (e.g. [81, 164]).

In this work we answer some of the questions that are raised when partial volume correction of cardiac PET datasets is aimed at.

### ***Attenuation correction***

The problem of attenuation correction of cardiac datasets has already been explored previously in literature. In particular, several studies have analysed the best way to correct a *motion-blurred* PET, in order to avoid artefacts due to the different temporal resolution of the PET and the CT dataset for AC [38–40]. To our knowledge however, the opposite issue (i.e. how to best correct a *motion-corrected* PET for attenuation) had not been thoroughly investigated so far, even though it is of fundamental importance for accurate myocardial quantification.

We explored the role of attenuation correction for gated myocardial PET images, not only for the optimal left-ventricular quantification but also to avoid the introduction of attenuation-derived artefacts in the final PET reconstruction (Chapter 1). This, in turn, could hamper the registration of the anatomical image to the PET datasets for subsequent partial volume correction. We observed that the use of an attenuation map that is acquired in a different *cardiac* phase (but in the same, fixed respiratory position) with respect to the PET gate produced acceptable results and is practically achievable in a clinical setting. Conversely, the use of an attenuation map that is mismatched with respect to the *respiratory* phase of the PET is not recommended, as it can generate artefactual hypo-perfused areas in the heart as well as other artefacts that might hamper a subsequent image registration. This

can happen, for example, if the patient inspires too much when requested to hold his/her breath, or when the attenuation map is acquired at end-inspiration but the reconstructed PET phase is at end-expiration, to maximise the amount of counts used for that reconstruction (e.g. when optimal gating strategies are considered).

The definition of the optimal attenuation correction strategy for dual-gated studies was helpful in the refinement of the protocol used for the acquisition of the subsequently measured animal datasets.

### ***Finding the optimal reconstruction***

Chapter 3 describes the validation of the partial volume correction techniques against the ground truth image produced by the microPET scans, using the *ex vivo* datasets. As mentioned earlier, the study aimed at assessing the possible benefits of partial volume correction techniques, with or without the use of side anatomical information, in the simplified case where no motion affects the measurements. The results of this study showed that the relative distribution of activity remained unchanged within the left ventricle of the available datasets, no matter the reconstruction algorithm that is used. However, the comparison of the absolute distributions of the tracer uptake showed the superiority of the regularised (either with anatomy-based or with non-anatomical priors) reconstructions against the standard reconstruction algorithms, both in terms of overall recovery of absolute values and in terms of stability against the way to construct the polar maps. Although the use of anatomical priors did not yield added value for left ventricle quantification, it did result in a better rendering of the smallest features in a PET image, such as the right ventricle. The study in Chapter 3 gives a first indication on the potential role of the anatomical side information for this purpose.

It is worth mentioning that in this chapter, as well as in several others, a regional comparison using polar maps is performed instead of a voxel-wise comparison of the available reconstructions. Surely, a voxel-wise comparison would be possibly the best and most precise way to compare two datasets. However, the benefit of a very accurate voxel-wise quantification would not be reflected into a comparable practical benefit in the clinical routine, at least in the first instance. Firstly, a reconstruction-based comparison would be beneficial only for the assessment of absolute quantification of activity, as for relative quantification it is difficult to pinpoint reproducible landmarks which delineate e.g. the septum and the lateral wall. Secondly, a registration is involved in all comparison, thus questioning the exactness of the voxel-wise comparison. Thirdly, most of the nuclear medicine applications for cardiac imaging – including the ones that were aimed at in the broader scope of our experiments (i.e. correlating metabolic parameters to myocardial workload) – rely on a region-based analysis. The polar maps are the most common tool to assess regional metabolic variability, to compare it to myocardial perfusion maps and to put it in relationship with other mechanical indicators (e.g. pressure-volume area values as a measure of myocardial workload). To additionally ensure consistency with previous literature and to verify whether we could obtain comparable results, we decided to use polar maps in most of this work.

In Chapter 4 we sought to explore, in parallel, the usefulness of prior information for the recovery of myocardial lesions. In fact, together with the assessment of regional inhomogeneities in left ventricular uptake, the accurate knowledge of the extent and residual activity of an ischemic area can be of interest to nuclear cardi-

ologists. We decided to perform a simulation study instead of utilizing the available *in vivo* datasets, as the use of simulations allows a better control over the generated motions and mismatches. Additionally, an animal model with (non-transmural) lesions was not available at the time the study was performed, but the effects of PVC on this kind of datasets was also of interest for future applications. Finally, the use of simulations guaranteed that the amount of activity that should be expected is homogeneous and constant in well-specified myocardial regions. This simulation study on the lesion quantification was combined with an analysis of the effects of misalignment between the anatomical image and the PET image. The results of this study highlight the deleterious effects of using side anatomical information that is misaligned of more than 2 mm with respect to the PET image, and suggest the use of a milder but less risky edge-preserving prior in case such optimal alignment cannot be guaranteed. The need for an accurate alignment of the anatomical and the emission datasets, highlighted in this work, might be of interest also outside of the scope of cardiac examinations. For example, brain studies could suffer from the same issues, if motion occurred between the acquisition of the PET and of the anatomical image for partial volume correction (e.g. the patient's head slightly moved).

### ***In vivo vs ex vivo experiments***

The elements collected and the results obtained in the previous studies allowed us to proceed to the last part of this work, whose objective was to correlate the activity concentrations of and the figures-of-merit extracted from the ground truth (microPET) dataset to those obtained from the corresponding *in vivo* PET datasets. The correction for motion of clinical, cardiac PET datasets, in the attempt to obtain quantitative images with reduced noise levels, was already subject of previous investigations [22, 76]. However, to our knowledge, none of the previous studies focused on accurate image quantification and aimed at reconstructions with fine spatial, on top of temporal, resolution. Additionally, these studies did not compare their findings to a ground-truth.

We explored this topic in Chapter 5. The correlation between the *in vivo* and the *ex vivo* datasets encountered a first difficulty in the increase of cardiac uptake during the scans, which made it harder to compare in absolute terms the microPET activity concentrations to the mean *in vivo* uptake. The resulting FDG datasets were not a pure static description of FDG uptake, but included un-modelled effects such as tracer dynamics and anaesthesia, which complicated our initial plan to compare *in-vivo* and *ex-vivo* activity concentrations more than initially expected. Unfortunately, the techniques available at present did not allow us to perform dual-gated, dynamic reconstructions as this would retain a too small fraction of counts/frame, thus we had to assume a steady state (also in agreement with clinical protocols, where the time of scanning is between 30 and 60 minutes post-injection). Performing the acquisition later, assuming a plateau of the uptake is obtained, would have been an option if anaesthesia was not required. In fact, the administration of prolonged of anaesthesia may exert negative effects on the cardiac physiology. The chosen *in vivo* scan time was therefore a compromise between these two opposing needs, together with choosing it as reflective of the actual clinical work flow.

A correction of the offset between the LV activity of the microPET and the *in vivo* datasets was proposed and, with that, the evaluation of the different motion correc-

tion algorithms in comparison to the ground truth was carried out. The results on the available cohort showed an improvement in absolute quantification when correction for the cardiac and the respiratory motion is performed before reconstruction. The relative quantification, i.e. the assessment of regional (in)homogeneity in the *in vivo* datasets when compared to the *ex vivo* ground truth was also evaluated. Similarly to what happened with the comparison of anatomical and non-anatomical priors, the use of motion correction algorithms before reconstruction did not significantly hamper the assessment of myocardial relative uptake, nor changed the conclusions that might be drawn from an un-gated myocardial study. Despite the few limitations of this animal study, among which also a small sheep cohort and the basic motion-correction algorithm used, the work gives a first indication on the usefulness of motion correction in combination with resolution modelling at least for what absolute quantification of activity is concerned. The motion correction does not seem to be a significant source of errors when only the relative distribution of activity is needed.

### ***Advantages and pitfalls of the used animal model***

The rationale behind the acquisition of animal datasets was both to validate the definition of a controllable model of left-ventricular remodelling using sheep, and to obtain realistic cardiac datasets in controlled conditions that could be used for the validation and the testing of the different partial volume correction techniques.

Such designed animal model, despite useful for providing the first datasets for testing the selected reconstruction and motion correction techniques, was however not fully optimal to demonstrate the potential impact of partial volume correction on cardiac datasets. The expected thinning of the septal wall, which should have reached a minimum thickness of 4-5 millimetres (or lower) for the PVEs to be evident and for the PVC to make a significant difference in the reconstruction outcome, was instead not as pronounced. Echocardiographic measures for the whole available animal cohort revealed an average thickness of 9.8 mm for the septum and 11.0 mm for the lateral wall (both evaluated at end-diastole), thus minimizing the potential benefits of PVC techniques applied to our datasets. However, from both the simulation study of Chapter 4 and the *ex vivo* study of Chapter 3, it emerged that anatomy-based PVC techniques can yield substantial improvements when thinner regions are considered. This could be the case, for example, of non-transmural lesions or naturally thin regions of the heart, such as the apex or the right ventricle. In the light of these findings, an animal model featuring a non-transmural scar or an extremely pronounced asymmetrical wall thinning could have been probably more effective to clearly assess the benefits introduced by the proposed PVC techniques.

In the second place, a mention to the use of anaesthesia in our experimental animal setup is necessary. Previous studies on small animals have already pointed out an effect of isoflurane on myocardial tracer uptake [175], thus leaving the question open on whether the reported absolute concentration values are representative of the actual myocardial uptake had the animal been scanned awake. This is surely a limitation of the current experimental setup which, however, could not have been avoided with the available instrumentation. Most large animal studies using PET, MR or CT require general anaesthesia, which reduces overall animal motion and provides better control of respiration. Performing the same experiment without the use of anaesthesia would have been logically infeasible. Even though the administration

of anaesthesia might affect the reported absolute activity concentration values, it would anyway not modify the effectiveness of PVC techniques or the comparison with the corresponding *ex vivo* hearts. Additionally, we would also expect the effect of anaesthesia to globally affect cardiac physiology, so the comparison of regional distributions would still hold true.

An interesting feature of the available datasets was the availability of ground-truth datasets. The measurement of cardiac tracer uptake with the aid of the microPET was justified by the superior spatial resolution of this imaging system. This, in turn, led us to consider the microPET reconstruction image as a reliable ground truth, that is to say an ideal partial volume- free dataset which retained a realistic cardiac shape. Additionally, the *ex vivo* datasets acquired on the microPET scanner seemed to represent the best way to validate the chosen partial volume correction techniques without the results being obfuscated by a possibly imprecise motion correction. Against our initial expectations, after analysis we found that the procedures we were using to reconstruct the PET datasets were sub-optimal and the resulting images as such were not ideal as a ground truth. For example, some of the clinical *ex vivo* datasets did not fully resemble the activity distribution of the pre-clinical image, no matter which partial volume correction technique was chosen. An investigation of the causes of such behaviour resulted in what is highlighted in Chapter 2. The large, non-conventional shape of the *ex vivo* hearts causes an unforeseen scatter behaviour in the microPET datasets. This is emphasized by the small size of the bore of the microPET, which led the scattered activity to be (erroneously) estimated within the heart walls, thus changing in some cases the relative tracer distribution. Additionally, the study in Chapter 2 highlighted the need for a decent and appropriately histogrammed attenuation map from which the scatter is estimated. If this is not the case, overestimation of the scatter (and, therefore, mis-quantification) can occur. The correction of the microPET datasets both for attenuation and for scatter greatly improved the similarity of the clinical and pre-clinical activity distributions, thus encouraging us to pursue on the idea of comparing the myocardial uptake in such ideal, motion-free scenario. The results obtained in Chapter 3 were made possible thanks to these improvements.

Despite the potential of the microPET datasets, we acknowledge the presence of a few pitfalls of the experimental procedure which hampered the final comparison of the ground-truth datasets to the *in vivo* datasets. Two main aspects are responsible for such non-ideal outcome. Firstly, the planned experimental setup accounted for an *in vivo* scan of the available animals and their subsequent sacrifice and heart explant to obtain the ground truth dataset. However, due to the hospital regulations and experimental logistics, the sacrifice of the animal and heart extraction did not happen immediately after the end of the *in vivo* scan (but about 20 minutes after it). Therefore, the accumulation of FDG in the left ventricle between the end of the scan and the sacrifice was unknown, leading to uncertainties when the LV activity of the *ex vivo* and the *in vivo* LV activities needed to be compared in absolute terms. Secondly, the scan of an explanted heart filled with foam is different from the scan of a heart enclosed in the thoracic cage and fully surrounded by attenuating and scattering tissues. The filling of the *ex vivo* hearts with the polyurethane foam was not strictly regulated, thus resulting in a few cases where the cavity was over-injected and a thinner wall was obtained. The deformation of the structures caused by such over-filling could be one of the reasons why the activity distribution of the

*in vivo* and *ex vivo* datasets did not completely match in our analysis (Chapter 5). Additionally, not only does the use of an explanted heart remove the effects of motion, but it also simplifies the attenuation and scattering conditions – both of which are known to cause mis-quantification. A better approach to gradually achieve an ideal ground-truth would have been to stop the heart and the respiration in the sheep immediately after the end of the *in vivo* scans, to scan the entire sheep in these conditions (so that the attenuation and scatter effects are unchanged, and only the motion is removed), and only then to extract the heart, perform the *ex vivo* scans and all the subsequent comparisons. By proceeding this way, we could have achieved more control both over the dynamic LV uptake and over the other non-ideal conditions that occur when the heart is in its natural setting.

Finally, even though we eventually concluded that the use of a well-tuned non-anatomical prior produces results similar to a well-tuned anatomy-based prior, a mention to the choice of the imaging modality to obtain the anatomical information for PVC for cardiac datasets is needed. The extremely promising specifications of the dual-headed Siemens Somatom Definition Flash CT system made us initially rely on such scanner to obtain images with sufficient spatial and temporal resolution for potential anatomy-based PVC of our *in vivo* datasets. However, the heart beat of the animals used in this work (110 bpm) was too high for a correct reconstruction of the datasets coming from this scanner, resulting in most cases in anatomical images that were a patchwork of several cardiac phases, none of which fully matched the emission dataset. Additionally, during the course of the analyses we observed that CT does not highlight the differences between the healthy tissue and scarred myocardial tissue, as they have an almost identical linear attenuation coefficient. This is not ideal when partial volume correction and lesion detection are aimed at. Therefore, the use of CT for PVC was discarded in the course of this work, unless no lesions and no motion were present in the datasets. Due to the enhanced soft tissue contrast and to the ability to discriminate between healthy and scarred myocardium, the use of specific gated MR sequences would be advisable instead, particularly if an animal model of non-transmural myocardial infarction was considered.

### ***Clinical applications***

The information gathered thanks to the studies of this work can be of use when clinical applications of cardiac PET are considered. With these regards, two studies have been started in the scope of a broader project investigating the relationship of myocardial metabolism to other mechanical or hemodynamic parameters. In both studies, the application of motion-correction and edge-preserving prior information will help to further corroborate the results of this work. Firstly, a patient study aiming at diagnosing in a non-invasive way the effects of cardiac remodelling and cardiac resynchronization therapy was commenced. Patients with heart failure with decreased ejection fraction and myocardial dissynchrony were enrolled in a multicenter study. In this project, it was proposed to select candidates for CRT implantation based on inhomogeneities present in the dyssynchronous failing hearts. In fact, previous studies have indicated that different parameters related to the functional status of the septum are diminished in dyssynchrony. We hypothesized that patients with left ventricular dissynchrony will show characteristic uptake patterns in glucose metabolism and myocardial perfusion, which would allow the identification of those patients that suffer most from dissynchrony and that could be the best candidates for CRT. At the moment of writing this dissertation, about 20 patients

have been through the scanning process and their datasets are ready to be analysed. However, a clear limitation of the available motion correction and motion extraction algorithms has already emerged. In fact, as already demonstrated in previous literature, baseline drifts and sudden changes in breathing patterns have been observed in the majority of the acquired datasets. These events had a high occurrence rate during our patient acquisitions, and no available motion correction technique can be applied without the risk of wrongly correcting for motion or throwing away too much data. Enhanced methods are needed to more accurately correct for the irregular respiratory motion that affects the datasets, and their development should be a priority before any further investigation can be done. In fact, the application of any partial volume correction technique on datasets where residual motion blur is present would be conceptually wrong. The use of data-driven methods to both free the clinical work flow from the time-consuming set-up of the respiratory belt and to extract a possibly more accurate respiratory trace is particularly interesting and should be the subject of further analyses. Nevertheless, this will not be the final solution if the drift and the irregular breathing is real. A way to extract the motion displacements of the heart during the whole duration of the scan, and to later on apply those displacements to the list-mode dataset to correct for motion, should be also investigated.

The second study that has been initiated stemmed from the observation of increased papillary muscle uptake in the available animal datasets. Such occurrence was proven to be significantly correlated to the sphericity of the heart, which is an indicator of dilated cardiomyopathy. These findings might have direct implication on the importance of papillary muscle preservation during cardiac surgery. A study assessing the relationship between papillary muscles and cardiac dilatation on sheep datasets is currently ongoing [176]. The use of motion and partial volume correction (edge-preserving) techniques will be encouraged, to recover the activity concentration of the papillary muscles more accurately.

### ***Future perspectives***

Firstly, this study is a starting point in the process of estimation of absolute myocardial uptake, but achieving a truly physiological quantification in nmol/g/min is not yet reality – at least with the current experimental setup. The absolute quantification in these terms requires kinetic modelling of the tracer uptake, which is nowadays not clinical routine. This was also out of the scope of this study, where more emphasis was put on the gating and on the changes occurring in the steady-state condition if the various reconstruction methods were used. The currently available tools did not allow us to reconstruct dual-gated dynamic images with sufficient quality, even though this would have been the best approach to both achieve absolute quantification in nmol/g/min and to avoid the confounding effects due to the dynamic uptake mentioned earlier. A different approach to correct for the cyclical heart motions (e.g. by applying an event-by-event, list-mode based motion correction), might at the same time be the way to both improve the image quality of the static reconstructions (by using all the events in one respiratory cycle) and to perform kinetic modelling using PV corrected images with sufficient amount of counts per frame. With these regards, we see the potential impact of the presented PVC techniques in the attempt to improve the kinetic parameters' estimation. To present, some methods exist which estimate the spill-in and spill-out effects in PET based either on a corresponding anatomical image or to parametric models. How-

ever, they have been reported to be acceptable but not fully reliable. For example, the performance of the available methods can often differ for e.g. septum and lateral wall, as for the septum the left and right ventricular blood pool functions are available (thus enabling an accurate estimate of the PVE), whereas there is no easy way to estimate spill-in and spill-out between the wall and the region outside the heart for the lateral wall. An interesting extension of this work would be the application of the presented MAP approaches for PVC to dynamic imaging and to compare the kinetic parameters estimation to that performed using the traditional (or no) approaches for the estimation of partial volume effects.

The combined use of PET/MR could offer additional ways to exploit the anatomical information coming from the MR section of the imaging protocol. With these regards, the recent advances in hybrid devices that combine a PET and an MR module is a promising field, if anatomy-based partial volume correction is aimed at. While the currently available hybrid PET/CT devices fail in delivering accurate temporal and spatial resolution in thoracic studies, the use of simultaneous gated MR sequences in combination with motion-corrected PET could effectively overcome this shortcoming. Additionally, if the acquisitions were truly simultaneous, the use of the anatomical MR information should be less subject to mismatches due to patient transfers or motion, which could otherwise easily occur when the anatomical information was acquired on a dedicated CT or MR scanner. However, the use of anatomical priors might have a realistic future only if truly simultaneous systems are used, provided that the technical advances in MRI imaging manage to reduce the geometrical distortions and artefacts that nowadays still affect the MR measurements. For example, this translates into the acquisition of an MR sequence in a "frozen" state with a sufficiently high resolution, in 3D, and within a time compatible with the clinical routine. This is, however, still a relatively young and open research topic [67, 177]. In parallel, the development of accurate motion-correction techniques is of higher priority. List-mode motion correction techniques are particularly interesting with these regards, as they could simultaneously solve the problem of noisy PET frames and of motion blurring, with minimal discomfort for the patient.

As a final future perspective, the use of anatomical information on simultaneous PET/MR acquisitions should be explored in comparison to motion-corrected acquisitions on a time-of-flight (TOF) PET scanner. In fact, very recent studies have evaluated the performances and the added value of TOF information in combination with resolution modelling during iterative reconstruction of cardiac datasets, finding substantial improvements in lesion detection and recovery of the activity values when both are considered [178, 179]. It would be interesting to verify whether anatomy-enhanced PET reconstruction would still outperform TOF-based PET reconstruction, or whether the technological advancement introduced by TOF-PET could avoid the need to acquire high resolution anatomical side information (with all the issues that come with it, including more time consuming acquisitions, necessity of additional trained technologists to perform the scans, risks of misalignments, ...).

### **Conclusion**

Partial volume correction on cardiac PET datasets requires the simultaneous consideration of multiple aspects to produce sensible results. Not only does cardiac

PET imaging require advanced image reconstruction methods, but attention to the attenuation correction and to motion correction is also of primary importance, if quantitatively informative images are aimed at.

The conclusions that can be drawn from this project take into account not only the strictly technical outcome, but also the technological and logistical limitations faced in the current clinical practice. All in all, for left ventricular quantification, the use of an edge-preserving prior (e.g. TV) is regarded as the preferred choice not only for easiness of acquisition and implementation, but also because it yields quantitatively and qualitatively reasonable reconstructions, closer to the true activity distribution than the sole modelling of the resolution, without any risk of obtaining the wrong quantification due to residual misalignments of the anatomical and the emission datasets. The use of anatomical information is not recommended with the currently available instrumentation, unless truly simultaneous anatomical/emission scanning systems are used and the smallest structures of the heart are of interest. Once simultaneous systems will be fully integrated in the clinical routine, the use of anatomical information would be less prone to the artefacts connected to misalignment. If all remaining technical pitfalls of simultaneous hybrid systems were eventually accounted for, the benefits of using anatomy-based reconstruction methods for the PET datasets would certainly outperform the ones obtained with the use of a simple edge-preserving prior when lesion, volume delineation and small structure quantification are of interest. This project also indicates that motion correction of the datasets is useful for accurate absolute quantification of the tracer uptake.

# BIBLIOGRAPHY

- [1] L. J. Anderson, C. Miyazaki, G. R. Sutherland, and J. K. Oh, “Patient selection and echocardiographic assessment of dyssynchrony in cardiac resynchronization therapy,” *Circulation*, vol. 117, no. 15, pp. 2009–2023, Apr 2008.
- [2] J.-U. Voigt, T.-M. Schneider, S. Korder, M. Szulik, E. Gürel, W. G. Daniel, F. Rademakers, and F. A. Flachskampf, “Apical transverse motion as surrogate parameter to determine regional left ventricular function inhomogeneities: a new, integrative approach to left ventricular asynchrony assessment,” *European heart journal*, vol. 30, no. 8, pp. 959–968, 2009.
- [3] M. Szulik, M. Tillekaerts, V. Vangeel, J. Ganame, R. Willems, R. Lenarczyk, F. Rademakers, Z. Kalarus, T. Kukulski, and J.-U. Voigt, “Assessment of apical rocking: a new, integrative approach for selection of candidates for cardiac resynchronization therapy,” *European Heart Journal-Cardiovascular Imaging*, p. jeq081, 2010.
- [4] E. S. Chung, A. R. Leon, L. Tavazzi, J.-P. Sun, P. Nihoyannopoulos, J. Merlini, W. T. Abraham, S. Ghio, C. Leclercq, J. J. Bax *et al.*, “Results of the predictors of response to CRT (PROSPECT) trial,” *Circulation*, vol. 117, no. 20, pp. 2608–2616, 2008.
- [5] K. Vernooy, X. Verbeek, M. Peschar, and F. Prinzen, “Relation between abnormal ventricular impulse conduction and heart failure.” *Journal of interventional cardiology*, vol. 16, no. 6, pp. 557–562, 2003.
- [6] O. A. Smiseth, K. Russell, and H. Skulstad, “The role of echocardiography in quantification of left ventricular dyssynchrony: state of the art and future directions,” *European Heart Journal-Cardiovascular Imaging*, vol. 13, no. 1, pp. 61–68, 2012.
- [7] K. Russell, O. A. Smiseth, O. Gjesdal, E. Qvigstad, P. A. Norseng, I. Sjaastad, A. Opdahl, H. Skulstad, T. Edvardsen, and E. W. Remme, “Mechanism of prolonged electromechanical delay in late activated myocardium during left bundle branch block,” *American Journal of Physiology-Heart and Circulatory Physiology*, vol. 301, no. 6, pp. H2334–H2343, 2011.
- [8] H. F. Choi, F. E. Rademakers, and P. Claus, “Left-ventricular shape determines intramyocardial mechanical heterogeneity,” *American Journal of Physiology-Heart and Circulatory Physiology*, pp. ajphheart–00 568, 2011.

- [9] T. Delhaas, T. Arts, F. W. Prinzen, and R. S. Reneman, “Regional fibre stress-fibre strain area as an estimate of regional blood flow and oxygen demand in the canine heart.” *The Journal of Physiology*, vol. 477, no. Pt 3, p. 481, 1994.
- [10] S. Urheim, S. I. Rabben, H. Skulstad, E. Lyseggen, H. Ihlen, and O. A. Smiseth, “Regional myocardial work by strain doppler echocardiography and LV pressure: a new method for quantifying myocardial function,” *American Journal of Physiology-Heart and Circulatory Physiology*, vol. 288, no. 5, pp. H2375–H2380, 2005.
- [11] K. Russell, M. Eriksen, L. Aaberge, N. Wilhelmsen, H. Skulstad, E. W. Remme, K. H. Haugaa, A. Opdahl, J. G. Fjeld, O. Gjesdal *et al.*, “A novel clinical method for quantification of regional left ventricular pressure-strain loop area: a non-invasive index of myocardial work,” *European heart journal, ehs016*, 2012.
- [12] B. Nowak, A. M. Sinha, W. M. Schaefer, K.-C. Koch, H.-J. Kaiser, P. Hanrath, U. Buell, and C. Stellbrink, “Cardiac resynchronization therapy homogenizes myocardial glucosemetabolism and perfusion in dilated cardiomyopathy and left bundle branch block,” *Journal of the American College of Cardiology*, vol. 41, no. 9, pp. 1523–1528, 2003.
- [13] J. Vecera, M. Penicka, M. Eriksen, K. Russell, J. Bartunek, M. Vanderheyden, and O. Smiseth, “Wasted septal work in left ventricular dyssynchrony: a novel principle to predict response to cardiac resynchronization therapy,” *Eur Heart J Cardiovasc Imaging*, p. jew019, 2016.
- [14] T. H. Schindler, “Cardiac PET/computed tomography applications and cardiovascular outcome,” *PET clinics*, vol. 10, no. 3, pp. 441–459, 2015.
- [15] V. L. Murthy, M. Naya, C. R. Foster, J. Hainer, M. Gaber, G. Di Carli, R. Blankstein, S. Dorbala, A. Sitek, M. J. Pencina *et al.*, “Improved cardiac risk assessment with noninvasive measures of coronary flow reserve,” *Circulation*, vol. 124, no. 20, pp. 2215–2224, 2011.
- [16] S. Dorbala, D. Vangala, J. Semer, C. Strader, J. R. Bruyere Jr, M. F. Di Carli, S. C. Moore, and R. H. Falk, “Imaging cardiac amyloidosis: a pilot study using 18f-florbetapir positron emission tomography,” *European journal of nuclear medicine and molecular imaging*, vol. 41, no. 9, pp. 1652–1662, 2014.
- [17] J. Knuuti, H. R. Schelbert, and J. J. Bax, “The need for standardisation of cardiac fdg pet imaging in the evaluation of myocardial viability in patients with chronic ischaemic left ventricular dysfunction,” *European journal of nuclear medicine and molecular imaging*, vol. 29, no. 9, pp. 1257–1266, 2002.
- [18] G. El Fakhri, A. Kardan, A. Sitek, S. Dorbala, N. Abi-Hatem, Y. Lahoud, A. Fischman, M. Coughlan, T. Yasuda, and M. F. Di Carli, “Reproducibility and accuracy of quantitative myocardial blood flow assessment with 82rb pet: comparison with 13n-ammonia pet,” *Journal of Nuclear Medicine*, vol. 50, no. 7, pp. 1062–1071, 2009.

- [19] B. Nowak, A. M. Sinha, W. M. Schaefer, K. C. Koch, H. J. Kaiser, P. Hanrath, U. Buell, and C. Stellbrink, “Cardiac resynchronization therapy homogenizes myocardial glucose metabolism and perfusion in dilated cardiomyopathy and left bundle branch block,” *J. Am. Coll. Cardiol.*, vol. 41, no. 9, pp. 1523–1528, May 2003.
- [20] S. Shcherbinin and A. Celler, “Assessment of the severity of partial volume effects and the performance of two template-based correction methods in a spect/ct phantom experiment,” *Physics in medicine and biology*, vol. 56, no. 16, p. 5355, 2011.
- [21] T. Jones, “Myocardial tissue fraction correction for partial volume effects and measure of tissue viability,” 1991.
- [22] F. Gigengack, L. Ruthotto, M. Burger, C. H. Wolters, X. Jiang, and K. P. Schafers, “Motion correction in dual gated cardiac PET using mass-preserving image registration,” *IEEE transactions on medical imaging*, vol. 31, no. 3, pp. 698–712, 2012.
- [23] T. Abraham and J. Feng, “Evolution of brain imaging instrumentation,” in *Seminars in nuclear medicine*, vol. 41, no. 3. Elsevier, 2011, pp. 202–219.
- [24] M. R. Patel, R. D. White, S. Abbara, D. A. Bluemke, R. J. Herfkens, M. Picard, L. J. Shaw, M. Silver, A. E. Stillman, and J. Udelson, “2013 ACCF/ACR/ASE/ASNC/SCCT/SCMR Appropriate utilization of cardiovascular imaging in heart failure. A joint report of the American College of Radiology, Appropriateness Criteria Committee and the American College of Cardiology Foundation Appropriate Use Criteria Task Force,” *Journal of the American College of Cardiology*, vol. 61, no. 21, pp. 2207–2231, 2013.
- [25] T. Dill, “Contraindications to magnetic resonance imaging,” *Heart*, vol. 94, no. 7, pp. 943–948, 2008.
- [26] T. R. DeGrado, F. Bhattacharyya, M. K. Pandey, A. P. Belanger, and S. Wang, “Synthesis and preliminary evaluation of 18F-fluoro-4-thia-oleate as a PET probe of fatty acid oxidation,” *Journal of Nuclear Medicine*, vol. 51, no. 8, pp. 1310–1317, 2010.
- [27] R. Chekol, O. Gheysens, J. Cleynhens, P. Pokreisz, G. Vanhoof, M. Ahamed, S. Janssens, A. Verbruggen, and G. Bormans, “Evaluation of PET radioligands for in vivo visualization of phosphodiesterase 5 (PDE5),” *Nuclear medicine and biology*, vol. 41, no. 2, pp. 155–162, 2014.
- [28] J. Kim, “Hyperinsulinemic clamp to assess insulin sensitivity in vivo,” in *Type 2 Diabetes*, ser. Methods in Molecular Biology, C. Stocker, Ed. Humana Press, 2009, vol. 560, pp. 221–238.
- [29] M. Brambilla, C. Secco, M. Dominietto, R. Matheoud, G. Sacchetti, and E. Inglese, “Performance Characteristics Obtained for a New 3-Dimensional Lutetium Oxyorthosilicate-Based Whole-Body PET/CT Scanner with the NEMA NU 2-2001 Standard.” *J Nucl Med*, vol. 46, no. 12, 2005.

- [30] Y.-C. Tai, A. Ruangma, D. Rowland, S. Siegel, D. F. Newport, P. L. Chow, and R. Laforest, “Performance evaluation of the microPET focus: a third-generation microPET scanner dedicated to animal imaging,” *Journal of nuclear medicine*, vol. 46, no. 3, pp. 455–463, 2005.
- [31] J. S. Kim, J. S. Lee, K. C. Im, S. J. Kim, S.-Y. Kim, D. S. Lee, and D. H. Moon, “Performance measurement of the microPET focus 120 scanner,” *Journal of Nuclear Medicine*, vol. 48, no. 9, pp. 1527–1535, 2007.
- [32] D. L. Bailey, “Transmission scanning in emission tomography,” *European journal of nuclear medicine*, vol. 25, no. 7, pp. 774–787, 1998.
- [33] P. Kinahan, D. Townsend, T. Beyer, and D. Sashin, “Attenuation correction for a combined 3D PET/CT scanner,” *Medical physics*, vol. 25, no. 10, pp. 2046–2053, 1998.
- [34] C. Burger, G. Goerres, S. Schoenes, A. Buck, A. Lonn, and G. Von Schulthess, “PET attenuation coefficients from CT images: experimental evaluation of the transformation of CT into PET 511-keV attenuation coefficients,” *European Journal of Nuclear Medicine and Molecular Imaging*, vol. 29, no. 7, pp. 922–927, 2002.
- [35] A. R. d. Pierro and F. Crepaldi, “Activity and attenuation recovery from activity data only in emission computed tomography,” *Computational & Applied Mathematics*, vol. 25, no. 2-3, pp. 205–227, 2006.
- [36] M. Defrise, A. Rezaei, and J. Nuyts, “Time-of-flight PET data determine the attenuation sinogram up to a constant,” *Physics in medicine and biology*, vol. 57, no. 4, p. 885, 2012.
- [37] J. Carney, D. W. Townsend, V. Rappoport, and B. Bendriem, “Method for transforming CT images for attenuation correction in PET/CT imaging.” *Medical physics*, vol. 33, no. 4, pp. 976–983, 2006.
- [38] A. M. Alessio, S. Kohlmyer, K. Branch, G. Chen, J. Caldwell, and P. Kinahan, “Cine CT for attenuation correction in cardiac PET/CT,” *J. Nucl. Med.*, vol. 48, no. 5, pp. 794–801, May 2007.
- [39] T. Pan, O. Mawlawi, S. A. Nehmeh, Y. E. Erdi, D. Luo, H. H. Liu, R. Castillo, R. Mohan, Z. Liao, and H. A. Macapinlac, “Attenuation correction of PET images with respiration-averaged CT images in PET/CT,” *J. Nucl. Med.*, vol. 46, no. 9, pp. 1481–1487, Sep 2005.
- [40] K. L. Gould, T. Pan, C. Loghin, N. P. Johnson, A. Guha, and S. Sdringola, “Frequent diagnostic errors in cardiac PET/CT due to misregistration of CT attenuation and emission PET images: a definitive analysis of causes, consequences, and corrections,” *J. Nucl. Med.*, vol. 48, no. 7, pp. 1112–1121, Jul 2007.
- [41] C. C. Watson, “New, faster, image-based scatter correction for 3D PET,” *IEEE Transactions on Nuclear Science*, vol. 47, no. 4, pp. 1587–1594, 2000.

- [42] C. C. Watson, D. Newport, M. Casey, R. Beanlands, M. Schmand *et al.*, “Evaluation of simulation-based scatter correction for 3D PET cardiac imaging,” *IEEE Transactions on Nuclear Science*, vol. 44, no. 1, pp. 90–97, 1997.
- [43] A. L. Goertzen, Q. Bao, M. Bergeron, E. Blankemeyer, S. Blinder, M. Cañadas, A. F. Chatzilooannou, K. Dinelle, E. Elhami, H.-S. Jans *et al.*, “NEMA NU 4-2008 comparison of preclinical PET imaging systems,” *Journal of Nuclear Medicine*, vol. 53, no. 8, pp. 1300–1309, 2012.
- [44] S. Naidoo-Variawa, W. Lehnert, R. Banati, and S. Meikle, “Scatter correction for large non-human primate brain imaging using microPET,” *Physics in medicine and biology*, vol. 56, no. 7, p. 2131, 2011.
- [45] F. J. Siepel, M. G. Van Lier, M. Chen, J. A. Disselhorst, A. P. Meeuwis, W. J. Oyen, O. C. Boerman, and E. P. Visser, “Scanning multiple mice in a small-animal PET scanner: influence on image quality,” *Nuclear Instruments and Methods in Physics Research Section A: Accelerators, Spectrometers, Detectors and Associated Equipment*, vol. 621, no. 1, pp. 605–610, 2010.
- [46] D. Brasse, P. E. Kinahan, C. Lartizien, C. Comtat, M. Casey, and C. Michel, “Correction methods for random coincidences in fully 3D whole-body PET: impact on data and image quality,” *Journal of nuclear medicine*, vol. 46, no. 5, pp. 859–867, 2005.
- [47] W. W. Moses, “Fundamental limits of spatial resolution in PET,” *Nuclear Instruments and Methods in Physics Research Section A: Accelerators, Spectrometers, Detectors and Associated Equipment*, vol. 648, pp. S236–S240, 2011.
- [48] P. E. Kinahan and J. Rogers, “Analytic 3D image reconstruction using all detected events,” *IEEE Transactions on Nuclear Science*, vol. 36, no. 1, pp. 964–968, 1989.
- [49] H. Wieczorek, “The image quality of FBP and MLEM reconstruction,” *Physics in medicine and biology*, vol. 55, no. 11, p. 3161, 2010.
- [50] A. J. Rockmore and A. Macovski, “A maximum likelihood approach to emission image reconstruction from projections,” *IEEE Transactions on Nuclear Science*, vol. 23, no. 4, pp. 1428–1432, 1976.
- [51] J. Nuyts, “Unconstrained image reconstruction with resolution modelling does not have a unique solution,” *EJNMMI Physics*, vol. 1, no. 1, pp. 1–7, 2014.
- [52] P. J. Green, “On use of the EM for penalized likelihood estimation,” *Journal of the Royal Statistical Society. Series B (Methodological)*, pp. 443–452, 1990.
- [53] J. Nuyts, D. Beque, P. Dupont, and L. Mortelmans, “A concave prior penalizing relative differences for maximum-a-posteriori reconstruction in emission tomography,” *IEEE Trans Nucl Sci*, vol. 49, pp. 56–60, 2002.
- [54] K. Vunckx, A. Atre, K. Baete, A. Reilhac, C. M. Deroose, K. Van Laere, and J. Nuyts, “Evaluation of three MRI-based anatomical priors for quantitative PET brain imaging,” *IEEE Trans Med Imaging*, vol. 31, no. 3, pp. 599–612, Mar 2012.

- [55] J. Nuyts, K. Baete, D. Bequé, and P. Dupont, “Comparison between MAP and postprocessed ML for image reconstruction in emission tomography when anatomical knowledge is available,” *IEEE transactions on medical imaging*, vol. 24, no. 5, pp. 667–675, 2005.
- [56] E. Jonsson, S.-c. Huang, and T. Chan, “Total variation regularization in positron emission tomography,” *CAM report*, vol. 9848, 1998.
- [57] A. Chambolle and T. Pock, “A first-order primal-dual algorithm for convex problems with applications to imaging,” *Journal of Mathematical Imaging and Vision*, vol. 40, no. 1, pp. 120–145, 2011.
- [58] T. Chan, A. Marquina, and P. Mulet, “High-order total variation-based image restoration,” *SIAM Journal on Scientific Computing*, vol. 22, no. 2, pp. 503–516, 2000.
- [59] Q. Chen, P. Montesinos, Q. S. Sun, P. A. Heng *et al.*, “Adaptive total variation denoising based on difference curvature,” *Image and Vision Computing*, vol. 28, no. 3, pp. 298–306, 2010.
- [60] K. Michielsen, “Maximum a posteriori reconstruction for digital breast tomosynthesis,” Ph.D. dissertation, KU Leuven, 2016.
- [61] J. Bowsher, H. Yuan, L. Hedlund, T. Turkington, G. Akabani, A. Badea, W. Kurylo, C. Wheeler, G. Cofer, M. Dewhirst, and G. Johnson, “Utilizing MRI information to estimate F18-FDG distributions in rat flank tumors,” *IEEE Nucl Sci Symp Conf Rec*, pp. 2488 –2492, 2004.
- [62] K. Vunckx and J. Nuyts, “Heuristic modification of an anatomical markov prior improves its performance,” in *2010 IEEE Nuclear Science Symposium Conference Record*, 2010, pp. 3262–3266.
- [63] K. Baete, J. Nuyts, W. Van Paesschen, P. Suetens, and P. Dupont, “Anatomical-based FDG-PET reconstruction for the detection of hypometabolic regions in epilepsy,” *IEEE Transactions on Medical Imaging*, vol. 23, no. 4, pp. 510–519, 2004.
- [64] X. Zhuang, “Challenges and methodologies of fully automatic whole heart segmentation: a review,” *Journal of healthcare engineering*, vol. 4, no. 3, pp. 371–408, 2013.
- [65] “Flash speed. Lowest dose. SOMATOM Definition Flash.” [http://www.radiology.vcu.edu/docs/CT\\_Definition\\_Flash.pdf](http://www.radiology.vcu.edu/docs/CT_Definition_Flash.pdf), 2009, [Online].
- [66] P. Kellman and A. E. Arai, “Cardiac imaging techniques for physicians: Late enhancement,” *Journal of Magnetic Resonance Imaging*, vol. 36, no. 3, pp. 529–542, 2012.
- [67] S. G. Nekolla, C. Rischpler, and K. P. Kunze, “PET/MRI for cardiac imaging: Technical considerations and potential applications,” in *Molecular and Multimodality Imaging in Cardiovascular Disease*. Springer, 2015, pp. 29–48.

- [68] J. Ma, J. Zhao, and A. L. Yuille, “Non-rigid point set registration by preserving global and local structures,” *IEEE Transactions on Image Processing*, vol. 25, no. 1, pp. 53–64, 2016.
- [69] F. Maes, A. Collignon, D. Vandermeulen, G. Marchal, and P. Suetens, “Multimodality image registration by maximization of mutual information,” *IEEE Trans Med Imaging*, vol. 16, no. 2, pp. 187–198, Apr 1997.
- [70] M. Rajaram, A. K. Tahari, A. H. Lee, M. A. Lodge, B. Tsui, S. Nekolla, R. L. Wahl, F. M. Bengel, and P. E. Bravo, “Cardiac PET/CT misregistration causes significant changes in estimated myocardial blood flow,” *J. Nucl. Med.*, vol. 54, no. 1, pp. 50–54, Jan 2013.
- [71] L. M. Nilsson, “Respiration signals from photoplethysmography,” *Anesthesia & Analgesia*, vol. 117, no. 4, pp. 859–865, 2013.
- [72] R. D. Beach, P. H. Pretorius, G. Boening, P. P. Bruyant, B. Feng, R. R. Fulton, M. A. Gennert, S. Nadella, and M. A. King, “Feasibility of stereo-infrared tracking to monitor patient motion during cardiac SPECTimaging,” *IEEE transactions on nuclear science*, vol. 51, no. 5, pp. 2693–2698, 2004.
- [73] S. H. Lim, E. Golkar, and A. A. A. Rahni, “Respiratory motion tracking using the Kinect camera,” in *Biomedical Engineering and Sciences (IECBES), 2014 IEEE Conference on*. IEEE, 2014, pp. 797–800.
- [74] F. Ernst and P. Saß, “Respiratory motion tracking using Microsofts Kinect v2 camera,” *Current Directions in Biomedical Engineering*, vol. 1, no. 1, pp. 192–195, 2015.
- [75] Y. Nam, Y. Kong, B. Reyes, N. Reljin, and K. H. Chon, “Monitoring of heart and breathing rates using dual cameras on a smartphone,” *PloS one*, vol. 11, no. 3, p. e0151013, 2016.
- [76] A. Martinez-Möller, D. Zikic, R. M. Botnar, R. A. Bundschuh, W. Howe, S. I. Ziegler, N. Navab, M. Schwaiger, and S. G. Nekolla, “Dual cardiac-respiratory gated PET: implementation and results from a feasibility study,” *European Journal of Nuclear Medicine and Molecular Imaging*, vol. 34, no. 9, pp. 1447–1454, 2007.
- [77] R. A. Bundschuh, A. Martínez-Moeller, M. Essler, M.-J. Martínez, S. G. Nekolla, S. I. Ziegler, and M. Schwaiger, “Postacquisition detection of tumor motion in the lung and upper abdomen using list-mode PET data: a feasibility study,” *Journal of Nuclear Medicine*, vol. 48, no. 5, pp. 758–763, 2007.
- [78] J. D. Hoisak, K. E. Sixel, R. Tirona, P. C. Cheung, and J.-P. Pignol, “Correlation of lung tumor motion with external surrogate indicators of respiration,” *International Journal of Radiation Oncology\* Biology\* Physics*, vol. 60, no. 4, pp. 1298–1306, 2004.
- [79] D. Ionascu, S. B. Jiang, S. Nishioka, H. Shirato, and R. I. Berbeco, “Internal-external correlation investigations of respiratory induced motion of lung tumors,” *Medical physics*, vol. 34, no. 10, pp. 3893–3903, 2007.

- [80] F. Gigengack, L. Ruthotto, M. Burger, C. H. Wolters, X. Jiang, and K. P. Schafers, “Motion correction in dual gated cardiac PET using mass-preserving image registration,” *IEEE Transactions on Medical Imaging*, vol. 31, no. 3, pp. 698–712, March 2012.
- [81] F. Buther, M. Dawood, L. Stegger, F. Wubbeling, M. Schafers, O. Schober, and K. P. Schafers, “List mode-driven cardiac and respiratory gating in PET,” *J. Nucl. Med.*, vol. 50, no. 5, pp. 674–681, May 2009.
- [82] K. Thielemans, P. Schleyer, P. Marsden, R. Manjeshwar, S. Wollenweber, and A. Ganin, “Comparison of different methods for data-driven respiratory gating of PET data,” in *Nuclear Science Symposium and Medical Imaging Conference, 2013 IEEE*, Oct 2013, pp. 1–4.
- [83] P. J. Schleyer, M. J. O’Doherty, S. F. Barrington, and P. K. Marsden, “Retrospective data-driven respiratory gating for PET/CT,” *Physics in medicine and biology*, vol. 54, no. 7, p. 1935, 2009.
- [84] D. Visvikis, O. Barret, T. Fryer, A. Turzo, F. Lamare, C. C. Le Rest, and Y. Bizais, “A posteriori respiratory motion gating of dynamic PET images,” in *Nuclear Science Symposium Conference Record, 2003 IEEE*, vol. 5. IEEE, 2003, pp. 3276–3280.
- [85] A. L. Kesner, R. A. Bundschuh, N. C. Detorie, M. Dahlbom, S. I. Ziegler, J. Czernin, and D. H. Silverman, “Respiratory gated PET derived in a fully automated manner from raw PET data,” *IEEE Transactions on Nuclear Science*, vol. 56, no. 3, pp. 677–686, 2009.
- [86] C. Liu, L. A. Pierce, A. M. Alessio, and P. E. Kinahan, “The impact of respiratory motion on tumor quantification and delineation in static PET/CT imaging,” *Phys Med Biol*, vol. 54, no. 24, pp. 7345–7362, Dec 2009.
- [87] W. van Elmpt, J. Hamill, J. Jones, D. De Ruysscher, P. Lambin, and M. Ollers, “Optimal gating compared to 3D and 4D PET reconstruction for characterization of lung tumours,” *Eur. J. Nucl. Med. Mol. Imaging*, vol. 38, no. 5, pp. 843–855, May 2011.
- [88] M. Dawood, F. Buther, N. Lang, O. Schober, and K. P. Schafers, “Respiratory gating in positron emission tomography: A quantitative comparison of different gating schemes,” *Medical Physics*, vol. 34, no. 7, p. 3067, Jun. 2007.
- [89] S. S. Jani, C. G. Robinson, M. Dahlbom, B. M. White, D. H. Thomas, S. Gaudio, D. A. Low, and J. M. Lamb, “A comparison of amplitude-based and phase-based positron emission tomography gating algorithms for segmentation of internal target volumes of tumors subject to respiratory motion,” *International Journal of Radiation Oncology\* Biology\* Physics*, vol. 87, no. 3, pp. 562–569, 2013.
- [90] B. Florian, M. He, K. P. Sch *et al.*, “Investigating the influence of baseline drifts of respiratory signals in amplitude-based gating for positron emission tomography,” in *2014 IEEE Nuclear Science Symposium and Medical Imaging Conference (NSS/MIC)*. IEEE, 2014, pp. 1–4.

- [91] W. P. Segars, G. Sturgeon, S. Mendonca, J. Grimes, and B. Tsui, “4D XCAT phantom for multimodality imaging research.” *Med Phys*, vol. 37, no. 9, p. 4902:15, 2010.
- [92] L. R. Dice, “Measures of the amount of ecologic association between species,” *Ecology*, vol. 26, no. 3, pp. 297–302, 1945.
- [93] M. J. Knuuti, P. Nuutila, U. Ruotsalainen, M. Ters, M. Saraste, R. Hrknen, A. Ahonen, U. Wegelius, A. Haapanen, and J. Bergman, “The value of quantitative analysis of glucose utilization in detection of myocardial viability by PET.” *J Nucl Med*, vol. 34, no. 12, p. 206875, Dec. 1993.
- [94] M. Rajaram, A. Tahari, A. Lee, M. Lodge, B. Tsui, S. Nekolla, R. Wahl, F. Bengel, and P. Bravo, “Cardiac PET/CT misregistration causes significant changes in estimated myocardial blood flow,” *J Nucl Med*, vol. 54, pp. 50–4, 2013.
- [95] F. Lamare, M. Ledesma Carbayo, T. Cresson, G. Kontaxakis, A. Santos, C. Le Rest, A. Reader, and D. Visvikis, “List-mode-based reconstruction for respiratory motion correction in PET using non-rigid body transformations.” *Phys Med Biol.*, vol. 7, no. 52(17), pp. 5187–204, Sep.
- [96] A. M. Alessio and P. E. Kinahan, “Improved quantitation for PET/CT image reconstruction with system modeling and anatomical priors.” *Med Phys*, vol. 33, p. 4095:4103, 2006.
- [97] K. Vunckx, A. Atre, K. Baete, A. Reilhac, C. M. Deroose, K. Van Laere, and J. Nuyts, “Evaluation of three MRI-based anatomical priors for quantitative PET brain imaging.” *IEEE Trans Med Imaging*, vol. 31, no. 3, p. 599612, Mar. 2012.
- [98] J. Cheng-Liao and J. Qi, “PET image reconstruction with anatomical edge guided level set prior,” *Phys Med Biol.*, vol. 56, no. 21, p. 6899, 2011.
- [99] G. Mok, T. Sun, T.-C. Huang, and M. I. Vai, “Interpolated average CT for attenuation correction in PET—A simulation study,” *IEEE Trans on Biomed Engineering*, vol. 60, no. 7, pp. 1927–1934.
- [100] R. Boellaard, “Standards for PET Image Acquisition and Quantitative Data Analysis.” *J Nucl Med*, vol. 50, no. Suppl 1, p. 11:20, 2009.
- [101] W. van Elmpt, J. Hamill, J. Jones, D. De Ruysscher, P. Lambin, and M. llers, “Optimal gating compared to 3D and 4D PET reconstruction for characterization of lung tumours,” *European Journal of Nuclear Medicine and Molecular Imaging*, vol. 38, no. 5, pp. 843–855, 2011.
- [102] A. Martinez-Möller, M. Souvatzoglou, N. Navab, M. Schwaiger, and S. Nekolla, “Artifacts from misaligned CT in cardiac perfusion PET/CT studies: frequency, effects, and potential solutions.” *J Nucl Med*, vol. 48, no. 2, pp. 188–93, Feb 2007.

- [103] K. Khurshid, R. J. McGough, and K. Berger, “Automated cardiac motion compensation in PET/CT for accurate reconstruction of pet myocardial perfusion images,” *Physics in Medicine and Biology*, vol. 53, no. 20, p. 5705, 2008.
- [104] A. Turco, J. Nuyts, O. Gheysens, J. Voigt, P. Claus, and K. Vunckx, “Registration between respiratory-gated PET/CT and high-resolution CT with XCAT simulations: Evaluation and optimization for subsequent PVC,” in *Nuclear Science Symposium and Medical Imaging Conference (NSS/MIC), 2013 IEEE*, Oct 2013, pp. 1–6.
- [105] M. D. Cerqueira, N. Weissman, V. Dilsizian, A. Jacobs, S. Kaul, W. Laskey, D. Pennell, J. Rumberger, T. Ryan, and M. Verani, “Standardized myocardial segmentation and nomenclature for tomographic imaging of the heart a statement for healthcare professionals from the cardiac imaging committee of the Council on Clinical Cardiology of the American Heart Association.” *Circulation*, vol. 105.4, pp. 539–542, 2002.
- [106] C. Studholme, D. L. G. Hill, and D. J. Hawkes, “An overlap invariant entropy measure of 3D medical image alignment.” *Pattern Recognition*, vol. 32, p. 71:86, 1999.
- [107] T. Sun, T.-H. Wu, S.-J. Wang, B.-H. Yang, N.-Y. Wu, and G. S. P. Mok, “Low dose interpolated average CT for thoracic PET/CT attenuation correction using an active breathing controller,” *Medical Physics*, vol. 40, no. 10, pp. –, 2013.
- [108] F. Maes, A. Collignon, D. Vandermeulen, G. Marchal, and P. Suetens, “Multimodality image registration by maximization of mutual information,” *IEEE Trans Med Imaging*, vol. 16, no. 2, pp. 187–198, Apr 1997.
- [109] R. Shekhar, V. Walimbe, S. Raja, V. Zagrodsky, M. Kanvinde, G. Wu, and B. Bybel, “Automated 3-dimensional elastic registration of whole-body PET and CT from separate or combined scanners,” *Journal of Nuclear Medicine*, vol. 46, no. 9, pp. 1488–1496, 2005.
- [110] J. A. Jarcho, “Biventricular pacing,” *New England Journal of Medicine*, vol. 355, no. 3, pp. 288–294, 2006.
- [111] K. Russell, M. Eriksen, L. Aaberge, N. Wilhelmsen, H. Skulstad, E. W. Remme, K. H. Haugaa, A. Opdahl, J. G. Fjeld, O. Gjesdal, T. Edvardsen, and O. A. Smiseth, “A novel clinical method for quantification of regional left ventricular pressure-strain loop area: a non-invasive index of myocardial work,” *European Heart Journal*, 2012.
- [112] D. Birnie, R. A. deKemp, T. D. Ruddy, A. S. Tang, A. Guo, K. Williams, R. Wassenar, M. Lalonde, and R. S. Beanlands, “Effect of lateral wall scar on reverse remodeling with cardiac resynchronization therapy,” *Heart Rhythm*, vol. 6, no. 12, pp. 1721 – 1726, 2009.
- [113] C. Liu, L. Pierce, A. Alessio, and P. Kinahan, “The impact of respiratory motion on tumor quantification and delineation in static PET/CT imaging.” *Phys Med Biol*, vol. 54, no. 24, pp. 7345–62.

- [114] A. Rezaei, M. Defrise, and J. Nuyts, “ML-reconstruction for TOF-PET with simultaneous estimation of the attenuation factors,” *IEEE Trans Med Imaging*, vol. 33, no. 7, pp. 1563–1572, Jul 2014.
- [115] A. Rezaei, M. Defrise, G. Bal, C. Michel, M. Conti, C. Watson, and J. Nuyts, “Simultaneous reconstruction of activity and attenuation in time-of-flight PET,” *IEEE Trans Med Imaging*, vol. 31, no. 12, pp. 2224–2233, Dec 2012.
- [116] K. Erlandsson, I. Buvat, P. H. Pretorius, B. A. Thomas, and B. F. Hutton, “A review of partial volume correction techniques for emission tomography and their applications in neurology, cardiology and oncology,” *Phys Med Biol*, vol. 57, no. 21, pp. R119–159, Nov 2012.
- [117] M. Burger, J. Müller, E. Papoutsellis, and C. B. Schnlieb, “Total variation regularization in measurement and image space for PET reconstruction,” *Inverse Problems*, vol. 30, no. 10, p. 105003, 2014.
- [118] A. Turco, J. Duchenne, J. Nuyts, O. Gheysens, J. Voigt, P. Claus, and K. Vunckx, “Validation of Anatomy-Enhanced Cardiac FDG-PET Imaging: an Ex Vivo Sheep Study,” *IEEE Nucl Sci Symp Conf Rec*, 2014.
- [119] M. E. Daube-Witherspoon and G. Muehllehner, “Treatment of axial data in three-dimensional PET,” *J Nucl Med*, vol. 28, no. 11, pp. 1717–1724, 1987.
- [120] J. Nuyts, P. Dupont, S. Stroobants, A. Maes, L. Mortelmans, and P. Suetens, “Evaluation of maximum-likelihood based attenuation correction in positron emission tomography,” *Nuclear Science, IEEE Transactions on*, vol. 46, no. 4, pp. 1136–1141, 1999.
- [121] J. Nuyts, L. Mortelmans, P. Suetens, A. Oosterlinck, and M. de Rou, “Model-based quantification of myocardial perfusion images from SPECT,” *J. Nucl. Med.*, vol. 30, no. 12, pp. 1992–2001, Dec 1989.
- [122] U. K. Sampson, S. Dorbala, A. Limaye, R. Kwong, and M. F. Di Carli, “Diagnostic accuracy of rubidium-82 myocardial perfusion imaging with hybrid positron emission tomography/computed tomography in the detection of coronary artery disease,” *Journal of the American College of Cardiology*, vol. 49, no. 10, pp. 1052–1058, 2007.
- [123] A. F. Schinkel, J. J. Bax, D. Poldermans, A. Elhendy, R. Ferrari, and S. H. Rahimtoola, “Hibernating myocardium: diagnosis and patient outcomes,” *Current problems in cardiology*, vol. 32, no. 7, pp. 375–410, 2007.
- [124] J. H. Rudd, E. Warburton, T. Fryer, H. Jones, J. Clark, N. Antoun, P. Johnström, A. Davenport, P. Kirkpatrick, B. N. Arch *et al.*, “Imaging atherosclerotic plaque inflammation with [18f]-fluorodeoxyglucose positron emission tomography,” *Circulation*, vol. 105, no. 23, pp. 2708–2711, 2002.
- [125] M. Soret, S. L. Bacharach, and I. Buvat, “Partial-volume effect in PET tumor imaging,” *J. Nucl. Med.*, vol. 48, no. 6, pp. 932–945, Jun 2007.

- [126] A. Turco, J. Nuyts, O. Gheysens, J. Duchenne, J.-U. Voigt, P. Claus, and K. Vunckx, “Lesion quantification and detection in myocardial 18f-fdg pet using edge-preserving priors and anatomical information from ct and mri: a simulation study,” *EJNMMI physics*, vol. 3, no. 1, pp. 1–32, 2016.
- [127] F. W. Prinzen, E. C. Cheriex, T. Delhaas, M. F. van Oosterhout, T. Arts, H. J. Wellens, and R. S. Reneman, “Asymmetric thickness of the left ventricular wall resulting from asynchronous electric activation: A study in dogs with ventricular pacing and in patients with left bundle branch block,” *American Heart Journal*, vol. 130, no. 5, pp. 1045 – 1053, 1995.
- [128] J. Duchenne, P. Claus, A. Turco, K. Vunckx, E. Pagourelias, P. Haemers, J. Van Puyvelde, O. Gheysens, F. Rega, and J. Voigt, “A new animal model of rapid pacing-induced dilated cardiomyopathy and lbbb,” *European Heart Journal - Cardiovascular Imaging*, vol. 16, no. suppl 2, p. Abstract No. P145., 2015.
- [129] J. H. Hubbell, S. M. Seltzer, N. I. of Standards, and T. (U.S.), *Tables of X-ray mass attenuation coefficients and mass energy-absorption coefficients 1 keV to 20 MeV for elements Z=1 to 92 and 48 additional substances of dosimetric interest*, web version. ed. U.S. Department of Commerce, Technology Administration, National Institute of Standards and Technology Gaithersburg, MD, 1996. [Online]. Available: <http://physics.nist.gov/PhysRefData/XrayMassCoef/cover.html>
- [130] J. Nuyts, “Unconstrained image reconstruction with resolution modelling does not have a unique solution,” *EJNMMI physics*, vol. 1, no. 1, p. 1, 2014.
- [131] J. Bowsher, H. Yuan, L. Hedlund, T. Turkington, G. Akabani, A. Badea, W. Kurylo, C. Wheeler, G. Cofer, M. Dewhirst, and G. Johnson, “Utilizing mri information to estimate f18-fdg distributions in rat flank tumors,” in *Nuclear Science Symposium Conference Record, 2004 IEEE*, vol. 4, Oct 2004, pp. 2488–2492 Vol. 4.
- [132] K. Vunckx and J. Nuyts, “Heuristic modification of an anatomical markov prior improves its performance,” in *Nuclear Science Symposium Conference Record (NSS/MIC), 2010 IEEE*, Oct 2010, pp. 3262–3266.
- [133] J. Nuyts, D. Beque, P. Dupont, and L. Mortelmans, “A concave prior penalizing relative differences for maximum-a-posteriori reconstruction in emission tomography,” *Nuclear Science, IEEE Transactions on*, vol. 49, no. 1, pp. 56–60, Feb 2002.
- [134] B. Fischl and A. M. Dale, “Measuring the thickness of the human cerebral cortex from magnetic resonance images,” *Proceedings of the National Academy of Sciences*, vol. 97, no. 20, pp. 11 050–11 055, 2000.
- [135] F. W. Prinzen, E. C. Cheriex, T. Delhaas, M. F. van Oosterhout, T. Arts, H. J. Wellens, and R. S. Reneman, “Asymmetric thickness of the left ventricular wall resulting from asynchronous electric activation: a study in dogs with ventricular pacing and in patients with left bundle branch block,” *American heart journal*, vol. 130, no. 5, pp. 1045–1053, 1995.

- [136] O. I. Soliman, M. L. Geleijnse, D. A. Theuns, A. Nemes, W. B. Vletter, B. M. van Dalen, A. K. Motawea, L. J. Jordaeans, and J. Folkert, “Reverse of left ventricular volumetric and structural remodeling in heart failure patients treated with cardiac resynchronization therapy,” *The American journal of cardiology*, vol. 101, no. 5, pp. 651–657, 2008.
- [137] S. Ho and P. Nihoyannopoulos, “Anatomy, echocardiography, and normal right ventricular dimensions,” *Heart*, vol. 92, no. suppl 1, pp. i2–i13, 2006.
- [138] S. Bokhari, A. Raina, E. B. Rosenweig, P. C. Schulze, J. Bokhari, A. J. Einstein, R. J. Barst, and L. L. Johnson, “Pet imaging may provide a novel biomarker and understanding of right ventricular dysfunction in patients with idiopathic pulmonary arterial hypertension,” *Circulation: Cardiovascular Imaging*, vol. 4, no. 6, pp. 641–647, 2011.
- [139] A. Turco, J. Nuyts, O. Gheysens, J. Duchenne, J.-U. Voigt, P. Claus, and K. Vunckx, “Lesion quantification and detection in myocardial 18f-fdg pet using edge-preserving priors and anatomical information from ct and mri: a simulation study,” *EJNMMI physics*, vol. 3, no. 1, pp. 1–32, 2016.
- [140] S. Nekolla, J. Dinges, and C. Rischpler, “Clinical impact of cardiac-gated PET imaging,” *PET Clinics*, vol. 8, no. 1, pp. 69–79, 2013.
- [141] F. Lamare, A. Le Maitre, M. Dawood, K. P. Schafers, P. Fernandez, O. E. Rimoldi, and D. Visvikis, “Evaluation of respiratory and cardiac motion correction schemes in dual gated PET/CT cardiac imaging,” *Med Phys*, vol. 41, no. 7, p. 072504, Jul 2014.
- [142] J. Ouyang, Q. Li, and G. E. Fakhri, “Magnetic resonance-based motion correction for positron emission tomography imaging,” *Seminars in Nuclear Medicine*, vol. 43, no. 1, pp. 60 – 67, 2013, pET/MRI.
- [143] K. Vunckx, P. Dupont, K. Goffin, W. Van Paesschen, K. Van Laere, and J. Nuyts, “Voxel-based comparison of state-of-the-art reconstruction algorithms for 18F-FDG PET brain imaging using simulated and clinical data,” *Neuroimage*, vol. 102 Pt 2, pp. 875–884, Nov 2014.
- [144] A. Turco, O. Gheysens, J. Nuyts, J. Duchenne, J. Voigt, P. Claus, and K. Vunckx, “Impact of CT-based attenuation correction on the registration between dual-gated cardiac PET and high-resolution CT,” *IEEE Trans Nuc Sci*, vol. 63, no. 1, pp. 180–192, Feb 2016.
- [145] A. Buades, B. Coll, and J. M. Morel, “A review of image denoising algorithms, with a new one,” *Multiscale Model Simul*, vol. 4, no. 2, pp. 490–530, 2005.
- [146] E. Inglese, L. Leva, R. Matheoud, G. Sacchetti, C. Secco, P. Gandolfo, M. Brambilla, and G. Sambuceti, “Spatial and temporal heterogeneity of regional myocardial uptake in patients without heart disease under fasting conditions on repeated whole-body 18F-FDG PET/CT,” *Journal of Nuclear Medicine*, vol. 48, no. 10, pp. 1662–1669, 2007.

- [147] J. G. Bogaert, H. T. Bosmans, F. E. Rademakers, E. P. Bellon, M. C. Herregods, J. A. Verschakelen, F. Van de Werf, and G. J. Marchal, “Left ventricular quantification with breath-hold MR imaging: comparison with echocardiography,” *MAGMA*, vol. 3, no. 1, pp. 5–12, Mar 1995.
- [148] M. A. Seliem, E. T. McWilliams, and M. Palileo, “Beat-to-beat variability of left ventricular indexes measured by acoustic quantification: influence of heart rate and respiration—correlation with M-mode echocardiography,” *J Am Soc Echocardiogr*, vol. 9, no. 3, pp. 221–230, 1996.
- [149] H. J. Berger, R. A. Davies, W. P. Batsford, P. B. Hoffer, A. Gottschalk, and B. L. Zaret, “Beat-to-beat left ventricular performance assessed from the equilibrium cardiac blood pool using a computerized nuclear probe,” *Circulation*, vol. 63, no. 1, pp. 133–142, Jan 1981.
- [150] A. Turco, J. Nuyts, O. Gheysens, J. Voigt, P. Claus, and K. Vunckx, “Partial Volume Correction of Doubly-Gated Cardiac Datasets using Anatomical and Edge-Preserving Priors.” *IEEE Nucl Sci Symp Conf Rec*, 2015.
- [151] P. Coup, J. V. Manjn, E. Gedamu, D. Arnold, M. Robles, and D. L. Collins, “Robust Rician noise estimation for MR images,” *Medical Image Analysis*, vol. 14, no. 4, pp. 483 – 493, 2010.
- [152] L. Livieratos, L. Stegger, P. M. Bloomfield, K. Schafers, D. L. Bailey, and P. G. Camici, “Rigid-body transformation of list-mode projection data for respiratory motion correction in cardiac PET,” *Physics in Medicine and Biology*, vol. 50, no. 14, p. 3313, 2005. [Online]. Available: <http://stacks.iop.org/0031-9155/50/i=14/a=008>
- [153] C.-H. Hsu, “A study of lesion contrast recovery for iterative PET image reconstructions versus filtered backprojection using an anthropomorphic thoracic phantom,” *Computerized Medical Imaging and Graphics*, vol. 26, no. 2, pp. 119 – 127, 2002.
- [154] D. Dickerscheid, J. Lavalaye, L. Romijn, and J. Habraken, “Contrast-noise-ratio (CNR) analysis and optimisation of breast-specific gamma imaging (BSGI) acquisition protocols,” *EJNMMI Res*, vol. 3, no. 1, p. 21, 2013.
- [155] J. Nuyts, L. Mortelmans, P. Suetens, A. Oosterlinck, and M. De Roo, “Model-Based Quantification of Myocardial Perfusion Images from SPECT.” *Journal of nuclear medicine*, vol. 30, pp. 1992–2001, 1989.
- [156] A. A. Isola, M. Grass, and W. J. Niessen, “Fully automatic nonrigid registration-based local motion estimation for motion-corrected iterative cardiac ct reconstruction,” *Medical Physics*, vol. 37, no. 3, 2010.
- [157] E. Kim, M. Lee, T. Inoue, and W.-H. Wong, *Clinical PET: Principles and Applications*, 2013.
- [158] G. Ginami, G. Bonanno, J. Schwitter, M. Stuber, and D. Piccini, “An iterative approach to respiratory self-navigated whole-heart coronary MRA significantly improves image quality in a preliminary patient study,”

- Magnetic Resonance in Medicine*, vol. 75, no. 4, pp. 1594–1604, 2016. [Online]. Available: <http://dx.doi.org/10.1002/mrm.25761>
- [159] L. Axel and R. Otazo, “Accelerated MRI for the assessment of cardiac function,” *The British Journal of Radiology*, 2016.
  - [160] J. Vontobel, R. Liga, M. Possner, O. F. Clerc, F. Mikulicic, P. Veit-Haibach, E. E. G. W. ter Voert, T. A. Fuchs, J. Stehli, A. P. Pazhenkottil, D. C. Benz, C. Gräni, O. Gaemperli, B. Herzog, R. R. Buechel, and P. A. Kaufmann, “MR-based attenuation correction for cardiac FDG PET on a hybrid PET/MRI scanner: comparison with standard ct attenuation correction,” *European Journal of Nuclear Medicine and Molecular Imaging*, vol. 42, no. 10, pp. 1574–1580, 2015.
  - [161] A. Turco, J. Nuyts, J. Duchenne, O. Gheysens, J. Voigt, P. Claus, and K. Vunckx, “Impact of partial volume correction on quantification and regional heterogeneity in cardiac pet,” *In preparation for submission to JNC*, 2016.
  - [162] M. M. Ter-Pogossian, S. R. Bergmann, and B. E. Sobel, “Influence of cardiac and respiratory motion on tomographic reconstructions of the heart: implications for quantitative nuclear cardiology.” *Journal of computer assisted tomography*, vol. 6, no. 6, pp. 1148–1155, 1982.
  - [163] M. A. Ahmed, P. Xiao, and Q. Xie, “New approach for simultaneous respiratory and cardiac motion correction in cardiac pet (namc-cpet),” *Physics in medicine and biology*, vol. 60, no. 19, p. 7779, 2015.
  - [164] T. Kokki, H. T. Sipilä, M. Teräs, T. Noponen, N. Durand-Schaefer, R. Klén, and J. Knuuti, “Dual gated PET/CT imaging of small targets of the heart: method description and testing with a dynamic heart phantom,” *Journal of nuclear cardiology*, vol. 17, no. 1, pp. 71–84, 2010.
  - [165] M. Dawood, F. Büther, N. Lang, O. Schober, and K. P. Schäfers, “Respiratory gating in positron emission tomography: a quantitative comparison of different gating schemes,” *Medical Physics*, vol. 34, no. 7, pp. 3067–3076, 2007.
  - [166] G. Cheng, A. Alavi, E. Lim, T. J. Werner, C. V. Del Bello, and S. R. Akers, “Dynamic changes of FDG uptake and clearance in normal tissues,” *Molecular Imaging and Biology*, vol. 15, no. 3, pp. 345–352, 2013.
  - [167] M. D. Cerqueira, N. J. Weissman, V. Dilsizian, A. K. Jacobs, S. Kaul, W. K. Laskey, D. J. Pennell, J. A. Rumberger, T. Ryan, M. S. Verani *et al.*, “Standardized myocardial segmentation and nomenclature for tomographic imaging of the heart a statement for healthcare professionals from the cardiac imaging committee of the council on clinical cardiology of the american heart association,” *Circulation*, vol. 105, no. 4, pp. 539–542, 2002.
  - [168] J. Nuyts, L. Mortelmans, P. Suetens, A. Oosterlinck, and M. de Rou, “Model-based quantification of myocardial perfusion images from SPECT,” *Journal of nuclear medicine: official publication, Society of Nuclear Medicine*, vol. 30, no. 12, p. 1992, 1989.

- [169] P. Zanco, A. Desideri, G. Mobilia, S. Cargnel *et al.*, “Effects of left bundle branch block on myocardial fdg pet in patients without significant coronary artery stenoses,” *The Journal of Nuclear Medicine*, vol. 41, no. 6, p. 973, 2000.
- [170] K. Yoshinaga and N. Tamaki, “Imaging myocardial metabolism,” *Current opinion in biotechnology*, vol. 18, no. 1, pp. 52–59, 2007.
- [171] D. G. Altman and J. M. Bland, “Measurement in medicine: the analysis of method comparison studies,” *The statistician*, pp. 307–317, 1983.
- [172] P. Zanco, F. Chierichetti, A. Fini, S. Cargnel, and G. Ferlin, “Myocardial perfusion, glucose utilization and oxidative metabolism in a patient with left bundle branch block, prior myocardial infarction and diabetes,” *The Journal of Nuclear Medicine*, vol. 39, no. 2, p. 261, 1998.
- [173] S. Hasegawa, H. Kusuoka, K. Maruyama, T. Nishimura, M. Hori, and J. Hatazawa, “Myocardial positron emission computed tomographic images obtained with fluorine-18 fluoro-2-deoxyglucose predict the response of idiopathic dilated cardiomyopathy patients to beta-blockers,” *Journal of the American College of Cardiology*, vol. 43, no. 2, pp. 224–233, 2004.
- [174] G. Vedala, P. Herrero, L. de las Fuentes, J. G. Rogers, D. P. Kelly, R. J. Gropler *et al.*, “Altered myocardial fatty acid and glucose metabolism in idiopathic dilated cardiomyopathy,” *Journal of the American College of Cardiology*, vol. 40, no. 2, pp. 271–277, 2002.
- [175] H. Toyama, M. Ichise, J.-S. Liow, D. C. Vines, N. M. Seneca, K. J. Modell, J. Seidel, M. V. Green, and R. B. Innis, “Evaluation of anesthesia effects on 18F-FDG uptake in mouse brain and heart using small animal PET,” *Nuclear medicine and biology*, vol. 31, no. 2, pp. 251–256, 2004.
- [176] J. Duchenne, A. Turco, P. Claus, K. Vunckx, J. Nuyts, E. Pagourelas, F. Rega, O. Gheysens, and J.-U. Voigt, “Papillary muscles contribute significantly to shortening of dilated left ventricles,” in *scheduled for oral presentation at the Young Investigator Award session*. Euroecho Congress 2016, Leipzig, 2016.
- [177] D. Bailey, B. Pichler, B. Gückel, H. Barthel, A. Beer, R. Botnar, R. Gillies, V. Goh, M. Gotthardt, R. Hicks *et al.*, “Combined PET/MRI: from status quo to status go. summary report of the fifth international workshop on PET/MR imaging; february 15–19, 2016; Tübingen, Germany,” *Molecular Imaging and Biology*, vol. 18, no. 5, pp. 637–650, 2016.
- [178] L. Presotto, L. Gianolli, M. Gilardi, and V. Bettinardi, “Evaluation of image reconstruction algorithms encompassing time-of-flight and point spread function modelling for quantitative cardiac pet: Phantom studies,” *Journal of Nuclear Cardiology*, vol. 22, no. 2, pp. 351–363, 2015.
- [179] R. Mattheoud, M. Lecchi, D. Lizio, C. Scabbio, C. Marcassa, L. Leva, A. Del Sole, C. Rodella, L. Indovina, C. Bracco *et al.*, “Comparative analysis of iterative reconstruction algorithms with resolution recovery and time of flight modeling for 18f-fdg cardiac pet: A multi-center phantom study,” *Journal of Nuclear Cardiology*, pp. 1–10, 2016.

# Curriculum Vitae

## Anna TURCO

**DOB:** 16 June 1988  
**Nationality:** Italian  
**Address:** Bogaardenstraat 28/003  
3000 Leuven, Belgium.  
**M** (+32) 491 919823  
**E** anna.turco.work@gmail.com

### Education

#### Ph.D. candidate in Biomedical Sciences, KU Leuven, Belgium.

- Starting date: Sep 2012
- Research topic: "Image processing methods for assessing myocardial energetics from FDG-PET/CT and 4D anatomical imaging".
- The research is supported by a research grant (OT) from KU Leuven and by the Fonds Wetenschappelijk Onderzoek – Research Foundation Flanders (FWO).
- Promotor: Prof. Dr. Piet Claus

#### M.Sc. in Biomedical Engineering, Universita degli studi di Padova, Italy.

- Date of graduation: July 2012
- Research topic: "Monte Carlo simulations of a small-animal PET scanner".
- The work was performed at the KTH Royal Institute of Technology, Stockholm.
- Supervisor: Prof. Dr. Massimiliano Colaristi-Tosti
- Grade: 110/110 cum laude

#### B.Sc in Biomedical Engineering, Universita degli studi di Padova, Italy.

- Date of graduation: July 2010
- Project in robotics, entitled: "Issues in hand rehabilitation of acute stroke patients".
- The project was performed with collaboration with the Mechanical Department.
- Supervisor: Prof. Dr. Giulio Rosati
- Grade: 110/110 cum laude

### Professional experience

#### PhD fellow on cardiac image processing

2012-present

Image processing expert and programmer at KU Leuven (Belgium).  
> Image processing and analysis (cardiac PET quantification)  
> Large animal experiments (acquisition, archiving and on-/off-line processing)  
> Usage and knowledge of several bio-imaging systems  
(Siemens Biograph 16 PET/CT, Siemens Somatom Definition Flash,  
Siemens Focus 220 microPET)

### Other relevant education and awards

#### IEEE Medical Imaging Conference (MIC) 2016 Student Award

November 2016

2nd best oral presentation award

#### Project management course

May 2016

Propellor ([www.propellor.be](http://www.propellor.be))

#### EIT Health Summer School for Innovation and Business Creation

July 2015

European Institute of Innovation and Technology (EIT), Health section

#### FWO fellow at KU Leuven (Belgium)

2013, 2015

Recipient of FWO fellowship in 2013 and 2015

> Fonds Wetenschappelijk Onderzoek/Research Foundation-Flanders  
(excellence-based funding organ of the Flemish government)

#### Exchange student at Boston University (USA)

Fall 2011

Grant awarded by Universita degli Studi di Padova (Italy)

## Skills

**Software:** Microsoft Office Suite,  
Adobe Photoshop/Lightroom

**Programming:** Assembly (basics), Java,  
MATLAB, IDL.

**Languages:** Italian (mother tongue),  
English (full working proficiency, IB-TOEFL score: 108/120),  
French (working proficiency),  
Dutch, Spanish (intermediate reading/listening proficiency),  
Swedish (very basic written understanding).

## Hobbies

Photography, swing-rock dancing, languages.

## List of publications

### International journal articles

- [1] **A. Turco**, O. Gheysens, J. Nuyts, J. Duchenne, J-U. Voigt, P. Claus, and K. Vunckx, “Impact of CT-based attenuation correction on the registration between dual-gated cardiac PET and high-resolution CT,” *IEEE Trans Nuc Sci*, 2016 Feb;63(1):180-92.
- [2] **A. Turco**, J. Nuyts, O. Gheysens, J. Duchenne, J-U. Voigt, P. Claus, and K. Vunckx, “Lesion quantification and detection in myocardial 18F-FDG PET using edge-preserving priors and anatomical information from CT and MRI: a simulation study.” *EJNMMI Physics*, 2016 Jun 17;3(1):9.
- [3] **A. Turco**, J. Nuyts, J. Duchenne, O. Gheysens, J-U. Voigt, P. Claus, and K. Vunckx, “Analysis of Partial Volume Correction on Quantification and Regional Heterogeneity in Cardiac PET.” *Accepted for publication in the Journal of Nuclear Cardiology*.
- [4] **A. Turco**, J. Nuyts, J. Duchenne, O. Gheysens, J-U. Voigt, P. Claus, and K. Vunckx, “Generating ground truth datasets for cardiac PET studies using a small-animal PET scanner.” *Under review in IEEE Transactions on Radiation and Plasma Medical Sciences*.

### Conference proceedings

- [1] **A. Turco**, J. Duchenne, J. Nuyts, O. Gheysens, J-U. Voigt, P. Claus, and K. Vunckx, “Registration between respiratory-gated PET/CT and high-resolution CT with XCAT simulations: Evaluation and optimization for subsequent PVC,” *IEEE Nucl Sci Symp Conf Rec*, pp. 1–6, 2013.
- [2] **A. Turco**, J. Duchenne, J. Nuyts, O. Gheysens, J-U. Voigt, P. Claus, and K. Vunckx, “Validation of Anatomy-Enhanced Cardiac FDG-PET Imaging: an Ex Vivo Sheep Study,” *IEEE Nucl Sci Symp Conf Rec*, 2014.
- [3] **A. Turco**, J. Nuyts, O. Gheysens, J-U. Voigt, P. Claus, and K. Vunckx, “Partial Volume Correction of Doubly-Gated Cardiac Datasets using Anatomical and Edge-Preserving Priors.” *IEEE Nucl Sci Symp Conf Rec*, 2015.

### Conference abstracts

- [1] **A. Turco**, J. Nuyts, O. Gheysens, J-U. Voigt, P. Claus, and K. Vunckx, “Anatomy-enhanced PET reconstructions using high resolution CT,” *Eur Heart J Cardiovasc Imaging Abstracts Supplement*, 2014.
- [2] J. Duchenne, P. Claus, **A. Turco**, K. Vunckx, E. Pagourelas, P. Haemers, J. Van Puyvelde, O. Gheysens, F. Rega, J-U. Voigt, “A new animal model of rapid pacing-induced dilated cardiomyopathy and LBBB.” *EuroEcho Imaging congress*, 2015.
- [3] J. Duchenne, **A. Turco**, P. Claus, K. Vunckx, E. Pagourelas, F. Rega, O. Gheysens, J-U. Voigt, “Relationship of FDG-PET and pressure-strain loops as novel measures of regional myocardial workload in LBBB-like dyssynchrony.” *EuroEcho Imaging congress*, 2015.
- [4] J. Duchenne, P. Claus, **A. Turco**, K. Vunckx, E. Pagourelas, F. Rega, O. Gheysens, J-U. Voigt, “Asynchronous electrical activation to induce dilated cardiomyopathy with left bundle branch block-like remodelling: A new ovine animal model.” *Acta Cardiologica: vol. 71 (1)*. Belgian Society of Cardiology. Brussels, Belgium, 28-29 January 2016.
- [5] J. Duchenne, **A. Turco**, P. Claus, K. Vunckx, E. Pagourelas, F. Rega, O. Gheysens, J-U. Voigt, “FDG-PET as novel, non-invasive measure of regional myocardial workload in LBBB-like dyssynchrony.”, *Acta Cardiologica: vol. 71 (1)*. Belgian Society of Cardiology. Brussels, Belgium, 28-29 January 2016.
- [6] J. Duchenne, **A. Turco**, P. Claus, K. Vunckx, E. Pagourelas, F. Rega, O. Gheysens, J-U. Voigt, “What is the papillary muscle contribution to LV function in dilated hearts?”, *ESC Congress*, 2016
- [7] J. Duchenne, **A. Turco**, P. Claus, K. Vunckx, E. Pagourelas, F. Rega, O. Gheysens, J-U. Voigt, “Papillary muscles contribute significantly to shortening of dilated left ventricles”, *accepted at EuroEcho congress (Dec 2016) for Young Investigator Award session*.